UNIVERZITA KARLOVA / CHARLES UNIVERSITY

LÉKAŘSKÁ FAKULTA V PLZNI / FACULTY OF MEDICINE IN PILSEN

Histologické hodnocení chirurgických experimentů u zvířecích modelů

Histological evaluation of surgical experiments in animal models

Dizertační práce/Ph.D. Thesis

MVDr. Martina Grajciarová

Školitel/Advisor: prof. MUDr. Mgr. Zbyněk Tonar, Ph.D.

Plzeň/Pilsen 2022

Bibliografické informace

Autor: MVDr. Martina Grajciarová

Název práce: Histologické hodnocení chirurgických experimentů u zvířecích modelů

Jazyk práce: český, anglický

Typ práce: Dizertační práce k získání akademického titulu Ph.D.

Univerzita: Univerzita Karlova

Fakulta: Lékařská fakulta v Plzni

Ústav: Ústav histologie a embryologie

Specializace: Anatomie, histologie, embryologie

Forma studia: prezenční

Školitel: prof. MUDr. Mgr. Zbyněk Tonar, Ph.D.

Počet stran: 175

Klíčová slova: kvantitativní histologie; stereologie; krkavice; koronární tepna; *arteria thoracica interna*; mikrocévy

Title: Histological evaluation of surgical experiments in animal models

Keywords: quantitative histology; stereology; carotid artery; coronary artery; internal thoracic artery; microvessels

Prohlášení:

Prohlašuji, že jsem závěrečnou práci zpracovala samostatně a že jsem řádně uvedla a citovala všechny použité prameny a literaturu. Současně prohlašuji, že práce nebyla využita k získání jiného nebo stejného titulu.

Souhlasím s trvalým uložením elektronické verze mé práce v databázi systému meziuniverzitního projektu Theses.cz za účelem soustavné kontroly podobnosti kvalifikačních prací.

V Plzni, 26.5.2022

Martina Grajciarová

Podpis

Abstrakt

Úvod: Dizertační práce je založena na šesti studiích, které se zaměřují na uplatnění kvantitativní histologie v hodnocení experimentů u zvířecích modelů. Zahrnuje představení postupů virtuální mikroskopie a strategií vzorkování obrazových polí, mapování změn mikroskopické struktury segmentů ovčích a prasečích krkavic a jejich porovnání s lidskými koronárními cévami a *arteria thoracica interna*, hodnocení vaskularizace u myšího modelu s xenografty lymfomů (PDX), vliv hyperbarické oxygenoterapie na tvorbu kolagenu typu III a na vaskularizaci v kožní ráně u Zucker Diabetic Fatty potkana.

Metody: Přehledový článek o virtuální mikroskopii byl zaměřen na ukázku příkladu vzorkování snímků z různých oblastí kvantitativní histologie. V ostatních studiích byly histologicky zpracované řezy barvené škálou metod zaměřených na stavbu cévní stěny, a buněčné osídlení (orcein, pikrosiriová červeň, Verhoeffův hematoxylin a zelený trichrom, Gillův hematoxylin, alcianová modř) a imunohistochemickým průkazem antigenů (α-hladký svalový aktin, neurofilamentový protein, CD-31, von Willebrandův faktor). Pomocí nevychýleného vzorkování a stereologických metod jsme kvantifikovali plošné podíly složek (elastin, kolagen, hladkosvalový aktin a chondroitinsulfát) použitím stereologické bodové mřížky; dvourozměrnou hustotu (jaderné profily, *nervi vasorum*, *vasa vasorum*, endotel mikrocév) pomocí počítacího rámečku; tloušťku cévní stěny jsme měřili lineárními sondami.

Výsledky: Rozdíly v mikroskopickém složení mezi levou a pravou krkavici stejného jedince byly podstatně větší u ovce nežli obdobné rozdíly prasete. Levé ovčí krkavice měly větší plošný podíl elastinu, menší podíl hladkosvalového aktinu a menší tloušťku intima-media než párové pravostranné krkavice. Prasečí krkavice měly na levé straně menší podíl elastinu a menší hustotu *vasa vasorum* v medii. U obou zvířecích modelů se podíl elastinu a chondroitinsulfátu snižoval v proximodistálním směru, naopak podíl hladkosvalového aktinu se zvyšoval. Ovčí krkavice měly po celé své délce svalový fenotyp, ale u prasečích došlo k změně fenotypu z elastického na svalový v proximodistálním směru. Krkavice obou zvířat se lišili od lidských koronárních cév a *arteria thoracica interna* ve většině histologických parametrů.

Srovnáním použití Dopplerovy ultrasonografie a kvantitativní histologie na stanovení plošného podílu mikrocév byly u lymfomů zjištěné značné rozdíly mezi těmito metodami.

U kvantitativní histologie byl plošný podíl malých PDX modelů nižší a velkých PDX modelů vyšší než u Dopplerovy ultrasonografie.

Hustota a plošný podíl mikrocév byly v myších xenoimplantátech významně nižší než v primárních lidských lymfomech.

Hyperbarická oxygenoterapie kožních ran u diabetických potkanů II. typu zvyšovala během hojení objemový podíl kolagenu typu III v hojící se dermis.

Závěr: Pomocí kvantitativní histologie jsme zjistili, že ovčí a prasečí krkavice nejsou ekvivalentní s lidskými koronárními cévami a *arteria thoracica interna*. Levé a pravé ovčí krkavice se lišili v mikroskopickém složení, což je limitující pro jejich vzájemnou ekvivalenci s kontrolními skupinami v chirurgických experimentech. Tyto rozdíly by měly být brány v úvahu při navrhování a interpretaci experimentů.

Studie vlivu hyperbarické oxygenoterapie naznačuje, že tato doplňková terapie by mohla urychlit hojení ischemických diabetických ran.

Součástí závěrů jednotlivých studií a jejich společným jmenovatelem jsou praktická doporučení pro optimalizaci designu studií s ohledem na jejich kvantitativní histologické hodnocení.

Abstract

Introduction: The dissertation is based on six studies that focus on the application of quantitative histology in animal model experiments. It includes a presentation of virtual microscopy procedures and image field sampling strategies, mapping changes in the microscopic structure of ovine and porcine carotid segments and their comparison with human coronary arteries and internal thoracic arteries, vascularization assessment in a mouse model of lymphoma xenografts (PDX), the effect of hyperbaric oxygen therapy on type III collagen production and on vascularization in a skin wound in a Zucker Diabetic Fatty rat.

Methods: The review article about virtual microscopy was focused on an example of sampling images from various areas of quantitative histology. In other studies, histologically processed sections were stained with a variety of methods for vascular wall construction, cell infiltration (orcein, picrosirius red, Verhoeff's hematoxylin and green trichrome, Gill's hematoxylin, alcian blue) and immunohistochemical antigen detection (α-smooth muscle actin, neurofilament protein, CD-31, von Willebrand factor). Using unbiased sampling and stereological methods, we quantified the area fraction of components (elastin, collagen, smooth muscle actin and chondroitin sulfate) using a stereological grid point; two-dimensional density (nuclear profiles, *nervi vasorum*, *vasa vasorum*, microvessel endothelium) using a counting frame; we measured the thickness of the artery wall using linear probes.

Results: The differences in microscopic composition between the left and right carotid artery of the same individual were significantly greater in sheep than in pigs. The left ovine carotid arteries had a greater area fraction of elastin, a smaller area fraction of smooth muscle actin and a thinner intima-media thickness than the paired right carotid arteries. The left porcine carotid arteries had a smaller area fraction of elastin and a smaller density of *vasa vasorum* in the tunica media. In both animal models, the area fraction of elastin and chondroitin sulfate decreased in the proximodistal direction, while the area fraction of smooth muscle actin increased. Ovine carotid arteries had a muscle phenotype along their entire length, but in pigs the phenotype changed from elastic to muscular in the proximodistal direction. The carotid arteries of both animal models differed from the human coronary arteries and the internal thoracic arteries in most histological parameters.

By comparing the use of Doppler ultrasonography and quantitative histology to determine the area fraction of microvessels, significant differences between these methods were found in lymphomas. In quantitative histology, the area fraction of small PDX models was smaller and large PDX models were greater than in Doppler ultrasonography.

Density and area fraction of microvessels were significantly lower in mouse xenografts than in primary human lymphomas.

Hyperbaric oxygen therapy of skin wounds in diabetic rats II. increased the volume fraction of type III collagen in the healing skin.

Conclusion:

Using quantitative histology, we found that ovine and porcine carotid arteries are not equivalent to human coronary arteries and the thoracic internal artery. The left and right ovine carotid arteries differed in microscopic composition, which is limiting their equivalence with control groups in surgical experiments. These differences should be taken into account when designing and interpreting experiments.

A study of the effect of hyperbaric oxygen therapy suggests that this adjunctive therapy could accelerate the healing of ischemic diabetic ulcers.

The conclusions of the individual studies and their common denominator include practical recommendations for optimizing study design with respect to quantitative histological assessment.

Předmluva

Dizertační práce s tématem „Histologické hodnocení chirurgických experimentů u zvířecích modelů" byla vypracována na Ústavu histologie a embryologie a v Laboratoři kvantitativní histologie Biomedicínského centra Lékařské fakulty v Plzni Univerzity Karlovy pod vedením školitele prof. MUDr. Mgr. Zbyňka Tonara, Ph.D. Práce je založena na šesti již publikovaných studiích, na kterých jsem se podílela následovně:

1.   Kolinko Y., … **Grajciarová M.** et al. (Anat Histol Embryol, 2022): Připravila jsem jeden z příkladů systematického nestranného vzorkování včetně fotodokumentace.

2.   Tomášek P., Tonar Z., **Grajciarová M.** et al. (Ann Anat, 2020): Rešerše literatury o prasečích krkavicích, o jejích anatomických, histologických a fyziologických vlastnostech a využití jako zvířecího modelu pro experimenty.

3.   **Grajciarová M.** et al. (Ann Anat, 2022): Moje prvoautorská studie, v které jsem se podílela na návrhu celé práce, odběru ovčích krkavic a na části histologických barvení. Zpracovala jsem celou fotodokumentaci a následně jsem pomocí kvantitativní histologie vyhodnotila mikrofotografie. Provedla jsem statistické hodnocení, sepsání a revizi manuskriptu. Studie byla podpořená projektem GA UK 1313420.

4.   Keša P., Pokorná E., **Grajciarová M.** et al. (Ultrasound Med Biol, 2021): Podílela jsem se na fotodokumentaci a kvantitativním hodnocení nádorových mikrocév, statistické analýze a přípravě části textu do manuskriptu.

5.   Jakša R., … **Grajciarová M.** et al. (Lab Invest, 2022): Podílela jsem se na fotodokumentaci a kvantitativním hodnocení nádorových mikrocév, přípravě histologické části textu do manuskriptu.

6.   Růžička, J., **Grajciarová M.** et al. (Physiol Res, 2021): Podílela jsem se na fotodokumentaci a kvantitativním hodnocení, statistické analýze a přípravě histologické části manuskriptu.

V Plzni dne 26.5.2022

Poděkování

Touto cestou bych se chtěla především poděkovat svému školiteli, prof. MUDr. Mgr. Zbyňkovi Tonarovi, Ph.D., za jeho odborné vedení, poskytnutí cenných odborných rad a připomínek, časté osobní konzultace a velkou trpělivost během celého mého studia.

Dále bych chtěla vyjádřit poděkování prof. MUDr. Mileně Králíčkové, Ph.D., a celému kolektivu Ústavu histologie a embryologie za vytvoření vynikajících pracovních podmínek.

V neposlední řadě chci poděkovat své rodině a příteli za podporu během celého mého studia.

Obsah

Seznam zkratek

A_A − area per area; plošný podíl (−)

AC   − *arteria coronaria;* koronární tepna

ACC   − *arteria carotis communis*; společný kmen krkavice

AKB   − aortokoronární bypass

ANOVA   − analysis of variance; analýza variance

ATI   − *arteria thoracica interna (a. mammaria)*; vnitřní hrudní tepna

CE   − coefficient of error; koeficient chyby

CTRL   − control group; kontrolní skupina

DLBCL   − diffuse large B-cell lymphoma; difuzní velkobuněčný B-lymfom

H_0 − nulová hypotéza

HBOT   − hyperbarická oxygenoterapie

IMT   − intima-media thickness; tloušťka intima a media (μm)

IWGDF   − Mezinárodní pracovní skupina pro diabetickou nohu

L_A − length per area; délková hustota (mm^{-1})

L_V − length per volume; dvourozměrná délková hustota (mm^{-2})

MCL   − mantle cell lymphoma, lymfom z plášťových buněk

MVA   − microvessel area; mikrocévní plošný podíl (−)

MVD   − microvessel density; mikrocévní hustota (mm^{-2})

NHL   − Non-Hodgkinův lymfom

N_V − number per volume; numerická hustota (mm^{-3})

P'_L − naměřená délková hustota průsečíku (mm^{-1})

PDX   − patient-derived xenografts, xenotransplantáty lymfomu

Q_A − quantity per area; dvourozměrná hustota objektů (mm^{-2})

SD   − standard deviation; směrodatná odchylka

SDN   − syndrom diabetické nohy

S_V − surface density; povrchová hustota (mm^{-1})

V_V − volume per volume; objemový podíl (−)

WT   − wall thickness; tloušťka stěny (μm)

ZDF   − Zucker Diabetic Fatty

1 Teoretický úvod

1.1 Kvantitativní histologie

V diagnostice morfologických změn ve stavbě tkání tradičně převažuje dosud kvalitativní histologie, založená na erudici a zkušenosti hodnotitele. Ve vědeckém výzkumu významně roste uplatnění kvantitativní histologie, která přináší údaje ve formě číselných dat, a to buďto v podobě semikvantitativních, nebo spojitých proměnných (Bolender, 1982; Kubínová et al., 2001; Pereira and Mandarim-de-Lacerda, 2001). K metodám kvantitativní histologie patří morfometrie a stereologie (Mandarim-de-Lacerda, 2003).

Morfometrie je běžně používanou histologickou technikou pro získávaní kvantitativních dát z histologických řezů. Její cílem je stanovení parametrů jako počet, délka, plocha nebo objem. Takto získaná data nám však neposkytuji informace o tkání jako celku a neberou v úvahu velikost, tvar a orientaci hodnocených částic, tj. neodrážejí kontextuální informaci o stavbě tkání (Brown, 2017; Pereira and Mandarim-de-Lacerda, 2001). Za zlatý standard získávaní kvantitativních morfologických údajů se považuje tzv. design-based stereologie, která je založena na kombinaci metod vzorkování a vlastních geometrických mřížek k získávání trojrozměrných informací o buňkách, tkáních či orgánech (Brown, 2017; Mühlfeld, 2014). Základní zásady tohoto oboru jsou zpracovány v klasických učebnicích (Howard and Reed, 2004; Mouton, 2013, 2011).

1.1.1 Stereologie

Stereologie (z řečtiny: *stereos* = těleso, pevná látka; *logos* = nauka) je vědní disciplína zaobírajíci se trojrozměrnou interpretaci rovinných řezů. Je založená na základních principech geometrie a statistického odvozování geometrických vlastností vzorek různého původu, velikosti a vnitřní struktury, přičemž je inspirována nejen obory biologickými, ale i materiálovými vědami, fraktografií, geologií, petrografií apod. (Baddeley and Jensen, 2004; Brown, 2017; Gardner et al., 2003; Tomaszewski et al., 2014; Tschanz et al., 2014). Kvantitativními daty tak můžeme popisovat stavbu a složení buněk, tkání a orgánů, popřípadě pak kvantitativní morfometrické parametry korelovat s fyziologickými a biochemickými údaji (Tschanz et al., 2014).

Základními parametry stereologie jsou objem, plocha, délka a počet, které mohou být vyjádřeny absolutně, popř. relativně v podobě jejich vzájemných poměrů (objemový podíl V_V, povrchová hustota S_V, délková hustota L_V a numerická hustota N_V) (Baddeley and Jensen, 2004; Brown, 2017; Peterson, 2010; Tomaszewski et al., 2014; Tonar, 2008; Tonar et al., 2007; Tschanz et al., 2014; Veras et al., 2014).

1.1.2 Plánovaní a realizace stereologické studie

Při přípravě a následném provedení stereologické studie je vhodné se vyhnout některým běžným nástrahám. Pro získání co nejpřesnějších a nevychýlených kvantitativních výsledků je rozhodující precizní naplánování studie, které zahrnuje celý postup experimentu od sběru orgánových vzorků, zpracování tkání až po samostatné histologické hodnocení. Už od samotného začátku je nutná spolupráce mezi všemi členy vědeckého týmu, včetně stereologa (Tschanz et al., 2014). Výsledky kvantitativní studie založené pouze na intuitivních základech a bez důkladného naplánování mohou být zkreslené náhodnými či systematickými chybami, popř. mohou být náchylné k nesprávné interpretaci (Mendis-Handagama and Ewing, 1990). Fáze plánování zahrnuje určení testovaného materiálu, místa a způsobu odběru vzorků, počtu vzorek, volbu strategie víceúrovňového vzorkování tkáňových bločků, řezů a zorných polí, volbu vhodného fixačního roztoku a barviv, plánování počtu mikroskopických snímků a zorných polí, vhodný výběr stereologické sondy a statistické metody (Gundersen et al., 1988; Hsia et al., 2010; Tschanz et al., 2014). Všechny této kroky pracovního postupu na sebe navzájem navazují, přičemž studie jako celek je validní do té míry, jako je její nejslabší článek (Tschanz et al., 2014). Proto je nanejvýš účelné, zmapovat variabilitu dat na každé z těchto úrovní zpracování a hodnocení.

Stereologický postup se skládá z dvou základných kroků: (i) nevychýlené vzorkování (unbiased sampling) na všech úrovních redukce materiálů od makroskopických vzorků až po zorná pole; (ii) nevychýlené (unbiased) hodnocení mikroskopických snímků s využitím vhodných geometrických mřížek (Tschanz et al., 2014).

Nejčastěji využívanou strategií vzorkování je tzv. systematický nestranný náhodný výběr (systematic uniform random sampling), který dává zpočátku všem částem hodnocených struktur stejnou pravděpodobnost, že budou hodnoceny (Baddeley and Jensen, 2004; Brown, 2017; Peterson, 2010; Tomaszewski et al., 2014; Tschanz et al., 2014). Orgán či tkáňový bloček je kompletně rozkrájen (exhaustive sectioning), přičemž pozice prvního

vybraného vzorku je určena náhodným číslem a následně se další vzorky odebírají systematicky v pravidelných vzorkovacích intervalech (Brown, 2017; Tschanz et al., 2014). Ty části makroskopického objektu, na nichž bude mikroskopické kvantitativní hodnocení založeno, se tak stávají součástí výběru s pravděpodobností přímo úměrnou četnosti svého výskytu a takový výběr můžeme pak považovat za reprezentativní (Boyce et al., 2010).

Při mikroskopickém hodnocení tkání řešíme zpravidla současně několik úrovní redukce hodnoceného materiálu (víceúrovňové vzorkování, multi-level sampling), přičemž na všech úrovních postupujeme dle stejné, výše popsané strategie. Obdobně postupujeme až na úroveň mikroskopických zorných polí, které, zejména při použití objektivů s vyšším zvětšením, nemusí zachytit celou část hodnoceného řezu. V tomto případě je nutné při snímkování řezů rovněž použít systematické nestranné náhodné vzorkování těch zorných polí, jejichž složení pak budeme hodnotit v dalším kroku pomocí geometrických stereologických mřížek či sond (Tschanz et al., 2014). Volba počtu potřebných zorných polí je zásadně ovlivněna mírou heterogenity distribuce námi hodnocených objektů a při nevhodně zvolené vzorkovací strategii může vést buďto k nadměrné pracnosti bez významného zpřesnění hodnocení (oversampling), nebo naopak k podhodnocení vzorkování vedoucímu k velkému nárůstu variability dat (undersampling) (Peterson, 2010; Tschanz et al., 2014).

Pokud máme vyřešeno vzorkování na všech úrovních redukce materiálu, přistupujeme k aplikaci geometrických sond na vybrané snímky. Z interakce geometrických mřížek známých vlastností (tzv. mřížkových konstant, grid constants) s námi hodnocenými strukturami vypočítáme geometrický statistický popis hodnocených struktur (Howard and Reed, 2004; Mouton, 2013, 2011). K tomu musejí být splněny dvě podmínky: (i) jednoznačná identifikace objektů našeho zájmu, které musí být možné bez pochybností rozlišit ve všech hodnocených částech vzorku; (ii) definice oblasti zájmu (region of interest), která může být tvořena buďto anatomicky přirozenými hranicemi (oblasti orgánů či jejich vrstvy), popřípadě jsme schopni ji definovat arbitrárními pravidly, ale vždy reprodukovatelně (například jedna třetina tloušťky cévní stěny).

Výběr vlastní stereologické sondy či mřížky závisí na veličině, kterou hodláme kvantifikovat. Z tzv. parametrů 1. řádu jsou to objemy, povrchy, délky, počty objektů, z parametrů vyšších řádů je to např. konektivita, shlukování a kolokalizace. Příkladem stereologických sond pro počítání objektů ve třech rozměrech je fyzikální či optický disektor; pro hodnocení délek se využívají plošné sondy; pro hodnocení ploch povrchů jsou

to lineární sondy a pro hodnocení objemů jsou to bodové testovací sondy. Součet geometrických rozměrů sondy a hodnoceného parametru musí být vždy minimálně tři, není tedy například možné hodnotit „počty buněk" běžných rozměrů z klasických histologických rutinních řezů. (Mandarim-de-Lacerda, 2003).

Pokud respektujeme výše uvedené principy, je již jen otázkou efektivity, ergonomie a nákladů, který konkrétní software pro stereologii zvolíme. Na kvantitativní stereologickou analýzu se používají různé komerčně dostupné stereologické programy, například program Ellipse (VIDITO, Kosice, Slovak Republic), systémy Stereotopix (Visiopharm, Aarhus, Denmark), Stereologer (SRC Biosciences, Tampa, FL, USA) (Hida et al., 2020; Mouton, 2013, 2011; Watson et al., 2020). Velké množství knihoven je k dispozici i v rámci volně dostupného balíku ImageJ a FIJI, které přinášejí výhodu uživatelům schopným programovat některé rutinní operace (Schindelin et al., 2012; Schneider et al., 2012).

1.2 Tepny

Systém krevních cév je tvořen tepnami, mikrocirkulací a žilami. Tepny na základě jejich stavby dělíme na elastické a svalové. K elastickým tepnám patří velké cévy v blízkosti srdce (aorta, odstupy větví aorty, plicnice) a jsou přizpůsobené velkým výkyvům tlakové amplitudy. Svalové tepny jsou středního až malého kalibru, tvoří většinu z tepen, jejichž úlohou je zabezpečit distribuci krve do všech tkání a orgánů (Shinaoka et al., 2013).

Z histologického hlediska tvoří stěnu tepen tunica intima, tunica media a tunica adventitia (Allaire et al., 1994; Katsimpoulas et al., 2015; Maschietto et al., 2017). Tunica intima je obvykle nejtenčí vrstvou, která se skládá z jedné vrstvy endoteliálních buněk nasedajících na bazální laminu a subendoteliální fibro-elastické vazivo (Li et al., 2014; Tennant and McGeachie, 1990). Endoteliální buňky, které jsou v přímým kontaktě s krví, hrají důležitou úlohu v homeostáze. Zúčastňují se trombolýzy a koagulačních procesů, tvoří difúzní bariéru, regulují vaskulární tonus a také jsou důležité pro zánětlivé a imunologické procesy.

Střetní vrstvou je tunica media tvořená elastickými lamelami, buňkami hladké svaloviny, kolagenem typu III a glykosaminoglykany. Množství elastinu a hladké svaloviny závisí od typu tepny. V elastických tepnách převládají elastická vlákna, v svalových naopak buňky hladké svaloviny. Ve větších krevních cévách mohou do vnější časti medie zasahovat

19

taky *vasa vasorum* z důvodu omezené difuze živin a metabolitů přes cévní stěnu (García et al., 2013, 2011; Li et al., 2014; Maschietto et al., 2017; Weizsäcker et al., 2014).

Poslední vnější vrstvou je tunica adventitia, která je složená hlavně z hrubých svazků kolagenu typu I, *vasa vasorum* a *nervi vasorum* (Witter et al., 2017, 2010).

1.2.1 Společný kmen krkavice u ovcí a prasat

Společný kmen krkavice (*arteria carotis communis*, ACC) je hlavní tepnou pro zásobení oblasti hlavy a krku okysličenou krví (Manbachi et al., 2011; Popesko et al., 1992; Schulz et al., 2016).

1.2.1.1 Anatomie a chirurgický přístup

ACC je párová tepna, která se nachází v úrovni krčních obratlů v hloubce přibližně 2 cm (Anderson et al., 2018; Manbachi et al., 2011; Popesko et al., 1992; Schulz et al., 2016). Její průměr je 2-6 mm, přičemž je větší v proximální části (Dondelinger et al., 1998; García et al., 2011). Ovčí a prasečí ACC se vyznačují snadným chirurgickým přístupem s možností použití stejného chirurgického instrumentária a šicího materiálu jako u člověka (Anderson et al., 2018). Při jejich anatomické poloze je možný monitoring jejich průchodnosti pomocí Dopplerove ultrasonografie a je taky poměrně snadná katetrizace (Anderson et al., 2018; Bastijanic et al., 2016; Dondelinger et al., 1998; Stewart et al., 2017).

Pro chirurgický zákrok je velmi důležitá znalost chirurga o anatomii samotné ACC ale i okolních anatomických struktur. Ve své proximální částí se ACC nachází na ventrální ploše průdušnice, pak prochází její dorzolaterálním povrchem (Popesko et al., 1992). Ventrálně od ACC se nachází *nervus laryngeus reccurrens*, dorzálně *truncus vagosympathicus* a laterálně *vena jugularis interna* (Popesko et al., 1992).

Pravá a levá ACC vznikají z *truncus bicaroticus*, který má svůj původ v *truncus brachiocephalicus* (Popesko et al., 1992; Rao et al., 2016). Jde o dlouhé cévy s minimálním větvením (ovce 7 větví, prase 5 větví) (Dondelinger et al., 1998; Popesko et al., 1992). Konkrétně se jedná o následující větve: *arteria thyroidea caudalis* (u prasete pouze na levé straně, u ovcí na obou stranách), nekonstantní svalové větve (*rami sternocleidomastoidei* (pouze u ovcí), *ramus pharyngeus* a *ramus laryngeus*), *arteria thyroidea cranialis*, *arteria*

laryngea cranialis, *arteria pharyngea ascendens* (pouze u ovcí), *arteria palatina ascendens* (pouze u ovcí) a *arteria carotis interna* (König and Liebich, 2002; Popesko et al., 1992). ACC pak pokračují přímo v podobě *arteria carotis externa* (Popesko et al., 1992).

1.2.1.2 Využiti v experimentech

Ovčí a prasečí ACC jsou preferovaným zvířecím modelem v experimentální chirurgii díky jejich anatomické a fyziologické podobnosti s kardiovaskulárním systémem člověka (Anderson et al., 2018; García et al., 2011; Schleimer et al., 2018).

Používají se například k testování jejich mechanických vlastností, které jsou důležité pro návrh vhodných stentů potřebných pro léčbu obstrukce nebo stenózy ACC a při akutní ischemické cévní mozkové příhodě (Fong et al., 2017; Jiang et al., 2016; Nikoubashman et al., 2018; Stewart et al., 2017; Zhou et al., 2016). Kromě toho jsou využívány pro testování cévních náhrad vyvíjených v rámci tkáňového inženýrství pro aortokoronární bypass (AKB), jako jsou například polytetrafluorethylen nebo poly-ε-kaprolaktonová nanovlákna (Fukunishi et al., 2016; Jaramillo et al., 2018; Mrówczyński et al., 2014; Tzchori et al., 2018; Wulff et al., 2017).

2 Cíle a hypotézy

Dizertační práce je tvořena souborem šesti studií zaměřených na kvantitativní histologii. První částí je přehledná práce metod víceúrovňového vzorkování s popisem jejich výhod a nevýhod. Dále jsem se zaměřila na kvantitativní hodnocení mikroskopického složení stěny ovčí a prasečí ACC, která je častým zvířecím modelem pro testování cévních štepů pro AKB. Získané histologická data stěny krkavic jsem porovnala s lidskýma koronárními cévami (*arteria coronaria*, AC) a *arteria thoracica interna* (ATI). V další časti jsem kvantitativně hodnotila mikrocévy, konkrétně v nádorovém mikroprostředí myších xenoimplantátu (PDX) odvozených od Non-Hodgkinova lymfomu (NHL) a v kožní ráně u Zucker Diabetic Fatty potkana (ZDF) po hyperbarické oxygenoterapii (HBOT). U ZDF potkanů jsme taky sledovali vliv HBOT na tvorbu kolagenu typu I a III.

Definovali jsme proto následující otázky:

1. Jaké jsou postupy virtuální mikroskopie? Jaké jsou výhody a nevýhody strategii víceúrovňového vzorkování v kvantitativní histologii?

2. Jsou pravá a levá prasečí ACC u stejného jedince ekvivalentní? Má prasečí ACC stejné mikroskopické složení v celé své délce? Jsou prasečí ACC shodné v mikroskopickém složení s lidskými AC a ATI?

3. Jsou pravá a levá ovčí ACC u stejného jedince zaměnitelné? Má ovčí ACC stejné mikroskopické parametry v celé své délce? Jsou ovčí ACC ekvivalentní s lidskými AC a ATI?

4. Jsou rozdíly mezi použitím Dopplerovy ultrasonografie a kvantitativní histologie při hodnocení hustoty nádorových mikrocév?

5. Jsou kvantitativní parametry mikrocév (microvessel density, MVD; microvessel area, MVA) v nádorovém mikroprostředí PDX modelů odvozených od NHL srovnatelné s primárními lidskými nádory typu NHL?

6. Jaký má vliv HBOT na tvorbu kolagenu typu I a III a na vaskularizaci v kožní ráně u ZDF potkana?

2.1 Vzorkování v kvantitativní histologii a stereologii

2.1.1 Motivace

Jedním ze základních problémů všech kvantitativně histologických studií je otázka víceúrovňového vzorkování. To obnáší redukci materiálu na úrovni odběru tkáňových bločků z makroskopických orgánů, dále výběr řezů pro barvení a hodnocení, výběr obrazových polí při zvoleném mikroskopickém zvětšení. Všechny tyto úrovně vyžadují definovanou strategii, aby bylo možné zhodnotit jejich podíl na celkové variabilitě výsledných dat. Výhodou takového přístupu je i možnost optimalizovat studii tak, aby největší pozornost bylo možné zaměřit na tu úroveň redukce materiálu, kde jsou rozdíly mezi vybíranými oblastmi největší, a tudíž zasluhují nejpodrobnější vzorkování. Tímto způsobem je možné nejen opodstatnit etickou stránku experimentů (počty jedinců zařazených do studie), ale i ekonomickou (množství bločků, řezů, obrazových polí). Bez zmapování zdrojů variability na jednotlivých úrovních také není možné posoudit, do jaké míry vlastní kvantitativně histologická data vypovídají o skutečné stavbě orgánů a tkání experimentálních zvířat, ani vyvrátit případné pochybnosti o vlivu vzorkování a variabilitě na výsledky testování hypotéz mezi porovnávanými skupinami v experimentu.

2.1.2 Cíle práce

Cílem studie bylo zmapovat nástroje a postupy virtuální mikroskopie, jimiž lze optimalizovat strategii vzorkování obrazových polí v kvantitativní histologii. Při hledání univerzálních postupů jsme testovali tyto přístupy na co nejširším spektru orgánů a přístupů (svalová tkáň, cévy, orgánové a nádorové mikrocévy, kostní implantáty, střevní anastomózy, osteochondrální defekty, neurony mozku a jiné). Jednalo se o metodicky orientovanou přehlednou práci, která netestovala žádnou nulovou hypotézu ve statistickém slova smyslu. Namísto toho bylo naším záměrem porovnat a diskutovat výhody a nevýhody více strategií vzorkování a formulovat doporučení pro nejčastější případy.

2.2 Histologické složeni segmentů prasečích krkavic

2.2.1 Motivace

Společný kmen prasečí krkavice je jednou z nejčastějších cév pro testování různých typů cévních štěpů pro AKB (Szafron et al., 2019). Tento zvířecí model se doporučuje vzhledem k anatomické a fyziologické podobnosti s lidskými tepnami malého průměru (García et al., 2011). Prasečí ACC, které mají svůj průměr (5-6 mm) podobný lidským AC, jsou snadno chirurgicky přístupné a dostupné pro sonografickou kontrolu průchodnosti a katetrizaci (Anderson et al., 2018; Dondelinger et al., 1998; García et al., 2011).

V současnosti je nedostatek kvantitativních dat, které by poskytovaly informace o mikroskopické struktuře prasečí ACC v průběhu celé její délky. Srovnání mikroskopického složení ACC s lidskými AC a ATI je potřebné pro odhalení výhod a nevýhod translační medicíny.

Použití zvířecích modelů v experimentální medicíně vyžaduje zmapování jejich anatomické variability. Toto je nezbytná podmínka pro provedení analýzy síly testu, aby se odůvodnil počet zvířat a biologických vzorků potřebných pro detekci předpokládaných biologických změn, na jejichž studium je experiment zaměřen.

2.2.2 Cíle a hypotézy práce

Cílem studie bylo zmapovat změny mikroskopické struktury ACC podél celé své délky a porovnat je s často nahrazovanými oblastmi lidských AC a se zástupcem štěpů využívaných pro revaskularizaci - ATI. Testovali jsme následující hypotézy:

H0(A): Levé a pravé prasečí ACC mají shodnou stavbu a mohou být během experimentu zaměnitelné či používány vzájemně jako kontroly.

H0(B): Proximodistální segmenty prasečích ACC nemají mezi sebou žádné rozdíly v mikroskopické stavbě.

H0(C): Mezi prasečími ACC, lidskými AC a ATI nejsou ve složení stěny žádné rozdíly.

2.3 Histologické porovnání ovčích a prasečích segmentů krkavic s lidskými koronárními a hrudními tepnami

2.3.1 Motivace

AKB je běžná kardiochirurgická metoda používaná po celém světě. Výroba a testování bioinženýrských cévních štěpů průměru 2-5 mm pro AKB je jedním z hlavních úkolů experimentální cévní chirurgie, který by byl přínosem pro pacienty, kteří postrádají nebo již vyčerpali autologní arteriální nebo venózní náhrady první či druhé volby. Umělé cévní náhrady s malým průměrem bohužel obvykle ztrácejí průchodnost v důsledku hyperplazie intimy a tvorby trombů (Walpoth et al., 2007), a proto jejich vývoj vyžaduje další optimalizaci (Szafron et al., 2019).

Pro *in vivo* testování nově vyvinutých cévních štěpů se běžně používají krkavice ovcí a prasat. Tyto velké zvířecí modely jsou používané v cévní chirurgii díky jejich velikosti srovnatelné s lidmi a díky vzájemné podobnosti kardiovaskulárního systému (García et al., 2011; Schleimer et al., 2018). Dodnes není známo, do jaké míry jsou tyto zvířecí modely zaměnitelné a zda lze levou a pravou krkavici stejných subjektů použít jako experimentální kontroly. V předcházející studii (Tomášek et al., 2020) bylo provedené rozsáhlé mapování histologické struktury všech segmentů prasečích ACC a diskutovalo se o výhodách a omezeních jejich použití jako umělých náhrad vhodných pro AKB u lidí. Při rešerši jsme nenašli žádnou kritickou morfologickou analýzu ovčích ACC, ani jejich srovnání s prasečími ACC nebo lidskými AC a nejběžnějším typem arteriálních náhrad, jako jsou ATI. Tato znalostní mezera znemožňuje porovnání a interpretaci výsledků získaných na těchto dvou velkých zvířecích modelech, stejně jako rozumné plánování dalších studií na obou modelech, které by odrážely biologickou variabilitu vaskulárních segmentů pro navigaci experimentálních chirurgických postupů. Jak odhalila nedávná práce na prasečích ACC (Tomášek et al., 2020), respektování variability histologického fenotypu proximodistálních segmentů ACC může výzkumníkům podstatně pomoci získat konzistentnější výsledky. Údaje o interindividuální a intraindividuální histologické variabilitě zvířecích ACC lze použít k odůvodnění minimálního počtu vzorků na skupinu při plánování dalších experimentů z etického i vědeckého hlediska. Získání těchto popisných dat, jmenovitě průměrů a směrodatných odchylek, by mohlo odstranit současné metodologické mezery a usnadnit návrh experimentů založených na analýze vzorků výkonu. Dalším praktickým

výstupem mapování interindividuálních a regionálních anatomických rozdílů mezi cévními segmenty ACC je poskytnutí realistických dat pro přizpůsobení vícevrstvých umělých cévních protéz.

2.3.2 Cíle a hypotézy práce

Zaměřili jsme se na porovnaní mikroskopické struktury párových levých a pravých ovčích a prasečích ACC v proximodistálním směru a na porovnaní těchto zvířecích modelových vzorků se vzorky lidských AC a ATI.

Cílem studie bylo otestovat následující nulové hypotézy:

H0(A): Mezi párovými levými a pravými ovčími ACC nejsou žádné rozdíly, lze je používat zaměnitelně jako kontroly během experimentu.

H0(B): Neexistují žádné proximodistální segmentální rozdíly ovčích ACC. Variabilní poloha chirurgických anastomóz během experimentů není možným zdrojem zkreslení.

H0(C): Mezi ovčími ACC, prasečími ACC, lidskými AC a lidskými ATI nejsou žádné rozdíly. Ovce a prasata lze považovat za ekvivalentní modely velkých zvířat, které dobře odpovídají modelovanému problému (tj. AKB u lidí).

H0(D): Studované histologické parametry spolu nekorelují.

Kromě toho bylo naším dalším cílem poskytnout deskriptivní statistiku vhodnou pro analýzu výkonových vzorků pro odhad minimálního počtu vzorků nezbytných pro detekci předpokládaného rozdílu ve všech sledovaných parametrech.

2.4 Histologické hodnocení vaskularizace myších xenoimplantátů lymfomu plášťových buněk

2.4.1 Motivace

Pro stanovení agresivity nádoru a úspešnosti jeho terapie je důležité znát oxygenaci nádoru a hodnoty jeho vaskularizace (Fukumura and Jain, 2007; Jing et al., 2019). Pro nádorová tkaniva je typická buněčná hypoxie, která může být analyzovaná pomocí fluorescenčních sond, imunohistochemickým barvením nebo počítačovou tomografií (Fleming et al., 2015; Takahashi et al., 2012). Jednou z nevýhod těchto technik je použití exogenních kontrastních

látek pro zobrazení anatomických a molekulárních vlastností nádoru. K vedlejším účinkům kontrastních látek patří ionizující záření nebo její interakce se složkami terapie nádoru.

Jednou z neinvazivní a neionizující možnosti zobrazování vaskularizace *in vivo* je duální ultrazvuk a fotoakustické zobrazování (Emelianov et al., 2009). Výhodou fotoakustického zobrazování je vynikající prostorové rozlišení dosahující do hloubky několik desítek mikrometrů a sledovaní více vlnových délek pro každý řez (Xia et al., 2014; Zhang et al., 2019). Dopplerovskou ultrasonografií můžeme detekovat vaskularizaci nádoru (Chen et al., 2013).

Jedním z typů B-buněčného NHL je lymfom z plášťových buněk (Klener, 2019). Zvířecí model založený na xenotransplantaci primárních lymfomových buněk do imunodeficientních myší je často používán pro preklinické testování léčebných metod (Prukova et al., 2019). V rámci rešerše jsme nenašli testování MVD, MVA a hodnoty oxygenace PDX modelů odvozených od pacientů s lymfomem z plášťových buněk. Kromě toho je tato práce první studií těchto PDX modelů s využitím fotoakustického zobrazování.

2.4.2 Cíle a hypotézy práce

V rámci studie se analyzovala úroveň okysličení a vaskularizace (MVA) v tkaních myšího modelu PDX použitím fotoakustického zobrazování a Dopplerovy ultrasonografie. Experiment byl doplněn daty kvantitativní histologie, konkrétně procentem vaskularizace MVA a MVD.

Testovali jsme následující nulové hypotézy:

H0(A): Hodnoty MVA v nádorových tkáních PDX jsou stejné při měření Dopplerem a kvantitativní histologii.

H0(B): Histologicky stanovené MVA a MVD mezi malým a velkým nádorem jsou stejné.

2.5 Histologické hodnocení vaskularizace myších xenoimplantátů Non-Hodgkinova lymfomu

2.5.1 Motivace

NHL je skupinou vážných nádorových onemocnění, které představují nejčastější hematologickou malignitu (Swerdlow et al., 2016; Swerdlow and Cook, 2020). Až kolem 85% těchto nádorů pochází z B lymfocytů, zbytek má původ z T nebo NK lymfocytů (Shankland et al., 2012).

Model založený na xenotransplantaci primárních lymfomových buněk do PDX modelu se využívá v preklinickým a translačním onkologickém výzkumu (Lai et al., 2017). PDX modely si uchovávají většinu genetických mutací se vzorkem primárního lidského lymfomu (Townsend et al., 2016). Dodnes je málo informací se srovnáním lymfomového mikroprostředí u PDX a primárního lymfomu (Burack et al., 2017). Některé studie jejich srovnáním potvrdily stejné histopatologické vlastnosti (Zhang et al., 2017). Dosud však chybí zhodnocení nemaligních buněk a struktur nádorového mikroprostředí, zejména makrofágů, NK buněk, T buněk a rovněž krevních mikrocév, tj. složek nádoru, které ovlivňují biologické chování NHL (Hanahan and Coussens, 2012; Shain et al., 2015).

2.5.2 Cíle a hypotézy práce

Cílem studie byla genetická a imunohistochemická analýza odvozených PDX modelů NHL a jejich srovnání s primárními lidskými NHL. V histologické částí jsme se zaměřili na hodnocení mikrocév nádorového mikroprostředí, konkrétně MVD a MVA.

Testovali jsme následující nulové hypotézy:

H0(A): MVD v PDX modelu je stejná jak v primárním lidském NHL.

H0(B): MVA v PDX modelu je stejná jak v primárním lidském NHL.

2.6 Vliv hyperbarické oxygenoterapie na tvorbu kolagenu typu III v ráně diabetického potkana

2.6.1 Motivace

Jednou z chronických komplikací diabetu je syndrom diabetické nohy (SDN), který může vést k destruktivnímu poškození tkání nohy ve formě diabetických vředů (Apelqvist, 2008). Příčinou vzniku SDN jsou vaskulopatie (onemocnění periferních tepen dolních končetin, ztráta elasticity arteriol a kapilár) a neuropatie (poškozené senzorické, autonomní a motorické nervy) (Hobizal and Wukich, 2012; Packer et al., 2022; Vinik et al., 2003).

Mezinárodní pracovní skupina pro diabetickou nohu (IWGDF) vydává doporučení pro léčbu SDN, která zahrnuje kombinaci lokální a systémové léčby (Lipsky et al., 2020; Waniczek et al., 2013). K doporučením IWGDF patří i HBOT jako doplňková léčba ischemických diabetických vředů, který by mohl urychlit hojení podpořením epitelizace (Aydin et al., 2013; Rayman et al., 2020).

Studie o účincích HBOT na diabetický vřed nejsou jednotné. Vliv HBOT terapie byl testován na ischemických a neischemických diabetických vředech u potkanů, kde byl zjištěn jeho pozitivní vliv jen u ischemických defektu (André-Lévigne et al., 2016). Huang et al. (2020) zjistili zvýšenu angiogenezi při léčbě vředů s HBOT u diabetických myší. Naopak jiné studie nepotvrdili pozitivní účinek HBOT (Tuk et al., 2014; van Neck et al., 2017).

Všechny zmíněné studie proběhly u zvířecích modelů s diabetem typu 1. V naši práci jsme se zaměřili na diabetes 2. typu, nakolik se u něj tvoří až 90% diabetického vředu (Packer et al., 2022). Jak zvířecí model byl vybrán ZDF potkan s rozvinutým diabetem 2. typu. Tento model je často používaný při studiích vlivu diabetu na hojení rán a neuropatii (Otto et al., 2011; Slavkovsky et al., 2011). V rámci rešerše jsme však nenašli studii, která by testovala vliv HBOT na léčbu kožních rán u ZDF potkanů.

2.6.2 Cíle a hypotézy práce

Cílem studie bylo vyhodnotit účinek HBOT na hojící se kožní ránu u ZDF potkanů. Zaměřili jsme se na testovaní následujících nulových hypotéz:

Cíle a hypotézy

H0(A): Mezi skupinou HBOT a kontrolní skupinou nejsou žádné rozdíly v objemovém podílu kolagenu typu I a III a poměru kolagenu I/III v hojící se ráně.

H0(B): Objemový podíl kolagenu typu I a III a poměr kolagenu I/III je stejný v kožní raně po 18. dnech hojení a v zdravé kůži v okolí hojící se rány ve skupině HBOT.

H0(C): Objemový podíl kolagenu typu I a III a poměr kolagenu I/III je stejný v kožní raně po 18. dnech hojení a v zdravé kůži v okolí hojící se rány ve kontrolní skupině.

H0(D): Dvojrozměrní hustota mikrocév je stejná v hojící se ráně a v zdravé tkání u obou skupin.

3 Materiály a metody

3.1 Vzorkování v kvantitativní histologii a stereologii

Přehledový článek je zaměřen na ukázku příkladu vzorkování virtuálních snímků z různých oblasti kvantitativní histologie. Při vzorkování je zapotřebí dodržet pravidla pro dodržení systematického, nestranného a náhodného výběru zorných polí. Pozice prvního zorného pole v rámci oblasti zájmu je vybrána náhodně. Na základě předem zvoleného vzorkovacího intervalu se následně urči pozice ostatních zorných polí. Práce obsahuje strategie histologického vzorkování v ilustrovaných příkladech. Použité kvantitativní morfometrické údaje jsou znázorněny v Tabulka 1.

Při odběru histologických vzorek obrazových polí dochází ve výsledných datech k různě velké variabilitě výsledných dát. Tuto variabilitu můžeme snížit zvýšením vzorkovací frekvence, co ale zvýší pracnost potřebné k dokončení výzkumu. Proto je potřebné zoptimalizovat postupy odběru vzorku z hlediska času a materiálních nákladu. Jako měřítka variability jsme použili směrodatnou odchylku výběru (standard deviation, SD), koeficient chyby (coefficient of error, CE) a odhady CE pro prostorově korelované objekty pomocí kvadratické Matheronovy aproximace s různými konstantami hladkosti (Gundersen and Jensen, 1987; Slomianka and West, 2005).

Tabulka 1. Kvantitativní morfometrické parametry (Kolinko et al., 2022).

kvantitativní parametr (veličina)	Definice
objemový podíl V_V (-)	podíl objemu složky zájmu v referenčním objemu
plošný podíl A_A (-)	podíl plochy složky zájmu v referenčním objemu, $A_A = V_V$
dvojrozměrná hustota Q_A (mm^{-2})	počet profilu složek zájmu v referenční ploše
skutečný počet průsečíku P'_L () (mm^{-1})	skutečný počet průsečíku profilu složky zájmu k celkovým profilům
dvojrozměrná délková hustota L_V (mm^{-2})	délka lineárních složek zájmu na jednotku objemu
délková hustota L_A (mm^{-1})	délka složek zájmu v referenčním prostoru

3.2 Histologické složeni segmentů prasečích krkavic

Materiálem použitým v studii byli prasečí krkavice, lidské koronární tepny a *arteria thoracica interna*. Párové prasečí ACC (n=41) pocházely od přeštických černostrakatých prasat (12 samic, 9 samců) ve věku 12–21 týdnů a váhy 20–65 kg. Každá z cév byla rozkrájená na sérii 1 cm dlouhých segmentů v proximodistálním směru. Tímhle způsobem se získalo 8–13 segmentů z každé cévy. Lidské AC (*arteria coronaria sinistra* a *arteria coronaria dextra*) a ATI (proximální, střední a distální segment) byly odebrány v rámci pitvy od 21 jedinců (7 žen, 14 mužů) ve věku 57–78 let.

Všechny arteriální vzorky byly fixovány v 10% roztoku formalínu, dehydratovány v etanolu, zalitý do parafínových bločků a nařezány na 5 μm silné řezy (Leica RM2255 mikrotom). Řezy byly obarveny pomocí kombinace troch histologických barvicích metod (orcein, pikrosiriová červeň, Verhoeffův hematoxylin a zelený trichrom) a jedné imunohistochemické reakce (protilátka anti-α-hladkosvalový aktin (klon 1A4, ředení 1:500, DakoCytomation, Glostrup, Denmark)) pro vizualizaci mikroskopických struktur stěny tepny. Pro následní histologické hodnocení bylo získáno více než 11 000 mikrofotografií na základě systematického, nestranného a náhodného odběru vzorek (Obrázek 1A).

Kvantitativní hodnocení zahrnovalo stanovení plošného podílu elastinu, kolagenu a hladkosvalového aktinu v intimě a medii použitím stereologické bodové mřížky a Cavalieriho principu (Obrázek 1B, C, D). Tloušťky intima-media a celkové steny cévy byly stanovené pomocí čtyř lineárních sond (Obrázek 1E, F).

Pro statistickou analýzu byly použity neparametrické testy, konkrétně Wilcoxonův párový test (porovnání levé a pravé krkavice u stejného jedince), Kruskalova–Wallisova ANOVA (rozdíly mezi prasečími a lidskými cévami), Spearmanův korelační kvocient (korelace mezi kvantitativními proměnnými).
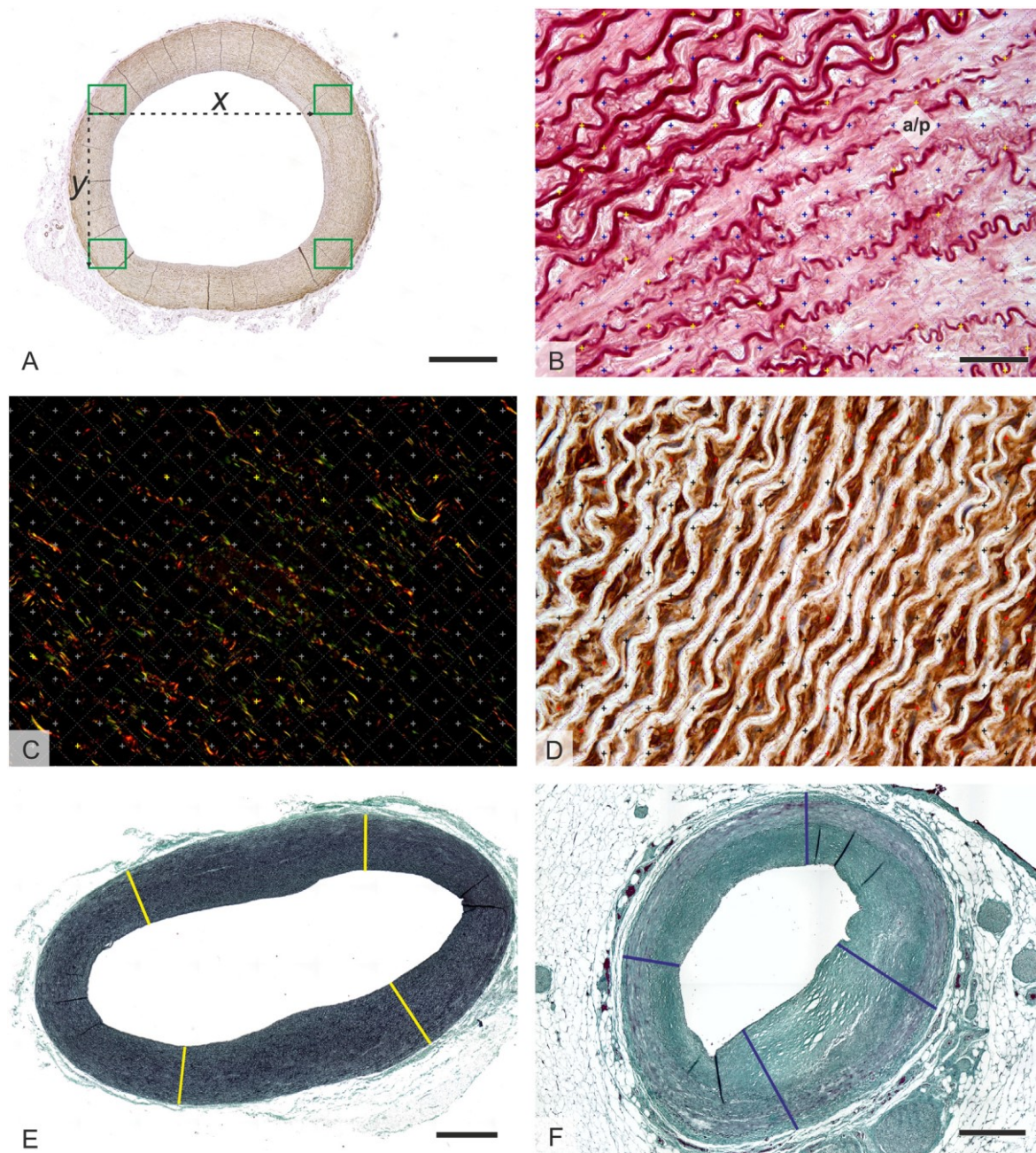
Obrázek 1. Histologické vzorkování a stereologické hodnocení cévních mikrostruktur (Tomášek et al., 2020).
Obdélníky proporcionálně znázorňují čtyři mikrofotografie odebrané systematickým způsobem z každého řezu (A). Plošný podíl elastinu (B), kolagenu (C) a aktinu (D) byl hodnocen pomocí stereologické bodové mřížky. Tloušťky intimy+medie (E) a celé arteriální stěny (F) byly hodnoceny pomocí lineárních sond. Měřítko 1000 µm (A, E), 50 µm (B–D) a 500 µm (F).

Materiály a metody

3.3 Histologické porovnání ovčích a prasečích segmentů krkavic s lidskými koronárními a hrudními tepnami

V studii byli použité levé a pravé párové ovčí ACC (n=44), které byly odebrány od ovcí Suffolk (11 samic, 11 samců) ve věku 24–144 týdnů a váhy 34–67 kg. Obojstranné krkavice byly chirurgicky vypreparovány od *truncus brachiocephalicus* až do místa větvení na *arteria interna* a *externa*. Cévy byli rozděleny na 1 cm dlouhé segmenty v proximodistálním směru, čím vzniklo 11–17 segmentů z každé cévy. Vzorky párových prasečích ACC (n=41), lidských AC (n=21) a ATI (n=21) byly získány ve formě archivních tkáňových bloků zalitých v parafínu z předchozí studie (Tomášek et al., 2020).

Všechny cévy byli histologicky spravovaný podle studie Tomášek et al. (2020). Histologické barvící metody a imunohistochemické reakce použité k vizualizaci složek cévní steny jsou znázorněny Tabulka 2. Mikrofotografie byly pořízeny na základě systematického odběru vzorků arteriální stěny (Kolinko et al., 2021; Tomášek et al., 2020) (Obrázek 2). V rámci celé studie bylo použitých 1 235 cévních segmentů a celkový počet mikrofotografií byl 30 924.

Plošný podíl elastinu, kolagenu typu I a III, hladkosvalového aktinu a chondroitinsulfátu byly hodnoceny pomocí stereologické bodové mřížky (Obrázek 3 A–D) (Howard and Reed, 2004), jak bylo dříve popsáno ve vaskulárním výzkumu (Eberlová et al., 2013; Tonar et al., 2015; Witter et al., 2010). Tento podíl byl vypočítán jako poměr struktur zájmu a referenční plochy. Bylo použito alespoň 150 průsečíků bodové sítě se zájmovou strukturou, jak doporučuje Tschanz et al. (2014). Dvojrozměrná hustota nukleárních profilů, *nervi vasorum* a *vasa vasorum* byly odhadnuty pomocí počítacího rámečku (Obrázek 3 E–G) (Gundersen, 1977). Tloušťka intima-media a tloušťka stěny cévy byly kvantifikovány jako průměr měření z čtyř lineárních sond (Obrázek 3 H). Všechny postupy stereologického hodnocení byly provedeny pomocí software Ellipse (ViDito, Košice, Slovenská republika).

Statistická analýza byla provedena pro všechny cévní segmenty pomocí softwarového balíčku Statistica Base 11 (StatSoft, Inc., Tulsa, OK, USA). Některá data neprošla Shapirovým–Wilksovým testem normality; byly tedy použity neparametrické metody. Levá a pravá krkavice byly porovnány pomocí Wilcoxonova párového testu, který testoval hypotézu H0(A). Kruskalova–Wallisova ANOVA test byl použit k porovnání ovčích a prasečích krkavic v proximodistálních segmentech při testování hypotézy H0(B) a k analýze rozdílů mezi ovčími krkavicemi, prasečími krkavicemi, lidskými koronárními tepnami a

Materiály a metody

lidskými *arteria thoracica interna* při testování hypotézy H0(C). Mannův–Whitneyův U test byl použit k porovnání ovčích krkavic s prasečími krkavicemi v proximálním, středním a distálním segmentu. Pro analýzu hypotézy korelace H0(D) byl použit Spearmanův korelační koeficient. Podle Chowa et al. (2008) jsme provedli analýzu síly testu k výpočtu velikosti vzorku potřebného k detekci očekávané změny frakcí a hustot v ovčích a prasečích krkavic.

Tabulka 2. Histologické metody barvení pro vizualizaci cévních mikrostruktur (Grajciarová et al., 2022).

kvantitativní parametr (veličina)	barvení	objektiv	počet fotografií
A_A (elastin, int+media) (-)	orcein (Tanzer´s orcein, Bowley Biochemical Inc., Danvers, MA, USA)	40x	4
A_A (kolagen typu I a III, int+media) (-)	pikrosiriová červeň (Rich and Whittaker, 2005; Calderón et al., 2019)	40x	4
A_A (aktin, int+media) (-)	protilátka anti-α-hladký svalový aktin (klon 1A4, ředění 1:500, DakoCytomation, Glostrup, Denmark)	40x	4
A_A (chondroitinsulfát, int+media) (-)	alcianová modř (Mulisch and Welsch, 2015)	40x	4
Q_A (jaderne profily, int+media) (mm^{-2})	Gillův hematoxylin	20x	2
Q_A (*nervi vasorum*, adventitia) (mm^{-2})	protílátka anti-neurofilamentový protein (klon 2F11, ředení 1:500, DakoCytomation, Glostrup, Denmark)	20x	4
Q_A (*vasa vasorum*, int+media) (mm^{-2})	u lidských cév protilátka anti-CD31 (klon JC70A, ředení 1:100, DakoCytomation, Glostrup,	40x	4
Q_A (*vasa vasorum*, adventitia) (mm^{-2})	Denmark); u ovčích a prasečích cév protilátka anti-von Willebrandův faktor (ředení 1:1000, DakoCytomation, Glostrup, Denmark)	40x	4
tloušťka intima-media (IMT) (μm)	Verhoeffův hematoxylin a zelený trichrom (Kocová, 1970)	4x	2
tloušťka celé stěny (WT) (μm)	Verhoeffův hematoxylin a zelený trichrom	4x	2
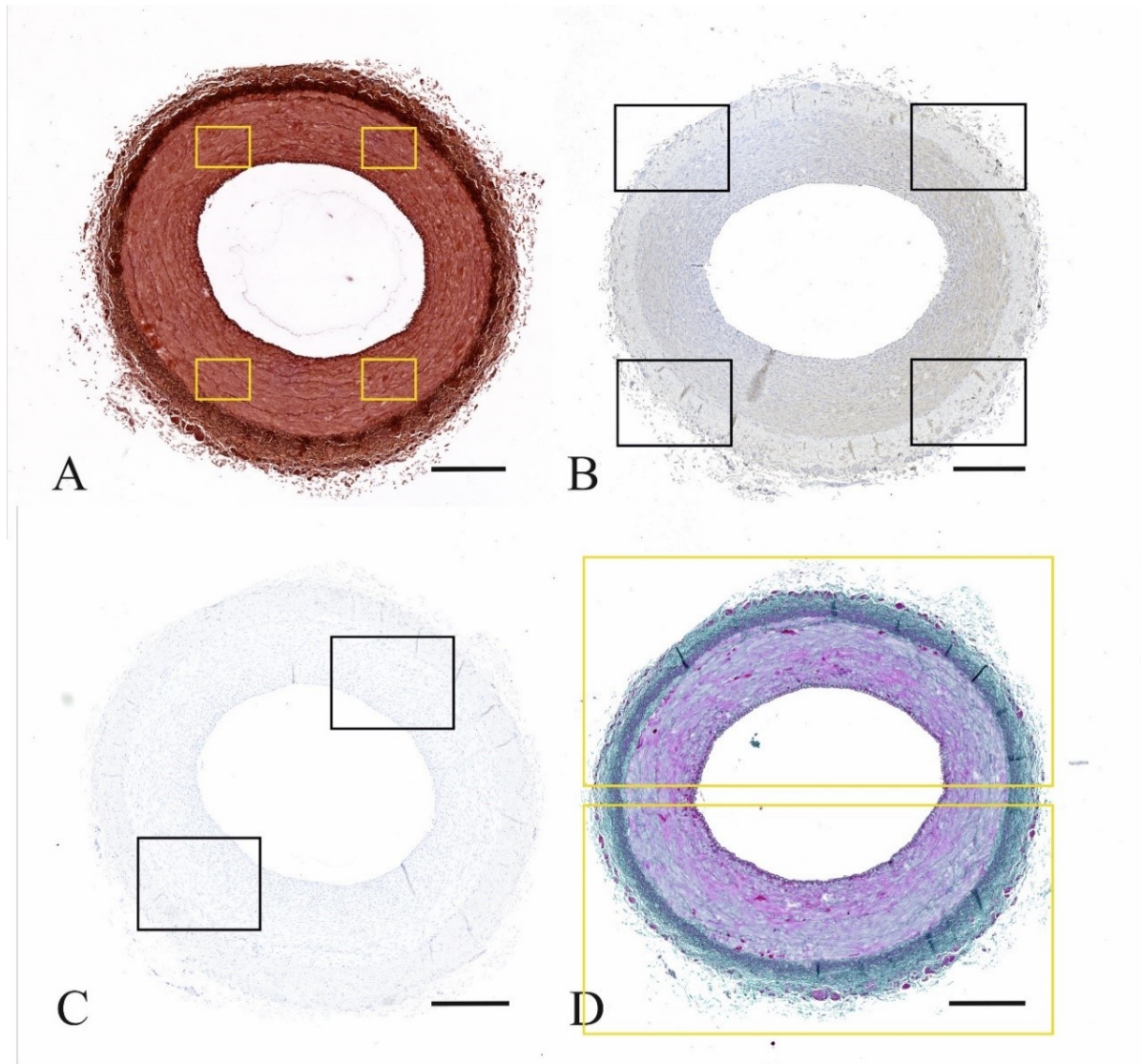
Obrázek 2. Jednotné vzorkování mikrofotografií (Grajciarová et al., 2022).
A, B – Čtyři proporcionálně znázorněné mikrofotografie byly použity k vyhodnocení plošného podílů elastinu, kolagenu, aktinu, chondroitinsulfátu a dvourozměrné hustoty *vasa vasorum*, *nervi vasorum*. C, D – Dvě mikrofotografie byly pořízeny pro vyhodnocení hustoty jaderných profilů, tloušťky intima-media a tloušťky stěny. Měřítko 500 μm (A–D).
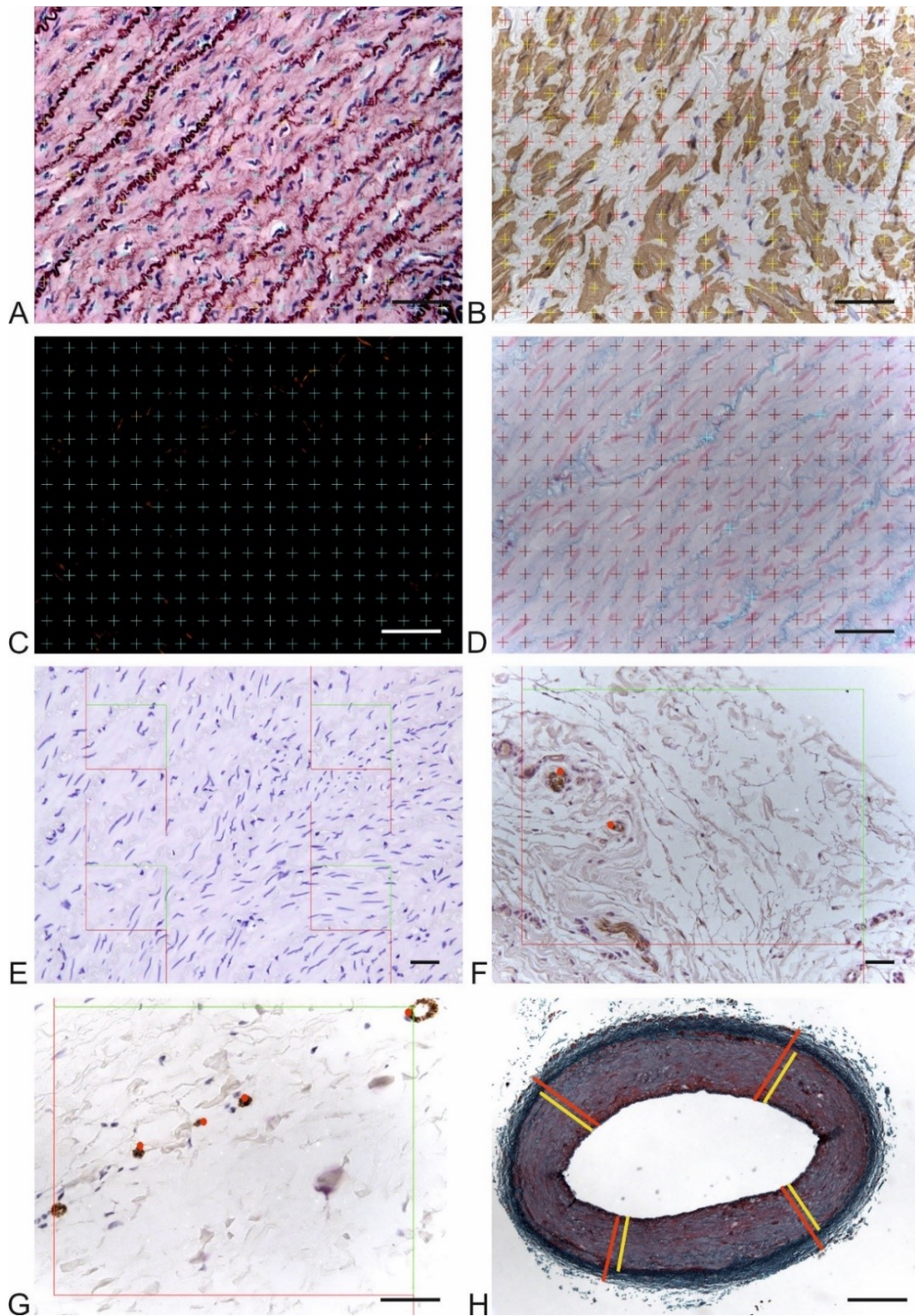
Obrázek 3. Kvantifikace složek stěny cév a tloušťky cévních segmentů (Grajciarová et al., 2022).
Stereologická bodová mřížka byla použita k vyhodnocení frakcí elastinu (A), aktinu (B), kolagenu (C) a chondroitinsulfátu (D). Ke kvantifikaci hustoty nukleárních profilů (E), profilů *vasa vasorum* (F) a *nervi vasorum* (F) byly využity stereologické počítací rámečky.

Tloušťka intima-media a celé stěny cévy byly hodnoceny pomocí lineárních sond (H). Měřítko 50 μm (A–G) a 500 μm (H).

3.4 Histologické hodnocení vaskularizace myších xenoimplantátů lymfomu plášťových buněk

Vzorky tkání myšího modelu založeného na xenotransplantaci primárních lymfomových buněk do imunodeficientních myších samic byly součástí studie týmu prof. MUDr. Pavla Klenera, Ph.D., z Prague Lymphoma Lab (https://lymphoma-lab.lf1.cuni.cz/) Ústavu patologické fyziologie 1. lékařské fakulty UK v Praze. V studii byli použité tři páry tkáňových bločků PDX modelů. V každém páru představovaly dva bločky malé podkožní nádory (1 cm v největším průměru) a další dva bločky velké podkožní nádory (2 cm v největším průměru). Z každého tkáňového bločku bylo ukrojeno pět náhodně orientovaných řezů. K vizualizaci endotelu byli preparáty barvené imunohistochemicky pomocí monoklonální protilátky anti-CD31 (klon SP38, Thermo Fisher Scientific, Rockford, IL, USA). Histologické zpracovaní všech tkání proběhlo na Ústavu patologie 1. lékařské fakulty a Všeobecné fakultní nemocnice v Praze.

Pomocí systematického nestranného vzorkování jsme z každého řezu získali 10 mikrosnímků při použitém objektivu 40x (Obrázek 4). Ke kvantifikaci intratumorálních mikrocév byly použity dva parametry. Nejprve byla kvantifikována MVD (Obrázek 5A) jako počet CD31-pozitivních profilů mikrocév na plochu řezu. Podobně jak u dříve zavedených postupů (Petrakis et al., 2019; Veselá et al., 2014) byla počitatelná céva definována jako jakýkoli profil CD31-pozitivních endoteliálních buněk nebo shluků endoteliálních buněk oddělených od sousedních mikrocév. Byly počítány všechny profily mikrocév, které se nacházejí zcela uvnitř nezaujatého počítacího rámce (Gundersen, 1977) nebo ty, které protínají čáru přijetí, ale ne čáru odmítnutí. Druhým hodnoceným parametrem byla MVA (Obrázek 5B), která byla odhadnuta jako součet plošných profilů CD31-pozitivních mikrocév dělený celkovou plochou tkáně (Petrakis et al., 2019). Histologická kvantifikace byla provedena pomocí modulů PointGrid a CountingFrame softwaru Ellipse (ViDiTo, Košice, Slovenská republika).

Pro analyzování získaných dat byl použit software OriginPro 8 (OriginLab Corporation, Northampton, MA, USA). Srovnání procenta vaskularizace (MVA) bylo pomocí jednosměrné analýzy rozptylu.
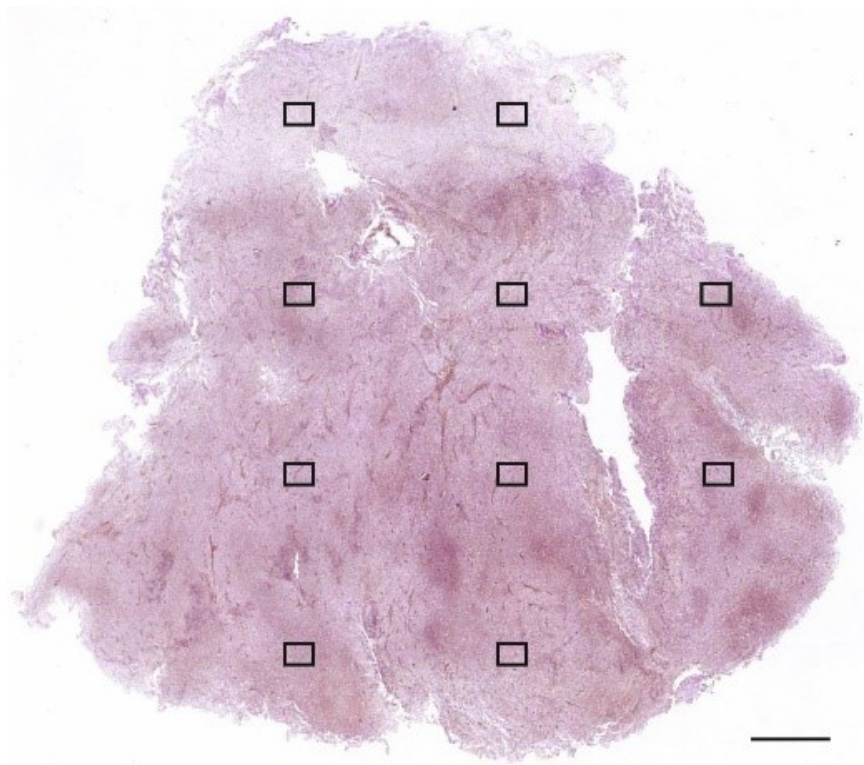
Obrázek 4. Systematické vzorkování PDX myšího modelu lymfomu (Jakša et al., 2021).
Obdélníky demonstrují deset mikrofotografií systematicky náhodně nestranně nasnímaných
z intratumorálního referenčního prostoru. Vzdálenosti mezi mikrofotografiemi byly
udržovány konstantní v konkrétním řezu, aby byl vybrán reprezentativní vzorek celé plochy
průřezu nádorem. Měřítko 500 μm.
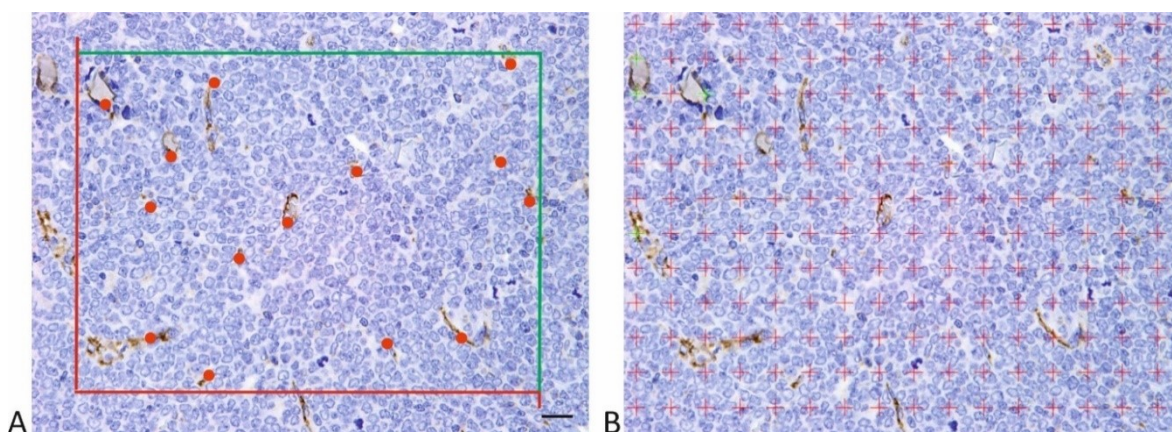
Obrázek 5. Kvantitativní hodnocení intratumorálnich mikrocév (Jakša et al., 2021).
Kvantifikace MVD (A) a MVA (B) CD31-pozitivních vaskulárních profilů (hnědá barva) v
PDX myším modelu lymfomu. Měřítko 20 μm.

3.5 Histologické hodnocení vaskularizace myších xenoimplantátů Non-Hodgkinova lymfomu

Vzorky tkání lidských lymfomu a od nich odvozených myších PDX modelů byly součástí studie týmu prof. MUDr. Pavla Klenera, Ph.D., z Prague Lymphoma Lab (https://lymphoma-lab.lf1.cuni.cz/) Ústavu patologické fyziologie 1. lékařské fakulty UK v Praze. Histologicky byly zkoumány čtyři páry tkáňových bločků. V každém páru jeden tkáňový blok představoval NHL získanou biopsii pacienta a další reprezentoval odpovídající myší model PDX. K hodnocení byli použité dva páry difúzních velkobuněčných B-lymfocytů a dva páry lymfomů z plášťových buněk. Z každého tkáňového bločku bylo zpracováno pět náhodných řezů, které byli histologicky zpracované a imunohistochemicky barvené pomoci monoklonální protilátky anti-CD31 k vizualizaci endotelu mikrocév.

Z každého řezu bylo získaných 10 zorných polí pomocí systematického, nestranného a náhodného vzorkování (Obrázek 4). Kvantitativní histologii se hodnotili parametry MVD a MVA stejným způsobem jak v předcházející práci při studii PDX modelů z plášťových buněk (Keša et al., 2021).

3.6 Vliv hyperbarické oxygenoterapie na tvorbu kolagenu typu III v ráně diabetického potkana

Materiál na histologické vyšetření pocházel z experimentu navrženého a provedeného v laboratoři Biomedicínského centra na lékařské fakultě v Plzni. Jako zvířecí model byli použití samci potkanů ZDF (n=14) v průměrném věku 140±12 dní a hmotnosti 392±49 g. U těchto potkanů byl rozvinut diabetes 2. typu s glykémii vyšší než 15 mmol/l. Na dorzální straně krku byli u každého potkana indukovány dvě kožní rány (1,5 x 1,5 cm). ZDF potkani byli rozdělení do dvou skupin; první byla kontrolní skupina (n=6) a druhá byla experimentální skupina, která byla podrobená léčbě pomocí HBOT (n=8).

Osmnáctý den experimentu byli odebrané vzorky kůže (hojící se defekt a okolní zdravá kůže bez defektu) fixovány v 10% roztoku formalínu, dehydratovány v ethanolu a zalité do parafínových bločků. Následovalo barvení 5 μm silných řezů pomocí histologických barviv znázorněných v Tabulka 3. Z každého řezu byli systematickým výběrem pořízeny

mikrofotografie, které představovaly vzorky hojící se rány a zdravou kůži přilehlou k hojící se lézi.

Kvantitativní histologické hodnocení zahrnovala stanovení objemového podílu (Vv) kolagenu typu I a III pomocí stereologické mřížky a dvourozměrné hustoty profilů mikrocév (Q_A) pomocí počítacího rámečku (Obrázek 6).

Statistika byla provedena pomocí R statistického software (R Development Core Team 2020). Data jsou uvedena jako průměr ± standardní odchylka.

Tabulka 3. Histologické metody barvení v kožním defektu ZDF potkana (Růžička et al., 2021).

kvantitativní parametr (veličina)	barvení	definice	objektiv	počet fotografií
V_V (kolagen typu I, kůže) (-)	pikrosiriová červeň (Merck Millipore, Darmstadt, Germany)	objemový podíl kolagenu typu I (žluto-červená barva) pozorovaného pod polarizovaným světlem	20x	2
V_V (kolagen typu III, kůže) (-)	(Rich and Whittaker, 2005; Calderón et al., 2019)	objemový podíl kolagenu typu I (zelena barva) pozorovaného pod polarizovaným světlem	20x	2
Q_A (krevné cévy, kůže) (-)	protilátka anti-von Willebrandův faktor (ředění 1:000, DakoCytomation, Glostrup, Denmark)	dvourozměrná hustota profilu krevních cév (hnědá barva) v kůži	40x	4
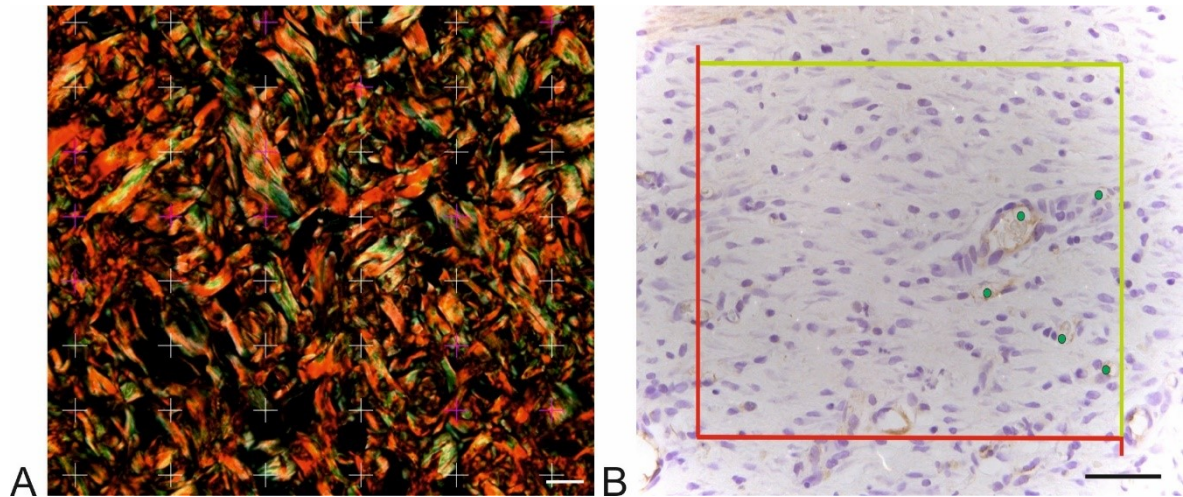
Obrázek 6. Kvantitativní hodnocení v kožním defektu ZDF potkana (Růžička et al., 2021).
Kvantifikace objemového podílu kolagenu typu I a III pomocí stereologické mřížky (A) a dvourozměrné hustoty profilů mikrocév pomocí počítacího rámečku (B). Meřítko 50 μm.

4 Výsledky

4.1 Vzorkování v kvantitativní histologii a stereologii

Na začátku plánování stereologického hodnocení je jednou z otázek způsob odběru zorných polí. V úvahu připadá analýza celého preparátu (whole slide analysis, vyžaduje skener) nebo jen jeho reprezentativní části. V studiích, v kterých je omezený počet vzorků nebo vzorky mají malé rozměry je vhodné vyhodnotit kompletní preparáty. U větších ploch preparátů je pro dosáhnutí co nejmenší variabilní odchylky důležité vybrat dostatečný počet zorných polí. Obrázek 7 znázorňuje příklady relativní vzorkovací chyby při různých intenzitách zorných polí. Tato chyba roste s klesajícím počtem zorných polí, ale u homogenních vzorků je přijatelně nízká. Proto u heterogenních vzorků je vhodné provést pilotní studii, na základě který určíme počet zorných polí pro danou studii. V některých případech vzorky, které mají různou absolutní velikost, vede odběr stejného počtu zorných polí k odlišné hustotě vzorkování. Při nízké biologické variabilitě to obvykle nepředstavuje vnesení významné chyby.
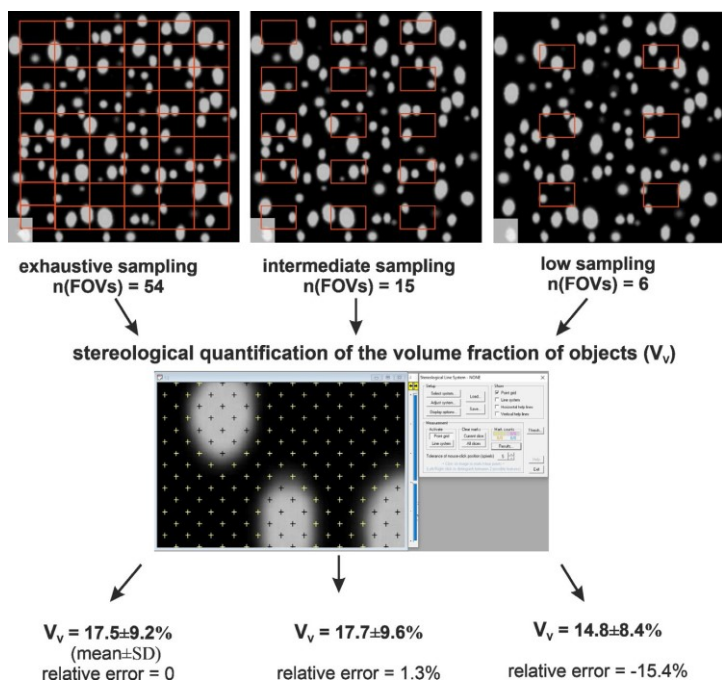
Obrázek 7. Vliv intenzity odběru vzorků na kvantitativní výsledky (Kolinko et al, 2022).

Výsledky

4.2 Histologické složeni segmentů prasečích krkavic

4.2.1 Rozdíly mezi pravou a levou prasečí krkavici

Při srovnání pravé a levé ACC u stejného zvířete jsme nezjistili žádné rozdíly v plošném podíle kolagenu a aktinu. Obdobně i tloušťka intima-media a tloušťka steny cévy nebyly odlišné. Rozdíl byl nalezen jen v podílu elastinu, který byl větší na pravé straně ACC (Wilcoxnův párový test, $p < 0,05$).

4.2.2 Proximodistální segmentální rozdíly prasečích krkavic

Mikroskopické složení tunica intima a media arteriálních segmentů prasečí ACC vykazovalo značné rozdíly v proximodistálním směru. V proximálních segmentech (cca 3 cm) tvořily opakující se elastické lamely převážnou složku cévy. Ve středních segmentech byl podíl elastinu k buňkám hladké svaloviny přibližně stejný. Distální část cévy byla už svalového typu, s převahou buněk hladké svaloviny. Plošný podíl elastinu v intima-media klesal v proximodistálnim směru (Kruskalova–Wallisova ANOVA, $p < 0,001$), naopak podíl aktinu hladké svaloviny rostl v stejném směru ($p < 0,001$). Podíl kolagenu byl po celé délce tepny stejný. Tloušťka intima-media se proximodistálním směru zmenšovala ($p < 0,001$), ale celková tloušťka stěny cévy se v distálních segmentech zvětšovala ($p < 0,001$).

4.2.3 Srovnání prasečích krkavic s lidskými koronárními cévami a *arteria thoracica interna*

Srovnáním plošného podílu elastinu, aktinu, kolagenu a tloušťky intima-media a celé stěny cévy jsme zjistili, že prasečí ACC nemohou být považovány za ekvivalent lidských AC nebo ATI z hlediska svého mikroskopického složení. U obou lidských cév byl menší podíl elastinu a aktinu než u prasat. Lidské AC na rozdíl od prasečích ACC postrádaly rotační symetrii elastinových vláken a obsahovaly početné excentrické aterosklerotické léze různých stadií. Střední a distální segmenty prasečí ACC se překrývaly v hodnotách tloušťky intima-media a celé stěny cévy s lidskými AC a ATI a z tohoto pohledu naopak mohou plnit roli modelového ekvivalentu.

Výsledky

4.2.4 Korelace mezi histologickými parametry

V segmentech prasečích ACC plošný podíl elastinu negativně koreloval s kolagenem (Spearmanův r = -0,156; p < 0,05), aktinem (R = -0,760) a pozitivně s tloušťkou intima-media (r = 0,302). U lidských AC podíl elastinu pozitivně koreloval jen s kolagenem (r = 0,230).

4.3 Histologické porovnání ovčích a prasečích segmentů krkavic s lidskými koronárními a hrudními tepnami

4.3.1 Rozdíly mezi krkavicemi na levé a pravé straně

Rozdíly mezi párovými vzorky levé a pravé ACC u ovcí byly podstatně větší než rozdíly u prasečích párových ACC (Tabulka 4).

Tabulka 4. Srovnání levostranných a pravostranných krkavic ovce a prasete (Grajciarová et al., 2022).
Data jsou zobrazena jako průměr a standardní odchylka (SD). Statisticky významné hodnoty (Wilcoxonův párový test) jsou uvedeny * pro p < 0,05, ** pro p < 0,01, *** pro p < 0,001, statisticky nevýznamné (-) pro p > 0,05.

kvantitativní parametr (rozměr veličiny)	ovčí krkavice		prasečí krkavice	
	levá (průměr±SD)	pravá (průměr±SD)	levá (průměr±SD)	pravá (průměr±SD)
A_A (elastin, int+media) (-)	větší (***) 0,15±0,11	menší (***) 0,13±0,11	menší (*) 0,30±0,16	větší (*) 0,33±0,17
A_A (kolagen typu I, int+media) (-)	0,01±0,01 (-)	0,01±0,01 (-)	0,05±0,03 (-)	0,05±0,03 (-)
A_A (kolagen typu III, int+media) (-)	0,0002±0,0006 (-)	0,0002±0,0004 (-)	0,003±0,004 (-)	0,003±0,004 (-)
A_A (aktin, int+media) (-)	menší (**) 0,575±0,11	větší (**) 0,583±0,11	0,40±0,11 (-)	0,39±0,12 (-)
A_A (chondroitinsulfát, int+media) (-)	0,10±0,03 (-)	0,10±0,03 (-)	0,09±0,04 (-)	0,09±0,04 (-)
Q_A (jaderné profily, int+media) (mm^2)	1448±253 (-)	1473±256 (-)	2448±369 (-)	2403±366 (-)
Q_A (*nervi vasorum*, int+media) (mm^2)	8.09±5,02 (-)	8,08±5,07 (-)	3,96±3,71 (-)	3,78±3,45 (-)
Q_A (*vasa vasorum*, int+media) (mm^2)	0,52±2,36 (-)	0,49±1,74 (-)	menší (***) 0,99±3,09	větší (***) 2,61±7,13
Q_A (*vasa vasorum*, adventitia) (mm^2)	45,76±21,40 (-)	45,05±20,76 (-)	64,73±29,60 (-)	66,56±26,49 (-)
tloušťka intima-media (IMT) (μm)	tenčí (***) 604±154	tlustší (***) 623±167	607±116 (-)	618±136 (-)
tloušťka stěny (WT) (μm)	875±180 (-)	890±196 (-)	907±172 (-)	926±184 (-)

Výsledky

4.3.2 Proximodistální segmentální rozdíly u krkavic

Ovčí krkavice měly po celé své délce svalový fenotyp, ale u prasečích ACC elastický typ
v proximálních segmentech postupně přecházel do svalového typu ve středních a distálních
segmentech. Všechny rozdíly mezi segmenty podél ovčích a prasečích ACC jsou shrnuty na
Obrázek 8 a Obrázek 9.
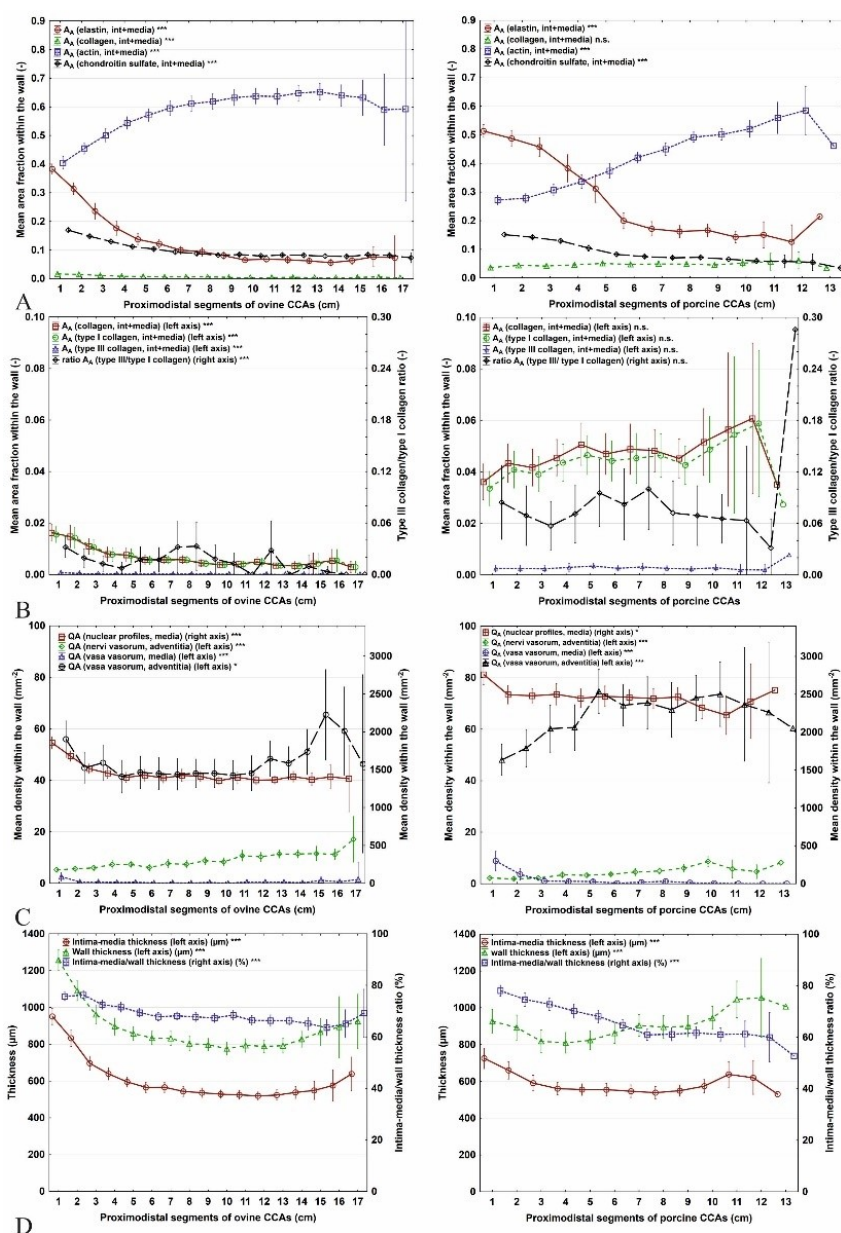
**Obrázek 8. Proximodistální segmentální rozdíly očích a prasečích krkavic
znázorněných v grafe (Grajciarová et al., 2022).**
Data jsou zobrazena jako průměr ± standardní chyba průměru. Hodnoty p (Kruskalova–
Wallisova ANOVA) jsou uvedeny * pro p < 0,05, ** pro p < 0,01, *** pro p < 0,001.

Výsledky
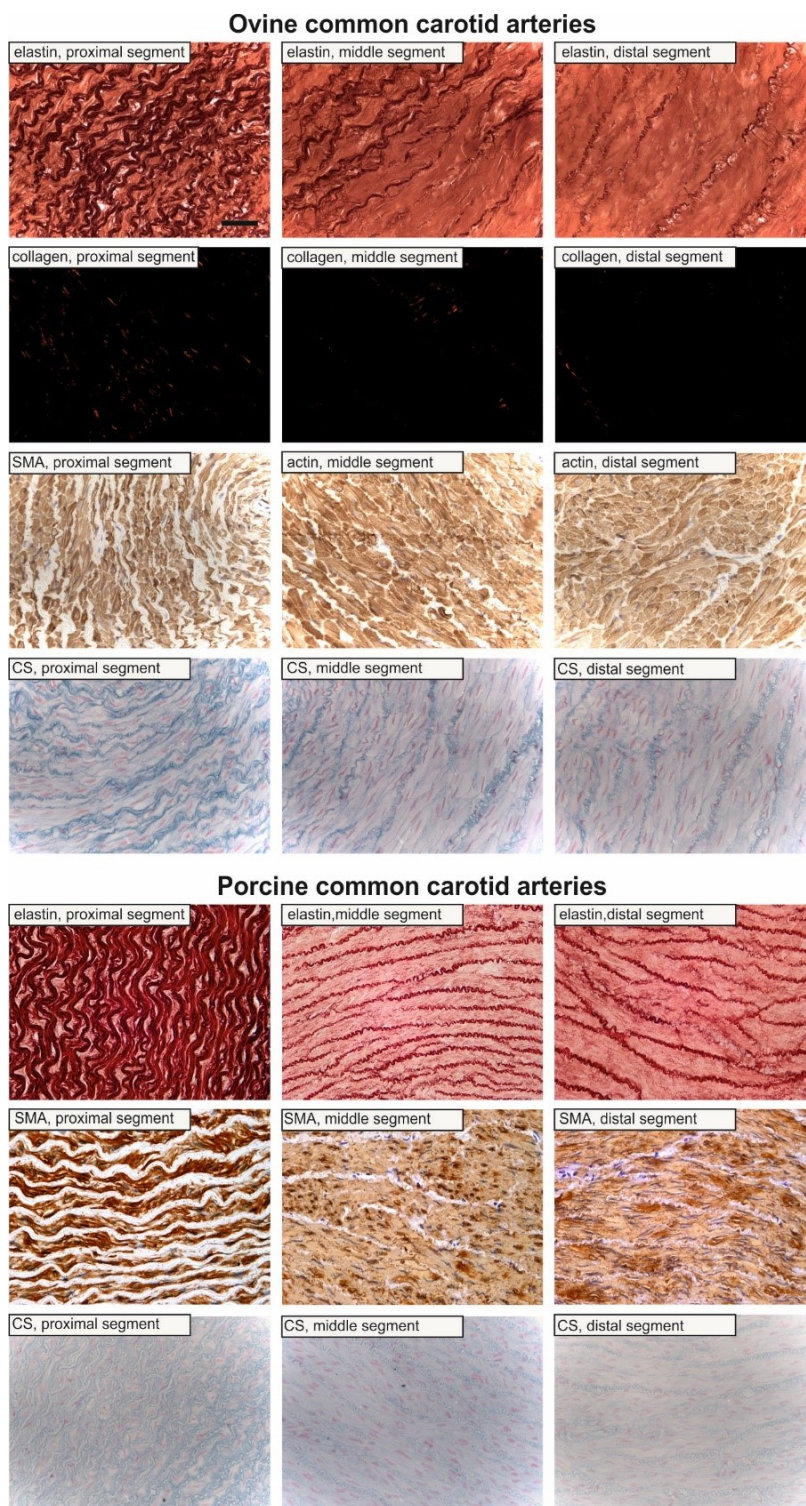
Obrázek 9. Proximodistální segmentální rozdíly ovčích a prasečích krkavic (Grajciarová et al., 2022).
U obou zvířecích modelu se snižovaly frakce elastinu a chondroitinsulfátu proximodistálním směrem (Kruskalova–Wallisova ANOVA p < 0,001). Frakce celkového kolagenu klesala u ovčích krkavic (p < 0,001) v proximodistálním směru. Plošný podíl aktinu se u ovčích i prasečích krkavic zvyšoval proximodistálním směrem (p < 0,001). Měřítko 50 μm.

Výsledky

4.3.3 Srovnání ovčích a prasečích krkavic s lidskými koronárními cévami a *arteria thoracica interna*

ACC obou zvířecích modelů se lišily od lidských AC a ATI ve většině kvantitativních parametrů (Tabulka 5). Ovčí ACC měly srovnatelný plošný podíl elastinu a chondroitinsulfátu s lidskou ATI. Frakce chondroitinsulfátu v prasečích ACC byla podobná lidským AC a ATI. Tloušťka intima-media a tloušťka stěny ACC byly u obou zvířecích modelů stejné, ale tyto tloušťky byly větší než u lidské AC a ATI (Kruskalova-Wallisova ANOVA test, p < 0,001).

Tabulka 5. Srovnaní ovčích a prasečích krkavic s lidskými AC a ATI (Grajciarová et al., 2022).
Data jsou zobrazena jako průměry a standardní odchylky (SD). Hodnoty p (Kruskalova–Wallisova ANOVA) jsou uvedeny * pro p < 0,05, ** pro p < 0,01, *** pro p < 0,001, statisticky nevýznamné (-) pro p > 0,05.

kvantitativní parametr (rozměr veličiny)	lidské AC	lidské ATI	ovčí ACC	prasečí ACC
A_A (elastin, int+media) (-)	0,06±0,04		větší (***) 0,14±0,11	větší (***) 0,30±0,17
		0,13±0,07	0,14±0,11 (-)	větší (***) 0,30±0,17
A_A (kolagen typu I, int+media) (-)	0,02±0,03		menší (***) 0,01±0,01	větší (***) 0,04±0,02
		0,005±0,01	větší (***) 0,007±0,01	větší (***) 0,04±0,02
A_A (kolagen typu III, int+media) (-)	0,003±0,004		menší (***) 0,0002±0,0005	0,003±0,004 (-)
		0,001±0,002	menší (***) 0,0002±0,0005	větší (***) 0,003±0,004
A_A (aktin, int+media) (-)	0,33±008		větší (***) 0,58±0,11	větší (***) 0,40±0,11
		0,35±0,08	větší (***) 0,58±0,11	větší (**) 0,40±0,11
A_A (chondroitinsulfát, int+media) (-)	0,09±0,03		větší (***) 0,10±0,03	0,10±0,04 (-)
		0,10±0,04	0,10±0,03 (-)	0,10±0,04 (-)
Q_A (jaderné profily, int+media) (mm^2)	1175±388		větší (***) 1460±254	větší (***) 2486±394
		1331±508	větší (**) 1460±254	větší (***) 2486±394
Q_A (*nervi vasorum*, int+media) (mm^2)	1,94±1,85		větší (***) 8,18±5,04	větší (***) 3,89±3,64
		1,26±1,43	větší (***) 8,18±5,04	větší (***) 3,89±3,64
Q_A (*vasa vasorum*, int+media) (mm^2)	3,92±5,19		menší (**)0,52±2,09	menší (***) 1,76±5,37
		1,93±3,11	menší (*) 0,52±2,09	menší (***) 1,76±5,37
Q_A (*vasa vasorum*, adventitia) (mm^2)	90,72±32,30		menší (***) 45,78±21,34	menší (***) 64,55±28,39
		58,94±26,89	menší (***) 45,78±21,34	64,55±28,39 (-)
tloušťka intima-media (IMT) (μm)	442±183		tlustší (***) 612±160	tlustší (***) 588±132
		297±83	tlustší (***) 612±160	tlustší (***) 588±132

tloušťka steny (WT) (μm)	612±223	tlustší (***) 881±188	tlustší (***) 881±190
	428±118	tlustší (***) 881±188	tlustší (***) 881±190

4.3.4 Korelace mezi histologickými parametry

V segmentech ovčích ACC pozitivně koreloval plošný podíl elastinu s kolagenem (Spearmanovo r = 0,576; p < 0,05), chondroitinsulfátem (r = 0,596), hustotami jaderných profilů (r = 0,387), hustotou *vasa vasorum* v medii (r = 0,125), tloušťkou intima-media (r = 0,513) a tloušťka stěny cévy (r = 0,425). Frakce elastinu negativně korelovala s frakcí aktinu (r = −0,580) a hustotou *nervi vasorum* (r = −0,368). Tyto korelace byly podobné jako korelace zjištěné dříve u prasečích ACC (Tomášek et al., 2020).

4.3.5 Popisná statistika pro účely analýzy síly testu

Tabulka 6 znázorňuje průměr a standardní odchylku čtyř proximálních, čtyř středních a čtyř distálních segmentů ovčích a prasečích ACC. Tato data jsou připravena k použití pro usnadnění výpočtu minimálního počtu vzorků při plánování experimentů na ACC. Například k detekci 20% poklesu obsahu aktinu ve středních segmentech ovčích ACC se známou biologickou variabilitou (SD), testovací silou 0,8 a chybou typu I 5 % by bylo potřeba 8 vzorků. Podobná analýza může být provedena pro jakýkoli parametr podle (Chow et al., 2008).

Výsledky

Tabulka 6. Popisná statistika vhodná pro výpočet minimálního počtu vzorků pro plánování experimentů na krkavicích ovcí a prasat (Grajciarová et al., 2022).
Uvedený p hodnoty (Mannův–Whitneyův U test) porovnávajících hodnoty ovčích vs. prasečích krkavic: * pro p < 0,05, ** pro p < 0,01, *** pro p < 0,001, statisticky nevýznamné (-) pro p > 0,05.

segmenty krkavic	kvantitativní parametr (rozměr veličiny)	ovčí krkavice		prasečí krkavice		p hodnota
		průměr	standardní odchylka	průměr	standardní odchylka	
proximální	A_A (elastin) (-)	0,249	0,116	0,460	0,117	***
	A_A (kolagen) (-)	0,011	0,011	0,042	0,023	***
	A_A (aktin) (-)	0,495	0,093	0,298	0,066	***
	A_A (chondroitinsulfát) (-)	0,132	0,033	0,132	0,032	(-)
	Q_A (jaderné profily) (mm^{-2})	1580	280	2560	405	***
	Q_A (*nervi vasorum*) (mm^{-2})	6,317	3,761	2,426	2,585	***
	Q_A (*vasa vasorum*, intima-media) (mm^{-2})	0,864	2,996	3,592	7,798	***
	Q_A (*vasa vasorum*, adventitia) (mm^{-2})	46,426	21,629	55,378	25,419	***
	IMT (μm)	743	182	634	157	***
	WT (μm)	1013	215	862	201	***
střední	A_A (elastin) (-)	0,092	0,047	0,211	0,117	***
	A_A (kolagen) (-)	0,005	0,005	0,049	0,027	***
	A_A (aktin) (-)	0,619	0,088	0,434	0,079	***
	A_A (chondroitinsulfát) (-)	0,085	0,017	0,075	0,022	***
	Q_A (jaderné profily) (mm^{-2})	1403	225	2456	389	***
	Q_A (*nervi vasorum*) (mm^{-2})	7,649	4,816	4,084	3,446	***
	Q_A (*vasa vasorum*, intima-media) (mm^{-2})	0,148	0,816	0,622	2,089	**
	Q_A (*vasa vasorum*, adventitia) (mm^{-2})	42,441	18,921	70,424	29,597	***
	IMT (μm)	548	87	549	104	(-)
	WT (μm)	808	121	871	182	***
distální	A_A (elastin) (-)	0,064	0,034	0,154	0,059	***
	A_A (kolagen) (-)	0,004	0,005	0,050	0,027	***
	A_A (aktin) (-)	0,643	0,093	0,521	0,069	***
	A_A (chondroitinsulfát) (-)	0,080	0,015	0,062	0,023	***
	Q_A (jaderné profily) (mm^{-2})	1382	195	2389	359,009	***
	Q_A (*nervi vasorum*) (mm^{-2})	10,969	5,447	6,628	4,320	***
	Q_A (*vasa vasorum*, intima-media) (mm^{-2})	0,518	1,707	0,247	1,049	(-)
	Q_A (*vasa vasorum*, adventitia) (mm^{-2})	48,621	23,436	71,802	26,823	***
	IMT (μm)	528	80	573	92	***
	WT (μm)	804	120	943	170	***

Výsledky

4.4 Histologické hodnocení vaskularizace myších xenoimplantátů lymfomu plášťových buněk

4.4.1 Oxygenace a měření MVA pomocí Dopplerovy ultrasonografie

V první části se tým prof. MUDr. Pavla Klenera, Ph.D., zaměřil na hodnocení oxygenace a stanovení MVA pomocí Dopplerova ultrazvuku. PDX modely VFN-M1 a VFN-M2 byly výrazně méně okysličené a měly několik nekrotických oblastí už u malých nádorů v porovnání s VFN-M5 R, navíc v jejich vaskularizaci došlo k významnému poklesu s rostoucí velikostí nádoru ($p < 0,01$). U PDX modelu VFN-M5 R1 došlo na začátku k poklesu vaskularizace a následně k jeho terminálnímu nárůstu.

4.4.2 Srovnání plošného podílu mezi Dopplerovou ultrasonografii a kvantitativní histologií

Histologické hodnoty MVA všech malých modelů PDX nádorů byly nižší než hodnoty zjištěné Dopplerovou ultrasonografií. Naopak u hodnocení MVA u velkých modelů PDX byli hodnoty v histologickém hodnocení významně vyšší než u použití Dopplerovy metody.

4.4.3 Srovnáni histologických MVA a MVD

Podle histologie nebyly žádné významné rozdíly v MVD nebo MVA mezi malými a velkými nádory VFN-M1 a VFN-M2 PDX. Naopak, rozdíly v MVD a MVA byli pozorovány mezi malými a velkými nádory VFN-M5 R1.

4.5 Histologické hodnocení vaskularizace myších xenoimplantátů Non-Hodgkinova lymfomu

V rámci histologické části studie jsme zjistili významně nižší MVD a MVA v myších PDX modelech v porovnaní s primárními lidskými biopsiemi NHL. Vaskulatura nádorů PDX modelů byla složena z cév myšího původu. Ve většině případů byl profil plochy mikrocév v lidských biopsiích podstatně větší než v odpovídajícím myším modelu (Obrázek 10).
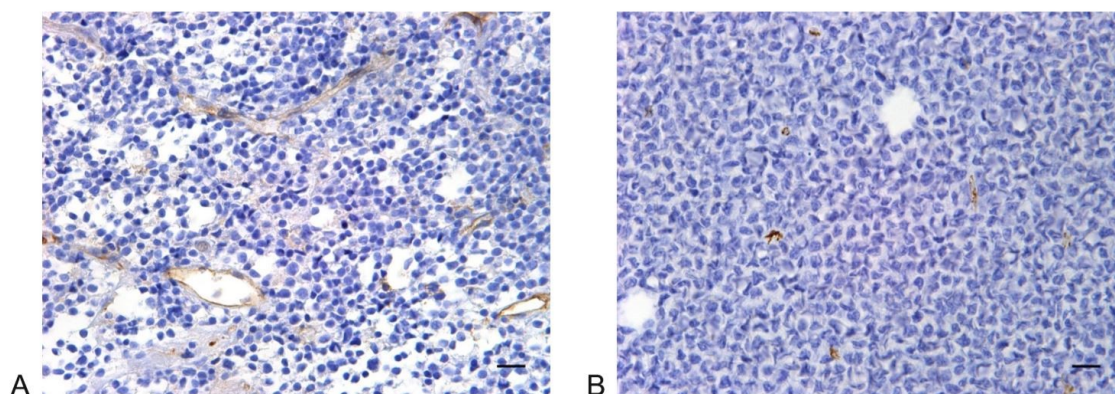
Obrázek 10. Profil mikrocév v PDX modelech (Keša et al., 2021).
Typický nález ilustrující větší profil mikrocév v lidských biopsiích (A) a menší profily v odpovídajících myších modelech PDX. Měřítko 20 μm.

4.6 Vliv hyperbarické oxygenoterapie na tvorbu kolagenu typu III v ráně diabetického potkana

4.6.1 Kvantitativní hodnocení kolagenu typu I a III

Objemový podíl kolagenu typu I a III byl nižší v kožní lézi než v sousední zdravé tkáni u skupiny HBOT aj CTRL (Obrázek 11). U obou skupin nebyl v kožním defektu zaznamenán rozdíl mezi objemovým podílem kolagenu typu I (HBOT 1,35±0,49; CTRL 1,94±0,67 %,) (Obrázek 12A), ale kolagen typu III měl u skupiny HBOT (1,41±0,81 %) vyšší objemový podíl než u skupiny CTRL (0,63±0,37; p <0,05) (Obrázek 12B). Poměr kolagenu I/III v kožní ráně byl u obou skupin stejný (Obrázek 12C).

4.6.2 Kvantitativní hodnocení angiogeneze

MVD mikrocév byla vyšší v kožních lezech než v okolitým zdravým tkanivu (MVD CTRL 206,5±41,8; MVD zdravá kůže 78,1±20,8; p < 0,001). Ve skupině CTRL jsme zaznamenali vyšší mikrovazální hustotu cév než v skupině HBOT (MVD HBOT 124±28,2; MVD CTRL 206,5±41,8; p<0,001).

Výsledky
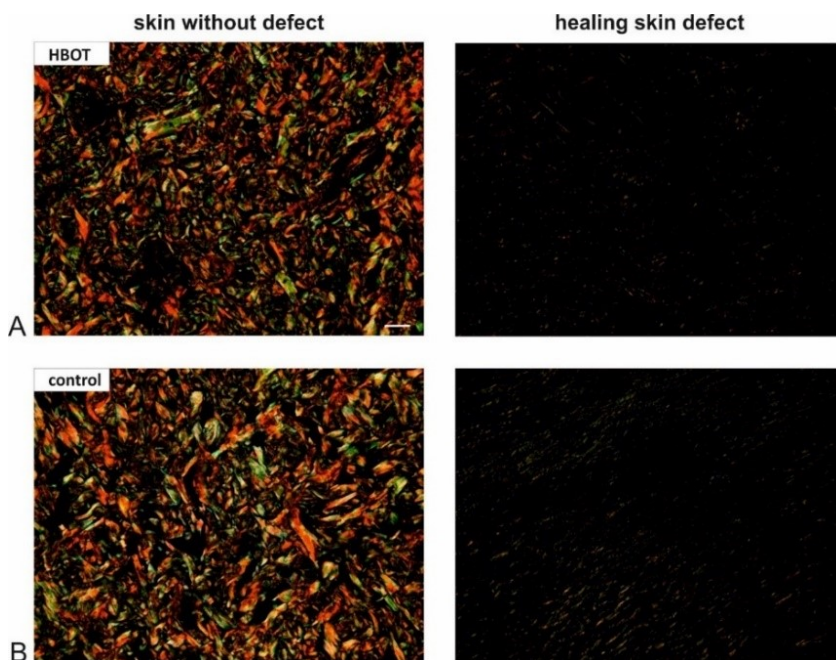
Obrázek 11. Porovnaní kolagenu typu I a III v zdravé kůži bez defektu a v kožní lézi (Růžička et al., 2021).

Vizualizace kolagenu typu I (žlutočervená barva) a III (zelená barva) pomoci barveni pikrosiriové červeně (A – B) pozorované pod polarizovaným světlem. Měřítko 50 μm.
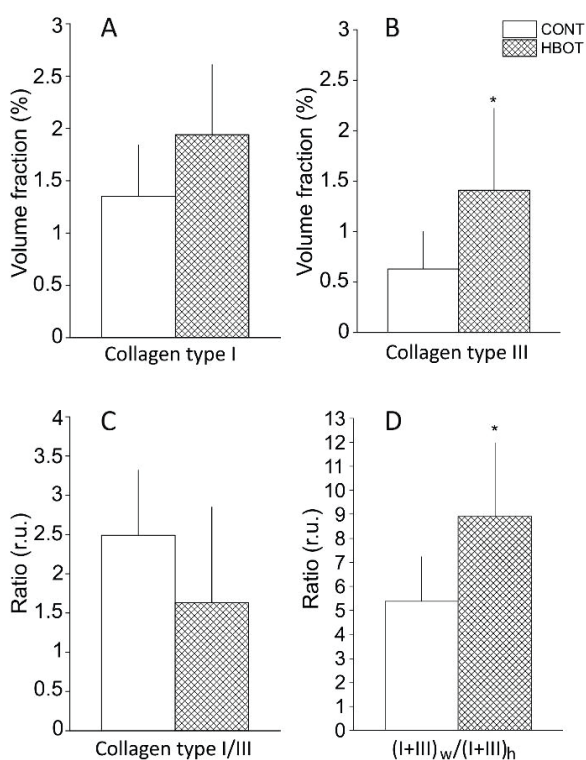
Obrázek 12. Grafické porovnání kolagenu typu I a III v zdravé kůži bez defektu a v kožní lézi (Růžička et al., 2021).

Hodnoty jsou znázorněny jak průměr ± směrodajná odchylka; * $p < 0.05$.

5 Diskuse

5.1 Vzorkování v kvantitativní histologii a stereologii

V každé studii, která je založená na histologické kvantifikaci musí být jasně barevně identifikované testované struktury a také hranice referenčního prostoru (Howard and Reed, 2004; Mouton, 2011). Samotná variabilita výsledků může být ovlivněna počtem objektu v testované skupině, způsobem odběru vzorků a odběrem zorných polí (Gundersen and ØSterby, 1981; Slomianka and West, 2005).

Při vzorkování řezů a zorných polí je lepší upřednostnit systematický jednotný náhodný výběr, protože pokrývá všechny studované části jednotně (Mayhew and Lucocq, 2015). Podle Tschanz et al. (2014) je vhodné vždy provést pilotní studii na typických vzorcích a zkoumaných skupinách. Při zbytečně zvýšené intenzitě vzorkování je finální práce pracnější a drahá bez poskytnutí nových informací. Naopak při nedostatečném vzorkování je těžké dosáhnout předem stanovené úrovně významnosti při testovaní statistické hypotézy. Popisná statistika pilotních dat (průměr a standardní odchylka) jsou užitečné pro analýzu síly testu (Chow et al., 2008).

5.2 Histologické složeni segmentů prasečích krkavic

V naší studii jsme pozorovali významné rozdíly v mikroskopické stavbě prasečí ACC podél její délky. Přibližně první 3 cm elastického typu cévy se postupně v distálním směru změnily na svalový typ, což odpovídá práci García et al. (2011). Naše výsledky se shodují s jinými studiemi na prasečí ACC (García et al., 2011; Kochová et al., 2012; Wyatt et al., 2016). Podíl elastinu zjištěný v práci Wyatt et al. (2016) a Kochová et al. (2012) je porovnatelní s podílem elastinu ve středních segmentech naší práce. Tato regionální rozdíly mají vliv na biomechanické vlastnosti cév, co může ovlivnit průběh a výsledky experimentů na těchto cévách (Avril et al., 2015; García et al., 2011).

5.3 Histologické porovnání ovčích a prasečích segmentů krkavic s lidskými koronárními a hrudními tepnami

5.3.1 Levé a pravé krkavice jsou zaměnitelné u prasat, ale ne u ovcí

Syntetické vaskulární náhrady pro AKB byly v některých studiích testovány na levé straně (Carmen Calles et al., 2002; Weber et al., 2018), na pravé straně (Ahmed et al., 2014) nebo na obou stranách ovčích a prasečích ACC (Hawthorne et al., 2002). Obvykle se při experimentech používá jedna strana ACC jako kontrola (Carmen Calles et al., 2002).

Výsledky naší studie ukázaly na vzájemnou zaměnitelnost levé a pravé ACC ve většině parametrů u prasete. Naopak, mezi levou a pravou stranou těchto cév jsme u ovci zjistili značné rozdíly. Nalezli jsme větší plošný podíl elastinu na levé straně a aktinu na pravé straně ovčí ACC. Intima-média levé ovčí ACC byla tenčí, podobně jak ve studii s použitím lidských krkavic (Willekes et al., 1999). Navzdory rešerši v literatuře jsme nenalezli žádné přímočaré anatomické vysvětlení stranových rozdílů zjištěných u pravé vs. levé krkavice ovce.

5.3.2 Ovčí krkavice byly většinou svalnaté; prasečí krkavice byly elastické až svalové povahy

Mikroskopické složení ovčích a prasečích ACC se lišilo podél jejich makroskopické délky. U ovčích cév měla celá délka většinou svalový fenotyp. Ale u prasečích ACC byly proximální segmenty (3–4 cm) elastického typu a postupně přešly do svalového typu cévy. Naše výsledky jsou v souladu s výsledky jiných studií, které zjistily, že frakce elastinu v prasečích krkavicích klesá a frakce hladké svaloviny roste proximodistálním směrem (García et al., 2011; Sokolis et al., 2011; Weizsäcker et al., 2014). Svalový fenotyp proximální ovčí ACC byl také popsán Bia et al. (2014), ovšem bez podrobných segmentálních rozdílů podél chirurgicky využívaného rozsahu tepny.

V naší studii jsme zjistili snížení plošného podílu elastinu a chondroitinsulfátu v proximodistálním směru, co lze částečně vysvětlit vazebnými místy mezi chondroitinsulfátem a elastickými vlákny (Dubey and Deng, 2018; Humphrey, 2013; Reinboth et al., 2002). Taky jsme zjistili pokles hustoty jaderných profilů u ovčích ACC v

proximodistálních segmentech. V jiné studii však nebyla hustota statisticky významná a jádra buněk hladkého svalstva byla distribuována rovnoměrně po délce ovčí ACC (Parchami et al., 2009).

Obecný problém při přechodu mezi makroskopickou a mikroskopickou úrovní popisu tepen, tj. do jaké míry se mění mikroskopické složení tepen podél jejich průběhu v řádu cm až desítek cm (Sokolis, 2007; Sokolis et al., 2008; Tonar et al., 2016) a jak tyto regionální rozdíly ovlivňují například jejich mechanické vlastnosti (Avril et al., 2015), zasluhuje jednoznačně další pozornost. Jak u člověka, tak u velkých zvířecích modelů jde o nepřehlédnutelný problém. Věříme, že naše srovnání může alespoň částečně vysvětlit mechanické podobnosti a rozdíly uvedené mezi ovčími a prasečími ACC Prim et al. (2018). Zůstává však nejasné, jak se údaje o tloušťce stěny a složení těchto tepen na základě histologicky zpracovaných vzorků vztahují k jejich rozměrům *in vivo* a hemodynamickým parametrům, jako je objemový průtok nebo místní změny krevního tlaku.

5.3.3 Ovčí a prasečí CCA většinou nereflektují strukturu lidských tepen

Z hlediska operačního přístupu je pro testování protéz nejvhodnější střední segment zvířecích krkavic. Důležitá je také tloušťka stěny krkavic, která byla podobná u ovcí a prasat. Tloušťka stěny AC a ATI byla tenčí než u obou krkavic, přičemž pro testování protézy byl nejvhodnější střední segment obou ACC.

Elastinová vlákna, kolagen a glykosaminoglykany jsou hlavními složkami extracelulární matrix (Bartolini et al., 2013; Mattson et al., 2017). ACC obou zvířecích modelů měly větší podíly elastinu a aktinu než lidské AC a ATI, ale svou hodnotou byly nejblíže střednímu segmentu ovčích ACC a distálnímu segmentu prasečích ACC.

5.4 Histologické hodnocení vaskularizace myších xenoimplantátů lymfomu plášťových buněk

V studii jsme pomocí Dopplerovy ultrasonografie sledovali pokles MVA u vzorek VFN-M1 a VFN-M2 PDX modelů se zvětšujícími se nádory, co může být způsobené rostoucím počtem nekrotizujících oblastí. Avšak, při kvantitativním histologickém hodnocení byla

vaskularizace MVA u těchto dvou modelech srovnatelná. Naproti tomu u modelu VFN-M5 R1 došlo k zvýšení vaskularizace ve velkých lymfomech oběma metodami hodnocení.

Rozdíly ve výsledcích mezi histologickým hodnocením a Dopplerovou ultrasonografií mohou mít několik příčin. Významnou roli hraje smrštění tkání během formolové fixace a parafinového procesu. Posmrtně a při excizi tkáňových bločků a při manipulaci s nimi dochází rovněž ke kolapsu cévního průsvitu, což vede následně k nižším naměřeným hodnotám MVA oproti stavu *in vivo* (West, 2013). To může být důvodem, proč MVA u malých nádoru v histologické studii bylo nižší než u měření pomocí Dopplerova principu *in vivo*. Dalším důvodem rozdílu může být ta skutečnost, že histologická analýza je provedena jen v určitých oblastech nádoru, zatímco *in vivo* sonografie hodnotí celý nádor, včetně nekrotických oblastí, které jsou pro histologické hodnocení nevhodné.

Podobná hodnota MVA z histologické analýzy a měření Dopplerem u vzorky VFN-M5 R1 souvisí s bohatou a chaoticky uspořádanou vaskularizaci.

5.5 Histologické hodnocení vaskularizace myších xenoimplantátů Non-Hodgkinova lymfomu

V histologické části studie jsme zaznamenali významně nižší hodnoty MVD a MVA u PDX modelů v porovnání s biopsiemi lidských NHL. Tyto nízké hodnoty mohou být důsledkem suboptimální stimulace myší angiogeneze lidským vaskulárním endoteliálním růstovým faktorem, který je produkovaný lymfomovými buňkami během hypoxie. Nízké hodnoty MVA a MVD mohou mít vliv na preklinické studie zkoumající např. kinetiku léků masivně akumulovaných v nádorové tkání (cytostatika zapouzdřená v liposomech), dále vliv na perfuzní časy kontrastních látek u dynamických zobrazovacích metod apod.

5.6 Vliv hyperbarické oxygenoterapie na tvorbu kolagenu typu III v ráně diabetického potkana

5.6.1 Kvantitativní hodnocení kolagenu typu I a III

Studie se zaměřila na sledování hojení rán u ZDF potkanů, u kterých byl rozvinout diabetes 2. typu a následně na kvantitativní analýzu objemového podílu kolagenu typu I a III v kožní

ráně na 18. den hojení. Model ZDF potkanů byl použit i v jiné studii při testovaní kožních ran (Slavkovsky et al., 2011).

Nová produkce kolagenu, jeho prostorová distribuce a metabolismus mají důležitou roli při obnově homeostázy při hojení kožních defektů (Wynn, 2008). Hojení zahrnují překrývající se fáze, jako je zánět, proliferace a remodelace tkáně (Guo and DiPietro, 2010; Menke et al., 2008; Velnar et al., 2009; Young and McNaught, 2011).

Během prvních tří dnů hojení je kožní rána bohatá na fibroblasty. Proliferace fibroblastů je stimulována transformujícím růstovým faktorem-ß (TGF-ß) a destičkovým růstovým faktorem (PDGF) (Guo and DiPietro, 2010; Velnar et al., 2009; Young and McNaught, 2011). Fibroblasty se během fází proliferace a remodelace účastní syntézy kolagenu, zejména typu III (Campelo et al., 2018; Velnar et al., 2009; Young and McNaught, 2011). Nejvyšší množství kolagenu typu III se objevuje pět dní po poranění a přispívá k tvorbě jizev (Campelo et al., 2018; Young and McNaught, 2011). Kolagen typu I je tvořen silnějšími a delšími svazky fibril nežli kolagen typu III (Wang et al., 2015). Během terminálních fází hojení, tedy remodelace, vzniká kolagen typu I z prekurzoru kolagenu typu III (Campelo et al., 2018; Wang et al., 2015). Výsledný nový kolagen typu je nositelem mechanické pevnosti a stability (Klinge et al., 2000).

Z těchto důvodů histologické hodnocení hojících se kožních defektů často zahrnuje hodnocení kolagenů typu I a III (Clore et al., 1979; Dale et al., 1996; Wang et al., 2015). To může být vyjádřeno buď jako objemová frakce kolagenu nebo jako poměr mezi kolagenem typu I a typu III. Tento poměr vyjadřuje, jak je během procesu hojení obnovena původní hustota sítě kolagenových vláken (Clore et al., 1979; Dale et al., 1996; Wang et al., 2015). Snížený poměr kolagenu I ku kolagenu III je doprovázen snížením pevnosti pojivové tkáně v tahu a je pozorován během prvních sedmi dnů hojení kožní rány, když fibroblasty produkují převážně kolagen typu III (Fleischmajer et al., 1990; Klinge et al., 2000; Sun et al., 2018). Tento poměr se naopak zvyšuje s tím, jak jizva prochází remodelací a zráním (Sun et al., 2018).

Podobně jak v studii Peña-Villalobos et al. (2018) jsme v naší studii na 18. den hojení zaznamenali u ZDF potkanů s HBOT léčbou zvýšený podíl kolagenu typu III, co naznačuje, že proces opravy byl skutečně pomocí HBOT urychlen.

5.6.2 Kvantitativní hodnocení angiogeneze

Během hojení kožních ran dochází vlivem zánětu v ranní fáze hojení zvýšená angiogeneze, která pak v pozdějších fázích hojení klesá (DiPietro, 2016). Ve skupině ZDF potkanů léčených působením HBOT jsme sledovali inhibici tvorby nových mikrocév, co mohlo být způsobené tím, že histologická analýza byla až v pozdních fázích hojení (18. den). V jiných studiích se zjistilo, že angiogeneze u HBOT terapie je zvýšená jen v hypoxických tkáních (Buckley and Cooper, 2022; Huang et al., 2020; Yamamoto et al., 2020).

6 Závěry práce

6.1 Vzorkování v kvantitativní histologii a stereologii

Otázka: Jaké jsou postupy virtuální mikroskopie? Jaké jsou výhody a nevýhody strategii víceúrovňového vzorkování v kvantitativní histologii?

Formulovali jsme praktické postupy pro nejběžnější situace, jako je vyčerpávající vzorkování oblastí zájmu, vzorkování oblastí zájmu různých velikostí, vzorkování stejných oblastí zájmu pro více histologických metod, vzorkování více oblastí zájmu s různou intenzitou nebo pomocí různých objektivů, vícefázové vzorkování a virtuální vzorkování. Byla poskytnuta doporučení pro pilotní studie o systematickém jednotném náhodném vzorkování zorných polí jako součást optimalizace účinnosti histologické kvantifikace, aby se zabránilo nadměrnému nebo nedostatečnému vzorkování.

6.2 Histologické složeni segmentů prasečích krkavic

Otázka: Jsou pravá a levá prasečí ACC u stejného jedince ekvivalentní? Má prasečí ACC stejné mikroskopické složení v celé své délce? Jsou prasečí ACC shodné v mikroskopickém složení s lidskými AC a ATI?

Srovnáním 5 morfometrických parametrů prasečích ACC s lidskými AC a ATI jsme zjistili následující:

(i)   Z histologického hlediska jsou levá a pravá prasečí ACC ekvivalentní.

(ii)   Prasečí ACC měnily svůj fenotyp z elastického na svalový v proximodistálním směru.

(iii)   Prasečí ACC měly tloušťku stěny cévy srovnatelnou s tloušťkou lidských AC a lidských ATI, ale histologické složení bylo odlišné.

6.3 Histologické porovnání ovčích a prasečích segmentů krkavic s lidskými koronárními a hrudními tepnami

Otázka: Jsou pravá a levá ovčí ACC u stejného jedince zaměnitelné? Má ovčí ACC stejné mikroskopické parametre v celé své délce? Jsou ovčí ACC ekvivalentní s lidskými AC a ATI?

Podrobné srovnání 11 morfometrických parametrů ve vzorcích ovčích a prasečích ACC a lidských AC a ATI odhalilo následující:

(i)   Z histologického hlediska byly levá a pravá ACC zaměnitelné u prasat, ale ne u ovcí.

(ii)   Ovčí ACC byly většinou svalového fenotypu, ale prasečí změnily svůj fenotyp z elastického na svalový v proximodistálním směru.

(iii)   Podobně jak prasečí ACC měly i ovčí tloušťku srovnatelnou s tloušťkou lidských AC a lidských ATI, ale histologické složení jak prasečích, tak ovčích ACC bylo odlišné od složení lidských AC a ATI.

(iv)   Vzory korelace mezi histologickými složkami v rámci ovčích ACC byly identické se vzorem nalezeným u prasečích ACC.

Rozdíly mezi histologickým složením ovčích a prasečích ACC zjištěných v naší studii prokázaly omezení, která je nutno mít na paměti při návrhu a při interpretaci poznatků získaných u experimentálních modelům velkých zvířat v kardiochirurgii. Kompletní morfometrická data získaná kvantitativním vyhodnocením arteriálních segmentů byla zveřejněna pro usnadnění analýzy síly testu nutné pro zdůvodnění minimálního počtu vzorků při plánování dalších experimentů. Střední nebo distální segmenty ovčích a prasečích ACC zůstávají nejrealističtějšími a pravděpodobně nejlépe charakterizovanými velkými zvířecími modely pro testování umělých arteriálních náhrad pro AKB. Zformulovali jsme praktická doporučení, jak navrhnout experimenty na ovčích ACC a jak tyto velké zvířecí modely používat způsobem, který maximalizuje validitu jejich histologického hodnocení.

6.4 Histologické hodnocení vaskularizace myších xenoimplantátů lymfomu plášťových buněk

Otázka: Jsou rozdíly mezi použitím Dopplerovy ultrasonografie a kvantitativní histologie při hodnocení hustoty nádorových mikrocév?

Míra vaskularizace patří k faktorům provázejícím agresivní růst nádoru. Fotoakustické zobrazování a Dopplerova ultrasonografie jsou novými metodami pro rychlé a přímé hodnocení vaskularizace a oxygenace nádorů, avšak MVA hodnoty získané touto metodou se liší od kvantitativního histologického hodnocení a bude zapotřebí další validace fotoakustického zobrazování vůči histologickému hodnocení.

6.5 Histologické hodnocení vaskularizace myších xenotransplantátů Non-Hodgkinova lymfomu

Otázka: Jsou kvantitativní parametry mikrocév (MVD a MVA) v nádorovém mikroprostředí PDX modelů odvozených od NHL srovnatelné s primárními lidskými nádory typu NHL?

PDX modely NHL jsou v dnešní době nejlépe charakterizovaným modelem pro translační výzkum díky jejich schopnosti zachovat si stejné genetické informace s původními lidskými NHL. Vnesení dat z histologické analýzy mikrocév ukázalo, že přestože u PDX myších modelů lymfomů je zachován stejný genetický profil, nedochází k rekapitulaci nádorové heterogenity vnitřního mikroprostředí.

6.6 Vliv hyperbarické oxygenoterapie na tvorbu kolagenu typu III v ráně diabetického potkana

Otázka: Jaký má vliv HBOT na tvorbu kolagenu typu I a III a na vaskularizaci v kožní ráně u ZDF potkana?

Na základě histologického hodnocení kožního defektu u ZDF potkanů jsme zjistili, že HBOT podporuje tvorbu kolagenu typu III a současně snižuje počet novotvořených mikrocév

v počáteční fázi hojení. Naopak, HBOT podle studie nemá vliv na tvorbu kolagenu typu I, který byl srovnatelný s kontrolní skupinou.

Zkušenost získaná během řešení uvedených studií nás opravňuje ke společnému závěru v tom smyslu, že analýzou variability morfometrických dat na různých úrovních vzorkování a dále důsledným zveřejňováním těchto dat v repozitářích vědeckých periodik můžeme významně přispět k opakovatelnosti morfometrických studií a rovněž formulovat praktická doporučení pro optimalizaci designu studií využívajících kvantitativní histologické hodnocení.

7 Literatura

Ahmed, M., Hamilton, G., Seifalian, A.M., 2014. The performance of a small-calibre graft for vascular reconstructions in a senescent sheep model. *Biomaterials* 35, 9033–9040. https://doi.org/10.1016/j.biomaterials.2014.07.008

Allaire, E., Guettier, C., Bruneval, P., Plissonnier, D., Michel, J.B., 1994. Cell-free arterial grafts: morphologic characteristics of aortic isografts, allografts, and xenografts in rats. *Journal of Vascular Surgery* 19, 446–456.

Anderson, J.H., Taggart, N.W., Edgerton, S.L., Cantero Peral, S., Holst, K.A., Cetta, F., Wanek Program Preclinical Pipeline, 2018. Ultrasound guided percutaneous common carotid artery access in piglets for intracoronary stem cell infusion. *Laboratory Animals* 52, 88–92. https://doi.org/10.1177/0023677217719923

André-Lévigne, D., Modarressi, A., Pignel, R., Bochaton-Piallat, M.-L., Pittet-Cuénod, B., 2016. Hyperbaric oxygen therapy promotes wound repair in ischemic and hyperglycemic conditions, increasing tissue perfusion and collagen deposition. *Wound Repair Regen* 24, 954–965. https://doi.org/10.1111/wrr.12480

Apelqvist, J., 2008. The foot in perspective. *Diabetes Metabolism Research and Reviews* 24 Suppl 1, S110-115. https://doi.org/10.1002/dmrr.834

Avril, S., Bersi, M.R., Bellini, C., Genovese, K., Humphrey, J.D., 2015. Regional identification of mechanical properties in arteries. C*omputer Methods in Biomechanics and Biomedical Engineering* 18, 1874–1875. https://doi.org/10.1080/10255842.2015.1070577

Aydin, F., Kaya, A., Karapinar, L., Kumbaraci, M., Imerci, A., Karapinar, H., Karakuzu, C., Incesu, M., 2013. IGF-1 Increases with Hyperbaric Oxygen Therapy and Promotes Wound Healing in Diabetic Foot Ulcers. *Journal of Diabetes Research* 2013, 567834. https://doi.org/10.1155/2013/567834

Baddeley, A., Jensen, E.B.V., 2004. Stereology for Statisticians. CRC Press.

Bartolini, B., Thelin, M.A., Svensson, L., Ghiselli, G., van Kuppevelt, T.H., Malmström, A., Maccarana, M., 2013. Iduronic acid in chondroitin/dermatan sulfate affects directional migration of aortic smooth muscle cells. *PLoS One* 8, e66704. https://doi.org/10.1371/journal.pone.0066704

Bastijanic, J.M., Marchant, R.E., Kligman, F., Allemang, M.T., Lakin, R.O., Kendrick, D., Kashyap, V.S., Kottke-Marchant, K., 2016. In vivo evaluation of biomimetic

fluorosurfactant polymer-coated expanded polytetrafluoroethylene vascular grafts in a porcine carotid artery bypass model. *Journal of Vascular Surgery* 63, 1620-1630.e4. https://doi.org/10.1016/j.jvs.2015.01.060

Bia, D., Zócalo, Y., Cabrera-Fischer, E., Wray, S., Armentano, R., 2014. Quantitative Analysis of the Relationship between Blood Vessel Wall Constituents and Viscoelastic Properties: Dynamic Biomechanical and Structural In Vitro Studies in Aorta and Carotid Arteries. *Physiology Journal* 2014, 1–9. https://doi.org/10.1155/2014/142421

Bolender, R.P., 1982. Stereology and Its Uses in Cell Biology. *Annals of the New York Academy of Sciences* 383, 1–16. https://doi.org/10.1111/j.1749-6632.1982.tb23158.x

Boyce, R.W., Dorph-Petersen, K.-A., Lyck, L., Gundersen, H.J.G., 2010. Design-based Stereology: Introduction to Basic Concepts and Practical Approaches for Estimation of Cell Number. *Toxicologic Pathology* 38, 1011–1025. https://doi.org/10.1177/0192623310385140

Brown, D.L., 2017. Bias in image analysis and its solution: unbiased stereology. *Journal of Toxicologic Pathology* 30, 183–191. https://doi.org/10.1293/tox.2017-0013

Buckley, C.J., Cooper, J.S., 2022. Hyperbaric Affects On Angiogenesis, in: StatPearls. StatPearls Publishing, Treasure Island (FL).

Burack, W.R., Spence, J.M., Spence, J.P., Spence, S.A., Rock, P.J., Shenoy, G.N., Shultz, L.D., Bankert, R.B., Bernstein, S.H., 2017. Patient-derived xenografts of low-grade B-cell lymphomas demonstrate roles of the tumor microenvironment. *Blood Advances* 1, 1263–1273. https://doi.org/10.1182/bloodadvances.2017005892

Campelo, M.B.D., Santos, J. de A.F., Maia Filho, A.L.M., Ferreira, D.C.L., Sant'Anna, L.B., Oliveira, R.A. de, Maia, L.F., Arisawa, E.Â.L., 2018. Effects of the application of the amniotic membrane in the healing process of skin wounds in rats. *Acta Cirurgica Brasileira* 33, 144–155. https://doi.org/10.1590/s0102-865020180020000006

Carmen Calles, M., Lima, M.A., Crisóstomo, V., Usón, J.M., Usón, J., 2002. End-to-end anastomosis in growing vessels using a novel suturing technique: VCS metallic staples. *Annals of Vascular Surgery* 16, 345–352. https://doi.org/10.1007/s10016-001-0032-9

Chen, J.-J., Fu, S.-Y., Chiang, C.-S., Hong, J.-H., Yeh, C.-K., 2013. A preclinical study to explore vasculature differences between primary and recurrent tumors using

ultrasound Doppler imaging. *Ultrasound in Medicine and Biology* 39, 860–869. https://doi.org/10.1016/j.ultrasmedbio.2012.11.005

Chow, S.C., Wang, H., Shao, J., 2008. Sample Size Calculations in Clinical Research, Second Edition. Chapman & Hall/CRC Biostatistics Series, Boca Raton.

Clore, J.N., Cohen, I.K., Diegelmann, R.F., 1979. Quantitation of Collagen Types I and III during Wound Healing in Rat Skin. P*roceedings of the Society for Experimental Biology and Medicine* 161, 337–340. https://doi.org/10.3181/00379727-161-40548

Dale, P.D., Sherratt, J.A., Maini, P.K., 1996. A mathematical model for collagen fibre formation during foetal and adult dermal wound healing. *Proceedings of the Royal Society* 263, 653–660. https://doi.org/10.1098/rspb.1996.0098

DiPietro, L.A., 2016. Angiogenesis and wound repair: when enough is enough. *Journal of Leukocyte Biology* 100, 979–984. https://doi.org/10.1189/jlb.4MR0316-102R

Dondelinger, R.F., Ghysels, M.P., Brisbois, D., Donkers, E., Snaps, F.R., Saunders, J., Devière, J., 1998. Relevant radiological anatomy of the pig as a training model in interventional radiology. *European Radiology* 8, 1254–1273. https://doi.org/10.1007/s003300050545

Dubey, N.K., Deng, W.-P., 2018. 20 - Polymeric gels for cartilage tissue engineering, in: Pal, K., Banerjee, I. (Eds.), Polymeric Gels, Woodhead Publishing Series in Biomaterials. *Woodhead Publishing*, pp. 505–525. https://doi.org/10.1016/B978-0-08-102179-8.00020-X

Eberlová, L., Tonar, Z., Witter, K., Křížková, V., Nedorost, L., Korabečná, M., Tolinger, P., Kočová, J., Boudová, L., Třeška, V., Houdek, K., Moláček, J., Vrzalová, J., Pešta, M., Topolčan, O., Valenta, J., 2013. Asymptomatic abdominal aortic aneurysms show histological signs of progression: a quantitative histochemical analysis. *Pathobiology* 80, 11–23. https://doi.org/10.1159/000339304

Emelianov, S.Y., Li, P.-C., O'Donnell, M., 2009. Photoacoustics for molecular imaging and therapy. *Physics Today* 62, 34–39.

Fleischmajer, R., Perlish, J.S., Burgeson, R.E., Shaikh-Bahai, F., Timpl, R., 1990. Type I and type III collagen interactions during fibrillogenesis. *Annals of the New York Academy of Sciences* 580, 161–175. https://doi.org/10.1111/j.1749-6632.1990.tb17927.x

Fleming, I.N., Manavaki, R., Blower, P.J., West, C., Williams, K.J., Harris, A.L., Domarkas, J., Lord, S., Baldry, C., Gilbert, F.J., 2015. Imaging tumour hypoxia with positron

emission tomography. *British Journal of Cancer* 112, 238–250. https://doi.org/10.1038/bjc.2014.610

Fong, P.-Y., Chuang, W.-Y., Huang, Y.-Z., Chang, C.-H., 2017. Safety of carotid artery stent in repetitive transcranial magnetic stimulation-The histopathological proof from swine carotid artery. *Neuroscience Letters* 657, 194–198. https://doi.org/10.1016/j.neulet.2017.08.011

Fukumura, D., Jain, R.K., 2007. Tumor microvasculature and microenvironment: Targets for anti-angiogenesis and normalization. *Microvascular Research* 74, 72–84. https://doi.org/10.1016/j.mvr.2007.05.003

Fukunishi, T., Best, C.A., Sugiura, T., Shoji, T., Yi, T., Udelsman, B., Ohst, D., Ong, C.S., Zhang, H., Shinoka, T., Breuer, C.K., Johnson, J., Hibino, N., 2016. Tissue-Engineered Small Diameter Arterial Vascular Grafts from Cell-Free Nanofiber PCL/Chitosan Scaffolds in a Sheep Model. *PLoS One* 11, e0158555. https://doi.org/10.1371/journal.pone.0158555

García, A., Martínez, M.A., Peña, E., 2013. Determination and modeling of the inelasticity over the length of the porcine carotid artery. *Journal of Biomechanical Engineering* 135, 31004. https://doi.org/10.1115/1.4023371

García, A., Peña, E., Laborda, A., Lostalé, F., De Gregorio, M.A., Doblaré, M., Martínez, M.A., 2011. Experimental study and constitutive modelling of the passive mechanical properties of the porcine carotid artery and its relation to histological analysis: Implications in animal cardiovascular device trials. *Medical Engineering and Phisics* 33, 665–676. https://doi.org/10.1016/j.medengphy.2011.01.016

Gardner, R.J., Jensen, E.B.V., Volčič, A., 2003. Geometric tomography and local stereology. *Advances in Applied Mathematics* 30, 397–423. https://doi.org/10.1016/S0196-8858(02)00502-X

Gundersen, H.J.G., 1977. Notes on the estimation of the numerical density of arbitrary profiles: the edge effect. *Journal of Microscopy* 111, 219–223. https://doi.org/10.1111/j.1365-2818.1977.tb00062.x

Gundersen, H.J.G., Bendtsen, T.F., Korbo, L., Marcussen, N., Møller, A., Nielsen, K., Nyengaard, J.R., Pakkenberg, B., Sørensen, F.B., Vesterby, A., West, M.J., 1988. Some new, simple and efficient stereological methods and their use in pathological research and diagnosis. *APMIS* 96, 379–394. https://doi.org/10.1111/j.1699-0463.1988.tb05320.x

Gundersen, H.J.G., Jensen, E.B., 1987. The efficiency of systematic sampling in stereology and its prediction. *Journal of Microscopy* 147, 229–263. https://doi.org/10.1111/j.1365-2818.1987.tb02837.x

Gundersen, H.J.G., ØSterby, R., 1981. Optimizing sampling efficiency of stereological studies in biology: or 'Do more less well!'. *Journal of Microscopy* 121, 65–73. https://doi.org/10.1111/j.1365-2818.1981.tb01199.x

Guo, S., DiPietro, L.A., 2010. Factors Affecting Wound Healing. *Journal of Dental Research* 89, 219–229. https://doi.org/10.1177/0022034509359125

Hanahan, D., Coussens, L.M., 2012. Accessories to the crime: functions of cells recruited to the tumor microenvironment. *Cancer Cell* 21, 309–322. https://doi.org/10.1016/j.ccr.2012.02.022

Hawthorne, W.J., Ao, P.Y., Fletcher, J.P., 2002. Vascular closure staples reduce intimal hyperplasia in prosthesis implantation. *ANZ Journal of Surgery.* 72, 862–866. https://doi.org/10.1046/j.1445-2197.2002.t01-1-02588.x

Hida, A.I., Omanovic, D., Pedersen, L., Oshiro, Y., Ogura, T., Nomura, T., Kurebayashi, J., Kanomata, N., Moriya, T., 2020. Automated assessment of Ki-67 in breast cancer: the utility of digital image analysis using virtual triple staining and whole slide imaging. *Histopathology* 77, 471–480. https://doi.org/10.1111/his.14140

Hobizal, K.B., Wukich, D.K., 2012. Diabetic foot infections: current concept review. *Diabetic Foot Ankle* 3. https://doi.org/10.3402/dfa.v3i0.18409

Howard, V., Reed, M., 2004. Unbiased Stereology: Three-Dimensional Measurement in Microscopy. Garland Science.

Hsia, C.C.W., Hyde, D.M., Ochs, M., Weibel, E.R., ATS/ERS Joint Task Force on Quantitative Assessment of Lung Structure, 2010. An official research policy statement of the American Thoracic Society/European Respiratory Society: standards for quantitative assessment of lung structure. *American Journal of Respiratory and Critical Care Medicine* 181, 394–418. https://doi.org/10.1164/rccm.200809-1522ST

Huang, Xu, Liang, P., Jiang, B., Zhang, P., Yu, W., Duan, M., Guo, L., Cui, X., Huang, M., Huang, Xiaoyuan, 2020. Hyperbaric oxygen potentiates diabetic wound healing by promoting fibroblast cell proliferation and endothelial cell angiogenesis. *Life Sciences* 259, 118246. https://doi.org/10.1016/j.lfs.2020.118246

Literatura

Humphrey, J.D., 2013. Possible Mechanical Roles of Glycosaminoglycans in Thoracic Aortic Dissection and Associations with Dysregulated TGF-β. *Journal of Vascular Research* 50, 1–10. https://doi.org/10.1159/000342436

Jaramillo, J., Valencia-Rivero, K.T., Cedano-Serrano, F.J., López, R., Sandoval, N., Briceño, J.C., 2018. Design and Evaluation of a Structural Reinforced Small Intestinal Submucosa Vascular Graft for Hemodialysis Access in a Porcine Model. *ASAIO Journal* 64, 270–277. https://doi.org/10.1097/MAT.0000000000000618

Jiang, Y., Li, Y., Xu, X., Yu, Y., Liu, W., Liu, X., 2016. An in vitro porcine model evaluating a novel stent retriever for thrombectomy of the common carotid artery. *Catheterization and Cardiovascular Interventions* 87, 457–464. https://doi.org/10.1002/ccd.26285

Jing, X., Yang, F., Shao, C., Wei, K., Xie, M., Shen, H., Shu, Y., 2019. Role of hypoxia in cancer therapy by regulating the tumor microenvironment. *Molecular Cancer* 18, 157. https://doi.org/10.1186/s12943-019-1089-9

Katsimpoulas, M., Morticelli, L., Michalopoulos, E., Gontika, I., Stavropoulos-Giokas, C., Kostakis, A., Haverich, A., Korossis, S., 2015. Investigation of the biomechanical integrity of decellularized rat abdominal aorta. *Transplantation Proceedings* 47, 1228–1233. https://doi.org/10.1016/j.transproceed.2014.11.061

Keša, P., Pokorná, E., Grajciarová, M., Tonar, Z., Vočková, P., Trochet, P., Kopeček, M., Jakša, R., Šefc, L., Klener, P., 2021. Quantitative In Vivo Monitoring of Hypoxia and Vascularization of Patient-Derived Murine Xenografts of Mantle Cell Lymphoma Using Photoacoustic and Ultrasound Imaging. *Ultrasound in Medicine and Biology* 47, 1099–1107. https://doi.org/10.1016/j.ultrasmedbio.2020.12.010

Klener, P., 2019. Advances in Molecular Biology and Targeted Therapy of Mantle Cell Lymphoma. *International Journal of Molecular Sciences* 20, E4417. https://doi.org/10.3390/ijms20184417

Klinge, U., Si, Z., Zheng, H., Schumpelick, V., Bhardwaj, S., Klosterhalfen, B., 2000. Abnormal Collagen I to III Distribution in the Skin of Patients with Incisional Hernia. European surgical research. Europäische chirurgische Forschung. *Recherches chirurgicales européennes* 32, 43–8. https://doi.org/10.1159/000008740

Kochová, P., Kuncová, J., Svíglerová, J., Cimrman, R., Miklíková, M., Liška, V., Tonar, Z., 2012. The contribution of vascular smooth muscle, elastin and collagen on the

passive mechanics of porcine carotid arteries. *Physiological Measurement* 33, 1335–1351. https://doi.org/10.1088/0967-3334/33/8/1335

Kolinko, Y., Malečková, A., Kochová, P., Grajciarová, M., Blassová, T., Kural, T., Trailin, A., Červenková, L., Havránková, J., Vištejnová, L., Tonarová, P., Moulisová, V., Jiřík, M., Zavaďáková, A., Tichánek, F., Liška, V., Králíčková, M., Witter, K., Tonar, Z., 2021. Using virtual microscopy for the development of sampling strategies in quantitative histology and design-based stereology. *Anatomia, Histologia, Embryologia* https://doi.org/10.1111/ahe.12765

König, H.E., Liebich, H.G., 2002. Anatómia domácich cicavcov 2 / Anatomie domácích savců 2. Hajko a Hajková.

Kubínová, L., Janáček, J., Ribarič, S., Čebašek, V., Eržen, I., 2001. Three-dimensional study of the capillary supply of skeletal muscle fibres using confocal microscopy. *Journal of Muscle Research and Cell Motility* 22, 217–227. https://doi.org/10.1023/A:1012201314440

Lai, Y., Wei, X., Lin, S., Qin, L., Cheng, L., Li, P., 2017. Current status and perspectives of patient-derived xenograft models in cancer research. *Journal of Hematology and Oncology* 10, 106. https://doi.org/10.1186/s13045-017-0470-7

Li, H., Lu, S., Liu, H., Ge, J., Zhang, H., 2014. Scanning electron microscope evidence of telocytes in vasculature. *Journal of Cellular and Molecular Medicine* 18, 1486–1489. https://doi.org/10.1111/jcmm.12333

Lipsky, B.A., Senneville, É., Abbas, Z.G., Aragón-Sánchez, J., Diggle, M., Embil, J.M., Kono, S., Lavery, L.A., Malone, M., van Asten, S.A., Urbančič-Rovan, V., Peters, E.J.G., International Working Group on the Diabetic Foot (IWGDF), 2020. Guidelines on the diagnosis and treatment of foot infection in persons with diabetes (IWGDF 2019 update). *Diabetes Metabolism Research and Reviews* 36 Suppl 1, e3280. https://doi.org/10.1002/dmrr.3280

Manbachi, A., Hoi, Y., Wasserman, B.A., Lakatta, E.G., Steinman, D.A., 2011. On the shape of the common carotid artery with implications for blood velocity profiles. *Physiological Measurement* 32, 1885–1897. https://doi.org/10.1088/0967-3334/32/12/001

Mandarim-de-Lacerda, C.A., 2003. Stereological tools in biomedical research. *Anais da Academia Brasileira de Ciências* 75, 469–486. https://doi.org/10.1590/S0001-37652003000400006

Maschietto, N., Semplicini, L., Ceolotto, G., Cattelan, A., Poser Dvm, H., Iacopetti, I., Gerardi, G., De Benedictis, G.M., Pilla, T., Bernardini, D., Aresu, L., Rizzo, S., Basso, C., Semplicini, A., Milanesi, O., 2017. Aortic stenting in the growing sheep causes aortic endothelial dysfunction but not hypertension: Clinical implications for coarctation repair. *Congenital Heart Disease* 12, 74–83. https://doi.org/10.1111/chd.12406

Mattson, J.M., Turcotte, R., Zhang, Y., 2017. Glycosaminoglycans Contribute to Extracellular Matrix Fiber Recruitment and Arterial Wall Mechanics. *Biomechanics and Modeling in Mechanobiology* 16, 213–225. https://doi.org/10.1007/s10237-016-0811-4

Mayhew, T.M., Lucocq, J.M., 2015. From gross anatomy to the nanomorphome: stereological tools provide a paradigm for advancing research in quantitative morphomics. *Journal of Anatomy* 226, 309–321. https://doi.org/10.1111/joa.12287

Mendis-Handagama, S.M.L.C., Ewing, L.L., 1990. Sources of error in the estimation of Leydig cell numbers in control and atrophied mammalian testes. *Journal of Microscopy* 159, 73–82. https://doi.org/10.1111/j.1365-2818.1990.tb03020.x

Menke, M.N., Menke, N.B., Boardman, C.H., Diegelmann, R.F., 2008. Biologic therapeutics and molecular profiling to optimize wound healing. *Gynecologic Oncology* 111, S87-91. https://doi.org/10.1016/j.ygyno.2008.07.052

Mouton, P.R., 2013. Neurostereology: Unbiased Stereology of Neural Systems, 1st edition. ed. Wiley-Blackwell.

Mouton, P.R., 2011. Unbiased Stereology: A Concise Guide, 1st edition. ed. Johns Hopkins University Press.

Mrówczyński, W., Mugnai, D., de Valence, S., Tille, J.-C., Khabiri, E., Cikirikcioglu, M., Möller, M., Walpoth, B.H., 2014. Porcine carotid artery replacement with biodegradable electrospun poly-e-caprolactone vascular prosthesis. Journal of Vascular Surgery 59, 210–219. https://doi.org/10.1016/j.jvs.2013.03.004

Mühlfeld, C., 2014. Quantitative morphology of the vascularisation of organs: A stereological approach illustrated using the cardiac circulation. *Annals of Anatomy* 196, 12–19. https://doi.org/10.1016/j.aanat.2012.10.010

Nikoubashman, O., Heringer, S., Feher, K., Brockmann, M.-A., Sellhaus, B., Dreser, A., Kurtenbach, K., Pjontek, R., Jockenhövel, S., Weis, J., Kießling, F., Gries, T., Wiesmann, M., 2018. Development of a Polymer-Based Biodegradable

Neurovascular Stent Prototype: A Preliminary In Vitro and In Vivo Study. *Macromolecular Bioscience* 18, e1700292. https://doi.org/10.1002/mabi.201700292

Otto, K.J., Wyse, B.D., Cabot, P.J., Smith, M.T., 2011. Longitudinal study of painful diabetic neuropathy in the Zucker diabetic fatty rat model of type 2 diabetes: impaired basal G-protein activity appears to underpin marked morphine hyposensitivity at 6 months. *Pain Medicine* 12, 437–450. https://doi.org/10.1111/j.1526-4637.2011.01067.x

Packer, C.F., Ali, S.A., Manna, B., 2022. Diabetic Ulcer, in: StatPearls. StatPearls Publishing, Treasure Island (FL).

Parchami, A., Dehkordi, R.F., Derakhshan, A., 2009. Comparative Histomorphometric Study of the Common Carotid Artery and its Terminal Branches in Sheep and Goats. *Bulgarian Journal of Veterinary Medicine* 12(3), 165-170

Peña-Villalobos, I., Casanova-Maldonado, I., Lois, P., Prieto, C., Pizarro, C., Lattus, J., Osorio, G., Palma, V., 2018. Hyperbaric Oxygen Increases Stem Cell Proliferation, Angiogenesis and Wound-Healing Ability of WJ-MSCs in Diabetic Mice. *Frontiers in Physiology* 9.

Pereira, L.M.M., Mandarim-de-Lacerda, C.A., 2001. Glomerular profile numerical density per area and mean glomerular volume in rats submitted to nitric oxide synthase blockade. *Histology and Histopathology* 16, 15–20.

Peterson, D.A., 2010. Stereology, in: Kompoliti, K., Metman, L.V. (Eds.), Encyclopedia of Movement Disorders. Academic Press, Oxford, pp. 168–170. https://doi.org/10.1016/B978-0-12-374105-9.00287-2

Petrakis, G., Veloza, L., Clot, G., Gine, E., Gonzalez-Farre, B., Navarro, A., Bea, S., Martínez, A., Lopez-Guillermo, A., Amador, V., Ribera-Cortada, I., Campo, E., 2019. Increased tumour angiogenesis in SOX11-positive mantle cell lymphoma. *Histopathology* 75, 704–714. https://doi.org/10.1111/his.13935

Popesko, P., Dvorský, P., Postníková, V., Jablonovský, F., 1992. Anatómia hospodárskych zvierat, 1. ed, Veterinárstvo. Príroda.

Prim, D.A., Mohamed, M.A., Lane, B.A., Poblete, K., Wierzbicki, M.A., Lessner, S.M., Shazly, T., Eberth, J.F., 2018. Comparative mechanics of diverse mammalian carotid arteries. *PLoS One* 13. https://doi.org/10.1371/journal.pone.0202123

Prukova, D., Andera, L., Nahacka, Z., Karolova, J., Svaton, M., Klanova, M., Havranek, O., Soukup, J., Svobodova, K., Zemanova, Z., Tuskova, D., Pokorna, E., Helman, K.,

Literatura

Forsterova, K., Pacheco-Blanco, M., Vockova, P., Berkova, A., Fronkova, E., Trneny, M., Klener, P., 2019. Cotargeting of BCL2 with Venetoclax and MCL1 with S63845 Is Synthetically Lethal In Vivo in Relapsed Mantle Cell Lymphoma. *Clinical Cancer Research* 25, 4455–4465. https://doi.org/10.1158/1078-0432.CCR-18-3275

Rao, N., Kishore, K., Sujatha, K., Rao, H.R., 2016. Aortic arch arteries in man and domestic animals: A comparative study. *International Journal of Anatomy and Research* 4, 3087–3091. https://doi.org/10.16965/ijar.2016.409

Rayman, G., Vas, P., Dhatariya, K., Driver, V., Hartemann, A., Londahl, M., Piaggesi, A., Apelqvist, J., Attinger, C., Game, F., International Working Group on the Diabetic Foot (IWGDF), 2020. Guidelines on use of interventions to enhance healing of chronic foot ulcers in diabetes (IWGDF 2019 update). *Diabetes Metabolism Research and Reviews* 36 Suppl 1, e3283. https://doi.org/10.1002/dmrr.3283

Reinboth, B., Hanssen, E., Cleary, E.G., Gibson, M.A., 2002. Molecular interactions of biglycan and decorin with elastic fiber components: biglycan forms a ternary complex with tropoelastin and microfibril-associated glycoprotein 1. *Journal of Biological Chemistry* 277, 3950–3957. https://doi.org/10.1074/jbc.M109540200

Schindelin, J., Arganda-Carreras, I., Frise, E., Kaynig, V., Longair, M., Pietzsch, T., Preibisch, S., Rueden, C., Saalfeld, S., Schmid, B., Tinevez, J.-Y., White, D.J., Hartenstein, V., Eliceiri, K., Tomancak, P., Cardona, A., 2012. Fiji: an open-source platform for biological-image analysis. *Nature Methods* 9, 676–682. https://doi.org/10.1038/nmeth.2019

Schleimer, K., Jalaie, H., Afify, M., Woitok, A., Barbati, M.E., Hoeft, K., Jacobs, M., Tolba, R.H., Steitz, J., 2018. Sheep models for evaluation of novel patch and prosthesis material in vascular surgery: tips and tricks to avoid possible pitfalls. *Acta Veterinaria Scandinavica* 60, 42. https://doi.org/10.1186/s13028-018-0397-1

Schneider, C.A., Rasband, W.S., Eliceiri, K.W., 2012. NIH Image to ImageJ: 25 years of image analysis. *Nature Methods* 9, 671–675. https://doi.org/10.1038/nmeth.2089

Schulz, S.-A., Wöhler, A., Beutner, D., Angelov, D.N., 2016. Microsurgical anatomy of the human carotid body (glomus caroticum): Features of its detailed topography, syntopy and morphology. *Annals of Anatomy* 204, 106–113. https://doi.org/10.1016/j.aanat.2015.11.009

Literatura

Shain, K.H., Dalton, W.S., Tao, J., 2015. The tumor microenvironment shapes hallmarks of mature B-cell malignancies. *Oncogene* 34, 4673–4682. https://doi.org/10.1038/onc.2014.403

Shankland, K.R., Armitage, J.O., Hancock, B.W., 2012. Non-Hodgkin lymphoma. *Lancet* 380, 848–857. https://doi.org/10.1016/S0140-6736(12)60605-9

Shinaoka, A., Momota, R., Shiratsuchi, E., Kosaka, M., Kumagishi, K., Nakahara, R., Naito, I., Ohtsuka, A., 2013. Architecture of the subendothelial elastic fibers of small blood vessels and variations in vascular type and size. *Microscopy and Microanalysis* 19, 406–414. https://doi.org/10.1017/S1431927612014341

Slavkovsky, R., Kohlerova, R., Tkacova, V., Jiroutova, A., Tahmazoglu, B., Velebny, V., Rezačová, M., Sobotka, L., Kanta, J., 2011. Zucker diabetic fatty rat: a new model of impaired cutaneous wound repair with type II diabetes mellitus and obesity. *Wound Repair Regen* 19, 515–525. https://doi.org/10.1111/j.1524-475X.2011.00703.x

Slomianka, L., West, M.J., 2005. Estimators of the precision of stereological estimates: an example based on the CA1 pyramidal cell layer of rats. *Neuroscience* 136, 757–767. https://doi.org/10.1016/j.neuroscience.2005.06.086

Sokolis, D.P., 2007. Passive mechanical properties and structure of the aorta: segmental analysis. A*cta Physiology (Oxf)* 190, 277–289. https://doi.org/10.1111/j.1748-1716.2006.01661.x

Sokolis, D.P., Boudoulas, H., Karayannacos, P.E., 2008. Segmental differences of aortic function and composition: clinical implications. *Hellenic Journal of Cardiology* 49, 145–154.

Sokolis, D.P., Sassani, S., Kritharis, E.P., Tsangaris, S., 2011. Differential histomechanical response of carotid artery in relation to species and region: mathematical description accounting for elastin and collagen anisotropy. *Medical and Biological Engineering Computing* 49, 867–879. https://doi.org/10.1007/s11517-011-0784-5

Stewart, J.K., Perkins, S.S., Kim, C.Y., 2017. Creation of an Extraluminal Arterial Bypass Graft Using a Commercially Available Self-Expanding Stent Graft: Feasibility Study in a Porcine Model. *Cardiovascular and Interventional Radiology* 40, 1447–1453. https://doi.org/10.1007/s00270-017-1672-7

Sun, L., Gao, W., Fu, X., Shi, M., Xie, W., Zhang, W., Zhao, F., Chen, X., 2018. Enhanced wound healing in diabetic rats by nanofibrous scaffolds mimicking the basketweave

pattern of collagen fibrils in native skin. *Biomaterials Science* 6, 340–349. https://doi.org/10.1039/c7bm00545h

Swerdlow, S.H., Campo, E., Pileri, S.A., Harris, N.L., Stein, H., Siebert, R., Advani, R., Ghielmini, M., Salles, G.A., Zelenetz, A.D., Jaffe, E.S., 2016. The 2016 revision of the World Health Organization classification of lymphoid neoplasms. *Blood* 127, 2375–2390. https://doi.org/10.1182/blood-2016-01-643569

Swerdlow, S.H., Cook, J.R., 2020. As the world turns, evolving lymphoma classifications-past, present and future. *Human Pathology* 95, 55–77. https://doi.org/10.1016/j.humpath.2019.08.019

Szafron, J.M., Ramachandra, A.B., Breuer, C.K., Marsden, A.L., Humphrey, J.D., 2019. Optimization of Tissue-Engineered Vascular Graft Design Using Computational Modeling. *Tissue Engineering Part C Methods* 25, 561–570. https://doi.org/10.1089/ten.TEC.2019.0086

Takahashi, S., Piao, W., Matsumura, Y., Komatsu, T., Ueno, T., Terai, T., Kamachi, T., Kohno, M., Nagano, T., Hanaoka, K., 2012. Reversible Off–On Fluorescence Probe for Hypoxia and Imaging of Hypoxia–Normoxia Cycles in Live Cells. *Journal of the American Chemical Society* 134, 19588–19591. https://doi.org/10.1021/ja310049d

Tennant, M., McGeachie, J.K., 1990. Blood vessel structure and function: a brief update on recent advances. *Aust N Z J Surgery* 60, 747–753. https://doi.org/10.1111/j.1445-2197.1990.tb07468.x

Tomášek, P., Tonar, Z., Grajciarová, M., Kural, T., Turek, D., Horáková, J., Pálek, R., Eberlová, L., Králíčková, M., Liška, V., 2020. Histological mapping of porcine carotid arteries - An animal model for the assessment of artificial conduits suitable for coronary bypass grafting in humans. *Annals of Anatomy* 228, 151434. https://doi.org/10.1016/j.aanat.2019.151434

Tomaszewski, J.E., Hipp, J., Tangrea, M., Madabhushi, A., 2014. Machine Vision and Machine Learning in Digital Pathology, in: McManus, L.M., Mitchell, R.N. (Eds.), Pathobiology of Human Disease. *Academic Press, San Diego*, pp. 3711–3722. https://doi.org/10.1016/B978-0-12-386456-7.07202-6

Tonar, Z., 2008. Atlas kvantitativni histologie.

Tonar, Z., Janáček, J., Poledne, R., 2007. Kvantitativní popis aterosklerotických lézí na úrovni optické mikroskopie. *Cor et Vasa* 49, 95–101. https://doi.org/10.33678/cor.2007.037

Literatura

Tonar, Z., Kochova, P., Cimrman, R., Perktold, J., Witter, K., 2015. Segmental differences in the orientation of smooth muscle cells in the tunica media of porcine aortae. *Biomechanics and Modeling in Mechanobiology* 14, 315–332. https://doi.org/10.1007/s10237-014-0605-5

Tonar, Z., Tomášek, P., Loskot, P., Janáček, J., Králíčková, M., Witter, K., 2016. Vasa vasorum in the tunica media and tunica adventitia of the porcine aorta. *Annals of Anatomy* 205, 22–36. https://doi.org/10.1016/j.aanat.2016.01.008

Townsend, E.C., Murakami, M.A., Christodoulou, A., Christie, A.L., Köster, J., DeSouza, T.A., Morgan, E.A., Kallgren, S.P., Liu, H., Wu, S.-C., Plana, O., Montero, J., Stevenson, K.E., Rao, P., Vadhi, R., Andreeff, M., Armand, P., Ballen, K.K., Barzaghi-Rinaudo, P., Cahill, S., Clark, R.A., Cooke, V.G., Davids, M.S., DeAngelo, D.J., Dorfman, D.M., Eaton, H., Ebert, B.L., Etchin, J., Firestone, B., Fisher, D.C., Freedman, A.S., Galinsky, I.A., Gao, H., Garcia, J.S., Garnache-Ottou, F., Graubert, T.A., Gutierrez, A., Halilovic, E., Harris, M.H., Herbert, Z.T., Horwitz, S.M., Inghirami, G., Intlekofer, A.M., Ito, M., Izraeli, S., Jacobsen, E.D., Jacobson, C.A., Jeay, S., Jeremias, I., Kelliher, M.A., Koch, R., Konopleva, M., Kopp, N., Kornblau, S.M., Kung, A.L., Kupper, T.S., LeBoeuf, N.R., LaCasce, A.S., Lees, E., Li, L.S., Look, A.T., Murakami, M., Muschen, M., Neuberg, D., Ng, S.Y., Odejide, O.O., Orkin, S.H., Paquette, R.R., Place, A.E., Roderick, J.E., Ryan, J.A., Sallan, S.E., Shoji, B., Silverman, L.B., Soiffer, R.J., Steensma, D.P., Stegmaier, K., Stone, R.M., Tamburini, J., Thorner, A.R., van Hummelen, P., Wadleigh, M., Wiesmann, M., Weng, A.P., Wuerthner, J.U., Williams, D.A., Wollison, B.M., Lane, A.A., Letai, A., Bertagnolli, M.M., Ritz, J., Brown, M., Long, H., Aster, J.C., Shipp, M.A., Griffin, J.D., Weinstock, D.M., 2016. The Public Repository of Xenografts Enables Discovery and Randomized Phase II-like Trials in Mice. *Cancer Cell* 29, 574–586. https://doi.org/10.1016/j.ccell.2016.03.008

Tschanz, S., Schneider, J.P., Knudsen, L., 2014. Design-based stereology: Planning, volumetry and sampling are crucial steps for a successful study. *Annals of Anatomy* 196, 3–11. https://doi.org/10.1016/j.aanat.2013.04.011

Tuk, B., Tong, M., Fijneman, E.M.G., van Neck, J.W., 2014. Hyperbaric Oxygen Therapy to Treat Diabetes Impaired Wound Healing in Rats. *PLoS One* 9. https://doi.org/10.1371/journal.pone.0108533

Tzchori, I., Falah, M., Shteynberg, D., Levin Ashkenazi, D., Loberman, Z., Perry, L., Flugelman, M.Y., 2018. Improved Patency of ePTFE Grafts as a Hemodialysis Access Site by Seeding Autologous Endothelial Cells Expressing Fibulin-5 and VEGF. *Molecular Therapy* 26, 1660–1668. https://doi.org/10.1016/j.ymthe.2018.04.003

van Neck, J.W., Tuk, B., Fijneman, E.M.G., Redeker, J.J., Talahatu, E.M., Tong, M., 2017. Hyperbaric oxygen therapy for wound healing in diabetic rats: Varying efficacy after a clinically-based protocol. *PLoS ONE* 12, e0177766. https://doi.org/10.1371/journal.pone.0177766

Velnar, T., Bailey, T., Smrkolj, V., 2009. The wound healing process: an overview of the cellular and molecular mechanisms. *Journal of International Medical Research* 37, 1528–1542. https://doi.org/10.1177/147323000903700531

Veras, M.M., Costa, N.S.X., Mayhew, T., 2014. 46 - Best Practice for Quantifying the Microscopic Structure of Mouse Placenta: The Stereological Approach, in: Croy, B.A., Yamada, A.T., DeMayo, F.J., Adamson, S.L. (Eds.), The Guide to Investigation of Mouse Pregnancy. *Academic Press, Boston,* pp. 545–556. https://doi.org/10.1016/B978-0-12-394445-0.00046-1

Veselá, P., Tonar, Z., Sálek, D., Vokurka, S., Trněný, M., Kodet, R., Moulis, M., Kašparová, P., Vernerová, Z., Velenská, Z., Stříteský, J., Michal, M., Boudová, L., 2014. Microvessel density of mantle cell lymphoma. A retrospective study of its prognostic role and the correlation with the Ki-67 and the mantle cell lymphoma international prognostic index in 177 cases. *Virchows Archiv* 465, 587–597. https://doi.org/10.1007/s00428-014-1632-4

Vinik, A.I., Maser, R.E., Mitchell, B.D., Freeman, R., 2003. Diabetic Autonomic Neuropathy. *Diabetes Care* 26, 1553–1579. https://doi.org/10.2337/diacare.26.5.1553

Walpoth, B.H., Zammaretti, P., Cikirikcioglu, M., Khabiri, E., Djebaili, M.K., Pache, J.-C., Tille, J.-C., Aggoun, Y., Morel, D., Kalangos, A., Hubbell, J.A., Zisch, A.H., 2007. Enhanced intimal thickening of expanded polytetrafluoroethylene grafts coated with fibrin or fibrin-releasing vascular endothelial growth factor in the pig carotid artery interposition model. *Journal of Thoracic and Cardiovascular Surgery* 133, 1163–1170. https://doi.org/10.1016/j.jtcvs.2007.01.029

Wang, T., Gu, Q., Zhao, J., Mei, J., Shao, M., Pan, Y., Zhang, J., Wu, H., Zhang, Z., Liu, F., 2015. Calcium alginate enhances wound healing by up-regulating the ratio of collagen types I/III in diabetic rats. *International Journal of Clinical and Experimental Pathology* 8, 6636–6645.

Waniczek, D., Kozowicz, A., Muc-Wierzgoń, M., Kokot, T., Swiętochowska, E., Nowakowska-Zajdel, E., 2013. Adjunct methods of the standard diabetic foot ulceration therapy. *Evidence Based Complementary and Alternative Medicine* 2013, 243568. https://doi.org/10.1155/2013/243568

Watson, M., Lea, D., Skaland, I., Hagland, H.R., Søreide, K., 2020. Loss of MSH3 Is Not Related to EMAST in Colorectal Cancer. Digitalised Automated Expression Analysis in a Population-Based Cohort. European *Journal of Surgical Oncology* 46, e108–e109. https://doi.org/10.1016/j.ejso.2019.11.270

Weber, C., Reinhardt, S., Eghbalzadeh, K., Wacker, M., Guschlbauer, M., Maul, A., Sterner-Kock, A., Wahlers, T., Wippermann, J., Scherner, M., 2018. Patency and in vivo compatibility of bacterial nanocellulose grafts as small-diameter vascular substitute. *Journal of Vascular Surgery* 68, 177S-187S.e1. https://doi.org/10.1016/j.jvs.2017.09.038

Weizsäcker, H.W., Zierler, E., Juch, H., 2014. A simple method for vital staining of elastin in arterial tissue. *Biomed Tech (Berl)* 59, 367–373. https://doi.org/10.1515/bmt-2013-0089

Willekes, C., Hoeks, A.P., Bots, M.L., Brands, P.J., Willigers, J.M., Reneman, R.S., 1999. Evaluation of off-line automated intima-media thickness detection of the common carotid artery based on M-line signal processing. *Ultrasound in Medicine and Biology* 25, 57–64. https://doi.org/10.1016/s0301-5629(98)00138-0

Witter, K., Tonar, Z., Matejka, V.M., Martinca, T., Jonák, M., Rokosný, S., Pirk, J., 2010. Tissue reaction to three different types of tissue glues in an experimental aorta dissection model: a quantitative approach. *Histochemistry and Cell Biology* 133, 241–259. https://doi.org/10.1007/s00418-009-0656-3

Witter, K., Tonar, Z., Schöpper, H., 2017. How many Layers has the Adventitia? - Structure of the Arterial Tunica Externa Revisited. *Anatomia, Histologia and Embryologia* 46, 110–120. https://doi.org/10.1111/ahe.12239

Wulff, B., Stahlhoff, S., Vonthein, R., Schmidt, A., Sigler, M., Torsello, G.B., Herten, M., 2017. Biomimetic Heparan Sulfate-Like Coated ePTFE Grafts Reduce In-graft

Neointimal Hyperplasia in Ovine Carotids. *Annals of Vascular Surgery* 40, 274–284. https://doi.org/10.1016/j.avsg.2016.09.015

Wyatt, H.L., Richards, R., Pullin, R., Yang, T.J., Blain, E.J., Evans, S.L., 2016. Variation in electrosurgical vessel seal quality along the length of a porcine carotid artery. *Proceedings of the Institution of Mechanical Engineers* 230, 169–174. https://doi.org/10.1177/0954411915621092

Wynn, T.A., 2008. Cellular and molecular mechanisms of fibrosis. *Journal of Pathology* 214, 199–210. https://doi.org/10.1002/path.2277

Xia, J., Yao, J., Wang, L.V., 2014. Photoacoustic tomography: principles and advances. E*lectromagn Waves (Camb)* 147, 1–22.

Yamamoto, N., Oyaizu, T., Enomoto, M., Horie, M., Yuasa, M., Okawa, A., Yagishita, K., 2020. VEGF and bFGF induction by nitric oxide is associated with hyperbaric oxygen-induced angiogenesis and muscle regeneration. *Scientific Reports* 10, 2744. https://doi.org/10.1038/s41598-020-59615-x

Young, A., McNaught, C.-E., 2011. The physiology of wound healing. *Surgery (Oxford), Wound Management* 29, 475–479. https://doi.org/10.1016/j.mpsur.2011.06.011

Zhang, H., Zhao, Y., Wang, M., Song, W., Sun, P., Jin, X., 2019. A promising therapeutic option for diabetic bladder dysfunction: Adipose tissue-derived stem cells pretreated by defocused low-energy shock wave. *Journal of Tissue Engineering and Regenerative Medicine* 13, 986–996. https://doi.org/10.1002/term.2844

Zhang, L., Nomie, K., Zhang, H., Bell, T., Pham, L., Kadri, S., Segal, J., Li, S., Zhou, S., Santos, D., Richard, S., Sharma, S., Chen, W., Oriabure, O., Liu, Y., Huang, S., Guo, H., Chen, Z., Tao, W., Li, C., Wang, Jack, Fang, B., Wang, Jacqueline, Li, L., Badillo, M., Ahmed, M., Thirumurthi, S., Huang, S.Y., Shao, Y., Lam, L., Yi, Q., Wang, Y.L., Wang, M., 2017. B-Cell Lymphoma Patient-Derived Xenograft Models Enable Drug Discovery and Are a Platform for Personalized Therapy. *Clinical Cancer Research* 23, 4212–4223. https://doi.org/10.1158/1078-0432.CCR-16-2703

Zhou, Z.-H., Peng, J., Meng, Z.-Y., Chen, L., Huang, J.-L., Huang, H.-Q., Li, L., Zeng, W., Wei, Y., Zhu, C.-H., Chen, K.-N., 2016. Novel A20-gene-eluting stent inhibits carotid artery restenosis in a porcine model. *Drug Design Development and Therapy* 10, 2341–2351. https://doi.org/10.2147/DDDT.S94984

8 Seznam tabulek

9 Seznam obrázků

10 Publikační činnost autorky

10.1 Publikace vztahující se k tématu dizertační práce

10.1.1 Časopisy s impakt faktorem

Kolinko, Y., Malečková, A., Kochová, P., **Grajciarová, M.**, Blassová, T., Kural, T., Trailin, A., Červenková, L., Havránková, J., Vištejnová, L., Tonarová, P., Moulisová, V., Jiřík, M., Zavaďáková, A., Tichánek, F., Liška, V., Králíčková, M., Witter, K., Tonar, Z. Using virtual microscopy for the development of sampling strategies in quantitative histology and design-based stereology. Anat. Histol. Embryol. 2022 Jan;51(1):3-22. DOI: 10.1111/ahe.12765. **IF(JCR2020)=1.114. Q3(Veterinary sciences)** https://pubmed.ncbi.nlm.nih.gov/34806204/

Tomášek, P., Tonar, Z., **Grajciarová, M.**, Kural, T., Turek D., Horáková, J., Pálek, R., Eberlová, L., Králíčková, M., Liška, V. Histological mapping of porcine carotid arteries – An animal model for the assessment of artificial conduits suitable for coronary bypass grafting in humans. Ann. Anat. 2020 Mar;228:151434. DOI: 10.1016/j.aanat.2019.151434. **IF(JCR2019)=2.388.** **Q1(Anatomy&Morphology)** https://pubmed.ncbi.nlm.nih.gov/31704146/

Grajciarová, M., Turek, D., Malečková, A., Pálek, R., Liška, V., Tomášek, P., Králičková, M., Tonar, Z. Are ovine and porcine carotid arteries equivalent animal models for experimental cardiac surgery: A quantitative histological comparison. Ann. Anat. 2022 Jun;242:151910. DOI: 10.1016/j.aanat.2022.151910 **IF(JCR2021)=2.698. Q1(Anatomy&Morphology)** https://pubmed.ncbi.nlm.nih.gov/35189268/

Keša, P., Pokorná, E., **Grajciarová, M.**, Tonar, Z., Vočková, P., Trochet, P., Kopeček, M., Jakša, R., Šefc, L., Klener, P. Quantitative In Vivo Monitoring of Hypoxia and Vascularization of Patient-Derived Murine Xenografts of Mantle Cell Lymphoma Using Photoacoustic and Ultrasound Imaging. Ultrasound. Med. Biol. 2021 Apr;47(4):1099-1107. DOI: 10.1016/j.ultrasmedbio.2020.12.010. **IF(JCR2021)=2.998. Q1(Acoustics and Ultrasonics)** https://pubmed.ncbi.nlm.nih.gov/33455807/

Publikační činnost autorky

Jakša, R., Karolová, J., Svatoň, M., Kazantsev, D., **Grajciarová, M.**, Pokorná, E., Tonar, Z., Klánová, M., Winkowská, L., Maláriková, D., Vočková, P., Forsterová, K., Renešová, N., Dolníková, A., Nožičková, K., Dundr, P., Froňková, E., Trněný, M., Klener, P. Complex genetic and histopathological study of 15 patient-derived xenografts of aggressive lymphomas. Lab. Invest. 2022 Apr 29. DOI: 10.1038/s41374-022-00784-w. **IF(JCR2021)=5,662 Q1(Physiology)** https://pubmed.ncbi.nlm.nih.gov/35488033/

Růžička, J., **Grajciarová, M.**, Vištejnová, L., Klein, P., Tichánek, F., Tonar, Z., Dejmek, J., Beneš, J., Bolek, L., Bajgar, R., Kuncová, J. Hyperbaric oxygen enhances collagen III formation in wound of ZDF rat. Physiol. Res. 2021 Nov29;70(5):787-798. DOI: 10.33549/physiolres.934684. **IF(JCR2020)=1.881. Q4(Physiology)** https://pubmed.ncbi.nlm.nih.gov/34505531/

11 Seznam příloh

11.1 Příloha I

Kolinko, Y., Malečková, A., Kochová, P., **Grajciarová, M.**, Blassová, T., Kural, T., Trailin, A., Červenková, L., Havránková, J., Vištejnová, L., Tonarová, P., Moulisová, V., Jiřík, M., Zavaďáková, A., Tichánek, F., Liška, V., Králíčková, M., Witter, K., Tonar, Z. Using virtual microscopy for the development of sampling strategies in quantitative histology and design-based stereology. Anat. Histol. Embryol. 2022 Jan;51(1):3-22. DOI: 10.1111/ahe.12765. **IF$_{(JCR2020)}$=1.114. Q3(Veterinary sciences)** https://pubmed.ncbi.nlm.nih.gov/34806204/

REVIEW

Using virtual microscopy for the development of sampling strategies in quantitative histology and design-based stereology

Yaroslav Kolinko[1,2] | Anna Malečková[3] | Petra Kochová[3] | Martina Grajciarová[1,2] |
Tereza Blassová[1,2] | Tomáš Kural[1] | Andriy Trailin[2] | Lenka Červenková[2,4] |
Jiřina Havránková[1,2] | Lucie Vištejnová[1,2] | Pavla Tonarová[2] | Vladimíra Moulisová[2] |
Miroslav Jiřík[2,3] | Anna Zavaďáková[2] | Filip Tichánek[2,5] | Václav Liška[2,6] |
Milena Králíčková[1,2] | Kirsti Witter[7] | Zbyněk Tonar[1,2] [ORCID]

[1]Department of Histology and Embryology, Faculty of Medicine in Pilsen, Charles University, Pilsen, Czech Republic

[2]Faculty of Medicine in Pilsen, Biomedical Center, Charles University, Pilsen, Czech Republic

[3]Faculty of Applied Sciences, European Centre of Excellence NTIS, University of West Bohemia, Pilsen, Czech Republic

[4]Department of Pathology, Third Faculty of Medicine, Charles University, Prague, Czech Republic

[5]Department of Pathological Physiology, Faculty of Medicine in Pilsen, Charles University, Pilsen, Czech Republic

[6]Department of Surgery and Biomedical Center, Faculty of Medicine in Pilsen, Charles University, Pilsen, Czech Republic

[7]Institute of Morphology, Department of Pathobiology, University of Veterinary Medicine Vienna, Vienna, Austria

Correspondence
Zbyněk Tonar, Department of Histology and Embryology, Faculty of Medicine in Pilsen, Charles University, Karlovarská 48, 301 66 Pilsen, Czech Republic.
Email: Zbynek.Tonar@lfp.cuni.cz

Funding information
Horizon 2020 Framework Programme, Grant/Award Number: 856620; Ministerstvo Zdravotnictví Ceské Republiky, Grant/Award Number: 15–29241A and AZV NU20J-08-00009; Ministerstvo Školství, Mládeže a Tělovýchovy, Grant/Award Number: LO1503; Univerzita Karlova v Praze, Grant/Award Number: GACR No. 1313420, Progres Q39, SVV 260 536 and UNCE/MED/006; European Regional Development Fund, Grant/Award Number: AMTMI CZ.02.1.01/0.0/0.0/17_048/0007280 and FIND CZ.02.1.01/0.0/0.0/16_019/0000787

Abstract

Only a fraction of specimens under study are usually selected for quantification in histology. Multilevel sampling or tissue probes, slides and fields of view (FOVs) in the regions of interest (ROIs) are required. In general, all parts of the organs under study should be given the same probability to be taken into account; that is, the sampling should be unbiased on all levels. The objective of our study was to provide an overview of the use of virtual microscopy in the context of developing sampling strategies of FOVs for stereological quantification. We elaborated this idea on 18 examples from multiple fields of histology, including quantification of extracellular matrix and muscle tissue, quantification of organ and tumour microvessels and tumour-infiltrating lymphocytes, assessing osseointegration of bone implants, healing of intestine anastomoses and osteochondral defects, counting brain neurons, counting nuclei in vitro cell cultures and others. We provided practical implications for the most common situations, such as exhaustive sampling of ROIs, sampling ROIs of different sizes, sampling the same ROIs for multiple histological methods, sampling more ROIs with variable intensities or using various objectives, multistage sampling and virtual sampling. Recommendations were provided for pilot studies on systematic uniform random sampling of FOVs as a part of optimizing the efficiency of histological quantification to prevent over- or undersampling. We critically discussed the pros and cons of using virtual sections for sampling FOVs from whole scanned sections. Our review

demonstrated that whole slide scans of histological sections facilitate the design of sampling strategies for quantitative histology.

KEYWORDS
histological slides, quantitative microscopy, sampling, stereology, study design, veterinary histology

1 | INTRODUCTION

Virtual microscopy or digital microscopy is the digital conversion of light microscopic specimens at full resolution and their presentation over a computer network. The term 'virtual' refers to the examination of the specimens without direct contact with the object slide or the light microscope (Smart In Media AG, 2021). Virtual microscopy makes samples accessible to specialists without needing to be present and without needing to have extensive equipment (Saliba et al., 2012). It is discussed intensively in the frame of diagnosis and treatment of different diseases (telepathology, more than 1400 Scopus entries in September 2021) in human as well as in veterinary medicine (e.g. Bertram & Klopfleisch, 2017), resulting in the first guidelines by the respective expert groups (Jahn et al., 2020).

Another huge field of application for virtual microscopy is education and training, fuelled even more by the increased demand for remote learning during the COVID-19 pandemic (for reviews, see, e.g., Bertram & Klopfleisch, 2017; Kuo & Leo, 2019).

In addition, virtual microscopy is also a powerful tool for research. Our review demonstrates how whole slide scans of histological sections facilitate the design of sampling strategies for quantitative histology and how they can be compared to other technical options.

1.1 | Design-based stereology

Design-based stereology is a set of tools that allows quantification without making assumptions regarding the shape, size, distribution or orientation of the structures of interest (Howard & Reed, 2005; Mouton, 2002). Strict sampling rules have to be followed to achieve this independence; that is, stereology includes detailed prescriptions of the sampling procedure and guidelines on how to test its quality. Stereology has become the gold standard in morphometry due to its reproducibility and assumption-free design. A number of both general and organ-specific protocols, recommendations and algorithms have been published to facilitate planning and conducting quantitative histology studies (Table 1).

1.2 | Sampling in an integral part of design-based stereology

All the guidelines mentioned in Table 1 refer to sampling strategies on all levels of any reduction of material in histological studies.

Only a fraction of specimens under study are usually selected for quantification in histology. This multilevel sampling includes (i) taking tissue probes from large macroscopic organs that cannot be processed completely (i.e. porcine liver, human brain); (ii) selecting histological slides from tissue blocks that undergo exhaustive sectioning (not all slides are selected for further analysis); and (iii) selecting microscopic fields of view (FOVs) that are captured and analysed to represent various regions of interest (ROIs). In general, all parts of the organs under study should have the same probability of being taken into account; that is, the sampling should be unbiased on all levels (Howard & Reed, 2005; Tschanz et al., 2014). One of the advantages of stereological concepts in morphometry is that sampling is inherent to stereology. The attention given to the sampling is comparable to that paid to the analysis of micrographs, as sampling actually is part of any unbiased estimation. If design-based stereology, including sampling, is not used for quantitation in histology, the lack of standardized sampling threatens the repeatability of research. More than 70% of researchers encounter problems when trying to repeat another scientist's experiments (Baker 2016). More than 90 researchers from five continents have recently formulated a strategy to improve the reproducibility of research based on light microscopy (Nelson et al., 2021). We propose that proper sampling of microscopic specimens might be a significant contribution to this issue. Citing the paper by Hsia et al. (2010), "the only effective way to avoid bias and ensure accuracy is via standardization of sampling".

1.3 | Sampling strategies and their benefits with regard to magnification

Sampling is of cardinal importance and a practical necessity in morphometrics (Mayhew & Lucocq, 2015). Depending on the uniformity of the distribution of the item of interest, the sampling intensity would have to be greater (in the case of heterogeneous samples) or smaller (in the case of homogeneous samples). Unfortunately, the biological variability of the microscopic structures on the scale of large organs is mostly unknown in human organs as well as in large animal models. There is ongoing work to map the variability in histopathology to enable researchers to plan the sampling of tissue probes, slides and fields of view efficiently. The theoretical foundations for predicting the efficiency of systematic sampling are quite well known (Gundersen & Jensen, 1987; Gundersen et al., 1999; Gundersen & Osterby, 1981). In

TABLE 1 Examples of studies with recommendations and guidelines for quantitative studies in histology

Research field	Brief characteristics	Reference
General guidelines for microanatomy	Planning, volumetry and sampling as crucial steps for a successful study in quantitative anatomy	Tschanz et al., 2014 Vatsos et al., 2021
Cardiovascular microanatomy	Quantitative 3D morphology in cardiac research Quantification of vascular beds Vascularization of organs 3D characterization of capillary networks Numbers and lengths of brain capillaries	Mühlfeld et al., 2010 Dockery & Fraher, 2007 Mühlfeld, 2014 Eržen et al., 2011 Lokkegaard et al., 2001; Kubíková et al., 2018
Neuroanatomy and neurohistology	Total number of neurons in the subdivisions of the hippocampus Assessment of developmental neurotoxicity Morphometry of brain Morphometry of grey and white matter of spinal cord Morphometry of the pineal gland	West et al., 1991 Bolon et al., 2011 Selcuk & Tipirdamaz, 2020; Sadeghinezhad et al., 2020 Sadeghinezhad & Nyengaard, 2021; Cakmak & Karadag, 2019 Bolat et al., 2018
Gastrointestinal microanatomy	Practical stereology of the stomach and intestine. Morphometry of the oesophagus Volumes and numbers in the liver 3D counting of hepatocytes Quantification of hepatic connective tissue Morphometry of intestinal mucosa in nutritional studies	Nyengaard & Alwasel, 2014 Goodarzi et al., 2019 Marcos et al., 2012; Junatas et al., 2017; Mik et al., 2018 Van Ginneken et al., 2002; Casteleyn et al., 2010
Respiratory system	Policy Statement of the American Thoracic Society/European Respiratory Society on quantitative assessment of lung structure Quantitative microscopy of the lung Study designs in diseases of the respiratory tract	Hsia et al., 2010 Ochs & Mühlfeld, 2013; Knudsen et al., 2021 Mühlfeld & Ochs, 2013
Urinary system	Application of stereology in kidney research	Nyengaard, 1999
Genital system	Stereology tools in testicular research	Noorafshan, 2014 Ferreira et al., 2021
Skeletal system	Stereology of femoral cartilage Standardized nomenclature for bone histomorphometry Quantification of bone microporosities	Noorafshan et al., 2016 Dempster et al., 2013, Parfitt et al., 1987 Tonar et al., 2011
Embryology	Stereology of the human placenta	Mayhew, 2014

Note: Papers compatible with design-based stereology are listed.

the past and in contrast, for example, to biochemistry, standards for sampling in histology seemed to have been neglected; not all authors customarily referred to sampling strategies, numbers of tissue probes, sections, FOVs or any repeatable rules for their selections. Currently, the sampling issue receives more attention as a part of quantitative morphomics that describes the 3D biological structures from gross anatomy to the micro- or even nanomorphome (Mayhew & Lucocq, 2015).

In microscopy, FOV sampling is closely related to the magnification used. When increasing the magnification, the area of the image field decreases quadratically, and the number of FOVs necessary to cover the same original area increases quadratically (Figure S1). Traditionally, it was recommended that the lowest magnification that enables the detection of the structures of interest be used (Howard & Reed, 2005; Mouton, 2002) to maximize the area of the FOVs. Introducing virtual slides into the research might seem to be a 'game changer'. However, whole slide sampling with automated quantitation still requires validation by humans to ensure that the readouts are correct. Combining the benefits of using slide scanners with a clever sampling strategy might be a very efficient tool in quantitative histology.

The aim of our paper was to provide an overview of the use of virtual microscopy in the context of developing sampling strategies for stereological quantification. We elaborated this idea on a number of examples from multiple fields of histology. We critically discussed the pros and cons of using virtual sections for sampling image fields (FOVs and ROIs) from whole scanned sections in quantitative histological studies.

2 | MATERIALS AND METHODS

2.1 | Origin of tissue blocks and histological staining

This paper uses examples of virtual slides from a number of studies representing various fields of quantitative histology. All the original illustrations were newly prepared from archive specimens for the purpose of this review. The origin of the specimen and their use for studying biological questions is summarized in Table 2. The staining methods used in the examples presented in this paper are summarized in Table 3.

TABLE 2 Origin of tissue samples and basic processing of the examples presented in this paper

Example	Origin	Biological question studied (Reference)
#1	Virtually generated standardized image datasets	Testing and calibrating quantification of volumes, surfaces, lengths and object counts (Jiřík et al., 2016, 2018).
#2	Human mesenchymal stem cells (hMSCs) isolated from bone marrow of healthy donors (A)	Metabolic activity assay comparing the ATP production rate and % of glycolysis and oxidative phosphorylation in hMSCs (Tonarova et al., 2021).
#S2	hMSCs isolated from bone marrow of healthy donors (B)	Cell growth assay and metabolic activity assay when studying the effects of different cross-linking conditions on collagen-based nanocomposite scaffolds; an in vitro evaluation using mesenchymal stem cells (Suchý et al., 2015).
#S3	Soft palate of an adult dog fixed in formalin, archive of (C)	Quantitation of connective tissue in the soft palate of the dog; pilot study to assess sampling intensity (unpublished results). This was motivated by assessment of operative outcome of veloplasty (e.g. Arai et al., 2016; Crosse et al., 2015; Dupré & Heidenreich, 2016; Pichetto et al., 2015; Tamburro et al., 2019).
#3	Porcine femurs with titan implants after 6 months of healing, (B)	Assessing osseointegration of titan implants with four different surface composition using quantification of bone-implant contact (BIC) according to Babuska et al. (2016).
#S4	Condylar cartilage and bone of rabbit femur (B)	Estimation of healing of osteochondral defects of condylar cartilage stimulated by three different tissue-engineered scaffolds (unpublished results).
#S5	Brains of female C57B1/6 mice (C)	Tracking the transduction of various viral vectors in neurons after being injected into mice brains (Hlavatý et al., 2017).
#4	Porcine liver (B)	Describe the propagation of the rupture caused by blunt trauma within liver parenchyma with respect to the liver microstructure, namely, the reticular fibres. Does the rupture propagate randomly or does the rupture follow some pattern through the tissue? (Malečková et al., 2021).
#S6	Porcine common carotid arteries (B)	Quantification of type I and type III collagen within tunica intima and media in porcine common carotid artery (Tomášek et al., 2020).
#S7	Archived canine lymph nodes and core biopsies from canine lymph nodes (C)	Quantification of microvessels in canine lymph nodes. Does the density of microvessels correlate with vascular endothelial growth factor expression? (Tonar et al., 2008; Wolfesberger et al., 2008).
	Patient-derived murine xenografts of mantle cell lymphoma (A)	Histological validation of quantitative in vivo monitoring of hypoxia and vascularization of patient-derived murine xenografts of mantle cell lymphoma using photoacoustic and ultrasound imaging (Keša et al., 2021).
#5	Small intestine of 12 to 14-week-old pigs used in research on healing of intestinal anastomoses (B)	Histological validation of healing of intestinal anastomosis, quantification of vascularization, inflammatory infiltration, and collagen formation (Rosendorf et al., 2020, 2021a, 2021b).
#S8	Human and ewe perineal body used for mechanical testing and microstructure quantification (D)	Quantification of volume fraction of smooth muscle, skeletal muscle, adipose cells, elastin, and type I collagen of the perineal body. Does the structure differ along the perineal body? (Kochová et al., 2019a, 2019b). Does the structure differ between the pregnant and post-menopausal ewe perineal bodies? (Kochová et al., 2019b)
#6	Resected human liver with hepatocellular carcinoma (E)	Quantification of CD8+ T cells in different regions of interest (tumour centre, inner and outer invasive margin, peritumoural area and non-tumour liver) can reflect the overall reaction of the immune system to tumour growth, penetration of immune cells through tumour border and expression of pro- and antiapoptotic factors by tumour cells and microenvironment (Andryi Trailin, unpublished results).
#S9	Mouse ovaries (B)	Discover the effects of exposure to bisphenol A analogs during breastfeeding on ovarian capacity of offspring. The quantification of primordial, primary, preantral, antral and atretic follicles (Nevoral et al., 2021).
#S10	The cerebellum of 3-month-old mouse model with degeneration of Purkinje cells (B)	Quantitative validation of potential abnormalities in total number of microvessels in the cerebellum layers of adult mice with degeneration of Purkinje cells (Kolinko et al., 2016).
#S11	Samples of human aortae collected during surgery for abdominal aortic aneurysm (AAA) repair (F)	Comparison of the expression of structural proteins, osteoprotegerin, and pentraxin 3 and the presence of immune factors (T and B lymphocytes, neutrophils and macrophages), microvessels and hypoxic cells in AAA and non-aneurysmatic aortic walls and exploration of their relationships (Blassova et al., 2019).

(Continues)

TABLE 2 (Continued)

Example	Origin	Biological question studied (Reference)
#7	Decellularized porcine liver tissue (B)	Quantitative analysis of morphological preservation of liver extracellular matrix (ECM) after decellularization with the purpose of generation a high-quality biological scaffold for liver tissue engineering (Moulisová et al., 2020)
#S12	3D collagen scaffolds containing dermal fibroblasts used as an in vitro model of dermis (B)	Development of a new method of total cell count determination in 3D collagen scaffolds in order to quantify cell proliferation (unpublished results).

Note: Most examples are based on studies already published, so references are provided for further details on the study design. All in vivo procedures were performed in compliance with the law of the Czech Republic, which is compatible with the legislation of the European Union and, wherever appropriate, were approved by the Ethics Committees in the following institutions where the samples originated: A – First Faculty of Medicine, Charles University; B – Faculty of Medicine in Pilsen, Charles University; C – Institute of Morphology, University of Veterinary Medicine Vienna, Austria; D – Centre for Surgical Technologies, KU Leuven, Leuven, Belgium; E – Department of Pathology, Faculty of Medicine in Pilsen, Czech Republic; and F – Department of Surgery, University Hospital in Pilsen. The examples are numbered according to their appearance in the Results section.

TABLE 3 Histological staining methods used in examples presented in the study

Example	Staining	Purpose and visualization of tissue components
#1	None (computer-generated virtual image).	Virtual sections through three-dimensional objects (spheres and cylinders) mimicking tissue components in X-ray microtomography.
#2	DAPI nuclear staining (Sigma-Aldrich).	Visualization of nuclei.
#S2	DAPI nuclear staining (Sigma-Aldrich, Burlington, MA) and Phalloidin-Alexa Fluor 488 (Life Technologies, Rockford, IL).	Visualization of nuclei and actin microfilaments.
#S3	Aniline blue and nuclear fast red.	Clear distinction of collagen fibres from other tissue components for automated quantitation.
#3	20% Giemsa's azur eosin methylene blue solution	New bone and connective tissue around titan implants within porcine femur.
#S4	Alcian blue staining and PAS reaction.	Detection of acidic and neutral glycosaminoglycans in newly formed cartilage.
#S5	Immunohistochemistry for enhanced green fluorescent protein (EGFP) (Chemicon International, Temecula, CA), counterstained with haematoxylin.	Identification of cells expressing the EGFP as a reporter gene detecting the cells transduced by a viral vector.
#4	Reticulin kit (BioGnost Ltd, Zagreb, Croatia).	Reticular fibres (collagen III) – component of extracellular matrix of connective tissue located in the interlobular septa and in the delicate network, that separates the hepatic sinusoids and hepatocytes
#S6	Picrosirius red (Direct Red 80, Sigma-Aldrich, Munich, Germany).	Type I collagen (yellow–red colour) and type III collagen (green colour) visualized in polarized light (Rich & Whittaker, 2005).
#S7	Immunohistochemical detection of von Willebrand factor (polyclonal rabbit anti-human antibody, Dako, Glostrup, Denmark) combined with lectin histochemistry (WGA, Vector laboratories, Burlingame, CA). Avidin-biotin-peroxidase complex detection (Vector Laboratories). Counterstaining Mayer's haematoxylin.	Endothelium of blood microvessels within canine lymph nodes.
	Immunohistochemical detection of CD31 (rabbit anti-mouse CD31 monoclonal IgG, clone SP38, Thermo Fisher Scientific, Rockford, IL). Counterstained with haematoxylin.	Endothelium of blood microvessels within patient-derived murine xenografts of mantle cell lymphoma.
#5	Immunohistochemical detection of von Willebrand factor (ab6994Abcam, Cambridge, UK).	Endothelium of blood microvessels

(Continues)

TABLE 3 (Continued)

Example	Staining	Purpose and visualization of tissue components
	Immunohistochemical detection of Calprotectin (Monoclonal Antibody—MAC387Invitrogen MA1-81381, Thermo Fisher Scientific). Counterstaining Mayer's haematoxylin.	Granulocytes and tissue macrophages.
	Picrosirius Red.	Collagen observed in circularly polarized light.
#S8	Verhoeff's haematoxylin and green trichrome (Kocová, 1970).	Overall morphology; smooth and skeletal muscle of the perineal body.
	Orcein (Tanzer's orcein, Bowley Biochemical Inc., Danvers, MA, USA).	Adipose cells and elastin of the perineal body.
.	Picrosirius red (Direct Red 80, Sigma-Aldrich, Munich, Germany)	Type I collagen of perineal body was observed in polarized light.
#6	Immunohistochemical detection of CD8+ T cells (BOND™ Ready-to-Use monoclonal primary anti-CD8 Antibody 4B11, Leica Biosystems Newcastle Ltd, UK). Counterstaining Mayer's haematoxylin.	Tumour-infiltrating cytotoxic T cells as actors of antitumour immunity.
#S9	Haematoxylin and eosin	Primordial, primary, preantral, antral and atretic follicles within mice ovaries.
#S10	Immunohistochemical detection of laminin (polyclonal rabbit anti-laminin antibody, Dako, Glostrup, Denmark), counterstained with haematoxylin.	Detection of microvessels in individual layers of the cerebellar cortex in a mouse model of neurodegeneration.
#S11	Immunohistochemical detection of pentraxin 3 (polyclonal rabbit anti-human pentraxin3 antibody, Thermo Fischer Scientific) and MAC387 (monoclonal mouse anti-human macrophages/monocytes antibody, Thermo Fisher Scientific). Counterstaining Gill's haematoxylin.	Detection of Pentraxin 3, a protein produced in response to inflammatory signals in aortic wall. Detection of macrophages infiltrating the aortic wall in abdominal aortic aneurysms.
#7	Haematoxylin & eosin	Visualization of ECM proteins (stained reddish with eosin) and absence of cell nuclei in decellularized samples (lack of blue haematoxylin stain).
#S12	DAPI nuclear staining (Thermo Fisher Scientific, Rockford, IL)	Staining cell nuclei as countable structures for cell counting.

2.2 | Scanning virtual slides

As the paper focuses mainly on the sampling strategies in the context of various histological studies, the devices and techniques used for acquiring the images in the paper are briefly summarized in Table 4.

2.3 | Systematic uniform random sampling of microscopic FOVs

Multistage sampling in quantitative microscopy comprises several levels (Mayhew & Lucocq, 2015). During each step, a sample size divided by the whole specimen size represents the sampling fraction. In this paper, two levels will be considered: If, for example, every 10th histological section is selected from an exhaustively sectioned tissue block, and the position of the 1st section was selected randomly, the section sampling fraction (ssf) is 1/10. When considering a single slide, selecting 5 FOVs out of the 50 FOVs covering the whole section would represent an area sampling fraction (asf) of 1/10. The rules for the systematic uniform random sampling (SURS) are simple, regardless of the technical implementation (slide scanners, motorized microscope stages, manual sampling). The position

of the first FOV within the ROI is chosen randomly, for example, by multiplying the maximum ranges of XY coordinates of the ROI by randomly generated numbers (RND function in MS Excel). A previously selected pattern, named a sampling interval, determines the positions of the other FOVs (see, e.g., Mayhew & Lucocq, 2015 for review).

2.4 | Stereological techniques

The sampling strategies illustrated among the examples that follow were part of histological quantitative studies. All the quantitative morphometric parameters used in the examples presented in this study are explained in Table 5.

2.5 | Statistics of sampling density and evaluating the variability of the sampling

The sampling in histology introduces an error into the resulting data. Increasing the sampling frequency reduces the variability of the data but also increases the labour needed to complete the research.

TABLE 4 Devices and techniques used for acquisition of examples demonstrated in this study

Device and manufacturer	Properties, settings, software	Used in Example #:
Aperio ScanScope CS2 automatic slide scanner (Leica Biosystems, Vienna, Austria).	Bright field transmitted light microscope, 20× and 40× lens. Scanning time of 1 cm^2 approx. 60 s (20× objective) or 90 s (40× objective) Automatic white balance Autofocus No immersion, no Z-stack tools SCANSCOPE 12.4.3 software. *SVS document format readable with freely downloadable IMAGESCOPE software, tiled images universally viewable in browsers. *.SVS can also be opened directly with IMAGEJ (Schneider et al., 2012) with the Bio-Formats Plugin or with FIJI (Schindelin et al., 2012).	#S3, #S5
Eclipse Ti-U microscope (Nikon, Tokyo, Japan), XYZ stepper motor focus drives Prior H117E1N4/F and PS3H122R_NB (Prior Scientific Instruments, Fulbourn, UK), Prior ProScan III stepper motor controller, digital camera Nikon DS-Fi2.	Bright field, polarized light and fluorescence microscopy 2×, 4×, 10×, 20×, 40×, 60× (oil immersion) objectives Scanning time of 1 cm^2 approx. 25 min (10× objective) or 3.5 h (20× objective) Scanning and montage controlled by the NIS Elements AR software (v 5.11.03) *ND2 document format readable with freely downloadable NIS-Elements Viewer software Scanning in XY plane and in Z-axis. Export to universal format TIFF images.	#2, #S2, #S4,#5, #S6, #S9, #S10
Zeiss Axio Scan.Z1 Slide Scanner (Zeiss, Jena, Germany).	Bright field microscopy 20× and 40× objectives Scanning time of 1 cm^2 approx. 5–10 min (20× objective) Scanning controlled by ZEISS ZEN BLUE software ZEISS ZEN MICROSCOPY free software offers both basic image analysis, as well as export functionality of the scanned images into TIFF or JPG file formats. Native pyramidal*.CZI files readable with FIJI.	#4, #S8, #S11, #7
Olympus CX41 microscope (Olympus, Tokyo, Japan) with Promicam 3-3CP camera (Promicra, Prague, Czech Republic).	Bright field and polarized light microscopy 2×, 4×, 10×, 20×, 40×, 60× (oil immersion) objectives Manual stage Scanning time of 1 cm^2 takes approx. 30 min (10× objective) of manual work Stitching virtual slides manually using the ImageStithing module of the QUICKPHOTO INDUSTRIAL 3.2 software (Promicra, Prague, Czech Republic) Export to TIFF.	#3, #S6, #S7

Stereologists are used to calculate the variability on each level of the sampling to identify the major source of potential bias and to optimize the sampling procedures in terms of time and material costs, provided that enough precision remains to draw conclusions on a pre-determined level of confidence. Several measures of variability are illustrated for this purpose, such as standard deviations (SD), coefficient of error (CE; standard error of the mean of repeated estimates divided by the mean) and the estimates of CE for spatially correlated objects using the Matheron quadratic approximation method with various smoothness constants (Gundersen & Jensen, 1987; Slomianka & West, 2005). The relative percentage error used for comparing the data based on whole slide analysis vs. various levels of subsampling was calculated as 100 × (measured value-expected value)/expected value.

3 | EXAMPLES

A number of combinations of imaging approaches, uses of virtual slides, scanners, or individually sampled micrographs with various magnifications are presented in sequence corresponding to Tables 2, 3 and 5. The examples were tailored to facilitate the solving of

biological problems described in Table 2, and the strong and weak points are illustrated. Due to the number of possible combinations, the examples are ordered approximately in increasing complexity.

3.1 | Whole slide analysis vs. density of sampling multiple micrographs

Figure 1 (Example #1) demonstrates the effect of the intensity of sampling on the accuracy of the quantitative results. This can be done in virtually generated scenes. Considering the whole slide as the 'true expected value', the relative error increases with decreasing sampling intensity. In this case, intermediate sampling would provide results with an acceptable relative error. Similarly, Figure 2 (Example #2) compares automated counting of cell nuclei in a single well of a cell culture miniplate with counting based on 15 image fields. In cases of a more homogeneous distribution (Figure S2, Example #S2), the relative error of the sample is acceptably low. It is worth performing a pilot study of heterogeneous histological samples with multiple tissue components (Figure S3, Example #S3) that shows how the moving average depends on the sampling intensity.

TABLE 5 Quantitative morphometric parameters used in the examples presented in this study

Example	Quantitative parameter abbreviation (units)	Definition, reference area, interpretation	Objective used	Image fields sampled per slide	Typical area sampling fraction
#1	V_V (objects, section) (–)	The volume fraction of objects within a virtually generated section.	Not applicable	6	6/54 (0.11)
#2	Q_A (nuclei, well) (mm^{-2})	Two-dimensional density of cell nuclei per area of the well bottom in an 8-well XPf cell culture miniplate (Agilent, Santa Clara, CA).	4×	Whole image processed	Whole image processed
			40×	15	15/160 (0.093)
#S2	Q_A (nuclei, well) (mm^{-2})	Two-dimensional density of cell nuclei per area of the well bottom in a 48-well cell culture plate (Thermo Scientific, Waltham, MA).	10×	Whole image processed	Whole image was processed
			40×	9	9/22 (0.41)
#S3	A_A (connective tissue, palate) (–)	Mean area fraction of connective tissue in whole histological sections of the soft palate of a dog (pilot study).	20× (whole slide scan)	Analysis of whole slide scan	One whole slide scan analysis 0.003 to 0.005 in relation to one complete palatal half
#3	BIC	Bone-implant contact as the ratio of the profile length of direct contact between the implant profile and bone tissue and the total profile length of the implant surface.	10×	15	15/70 (0.214) related to the whole scan 15/15 (1.00) related to the bone-implant interface
#S4	V_V (cartilage, defect) (–)	The volume fraction of Alcian blue and PAS-positive cartilage within the healing bone defect.	10×	22	21/22 (0.95)
#S5	N (EGFP-positive neurons, brain) (–)	Absolute number of EGFP-positive neurons in the injected half of mouse brain.	40× (oil immers)	45–55	1/1 (exhaustive sampling)
#4	P'_L (interlobular septa, and P_L (interlobular septa) (mm^{-1})	Real number of intersections of interlobular septa with rupture and predicted number of intersections based on the total length of the interlobular septa	Whole slide scan	Not applicable	Whole slide scan
	P'_L (reticular fibres) and P_L (reticular fibres) (mm^{-1})	Real number of intersections of reticular fibres with rupture and predicted number of intersections based on the total length of the reticular fibres	40×	10	Between 10/40 (0.25) and 10/50 (0.2)
#S6	A_A (type I collagen, int + med) (–)	The area fraction of type I collagen within the tunica intima and media ROI	40×	4	Between 4/23 (0.17) and 4/37 (0.11)
	A_A (type III collagen, int + med) (–)	The area fraction of type III collagen within the tunica intima and media ROI	40×	4	Between 4/23 (0.17) and 4/37 (0.11)
#S7	Q_A (vWF and WGA-positive microvessels, lymph node) (mm^{-2})	The number of profiles of stained microvessels per sectional area of the lymph node.	40×	50–70	Between 50/1800 (0.028) and 70/2500 (0.03)
	L_V (CD31+ microvessels, lymphoma) (mm^{-2})	The length density of stained microvessels per volume unit of lymphoma	40×	10	Between 10/40 (0.25) and 10/80 (0.125)
#5	V_V (objects, intestinal wall without mucosa located 3 mm proximally and distally from the anastomosis centre) (–)	The volume fraction of vWF positive cells within the ROI	20×	5–38 vWF	Between 1/5 (0.20) and 1/3 (0.35)
		The volume fraction of MAC387-positive cells within the ROI	20×	12–53 MAC387	Approx. 1/2 (0.49)
		The volume fraction of collagen within the ROI	20×	8–24 PSR	Between 1/3 (0.33) and 1/5 (0.22)

TABLE 5 (Continued)

Example	Quantitative parameter abbreviation (units)	Definition, reference area, interpretation	Objective used	Image fields sampled per slide	Typical area sampling fraction
#S8	V_V (smooth muscle; skeletal muscle, perineal body)	The volume fraction of smooth muscle and skeletal muscle within the ROI	10×	12	12/42 (0.3)
	V_V (adipose cells; elastin, perineal body)	The volume fraction of adipose cells and elastin within the ROI	10×	12	12/42 (0.3)
	V_V (type I collagen, perineal body)	The volume fraction of type I collagen within the ROI	10×	12	12/42 (0.3)
#6	Q_A (CD8-positive T cells, liver) (mm^{-2})	The number of profiles of stained CD8+ T cells per sectional area of the ROI of the liver.	20×	8 per ROI / 40 per slide	8/133 0.064 in TC and NT ROIs: / 8/25 (0.32) in IL, OL and PT ROIs
#S9	N (different types of follicles)	The number of primordial, primary, preantral, antral and atretic follicles	20×	14	14/25 (0.56)
#S10	V_V (cerebellar layers, cerebellum) (–)	The volume fractions of histological layers of cerebellum.	20×	4–7	0.33
	N (microvessels, cerebellum) (–)	Number of microvessels calculated from the number of branching nodes according to Gundersen et al. (1993).	60×	20–40	0.33
#S11	A_A (pentraxin 3, wall) (–)	The area fraction of the pentraxin 3-positive cells within the whole wall reference area	40×	4	Between 4/112 (0.035) and 4/328 (0.012)
	A_A (MAC387, wall) (–)	The area fraction of the MAC387-positive macrophages within the whole wall reference area.	20×	4	Between 4/28 (0.143) and 4/82 (0.049)
#7	L (skeleton length, liver) (mm) / L_A (ECM fibres, liver) (mm^{-2}) / Q_A (ECM branches, liver) (mm^{-2})	Length and 2D length density of the ECM within liver lobules. Number of EMC branching nodes per sectional area of liver lobules. Both parameters refer to the quality of network structure of sinusoidal vessel ECM in the decellularized scaffold.	40×	10	Typically 5/100 (0.05)
#S12	N (nuclei, scaffold) (–)	Total cell number in the whole scaffold estimated from cell number in 1 column.	10×	9 columns from the 3D scaffold	9 × 1.4 µl/200 µl = 0.063 (9 columns per scaffold)

Note: The magnification of the microscope objective, which was an approximate equivalent to the sampled image field area used for quantification of each parameter, is provided. The number of image fields that were sampled in each study is shown as well.

Abbreviations: A_A (*component, space*), Area fraction of the respective components within their reference spaces; BIC, bone-implant contact; L_V (*component, space*), Length density of objects per reference volume; N_V (*component, space*), Numerical density of objects per reference volume; Q_A (*component, space*), number of object profiles per section area; V_V (*component, space*), Volume fraction of the respective components within their reference spaces.
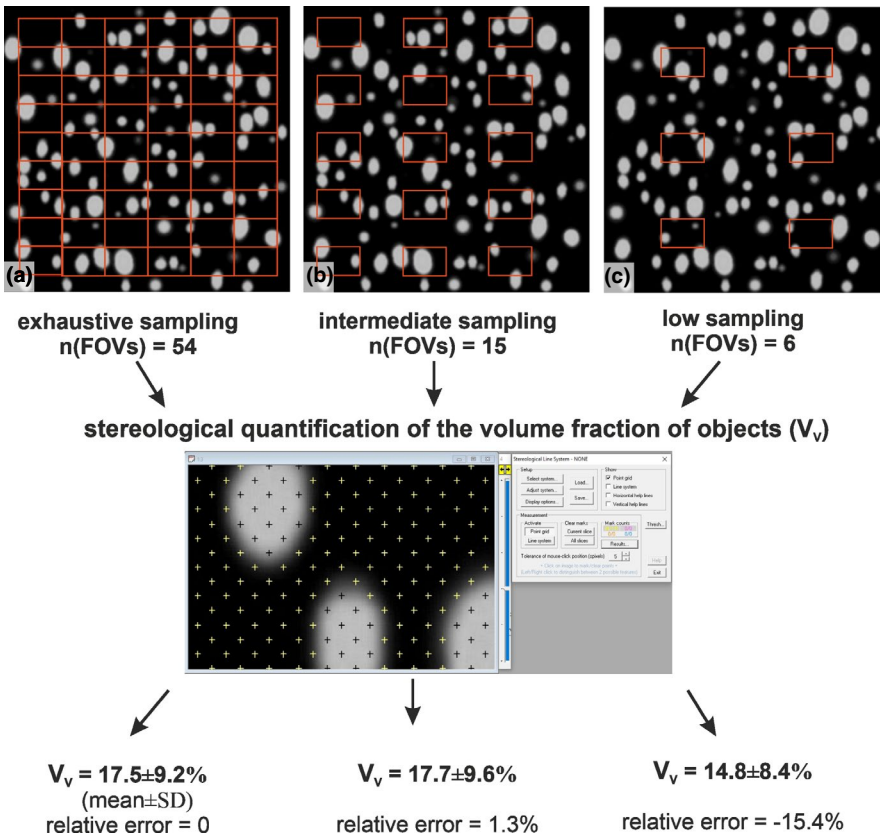
FIGURE 1 Example #1 demonstrates the effect of the intensity of sampling on the quantitative results in virtually generated slides with precisely known volume fractions of objects. A virtual slide was generated using TEIGEN software (Jiřík et al., 2018) with a precisely known volume fraction (V_V) of the white objects on the black background, mimicking the sectional profiles of cell bodies or matrix fibres. The scene was sampled with simulated fields of view (FOVs) exhaustively (a), with intermediate (b) and low (c) intensity. After stereological quantification using the point grid, the V_V was expressed as the mean ± standard deviation (SD), and the relative percentage error of the estimate was calculated for each sampling intensity

3.2 | Slides requiring exhaustive sampling of the ROIs

In some studies, it is advisable to evaluate the complete ROI. This strategy prevails when the number of slides available is limited, such as in ground sections of bone implants (Figure 3, Example #3). Similar situations occur when the ROI has small dimensions, for example central regions of experimental bone defects in small animal models (Figure S4, Example #S4). Exhaustive sampling might also be needed in cases with significant biological variability among the study groups when counting every few cells matters, such as in counting virus-transduced neurons in mouse brains (Figure S5, Example #S5).

3.3 | Using the same sampling count but in ROIs of different absolute sizes

In some study designs without excessive biological variability, it is possible to maintain the same number of FOVs (Figure 4, Example #4). When the size of the specimens and ROI varies, this will result in a variable sampling density (the numerator is the same, the denominator varies), as in samples of proximal vs. distal segments of blood vessels (Figure S6, Example #S6) or large vs. small lymph nodes (Figure S7B, Example #S7). The case presented in Figure S7A (Example #S7) shows a very extensive sampling, the ex post analysis of which identified as an unnecessary and laborious oversampling when compared to Figure S7B.

## 3.4 | Sampling the same ROI for more histological staining methods

Quantifying the volume fractions of tissue components within the same ROI might require more histological staining. Figure 5 (Example #5) shows three stains within the same ROI and objective. It is of great advantage when the sampling is facilitated by a map that helps adjust the sampling density according to the variability of the structures under study, as provided by the estimates of CE in the STEREOLOGER software (v11.0; SRC Biosciences, Tampa, Florida, USA) (Figure 5H-I). When the CE becomes unacceptably high (Figure 5I), it is recommended to increase the ssf, asf or the density of the stereological grid. Figure S8 (Example #S8) shows a similar design.

## 3.5 | Sampling one or more ROIs with a variable intensity or using various objectives

Figure 6 (Example #6) illustrates a complex sampling problem that would be difficult to solve without planning on virtual slides. There were five ROIs in every slide, representing the tumoural area, three zones of the tumour invasive margin and healthy non-tumorous tissue. In all five ROIs, multiple structures of interest were identified immunohistochemically (CD8+ T lymphocytes shown, CD3+ T lymphocytes only discussed), and their occurrence within these ROIs was very variable and with different biological interpretations. To maintain the feasibility of such a complex task, two sampling densities were chosen, and part of the sampling variability was

FIGURE 2 Example #2 compares automated counting of cell nuclei in a composite image of a single well in a 8-well XFp cell culture miniplate (captured and stitched with a 4× objective) vs. automated counting in 15 image fields taken from the same well with a 40× objective after 24 h of cultivation (seeding cell density 70,000/cm²). (a) Raw image stitched from two fields of view of a 4× objective shows most of the well microplate. (b) All the nuclei were segmented, counted and highlighted using a watershed algorithm in CELLPROFILER 4.2.1 software (McQuin et al., 2018). The obvious benefit of this procedure was that the quantification was based on counting nearly 1900 nuclei. (c) As an alternative approach, 15 fields of view (FOVs) were sampled with a 40× objective (green rectangles) in a systematic uniform random manner from the well (outlined with a yellow polygon). The three rounded spaces for inserting sensor probes that were part of the well bottom profile were avoided. (d) Example of one of the 15 images that were processed in the same way as in b. The analysis provided a value of density of nuclei with a 4.4% error relative to the whole image analysis (b). The benefits of the sampling (c-d) were that the 40× objective provided a greater optical resolution. Fluorescence images, cell nuclei in blue stained with DAPI. Scale bars 500 μm (a–c), and 40 μm (d)
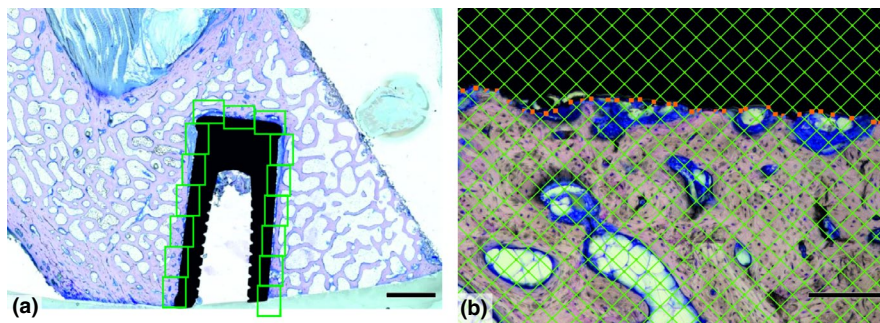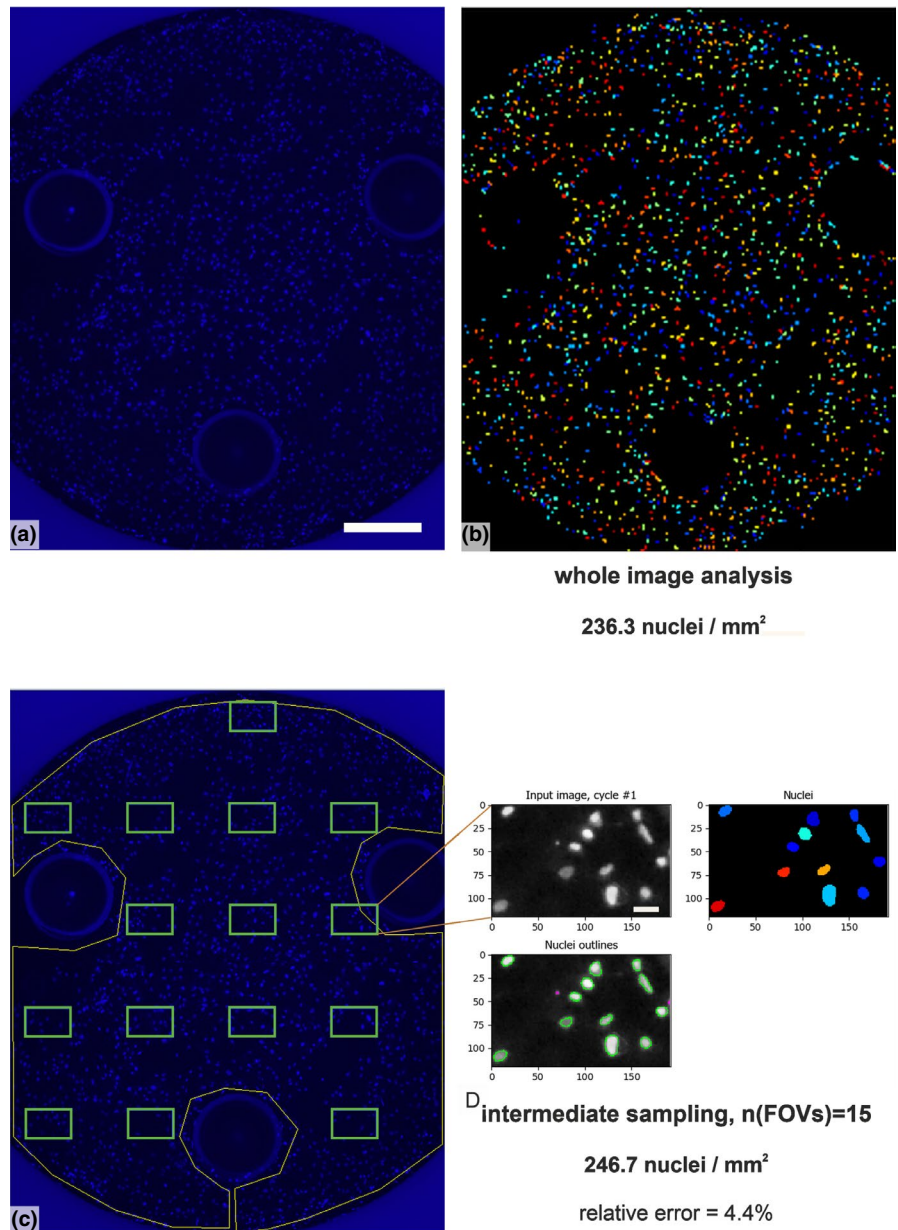
FIGURE 3 Example #3 shows the strategy of exhaustive sampling of an ROI in quantification of bone-implant contact (Babuska et al., 2016). (a) Fifteen ROIs from the bone-implant interface were taken from each slide. All adjacent fields showing the implant surface (black), bone (purple) and connective tissue (blue) were captured exhaustively. (b) Stereological grid randomly positioned over the micrograph; intersections between the test lines and the implant surface (orange points) and intersections between the implant-bone interface and test lines (light blue points). Giemsa's azur eosin methylene blue solution. Scale bar: 2 mm (a), 200 μm (b)
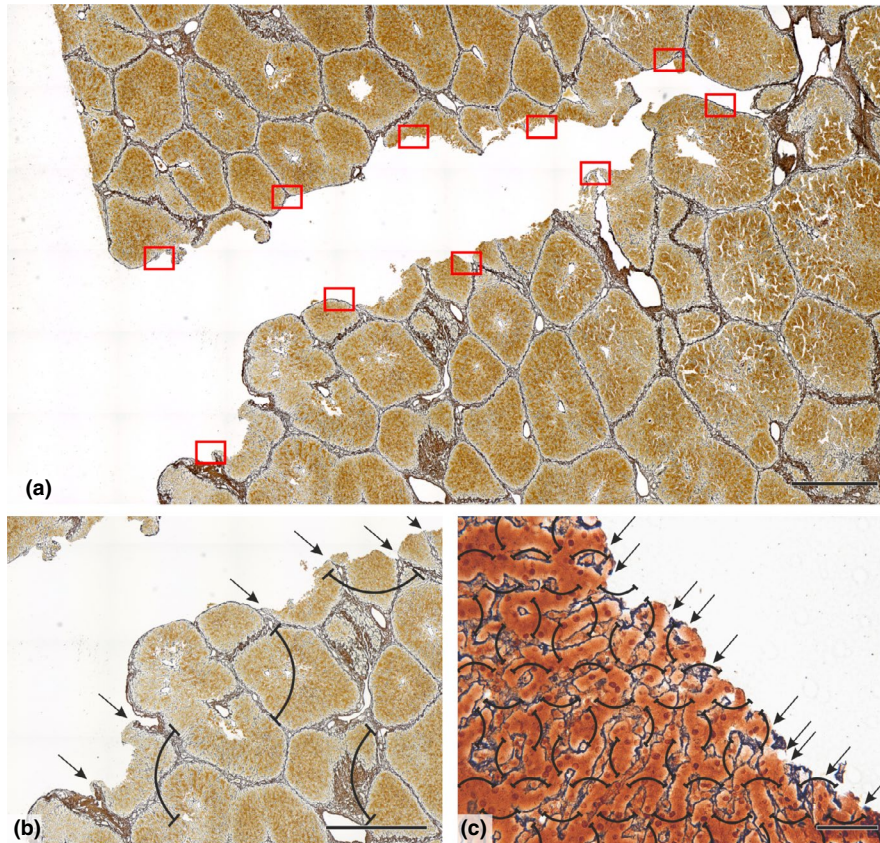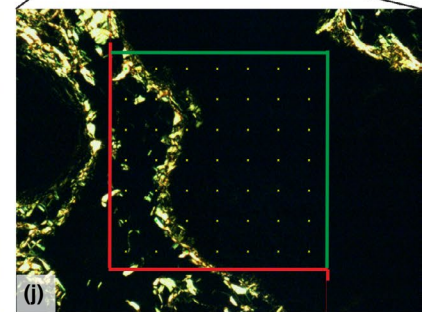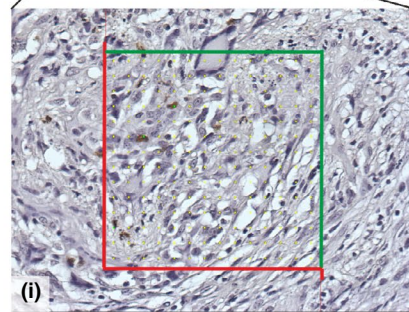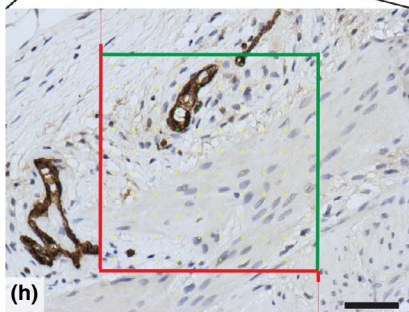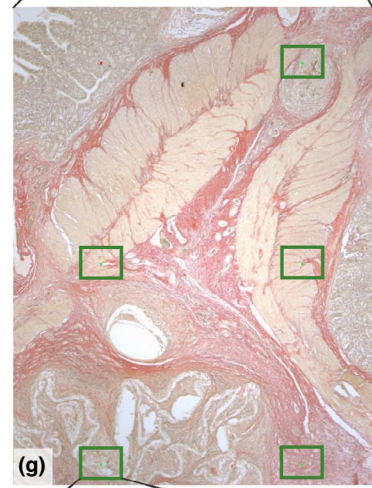
FIGURE 4 Example #4 shows the strategy of tissue sampling for the evaluation of rupture propagation through the porcine liver (Maleckova et al., 2021). (a) An overview of the scanned porcine liver sample showing a rupture in full length. The scanned samples were used to assess the spatial relationship of the rupture and the interlobular septa (analysis was performed along the entire length of the rupture [b]) and the spatial relationship of the rupture and the reticular fibres (analysis was performed in 10 fields of view taken in a systematic manner [red rectangles, C]). (b) Close-up of a part of the 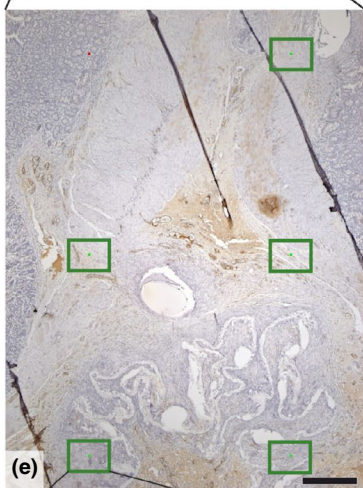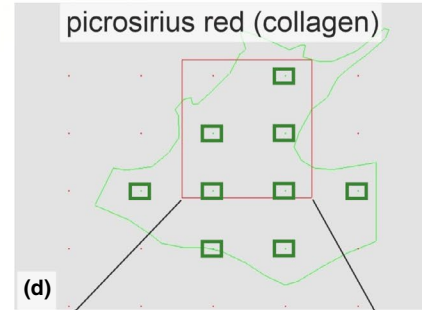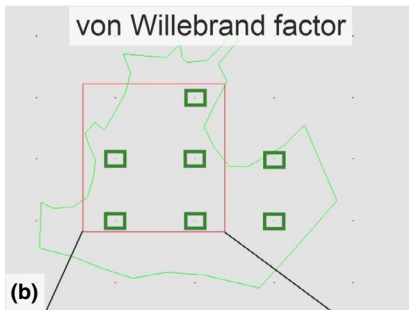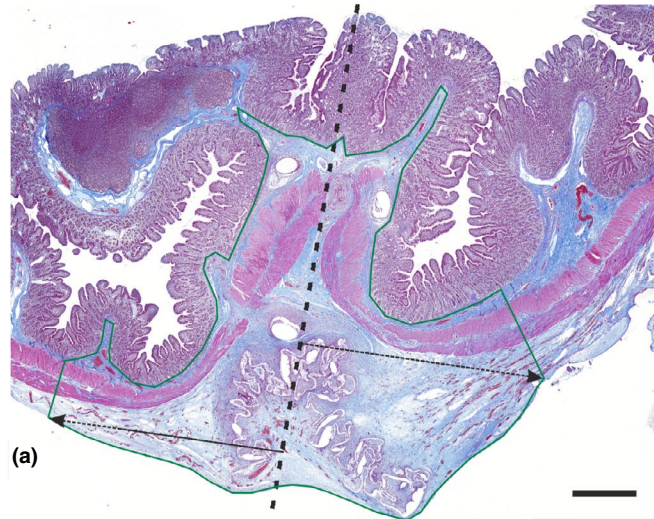rupture-spatial relationship of the rupture and the interlobular septa that were assessed in 7 scanned histological slides (c) An actual field of view taken with a 40× objective shows spatial relationship of the rupture and the reticular fibres. This was determined by comparing the number of the intersections of the interlobular septa/reticular fibres with the rupture (arrows) and the theoretical intersection intensity based on the length density of the interlobular septa/reticular fibres. The length density was estimated using circular arc probes (black curves) as available in the ELLIPSE stereological software (ViDiTo). Reticulin kit staining was used for reticular fibre visualization. Scale bar: 1000 μm (a, b), 50 μm (c)

compensated with more or less dense counting grids (Figure 6B-D). Similarly, Figure S9 (Example #S9) demonstrates that the present settings were suitable for frequently occurring types of ovarian follicles but too low for the rare types. Figure S10 (Example #S10) shows a solution using lower magnification and less intense sampling for the volume fractions of histological layers of cerebellum but a greater magnification and more intense sampling for counting cerebellar microvessels within the layers. Similarly, Figure S11 (Example #S11) shows two magnifications useful for two different components of the aortic wall.

FIGURE 5 Example #5 demonstrates three different sampling densities used for quantification of three parameters when evaluating the healing of intestinal anastomoses. The sampling was facilitated using STEREOLOGER software (Rosendorf et al., 2020, 2021a, 2021b). (a) Scanned slide shows the porcine small intestine. The centre of the healing anastomosis is highlighted with a dashed line. The green outline shows the ROI under study comprising the submucosa, muscularis, and serosa no more than 3 mm proximally and distally (dashed arrows) from the centreline. (b-d) Pan window maps of the scanned areas are screenshots captured from the STEREOLOGER software used for planning the sampling. The green polygon outlines the ROI, from which image fields of 20× objectives (green rectangles) were sampled in a systematic random uniform manner. The red rectangle shows the simulated image field of a 2× objective used for overview. The XY sampling step was 1500 μm for quantification of vWF and collagen (b, d, e, g) or 1000 μm for quantification of MAC387 (c, f). (e-g) Actual fields of view of 2× objectives for all three staining methods. The planned sampling for the 20× objectives is shown (green rectangles). (h–i) Actual fields of view of the 20× objectives for each staining method. Unbiased counting frames and the stereological point grid method were used for quantification of the volume fractions of individual components of the intestinal wall. On the bottom, recommendations on the total sampling variability (coefficient of error, CE, also considering the number of sections) are shown as provided in the Stereologer protocol. In vWF (h) and picrosirius red (i), the CE was sufficiently low. In MAC387, a greater point density is recommended due to the spatial variability of the distribution of inflammatory cells. Gomori trichrome kit (a), vWF immunohistochemistry (e, h), MAC387 immunohistochemistry (f, i), picrosirius red in bright field (g) and circularly polarized light (j). Scale bars 1 mm (a), 500 μm (e–g) and 50 μm (h–j)

(a)

von Willebrand factor

(b)

MAC387 (calprotectin)

(c)

picrosirius red (collagen)

(d)

(e)

(f)

(g)

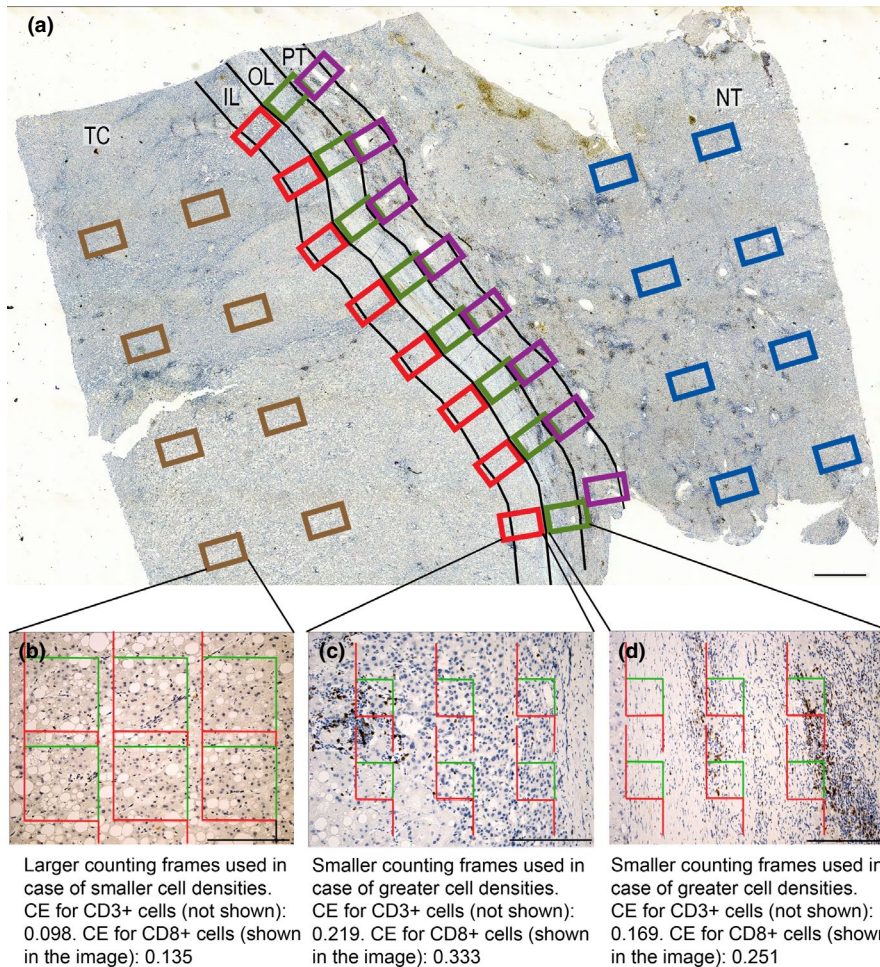(h)

(i)

(j)
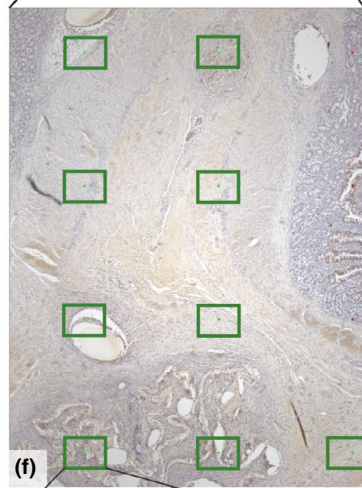
Probe   Volume Fraction (vWF)
CE   0.1294
Recommendations CE is acceptable.

Probe   Volume Fraction (MAC387)
CE   0.2595
Recommendations Decrease the Area per Point.

Probe   Volume Fraction (collagen)
CE   0.1188
Recommendations CE is acceptable.

Larger counting frames used in case of smaller cell densities. CE for CD3+ cells (not shown): 0.098. CE for CD8+ cells (shown in the image): 0.135

Smaller counting frames used in case of greater cell densities. CE for CD3+ cells (not shown): 0.219. CE for CD8+ cells (shown in the image): 0.333

Smaller counting frames used in case of greater cell densities. CE for CD3+ cells (not shown): 0.169. CE for CD8+ cells (shown in the image): 0.251

FIGURE 6 Example #6 demonstrates different sampling strategies in multiple ROIs for quantification of tumour-infiltrating CD8+ T cell infiltration in resected samples of human hepatocellular carcinoma. (a) Scanned slide with multiple ROIs: tumour centre (TC), inner layer (IL) of tumour invasive margin (TIM), outer layer (OL) of TIM, peritumoural area (PT) and non-tumour area (NT). The inner TIM and outer TIM were defined as 500 μm on each side of the border separating the malignant cell nests and adjacent non-tumour liver tissue or fibrous capsule (Hendry et al., 2017) towards TC or non-tumour liver, respectively. The TC represented the remaining tumour area. The PT region was defined as the 500 mcm thick region immediately adjacent to the OL. Using a 20× objective, eight equidistant fields of view (FOVs) were taken from each ROI using systematic uniform random sampling (SURS). (b-d) CD8-immunopositive cell profiles were counted using unbiased counting frames. The choice of the number and size of unbiased counting frames (UCFs) varied depending on the cell density at a glance. For TC and NT, areas of UCF (from 8700 to 34,801 μm^2) and their number (6–9) per image varied according to the lymphocytic density, and therefore, sampling fraction per ROI varied as well. Six UCFs per image were used for the inner and outer TIM and for the PT region. The coefficients of error (CE) calculated for the whole population of CD3+ T lymphocytes (not shown in the micrographs) and for the CD8+ subpopulation separately (shown on the micrographs). CD8 immunohistochemistry (a-d). Scale bars 1000 μm (a), 200 μm (b-d)

## 3.6 | Multistage sampling of FOVs and virtual sampling

Figure 7 (Example #7) shows a special case of multiscale sampling and analysis performed by a semiautomatic software tool when evaluating the quality and composition of decellularized liver. This demonstrates that tailoring a software tool to a specific problem might increase the efficiency of the whole work significantly, especially when the sampling of FOVs is an integral part of the quantification procedure. Figure S12 (Example #S12) demonstrates virtual sampling when counting fibroblasts within a 3D scaffold in vitro; such an approach requires programming skills, but the users are rewarded by a reasonable mapping of the variability of their results.

4 | DISCUSSION

4.1 | Sampling FOVs is only a part of a 3D multistage sampling

For any quantification, at least two criteria are to be met: (i) the staining should allow for a clear identification of all the structures under study, and (ii) borders of the reference space are clearly defined, either anatomically or by convention (Howard & Reed, 2005; Mouton, 2002). We would like to point out explicitly that the sampling of FOVs in virtual scanned sections illustrated above represents only a small part of the whole multistage sampling in quantitative histology. Therefore, the variability of results affected
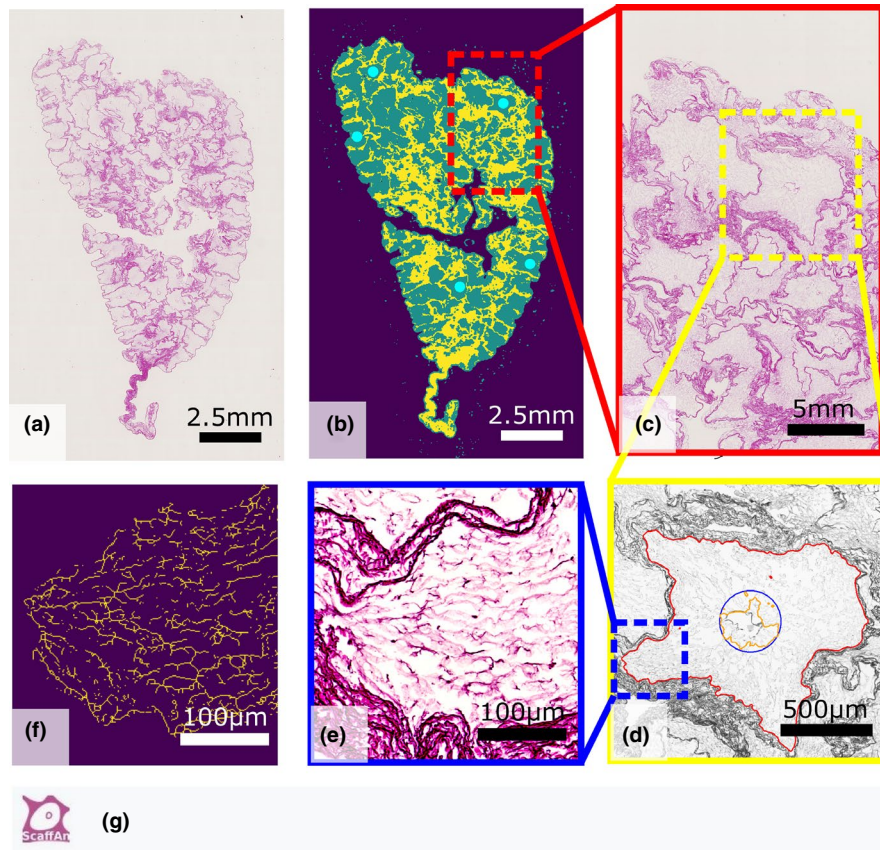
PIG-003_J-18-0170_HE.ndpi

	Skeleton length	Branch number	Area [mm^2]	Scan Segmentation Empty Area [mm^2]	Scan Segmentation Septum Area [mm^2]	Scan Segmentation Sinusoidal Area [mm^2]
0	49.284	23278	0.953975	74.561654	25.290709	89.24516
1	39.998	19469	0.835566	74.561654	25.290709	89.24516
2	50.942	24941	0.939373	74.561654	25.290709	89.24516

FIGURE 7 Example #7 shows a quantitative assessment of the morphological quality of decellularized porcine liver to be used as a high-quality scaffold for liver tissue engineering. (a) Slide scans are evaluated by in-house developed open source software SCAFFAN (http://scaffan.kky.zcu.cz/) as an integral part of a multiscale analysis (Moulisová et al., 2020). The resulting parameters describe the level of ECM structure preservation within individual lobules. It is a two-step procedure: (b) The first step is a whole scan analysis separating the lobules (segmentation to distinguish the sinusoidal ECM from more dense interlobular septa, triads and vessels) (Jirik et al., 2020, 2021). Typically, 5 lobules are then selected either manually by the end user or automatically (marked with cyan dots in b). The sampling is defined by a single lobule area and is not random, but it systematically reflects the morphological diversity of the sample (e.g. large vessels that are not the subject of analysis). (c) A close-up of a part of the analysed area. (d) The second step is lobular network analysis calculating parameters for individual lobules. Output parameters such as structure/skeleton lengths (mm) or branching points characterize the integrity of the sinusoidal vessel ECM network (detailed in e). These parameters are generated by using a set of algorithms, including image segmentation by the active contour model (Kass et al., 1988), texture analysis by the grey level cooccurrence matrix (Haralick, 1979) and skeletonization of the sinusoidal network (f). (g) An example of the online software output data

by the sampling of FOVs in a single slide represents only a small part of the total variability of data in the whole study. Other levels of sampling should also be emphasized, such as the number of subjects per study group, the sampling of tissue probes from organs, and the sampling of slides. We highly recommend classical papers on this topic (Gundersen & Osterby, 1981; Slomianka & West, 2005).

The importance of proper sampling of sections is elaborated in Figure S3. We found that the tissue composition of the canine soft palate was so heterogeneous that a whole half of the velum had to be sampled using a minimum of 10–15 sections distributed approximately uniformly throughout the complete tissue block to obtain reliable and robust results. Single sections cannot be used as 'representative' of this organ. Justifying the number of sections required

for a valid quantitative histological study is suggested in Figure S3D-E. However, even when a single slide is available (e.g. in archive material), the repeatability, reliability and correctness, even of simple quantification, might greatly benefit from correct FOV sampling.

4.2 | Choosing the FOV sampling intensity and practical implications

In all the examples presented, our effort was to spread the sampling items evenly and widely throughout the ROIs and specimens. This strategy is called systematic uniform random sampling, and it is superior and more efficient than simple (independent) random sampling, as it covers all parts under study uniformly (Mayhew & Lucocq, 2015). The examples illustrated above do not involve all possible situations in 2D sampling of FOVs in quantitative histology but might provide clues to the reader to most of these. We included mostly examples of sampling optimized in pilot studies but also problematic cases. Unnecessary intensive sampling (oversampling), for example in Figure 1A and Figure S7A, makes the work more laborious and expensive without providing new information. In contrast, insufficient sampling (undersampling), for example in Figure 1C and Figure S9C, Figure S10B,C, might compromise the study design and make it difficult to reach a pre-determined level of significance when testing statistical hypotheses, although biological differences might be present in the samples under study.

As the sampling error (introduced by all levels of the sampling procedure), represented by CE estimates, sums up with the biological variance (i.e. the differences between the samples themselves), according to Tschanz et al. (2014), it is always advisable to perform a pilot study on typical samples and groups under research. This allows for calculating a power sample analysis. Mapping both the total variability of our data and its components is an essential step when designing further studies on the same material, which involves calculating the minimum number of samples needed to compare the groups under study. Descriptive statistics of the pilot data (mean and standard deviation) are useful for the power sample analysis (Chow et al., 2008); for example, when planning an experiment and expecting one of the histological quantitative parameters to be increased by 20%, the minimum number of samples required per group would be calculated using the typical test power $\beta = 0.8$ (the type II error) and $\alpha = 0.05$ (type I error).

4.3 | Whole slide scanning vs. taking multiple micrographs

Currently, researchers have more technical options for acquiring virtual slides and planning the sampling of FOVs. The pros and cons of whole slide scanning vs. taking multiple individual micrographs are summarized in Table 6. An inexpensive alternative for acquiring virtual slides with large areas but high resolution might

TABLE 6 Pros and cons of two technical ways of sampling: Whole slide scanning vs. sampling multiple individual micrographs

Scanning whole slides	Sampling multiple individual micrographs
Histological scanner required.	Can be done even on routine microscopes with motorized or manual stage.
The data from the whole slide are always available, so more ROIs can be added when necessary.	Usually, is done once.
Can be fast and efficient when automated. However, issues occurring during the automated scanning do not appear until checked.	Usually, takes more time to be done. Any technical issues can be seen and solved immediately.
Problems with atypical size of archive slides might occur (Leica Biosystems, 2021). Either the holders are not adapted, or the slides might get stuck within the device.	Can be performed even if archive slides sometimes do not fit the feeding trays or holders of scanners (uniform slide dimensions and thickness required).
In some scanners, only bright field illumination technique and a limited choice of objectives are available. The use of immersion oil objectives is rare.	Can be done using any observation technique available of the microscope, for example fluorescence imaging, phase contrast, polarizing microscopy. No issues with using oil immersion easily.
Generates large datasets (typically 0.5–2 GB per typical histological slide). The pyramidal architecture of the files is usually optimized for viewing.	No special data infrastructure required.
Corresponds to state-of-the art of the whole-mount pathology (Look Hong et al., 2016; Rashid et al., 2019).	Does not permit whole-mount analysis (or this becomes extremely laborious).
In some scanners, multiplane (z-stack) scanning is possible to reflect the thickness of the slide. This might depend on the availability of high-aperture oil immersion objectives. Depth of focus problems might occur that cannot be solved automatically by the scanner software.	Optical sections could be captured in stacks using oil immersion objectives with high numerical aperture. Multiplane scanning might be crucial for studies involving confocal microscopy and requiring not only lateral resolution but also 3D information.
Using automated image-processing methods, the texture pattern of the whole sampling area can be analysed.	Analysing the whole slide would be very laborious or impossible. Texture patterns that exceed the size of individual micrographs are lost and cannot be analysed.

be image stitching, supported currently by stitching modules in most of the proprietary camera software solutions (extra costs in Nikon NIS ELEMENTS BR; ZEISS ZEN CORE, LEICA LAS). Moreover, free IMAGEJ (Schneider et al., 2012) and FIJI software can be used as well (Schindelin et al., 2012). However, stitched images do not support the pyramidal file architecture, and they may require more RAM than the optimized file formats of the slide scanners. Stitching algorithm also fail in case of optically empty regions.

5 | CONCLUSION

We conclude that combining scanning virtual slides in histology with efficient use of unbiased sampling is fully compatible with the plethora of data from quantitative microscopy, which can be expressed as the 'Do less well' rule (Gundersen & Osterby, 1981). Virtual microscopy proved to be extremely helpful to facilitate correct sampling at the level of individual slides. Uniform distribution of FOVs can also be reached using motorized microscope stages. Principles of SURS are beneficial not only for validity, efficiency and ethics of quantitative studies but also for improving accuracy and repeatability in qualitative studies. We suggest that modules supporting the SURS of FOVs with variable settings of ROIs and sampling intensity should be natively supported by all virtual slide scanners intended for scientific use.

CONFLICT OF INTEREST
The authors declare no conflict of interest.

ORCID
Zbyněk Tonar https://orcid.org/0000-0002-7200-9894

REFERENCES
Arai, K., Kobayashi, M., Harada, Y., Hara, Y., Michishita, N., Ohkusu-Tsukada, K., & Takahashi, K. (2016). Histopathologic and immunohistochemical features of soft palate muscles and nerves in dogs with an elongated soft palate. *American Journal of Veterinary Research*, 77(1), 77–83. https://doi.org/10.2460/ajvr.77.1.77

Babuska, V., Moztarzadeh, O., Kubikova, T., Moztarzadeh, A., Hrusak, D., & Tonar, Z. (2016). Evaluating the osseointegration of nanostructured titanium implants in animal models: Current experimental methods and perspectives (Review). *Biointerphases*, 11, 030801. https://doi.org/10.1116/1.4958793

Baker, M. (2016). 1,500 scientists lift the lid on reproducibility. *Nature*, 533, 452–454. https://doi.org/10.1038/533452a

Bertram, C. A., & Klopfleisch, R. (2017). The Pathologist 2.0: An update on digital pathology in veterinary medicine. *Veterinary Pathology*, 54, 756–766. https://doi.org/10.1177/0300985817709888

Biosystems, L. (2021). *Tips for digital pathology slide scanning.* https://www.leicabiosystems.com/resources/four-tips-for-digital-pathology-slide-scanning

Blassova, T., Tonar, Z., Tomasek, P., Hosek, P., Hollan, I., Treska, V., & Molacek, J. (2019). Inflammatory cell infiltrates, hypoxia, vascularization, pentraxin 3 and osteoprotegerin in abdominal aortic aneurysms – A quantitative histological study. *PLoS One*, 14, e0224818. https://doi.org/10.1371/journal.pone.0224818

Bolat, D., Kürüm, A., & Canpolat, S. (2018). Morphology and quantification of sheep pineal glands at pre–pubertal, pubertal and post–pubertal periods. *Anatomia, Histologia, Embryologia*, 47(4), 338–345. https://doi.org/10.1111/ahe.12359

Bolon, B., Garman, R. H., Gundersen, H. J. G., Allan Johnson, G., Kaufmann, W., Krinke, G., Little, P. B., Makris, S. L., Mellon, R. D., Sulik, K. K., & Jensen, K. (2011). Continuing education course #3: Current practices and future trends in neuropathology assessment for developmental neurotoxicity testing. *Toxicologic Pathology*, 39(1), 289–293. https://doi.org/10.1177/0192623310386247

Cakmak, G., & Karadag, H. (2019). A stereological study on calculation of volume values regarding lumbosacral segments of quails. *Anatomia, Histologia, Embryologia*, 48, 164–174. https://doi.org/10.1111/ahe.12437

Casteleyn, C., Rekecki, A., Van Der Aa, A., Simoens, P., & Van Den Broeck, W. (2010). Surface area assessment of the murine intestinal tract as a prerequisite for oral dose translation from mouse to man. *Laboratory Animals*, 44(3), 176–183. https://doi.org/10.1258/la.2009.009112

Chow, S. C., Wang, H., & Shao, J. (2008). *Sample size calculations in clinical research*, 2nd ed. Chapman & Hall/CRC Biostatistics Series.

Crosse, K. R., Bray, J. P., Orbell, G. M. B., & Preston, C. A. (2015). Histological evaluation of the soft palate in dogs affected by brachycephalic obstructive airway syndrome. *New Zealand Veterinary Journal*, 63(6), 319–325. https://doi.org/10.1080/00480169.2015.1061464

Dempster, D. W., Compston, J. E., Drezner, M. K., Glorieux, F. H., Kanis, J. A., Malluche, H., Meunier, P. J., Ott, S. M., Recker, R. R., & Parfitt, A. M. (2013). Standardized nomenclature, symbols, and units for bone histomorphometry: A 2012 update of the report of the ASBMR

Histomorphometry Nomenclature Committee. *Journal of Bone and Mineral Research*, 28(1), 2–17. https://doi.org/10.1002/jbmr.1805

Dockery, P., & Fraher, J. (2007). The quantification of vascular beds: A stereological approach. *Experimental and Molecular Pathology*, 82, 110–120. https://doi.org/10.1016/j.yexmp.2006.12.011

Dorph-Petersen, K. A., Nyengaard, J. R., & Gundersen, H. J. (2001). Tissue shrinkage and unbiased stereological estimation of particle number and size. *Journal of Microscopy*, 204, 232–246. https://doi.org/10.1046/j.1365-2818.2001.00958.x

Dupré, G., & Heidenreich, D. (2016). Brachycephalic syndrome. *Veterinary Clinics of North America: Small Animal Practice*, 46(4), 691–707. https://doi.org/10.1016/j.cvsm.2016.02.002

Eržen, I., Janáček, J., & Kubínová, L. (2011). Characterization of the capillary network in skeletal muscles from 3D data. *Physiological Research*, 60, 1–13. https://doi.org/10.33549/physiolres.931988

Ferreira, V. F., Dias, F. C. R., Costa, K. L. C., da Matta, S. L. P., de Melo, F. R., & de Melo, F. C. S. A. (2021). Descriptive morphometry and stereology in accessing the testis structure and function of the marsupial *Philander frenatus* (Olfers, 1818) (Didelphimorphia: Didelphidae). *Anatomia, Histologia, Embryologia*, 50, 379–386. https://doi.org/10.1111/ahe.12642

Goodarzi, N., Akbari Bazm, M., Naseri, L., & Hosseinipour, M. (2019). Histomorphometrical and stereological study of the oesophagus in the adult male Persian squirrel (*Sciurus anomalus*). *Anatomia, Histologia, Embryologia*, 48, 444–448. https://doi.org/10.1111/ahe.12465

Greiner, C., Grainger, S., Farrow, S., Davis, A., Su, J. L., Saybolt, M. D., Wilensky, R., Madden, S., & Sum, S. T. (2021). Robust quantitative assessment of collagen fibers with picrosirius red stain and linearly polarized light as demonstrated on atherosclerotic plaque samples. *PLoS One*, 16, e0248068. https://doi.org/10.1371/journal.pone.0248068

Gundersen, H. J., Boyce, R. W., Nyengaard, J. R., & Odgaard, A. (1993). The Conneulor: Unbiased estimation of connectivity using physical disectors under projection. *Bone*, 14, 217–222. https://doi.org/10.1016/8756-3282(93)90144-y

Gundersen, H. J., & Jensen, E. B. (1987). The efficiency of systematic sampling in stereology and its prediction. *Journal of Microscopy*, 147, 229–263. https://doi.org/10.1111/j.1365-2818.1987.tb02837.x

Gundersen, H. J., & Osterby, R. (1981). Optimizing sampling efficiency of stereological studies in biology: Or 'do more less well!'. *Journal of Microscopy*, 121, 65–73. https://doi.org/10.1111/j.1365-2818.1981.tb01199.x

Gundersen, H. J. G., Vedel Jensen, E. B., Kieu, K., & Nielsen, J. (1999). The efficiency of systematic sampling in stereology reconsidered. *Journal of Microscopy*, 193, 199–211. https://doi.org/10.1046/j.1365-2818.1999.00457.x

Haralick, R. M. (1979). Statistical and structural approaches to texture. *Proceedings of the IEEE*, 67, 786–804. https://doi.org/10.1109/PROC.1979.11328

Hendry, S., Salgado, R., Gevaert, T., Russell, P. A., John, T., Thapa, B., Christie, M., van de Vijver, K., Estrada, M. V., Gonzalez-Ericsson, P. I., Sanders, M., Solomon, B., Solinas, C., den Van Eynden, G. G. G. M., Allory, Y., Preusser, M., Hainfellner, J., Pruneri, G., Vingiani, A., … Fox, S. B. (2017). Assessing tumor-infiltrating lymphocytes in solid tumors: A Practical review for pathologists and proposal for a standardized method from the International Immunooncology Biomarkers Working Group: Part 1: Assessing the host immune response, TILs in invasive breast carcinoma and ductal carcinoma in situ, metastatic tumor deposits and areas for further research. *Advances in Anatomic Pathology*, 24, 235–251. https://doi.org/10.1097/PAP.0000000000000162

Hlavatý, J., Tonar, Z., Renner, M., Panitz, S., Petznek, H., Schweizer, M., Schüle, S., Kloke, B. P., Moldzio, R., & Witter, K. (2017). Tropism, intracerebral distribution, and transduction efficiency of HIV- and SIV-based lentiviral vectors after injection into the mouse brain: A qualitative and quantitative in vivo study. *Histochemistry and Cell Biology*, 148, 313–329. https://doi.org/10.1007/s00418-017-1569-1

Howard, C. V., & Reed, M. G. (2005). *Unbiased stereology: Three-dimensional measurement in microscopy*, 2nd ed. Garland Science.

Hsia, C. C. W., Hyde, D. M., Ochs, M., & Weibel, E. R. (2010). An official research policy statement of the American Thoracic Society/European Respiratory Society: Standards for quantitative assessment of lung structure. *American Journal of Respiratory and Critical Care Medicine*, 181(4), 394–418. https://doi.org/10.1164/rccm.200809-1522ST

Jahn, S. W., Plass, M., & Moinfar, F. (2020). Digital pathology: Advantages, limitations and emerging perspectives. *Journal of Clinical Medicine*, 9(11), 3697. https://doi.org/10.3390/jcm9113697

Jiřík, M., Bartoš, M., Tomášek, P., Malečková, A., Kural, T., Horáková, J., Lukáš, D., Suchý, T., Kochová, P., Hubálek Kalbáčová, M., Králíčková, M., & Tonar, Z. (2018). Generating standardized image data for testing and calibrating quantification of volumes, surfaces, lengths, and object counts in fibrous and porous materials using X-ray microtomography. *Microscopy Research and Techniques*, 81, 551–568. https://doi.org/10.1002/jemt.23011

Jirik, M., Gruber, I., Moulisova, V., Schindler, C., Cervenkova, L., Palek, R., Rosendorf, J., Arlt, J., Bolek, L., Dejmek, J., Dahmen, U., Zelezny, M., & Liska, V. (2021). Semantic segmentation of intralobular and extralobular tissue from liver scaffold H&E images. *Sensors*, 20, 7063. https://doi.org/10.3390/s20247063

Jirik, M., Moulisova, V., Schindler, C., Cervenkova, L., Palek, R., Rosendorf, J., Arlt, J., Bolek, L., Dejmek, J., Dahmen, U., Jirikova, K., Gruber, I., Liska, V., & Zelezny, M. (2020). MicrAnt: Towards regression task oriented annotation tool for microscopic images. *Lecture Notes in Computer Science*, 12148, 209–218. https://doi.org/10.1007/978-3-030-51002-2_15

Jiřík, M., Tonar, Z., Králíčková, A., Eberlová, L., Mírka, H., Kochová, P., Gregor, T., Hošek, P., Svobodová, M., Rohan, E., Králíčková, M., & Liška, V. (2016). Stereological quantification of microvessels using semiautomated evaluation of X-ray microtomography of hepatic vascular corrosion casts. *International Journal of Computer Assisted Radiology and Surgery*, 11, 1803–1819. https://doi.org/10.1007/s11548-016-1378-3

Junatas, K. L., Tonar, Z., Kubíková, T., Liška, V., Pálek, R., Mik, P., Králíčková, M., & Witter, K. (2017). Stereological analysis of size and density of hepatocytes in the porcine liver. *Journal of Anatomy*, 230, 575–588. https://doi.org/10.1111/joa.12585

Kass, M., Witkin, A., & Terzopoulos, D. (1988). Snakes: Active contour models. *International Journal of Computer Vision*, 1, 321–331. https://doi.org/10.1007/BF00133570

Keša, P., Pokorná, E., Grajciarová, M., Tonar, Z., Vočková, P., Trochet, P., Kopeček, M., Jakša, R., Šefc, L., & Klener, P. (2021). Quantitative in vivo monitoring of hypoxia and vascularization of patient-derived murine xenografts of mantle cell lymphoma using photoacoustic and ultrasound imaging. *Ultrasound in Medicine & Biology*, 47, 1099–1107. https://doi.org/10.1016/j.ultrasmedbio.2020.12.010

Knudsen, L., Brandenberger, C., & Ochs, M. (2021). Stereology as the 3D tool to quantitate lung architecture. *Histochemistry and Cell Biology*, 155, 163–181. https://doi.org/10.1007/s00418-020-01927-0

Kochová, P., Cimrman, R., Jansová, M., Michalová, K., Kališ, K., Kubíková, T., & Tonar, Z. (2019). The histological microstructure and in vitro mechanical properties of the human female postmenopausal perineal body. *Menopause – The Journal of the North American Menopause Society*, 26, 66–77. https://doi.org/10.1097/GME.0000000000001166

Kochová, P., Hympánová, L., Rynkevic, R., Cimrman, R., Tonar, Z., Deprest, J., & Kališ, V. (2019). The histological microstructure and in vitro mechanical properties of pregnant and postmenopausal ewe perineal body. *Menopause – The Journal of the North American*

Menopause Society, 26, 1289–1301. https://doi.org/10.1097/GME.0000000000001395

Kocová, J. (1970). Overall staining of connective tissue and the muscular layer of vessels. Folia Morphologica, 18, 293–295.

Kolinko, Y., Cendelin, J., Kralickova, M., & Tonar, Z. (2016). Smaller absolute quantities but greater relative densities of microvessels are associated with cerebellar degeneration in Lurcher mice. Frontiers in Neuroanatomy, 10, 35. https://doi.org/10.3389/fnana.2016.00035

Kubíková, T., Kochová, P., Tomášek, P., Witter, K., & Tonar, Z. (2018). Numerical and length densities of microvessels in the human brain: Correlation with preferential orientation of microvessels in the cerebral cortex, subcortical grey matter and white matter, pons and cerebellum. Journal of Chemical Neuroanatomy, 88, 22–32. https://doi.org/10.1016/j.jchemneu.2017.11.005

Kuo, K.-H., & Leo, J. M. (2019). Optical versus virtual microscope for medical education: A systematic review. Anatomical Sciences Education, 12(6), 678–685. https://doi.org/10.1002/ase.1844

Lokkegaard, A., Nyengaard, J. R., & West, M. J. (2001). Stereological estimates of number and length of capillaries in subdivisions of the human hippocampal region. Hippocampus, 11, 726–740. https://doi.org/10.1002/hipo.1088

Look Hong, N. J., Clarke, G. M., Yaffe, M. J., & Holloway, C. M. B. (2016). Cost–effectiveness analysis of whole–mount pathology processing for patients with early breast cancer undergoing breast conservation. Current Oncology, 23, S23–S31. https://doi.org/10.3747/co.23.2917

Malečková, A., Kochová, P., Pálek, R., Liška, V., Mik, P., Bońkowski, T., Horák, M., & Tonar, Z. (2021). Blunt injury of liver: Mechanical response of porcine liver in experimental impact test. Physiological Measurement, 42, 025008. https://doi.org/10.1088/1361-6579/abdf3c

Marcos, R., Monteiro, R. A., & Rocha, E. (2012). The use of design–based stereology to evaluate volumes and numbers in the liver: A review with practical guidelines. Journal of Anatomy, 220, 303–317. https://doi.org/10.1111/j.1469-7580.2012.01475.x

Mayhew, T. M. (2014). Estimating oxygen diffusive conductances of gas–exchange systems: A stereological approach illustrated with the human placenta. Annals of Anatomy, 196, 34–40. https://doi.org/10.1016/j.aanat.2012.08.002

Mayhew, T. M., & Lucocq, J. M. (2015). From gross anatomy to the nano-morphome: Stereological tools provide a paradigm for advancing research in quantitative morphomics. Journal of Anatomy, 226, 309–321. https://doi.org/10.1111/joa.12287

McQuin, C., Goodman, A., Chernyshev, V., Kamentsky, L., Cimini, B. A., Karhohs, K. W., Doan, M., Ding, L., Rafelski, S. M., Thirstrup, D., Wiegraebe, W., Singh, S., Becker, T., Caicedo, J. C., & Carpenter, A. E. (2018). Cell profiler 3.0: Next–generation image processing for biology. PLoS Biology, 16(7), e2005970. https://doi.org/10.1371/journal.pbio.2005970

Mik, P., Tonar, Z., Malečková, A., Eberlová, L., Liška, V., Pálek, R., Rosendorf, J., Jiřík, M., Mírka, H., Králíčková, M., & Witter, K. (2018). Distribution of connective tissue in the male and female porcine liver: Histological mapping and recommendations for sampling. Journal of Comparative Pathology, 162, 1–13. https://doi.org/10.1016/j.jcpa.2018.05.004

Moulisová, V., Jiřík, M., Schindler, C., Červenková, L., Pálek, R., Rosendorf, J., Arlt, J., Bolek, L., Šůsová, S., Nietzsche, S., Liška, V., & Dahmen, U. (2020). Novel morphological multi–scale evaluation system for quality assessment of decellularized liver scaffolds. Journal of Tissue Engineering, 11, 2041731420921121. https://doi.org/10.1177/2041731420921121

Mouton, P. R. (2002). Principles and practices of unbiased stereology. An introduction for bioscientists. The Johns Hopkins University Press.

Mühlfeld, C. (2014). Quantitative morphology of the vascularisation of organs: A stereological approach illustrated using the

cardiac circulation. Annals of Anatomy, 196, 12–19. https://doi.org/10.1016/j.aanat.2012.10.010

Mühlfeld, C., Nyengaard, J. R., & Mayhew, T. M. (2010). A review of state–of–the–art stereology for better quantitative 3D morphology in cardiac research. Cardiovascular Pathology, 19, 65–82. https://doi.org/10.1016/j.carpath.2008.10.015

Mühlfeld, C., & Ochs, M. (2013). Quantitative microscopy of the lung: A problem–based approach. Part 2: Stereological parameters and study designs in various diseases of the respiratory tract. American Journal of Physiology, Lung Cellular and Molecular Physiology, 305, L205–L221. https://doi.org/10.1152/ajplung.00427.2012

Nelson, G., Boehm, U., Bagley, S., Bajcsy, P., Bischof, J., Brown, C. M., Dauphin, A., Dobbie, I. M., Eriksson, J. E., Faklaris, O., Fernandez-Rodriguez, J., Ferrand, A., Gelman, L., Gheisari, A., Hartmann, H., Kukat, C., Laude, A., Mitkovski, M., Munck, S., ... Nitschke, R. (2021). QUAREP-LiMi: A community-driven initiative to establish guidelines for quality assessment and reproducibility for instruments and images in light microscopy. Journal of Microscopy, 284, 56–73. https://doi.org/10.1111/jmi.13041

Nevoral, J., Havránková, J., Kolinko, Y., Prokešová, Š., Fenclová, T., Monsef, L., Žalmanová, T., Petr, J., & Králíčková, M. (2021). Exposure to alternative bisphenols BPS and BPF through breast milk: Noxious heritage effect during nursing associated with idiopathic infertility. Toxicology and Applied Pharmacology, 413, 115409. https://doi.org/10.1016/j.taap.2021.115409

Noorafshan, A. (2014). Stereology as a valuable tool in the toolbox of testicular research. Annals of Anatomy, 196, 57–66. https://doi.org/10.1016/j.aanat.2012.07.008

Noorafshan, A., Niazi, B., Mohamadpour, M., Hoseini, L., Hoseini, N., Owji, A. A., Rafati, A., Sadeghi, Y., & Karbalay-Doust, S. (2016). First and second order stereology of hyaline cartilage: Application on mice femoral cartilage. Annals of Anatomy, 208, 24–30. https://doi.org/10.1016/j.aanat.2016.07.011

Nyengaard, J. R. (1999). Stereologic methods and their application in kidney research. Journal of the American Society of Nephrology, 10, 1100–1123. https://doi.org/10.1681/ASN.V1051100

Nyengaard, J. R., & Alwasel, S. H. (2014). Practical stereology of the stomach and intestine. Annals of Anatomy, 196, 41–47. https://doi.org/10.1016/j.aanat.2013.10.007

Ochs, M., & Mühlfeld, C. (2013). Quantitative microscopy of the lung: A problem–based approach. Part 1: Basic principles of lung stereology. American Journal of Physiology, Lung Cellular and Molecular Physiology, 305, L15–L22. https://doi.org/10.1152/ajplung.00429.2012

Parfitt, A. M., Drezner, M. K., Glorieux, F. H., Kanis, J. A., Malluche, H., Meunier, P. J., Ott, S. M., & Recker, R. R. (1987). Bone histomorphometry: Standardization of nomenclature, symbols, and units: Report of the ASBMR Histomorphometry Nomenclature Committee. Journal of Bone and Mineral Research, 2(6), 595–610. https://doi.org/10.1002/jbmr.5650020617

Pichetto, M., Arrighi, S., Gobbetti, M., & Romussi, S. (2015). The anatomy of the dog soft palate. III. Histological evaluation of the caudal soft palate in brachycephalic neonates. Anatomical Record, 298(3), 618–623. https://doi.org/10.1002/ar.23054

Rashid, S., Nir, G., Fazli, L., Boag, A. H., Siemens, D. R., Goldenberg, S. L., Abolmaesumi, P., & Salcudean, S. E. (2019). Automatic pathology of prostate cancer in whole mount slides incorporating individual gland classification. Computer Methods in Biomechanics and Biomedical Engineering: Imaging & Visualization, 3, 336–347. https://doi.org/10.1080/21681163.2018.1514280

Rich, L., & Whittaker, P. (2005). Collagen and picrosirius red staining. A polarized light assessment of fibrillar hue and spatial distribution. Journal of Morphological Sciences, 22, 97–104.

Rosendorf, J., Horakova, J., Klicova, M., Palek, R., Cervenkova, L., Kural, T., Hosek, P., Kriz, T., Tegl, V., Moulisova, V., Tonar, Z., Treska, V., Lukas, D., & Liska, V. (2020). Experimental fortification of intestinal

anastomoses with nanofibrous materials in a large animal model. *Scientific Reports*, 10, 1134. https://doi.org/10.1038/s41598-020-58113-4

Rosendorf, J., Klicova, M., Cervenkova, L., Horakova, J., Klapstova, A., Hosek, P., Palek, R., Sevcik, J., Polak, R., Treska, V., Chvojka, J., & Liska, V. (2021). Reinforcement of colonic anastomosis with improved ultrafine nanofibrous patch: Experiment on pig. *Biomedicines*, 9, 102. https://doi.org/10.3390/biomedicines9020102

Rosendorf, J., Klicova, M., Cervenkova, L., Palek, R., Horakova, J., Klapstova, A., Hosek, P., Moulisova, V., Bednar, L., Tegl, V., Brzon, O., Tonar, Z., Treska, V., Lukas, D., & Liska, V. (2021). Double–layered nanofibrous patch for prevention of anastomotic leakage and peritoneal adhesions, experimental study. *In Vivo*, 35, 731–741. https://doi.org/10.21873/invivo.12314

Sadeghinezhad, J., Aghabalazadeh Asl, M., Saeidi, A., & De Silva, M. (2020). Morphometrical study of the cat cerebellum using unbiased design–based stereology. *Anatomia, Histologia, Embryologia*, 49, 788–797. https://doi.org/10.1111/ahe.12583

Sadeghinezhad, J., & Nyengaard, J. R. (2021). Morphometry of cervical spinal cord in cat using design–based stereology. *Anatomia, Histologia, Embryologia*, 50, 746–755. https://doi.org/10.1111/ahe.12719

Saliba, V., Legido-Quigley, H., Hallik, R., Aaviksoo, A., Car, J., & McKee, M. (2012). Telemedicine across borders: A systematic review of factors that hinder or support implementation. *International Journal of Medical Informatics*, 81(12), 793–809. https://doi.org/10.1016/j.ijmedinf.2012.08.003

Schindelin, J., Arganda-Carreras, I., Frise, E., Kaynig, V., Longair, M., Pietzsch, T., Preibisch, S., Rueden, C., Saalfeld, S., Schmid, B., Tinevez, J. Y., White, D. J., Hartenstein, V., Eliceiri, K., Tomancak, P., & Cardona, A. (2012). Fiji: An open–source platform for biological–image analysis. *Nature Methods*, 9, 676–682. https://doi.org/10.1038/nmeth.2019

Schneider, C. A., Rasband, W. S., & Eliceiri, K. W. (2012). NIH Image to ImageJ: 25 years of image analysis. *Nature Methods*, 9, 671–675. https://doi.org/10.1038/nmeth.2089

Selçuk, M. L., & Tipirdamaz, S. (2020). A morphological and stereological study on brain, cerebral hemispheres and cerebellum of New Zealand rabbits. *Anatomia, Histologia, Embryologia*, 49, 90–96. https://doi.org/10.1111/ahe.12489

Slomianka, L., & West, M. J. (2005). Estimators of the precision of stereological estimates: An example based on the CA1 pyramidal cell layer of rats. *Neuroscience*, 136, 757–767. https://doi.org/10.1016/j.neuroscience.2005.06.086

Smart In Media AG. (2021, September 3). *Virtual microscopy—Overview and definition*. https://www.virtual-microscopy.net

Suchý, T., Šupová, M., Sauerová, P., Verdánová, M., Sucharda, Z., Rýglová, Š., Žaloudková, M., Sedláček, R., & Kalbáčová, M. H. (2015). The effects of different cross–linking conditions on collagen–based nanocomposite scaffolds–an in vitro evaluation using mesenchymal stem cells. *Biomedical Materials*, 10, 065008. https://doi.org/10.1088/1748-6041/10/6/065008

Tamburro, R., Brunetti, B., Muscatello, L. V., Mantovani, C., & De Lorenzic, D. (2019). Short–term surgical outcomes and histomorphological evaluation of thermal injury following palatoplasty performed with diode laser or air plasma device in dogs with brachycephalic airway obstructive syndrome. *The Veterinary Journal*, 253, 105391. https://doi.org/10.1016/j.tvjl.2019.105391

Tomášek, P., Tonar, Z., Grajciarová, M., Kural, T., Turek, D., Horáková, J., Pálek, R., Eberlová, L., Králíčková, M., & Liška, V. (2020). Histological mapping of porcine carotid arteries – An animal model for the assessment of artificial conduits suitable for coronary bypass grafting in humans. *Annals of Anatomy*, 228, 151434. https://doi.org/10.1016/j.aanat.2019.151434

Tonar, Z., Egger, G. F., Witter, K., & Wolfesberger, B. (2008). Quantification of microvessels in canine lymph nodes. *Microscopy Research and Techniques*, 71, 760–772. https://doi.org/10.1002/jemt.20619

Tonar, Z., Khadang, I., Fiala, P., Nedorost, L., & Kochová, P. (2011). Quantification of compact bone microporosities in the basal and alveolar portions of the human mandible using osteocyte lacunar density and area fraction of vascular canals. *Annals of Anatomy*, 193, 211–219. https://doi.org/10.1016/j.aanat.2011.02.001.s

Tonarova, P., Lochovska, K., Pytlik, R., & Hubalek Kalbacova, M. (2021). The impact of various culture conditions on human mesenchymal stromal cells metabolism. *Stem Cells International*, 2021, 6659244. https://doi.org/10.1155/2021/6659244

Tschanz, S., Schneider, J. P., & Knudsen, L. (2014). Design–based stereology: Planning, volumetry and sampling are crucial steps for a successful study. *Annals of Anatomy*, 196, 3–11. https://doi.org/10.1016/j.aanat.2013.04.011

Van Ginneken, C., Meir, F. V., Sys, S., & Weyns, A. (2002). Stereologic characteristics of pig small intestine during normal development. *Digestive Diseases and Sciences*, 47(4), 868–878. https://doi.org/10.1023/A:1014768806773

Vatsos, I. N. (2021). Planning and reporting of the histomorphometry used to assess the intestinal health in fish nutrition research—Suggestions to increase comparability of the studies. *Frontiers in Veterinary Science*, 8, 666044. https://doi.org/10.3389/fvets.2021.666044

West, M. J., Slomianka, L., & Gundersen, H. J. (1991). Unbiased stereological estimation of the total number of neurons in the subdivisions of the rat hippocampus using the optical fractionator. *Anatomical Record*, 231, 482–497. https://doi.org/10.1002/ar.1092310411

Wolfesberger, B., Tonar, Z., Witter, K., Guija de Arespacohaga, A., Skalicky, M., Walter, I., Thalhammer, J. G., & Egger, G. F. (2008). Microvessel density in normal lymph nodes and lymphomas of dogs and their correlation with vascular endothelial growth factor expression. *Research in Veterinary Science*, 85, 56–61. https://doi.org/10.1016/j.rvsc.2007.07.008

SUPPORTING INFORMATION

Additional supporting information may be found in the online version of the article at the publisher's website.

11.2 Příloha II

Tomášek, P., Tonar, Z., **Grajciarová, M.**, Kural, T., Turek D., Horáková, J., Pálek, R., Eberlová, L., Králíčková, M., Liška, V. Histological mapping of porcine carotid arteries – An animal model for the assessment of artificial conduits suitable for coronary bypass grafting in humans. Ann. Anat. 2020 Mar;228:151434. DOI: 10.1016/j.aanat.2019.151434.

IF(JCR2019)=2.388.   **Q1(Anatomy&Morphology)**

https://pubmed.ncbi.nlm.nih.gov/31704146/
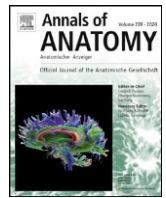
RESEARCH ARTICLE

Histological mapping of porcine carotid arteries — An animal model for the assessment of artificial conduits suitable for coronary bypass grafting in humans

Petr Tomášek [a,b], Zbyněk Tonar [a,*], Martina Grajciarová [a], Tomáš Kural [a], Daniel Turek [c,d], Jana Horáková [e], Richard Pálek [f], Lada Eberlová [g], Milena Králíčková [a], Václav Liška [f]

[a] Department of Histology and Embryology and Biomedical Center, Faculty of Medicine in Pilsen, Charles University, Karlovarska 48, 301 66 Pilsen, Czech Republic
[b] Department of Forensic Medicine, Second Faculty of Medicine, Charles University and Na Bulovce Hospital, Budinova 2, 180 81 Prague, Czech Republic
[c] First Faculty of Medicine, Charles University in Prague, Katerinska 32, 121 08 Prague 2, Czech Republic
[d] Department of Cardiac Surgery, Institute for Clinical and Experimental Medicine, Videnska 1958/9, 140 21 Prague, Czech Republic
[e] Department of Nonwovens and Nanofibrous Materials, Faculty of Textile Engineering, Technical University of Liberec, Studentska 2, 461 17 Liberec, Czech Republic
[f] Department of Surgery and Biomedical Center, Faculty of Medicine in Pilsen, Charles University, Husova 3, 306 05 Pilsen, Czech Republic
[g] Department of Anatomy, Faculty of Medicine in Pilsen, Charles University, Karlovarska 48, 301 66 Pilsen, Czech Republic

article info

abstract

Background: Using animal models in experimental medicine requires mapping of their anatomical variability. Porcine common carotid arteries (CCA) are often preferred for the preclinical testing of vascular grafts due to their anatomical and physiological similarity to human small-diameter arteries. Comparing the microscopic structure of animal model organs to their human counterparts reveals the benefits and limitations of translational medicine.
Methods: Using quantitative histology and stereology, we performed an extensive mapping of the regional proximodistal differences in the fractions of elastin, collagen, and smooth muscle actin as well as the intima-media and wall thicknesses among 404 segments (every 1 cm) of porcine CCAs collected from male and female pigs (n = 21). We also compared the microscopic structure of porcine CCAs with segments of human coronary arteries and one of the preferred arterial conduits used for the coronary artery bypass grafting (CABG), namely, the internal thoracic artery (ITA) (n = 21 human cadavers).
Results: The results showed that the histological structure of left and right porcine CCA can be considered equivalent, provided that gross anatomical variations of the regular branching patterns are excluded. The proximal elastic carotid (51.2% elastin, 4.2% collagen, and 37.2% actin) transitioned to more muscular middle segments (23.5% elastin, 4.9% collagen, 54.3% actin) at the range of 2–3 centimeters and then to even more muscular distal segments (17.2% elastin, 4.9% collagen, 64.0% actin). The resulting morphometric data set shows the biological variability of the artery and is made available for biomechanical modeling and for performing a power analysis and calculating the minimum number of samples per group when planning further experiments with this widely used large animal model.
Conclusions: Comparison of porcine carotids with human coronary arteries and ITA revealed the benefits and the limitations of using porcine CCAs as a valid model for testing bioengineered small-diameter CABG vascular conduits. Morphometry of human coronary arteries and ITA provided more realistic data for tailoring multilayered artificial vascular prostheses and the ranges of values within which the conduits should be tested in the future. Despite their limitations, porcine CCAs remain a widely used and well-characterized large animal model that is available for a variety of experiments in vascular surgery.

© 2019 Elsevier GmbH. All rights reserved.

1. Introduction

Using animal models in experimental medicine requires mapping of their anatomical variability. This is a necessary condition

* Corresponding author.
    E-mail address: tonar@lfp.cuni.cz (Z. Tonar).

for performing a power analysis to justify the numbers of animals and biological samples required for detecting any biological effects targeted in the experiment. Comparing the microscopic structure of animal model organs to their human counterparts reveals the benefits and limitations of translational medicine. This approach is needed for a realistic interpretation of the results gained in animal models and for bridging the gaps between experimental medicine and possible benefits for human patients where translational research is concerned (Lossi et al., 2016). One of the important issues in vascular medicine is the manufacturing of bioengineered vascular grafts for coronary artery bypass grafting (CABG), their optimization (Szafron et al., 2019) and their testing in animal models. The present study was motivated by the lack of quantitative data mapping the microscopic structure of one of the important models in vascular surgery, namely, the porcine common carotid artery (CCA).

1.1. Porcine CCAs as animal models in experimental studies

The porcine CCA is often preferred for the preclinical testing of vascular grafts due to its anatomical and physiological similarity to human small-diameter arteries (García et al., 2011). Porcine CCAs are currently often used as an experimental model in vascular surgery, such as designing stents used in the treatment of CCA obstruction or stenosis and in acute ischemic stroke (Fong et al., 2017; Jiang et al., 2016; Nikoubashman et al., 2018; Stewart et al., 2017; Sun et al., 2019; Zhou et al., 2016). To date, porcine CCAs have been used for testing various types of bioengineered vascular grafts, such as polytetrafluoroethylene (PTFE) and electrospun poly-c-caprolactone nanofibers (PCL) (Kritharis et al., 2012; Jaramillo et al., 2018; Mrowczynski et al., 2014; Tzchori et al., 2018).

The CCA is a paired artery located in the area of the neck vertebrae approximately 2–2.5 cm under the skin (Anderson et al., 2018). Both arteries originate from the brachiocephalic trunk, which in turn stems from the aortic arch (Dondelinger et al., 1998; Popesko, 1978). The CCA passes along the ventral surface from its source of origin and then through the dorsolateral surface of the trachea. The recurrent laryngeal nerve is on the ventral side of the CCA, the vagosympathetic trunk is on the dorsal side and the internal jugular vein is on the lateral side (Popesko, 1978). CCA branching occurs in the following order: caudal thyroid artery (which is only on the left side), cranial thyroid artery, cranial laryngeal artery, internal carotid artery and external carotid artery (Popesko, 1978). In adult pigs, the proximal diameter is approximately 5–6 mm (Dondelinger et al., 1998; García et al., 2011).

From an anatomical and surgical point of view there are several advantages, such as easy surgical access with the possibility of using the same surgical instruments and suture materials as employed in humans (Anderson et al., 2018). Porcine CCA is easily accessible for catheterization (Dondelinger et al., 1998). The sufficient length of porcine CCA with minimum branching makes the implantation of grafts feasible. The patency of the grafts can be easily monitored using Doppler USG sonography (Anderson et al., 2018). Porcine CCA exhibits a comparable pressure resistance to that of autologous grafts for CABG, namely, the human saphenous veins (Negishi et al., 2011).

From the viewpoint of histology, the proximal porcine CCA was reported to contain more elastin than its distal segments (Sokolis et al., 2011; García et al., 2013, 2011). Distally, elastin is substituted by smooth muscle cells (García et al., 2013, 2011; Weizsäcker et al., 2014).

1.2. Autologous conduits for CABG

CABG is the most common cardiac surgery procedure performed worldwide. Appropriate graft selection, in addition to precise sur-

gical techniques, is essential to acquire good long-term results. The severity of natural vessel stenosis and capacious (ample) target vessel run-off are among the well-known factors determining long-term graft patency. In terms of patients' 10-year survival, the superiority of the left internal thoracic artery (ITA) anastomozed to the left anterior descending coronary artery (LAD; anterior interventricular branch of the left coronary artery) was proven more than 30 years ago (Loop et al., 1986), and left ITA to LAD grafting remains the cornerstone of modern coronary bypass surgery. ITA, as a small-diameter elastic type artery, is known to be resistant to vasospasms, neointimal hyperplasia and atherosclerosis due to a considerable production of anti-inflammatory and vasoactive substances, especially nitric oxide (Sisto and Isola, 1989; Wharton et al., 1994; Otsuka et al., 2013). According to a functional classification of arterial grafts, the ITA is a somatic artery with considerable amounts of elastic lamellae and with a lower tendency towards spasticity than other autologous conduits used for CABG (He, 2013). Other commonly used autologous grafts include radial artery (Gaudino et al., 2005), saphenous veins (Yazdani et al., 2013), the right gastroepiploic artery (Martínez-González et al., 2017) and some other rarely used alternative grafts used in patients with a complete lack of suitable conduits (Loskot et al., 2016).

1.3. Tissue-engineered small diameter vascular grafts

Blood vessel replacement with a small-diameter (<6 mm) graft represents the holy grail of peripheral vascular surgery (Kakisis et al., 2005). Various materials and production techniques have been developed in the search for vascular prostheses (Chlupac et al., 2009; Naito et al., 2011; Pashneh-Tala et al., 2016; Ong et al., 2017). Prostheses based on polyethylene terephthalate (PETE), PTFE or polyurethane work well in the replacement of vessels with large diameters. When such prostheses are used as a small-diameter replacement, an unfavorable healing process has been described in terms of thrombogenicity as a reason for the lack of endothelium together with anastomotic intimal hyperplasia caused by local changes in blood flow (Sarkar et al., 2007; Chlupac et al., 2009). Therefore, novel biodegradable materials based on, for example, polyesters (de Valence et al., 2012a,b; Tara et al., 2014), collagen (Menasche et al., 1984), elastin (Wise et al., 2011; Koens et al., 2015) and silk fibroin (Wang et al., 2010; McClure et al., 2012) are under development of ideal vascular grafts. These materials gen- erally support the endothelialization of the inner surface of the prosthesis, ensuring a long-term nonthrombogenic surface, facilitating healing and enabling the regeneration of functional vessels. However, degradation happens concurrently with the healing process, which is difficult to predict.

In addition to the degradation process and its function under in vivo conditions that ensures the ability to remodel, other structural and functional parameters of vascular grafts must be carefully considered. From the viewpoint of mechanics, vessel replacements must be compliant and possess sufficient burst strength. For surgical handling, suture retention strength is required. A comparison of the mechanical properties of clinically available grafts and human vessels is reported in a study by Johnson et al. (2015). Last but not least, the prosthesis has to be easily handled during surgeries and be immediately available in various sizes. The production cost should be economically favorable, and its storage should be uncomplicated and long-term (Arrigoni et al., 2006).

Bioengineered vascular prostheses can also be modified by the addition of various active substances, such as growth factors (Shin et al., 2012; Wang et al., 2017), heparin (Liu et al., 2014; Qiu et al., 2017), and nitric oxide donors (Koh et al., 2013; Rychter et al., 2016). Another strategy of producing artificial small-diameter grafts suitable for CABG relies on decellularized conduits (e.g., Lawson et al., 2016; Lindsey et al., 2017). Regardless of the manufacturing

strategy, the performance of newly developed grafts is tested in animal models such as rats, rabbits, pigs and sheep (Byrom et al., 2010). Replacement of the carotid artery in a porcine model was used in studies of tissue-engineered vascular grafts prepared from decellularized arteries (Quint et al., 2011; Dahan et al., 2017) or electrospun PCL vascular grafts (Mrowczynski et al., 2014). The ideal vascular graft for clinical application in CABG should have the following attributes: adequate handling characteristics for surgical implantation, ability to maintain the diameter in stress conditions (resistance to kinking, and bending), routing compliance for sequential anastomosis construction, capability to withstand systemic pressure changes over a long time period, low rates of thromboembolic events in low-flow, low-diameter conditions, and low susceptibility to competitive flow. Following implantation, the graft should have growth potential and resistance to infection. The graft is supposed to be capable of remodeling, responding to a variety of stimuli similarly to a native vessel. The manufacturing range of the conduits required for CABG is expected to be 3–5 mm in diameter to meet the needs of various coronary regions, with acceptable short- and long-term patency comparable at least with saphenous vein grafts. However, proportions between the size of grafts and the native vessels are still under debate (Best et al., 2018).

1.4. Aims of the study

To the best of our knowledge, no quantitative histological studies are available that demonstrate how the microscopic structure changes along the macroscopic segments of the relatively long CCA. Moreover, we found no quantitative evidence comparing the histological structure of various segments of porcine CCAs with human coronary arteries or with arteries most frequently used as autologous grafts. Significant differences should be expected between the structure of coronary arteries of elderly humans, i.e., the vessels to which the conduits should be applied in patients undergoing CABG, and the porcine carotids as their animal model in relatively young pigs. At the same time, manufacturing porous and multilayered nanofibrous vascular prostheses prepared for in vivo studies in pigs would greatly benefit from morphometry showing the composition and proportions of real blood vessels in humans.

The first aim was to map the differences in the fraction of elastin, collagen, and smooth muscle actin within the intima and media, as well as the intima-media thickness and wall thickness among the segments of porcine CCAs on both the right and left sides. The second aim was to compare the microscopic structure of porcine CCAs with human coronary arteries and one of the preferred arterial conduits, namely, the ITA. These differences should reveal the limitations of using porcine CCAs as a valid model for testing CABG conduits and reveal the ranges of values within which the conduits should be tested in the future.

2. Materials and methods

2.1. Collecting porcine CCAs

Whole CCAs (n = 41) and adjacent arterial branches were obtained from 21 healthy male and female Prestice Black-Pied pigs (Vrtkova, 2015) aged 12–21 weeks and weighing 20–65 kg (35.8 ±13.3 kg, mean ±SD). The female pigs (n = 12) were, on average, aged 17.3 ± 3 weeks and weighed 40.7 ± 14.5; the male pigs (n = 9) were aged 14.6 ± 2.7 weeks and weighed 39.2 ± 7.2 kg. The animals were part of other research projects on experimental liver surgery and projects approved for training on surgical skills. All the projects numbers (MSMT-42178/2015-4, MSMT-29543/2015-6, MSMT-32067/2015-5) were approved by the local ethical authorities and by the Faculty Committee for the Prevention of Cruelty

to Animals. All the animals received humane care in compliance with the European Convention on Animal Care at the Experimental Surgery Facility, Biomedical Center, Faculty of Medicine in Pilsen, Charles University. As described previously (Junatas et al., 2017), the animals were premedicated (with atropine, ketamine and azaperone), anaesthetized (with propofol and fentanyl), relaxed (with pancuronium), intubated, and mechanically ventilated. Fluid infusion and volume restoration were provided (Plasmalyte solution and Gelofusine solution; B-Braun AG, Melsungen, Germany). The animals were sacrificed under anesthesia by administration of cardioplegic potassium chloride solution. Immediately after sacrifice, both left and right CCAs were dissected as shown in Fig. 1A. This resulted in 21 left CCAs and 20 right CCAs (i.e., 20 pairs of right and left CCAs plus one additional left CCA, because the preparation of the right side resulted in a damaged sample in one animal). After dissection, the arteries were photographed and then rinsed, perfused, and immersed in 10% neutral buffered formalin solution. For further histological analyses, each CCA was exhaustively cut into a series of 1-cm long segments, which were consecutively numbered in the proximodistal direction (Fig. 1A). As the length of the CCA varied between 8–13 cm, also the number of segments ranged between 8 and 13 (Supplement 1); each of these segments was examined separately using histology.

2.2. Collecting segments of coronary arteries from human cadavers

Vascular segments representing three human coronary arteries were obtained from 21 human cadavers aged 57–78 years (n = 14 females aged 64.8 ± 5.6 years; n = 7 males aged 71.6 ± 6.5 years) dissected during 2017 at the Department of Forensic Medicine, Second Faculty of Medicine, Charles University. The male-to-female ratio was 2:1 as common in patients undergoing CABG. Collection of samples of organs routinely reviewed during a forensic autopsy is permitted according to the Czech law for educational and scientific purposes. The postmortem interval ranged from 9 to 59 h (29.4 ±16.3 h). If there was any apparent autolysis detected during the autopsy, the sample was excluded. The immediate cause of death was not taken into account. Although there were no macroscopically injured coronary arteries, all hearts damaged by trauma were excluded.

From the hearts dissected from the thoracic cavities, segments of coronary arteries were taken according to the sampling scheme shown in Fig. 1B–E. From the human left coronary artery (LCA), samples were taken and labeled from the circumflex branch (A1), from the left marginal branch (A2), from the anterior interventricular branch (B1), and from the diagonal branch (B2). From the human right coronary artery (RCA), samples were taken on the right border of the heart (C1), from the posterior interventricular branch (C2), and from the right posterolateral branch (C3). In most of the deceased individuals, circular samples were cut off perpendicularly to the long axis, but if it was necessary (for operational reasons) to collect the samples after the autopsy, the transversal cuts from longitudinally cut coronary arteries were taken perpendicularly to the longitudinal axis of the artery. The arterial segments were fixed in neutral 10% formaldehyde. Only hearts with typical anatomical arrangements of coronary arteries were examined, while the hearts of several individuals with undeveloped posterolateral branches were omitted.

2.3. Collecting segments of ITA from human cadavers

From every individual from whom the samples of coronary arteries were collected, either the whole left ITA was dissected out with the adjacent part of subclavian artery or a stitch mark was made to unambiguously identify the proximal end of the artery for
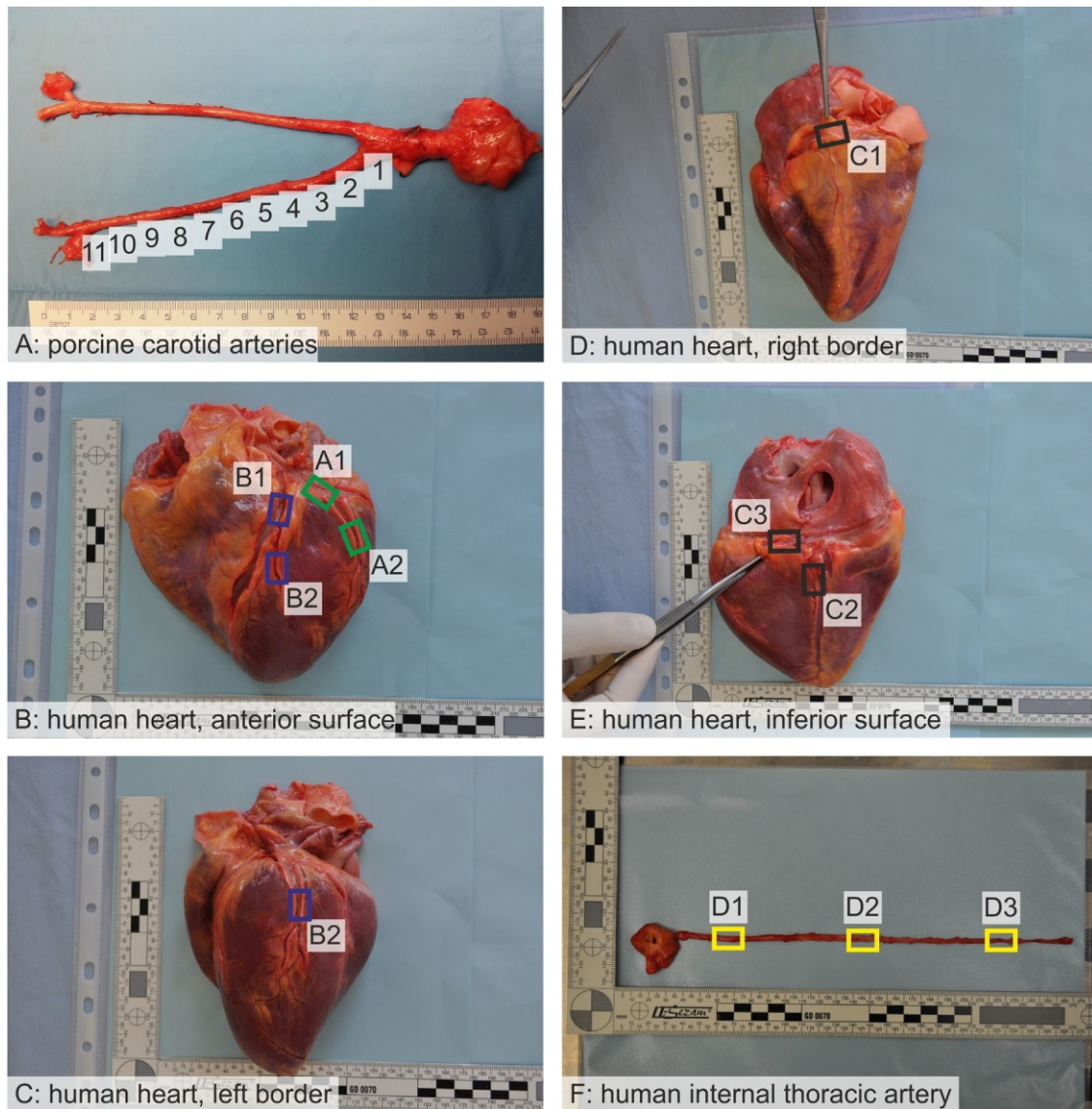
Fig. 1. Position and sampling of the arterial segments under study. (A) Porcine carotid arteries, ventral view. The proximodistal segments were labeled 1–11 (shown in the right carotid artery only). (B) From the human left coronary artery (h-LCA), samples were taken and labeled from the circumflex branch (A1), from the left marginal branch (A2), from the anterior interventricular branch (B1) and from the diagonal branch (B2). (C) The position of the sample taken from the diagonal branch of the anterior interventricular branch is shown from another view as the diagonal branch runs across the left ventricle towards the apex of the heart. (D) From the human right coronary artery (h-RCA), labeled samples (C1) were taken from the right border of the heart. (E) More samples representing the h-RCA came from the posterior interventricular branch (C2) and from the right posterolateral branch (C3). (F) The human left internal thoracic artery was represented by three arterial segments: the middle of the proximal third (D1), middle third (D2), and the distal third (D3).

sampling. Three segments were taken for histological examination (Fig. 1F), representing the proximal third (D1), the middle third (D2), and the distal third (D3) of the artery.

2.4. Histological sectioning and staining

Each arterial segment was and processed in the Leica TP1020 tissue processor (Leica Biosystems GmbH, Nussloch, Germany) and embedded into paraffin. Fourteen serial histological sections per arterial segment were cut (section thickness of 5 μm, Leica RM2255 microtome) perpendicular to the longitudinal axis of each artery. The sections were mounted on histological slides, deparaffinized, and rehydrated. Sections were stained using a set of five staining methods for assessment of overall morphology and wall thickness (hematoxylin-eosin; Verhoeff's hematoxylin and green trichrome), and analysis of main tissue components (orcein stain for elastin; picrosirius red stain for collagen; immunohistochemical detection of a-smooth muscle actin a vascular smooth muscle marker). The number of sections per stain as well as the details on the staining methods, including the manufacturers, are summarized in Table 1. For immunohistochemical detection of actin, the slides were incubated at 4 °C overnight with Monoclonal Mouse Anti-Human Smooth Muscle Actin antibody, Clone 1A4 DakoCytomation (Glostrup, Denmark), using a 1:500 dilution. This reaction was preceded by a heat-induced epitope retrieval process using Epitope Retrieval Solution pH 9 (Novocastra Leica, Leica Biosystems GmbH, Nussloch, Germany) for five minutes. Visualization of the immunohistochemical reaction was based on diaminobenzidine (DAB+, Liquid; DakoCytomation). Immunohistochemical sections were counterstained with Gill's hematoxylin. All sections were dehydrated in graded ethanol solutions and mounted with a xylene-soluble medium.

Table 1
Histological staining methods used in the study.

Staining	Purpose and visualization of aortic wall components	Number of sections stained
Hematoxylin-eosin (Bancroft and Stevens, 1996)	Overall morphology of the arterial wall	4
Verhoeff's hematoxylin and green trichrome (Kochová, 1970)	Overall morphology, differentiating connective tissue, smooth muscle, measurement of the intima-media and wall thicknesses	4
Picrosirius red (Direct Red 80, Sigma Aldrich, Munich, Germany) (Rich and Whittaker, 2005)	Type I and type III collagen when observed under circularly polarized light	2
Orcein (Tanzer's orcein, Bowley Biochemical Inc., Danvers, MA, USA)	Elastic membranes, elastic fibers	2
Immunohistochemical detection of alpha-smooth muscle actin	Vascular smooth muscle cells	2

2.5. Micrographs

For quantification of elastin, collagen, and actin, four micrographs were taken in a systematic, uniform, random manner per staining method using a 40 $\times$ objective mounted on an Olym- pus BX51 microscope (Olympus Optical Co., Ltd., Tokyo, Japan) (Table 2). In this way, representative samples of the intima and media region were further evaluated (Fig. 2A), similar to Tonar et al. (2015). Measurement of the thicknesses was based on two micrographs captured under a 4$\times$ objective, where two opposite micrographs were sufficient to represent the whole arterial profile. As the identical sampling of photographs was performed for each of the 614 vascular segments under study, the total number of micrographs used for quantification exceeded 11,000.

2.6. Morphometry of the arterial wall

The area fractions of elastin, collagen, and actin within the tunica intima and tunica media were assessed using a stereological point grid as implemented in the PointGrid module of the Ellipse software (ViDito, Slovak Republic), cf. Howard and Reed (1998) as described and thoroughly tested in vascular research previously (Witter et al., 2010; Eberlova et al., 2013; Tonar et al., 2015; Kubíková et al., 2017). For each staining method and arterial segment, a set of four images (Fig. 2A) was loaded, and the point grid was randomly superposed on the set of micrographs. The number of points hitting the highlighted tissue component (Fig. 2B–D) was counted semiautomatically. Preliminary counting was performed using the Threshold function of the PointGrid module, and the status of each point (i.e., counted in or not counted in) was then visually checked and manually corrected, if necessary. The point grid method also allowed for individual corrections of the tunica intima and media for microcracks, folds or any other possible artifacts. At least 150 intersections of the point grid per section and method (Tschanz et al., 2014) were always used for estimating the area fractions. The precision of the point grid estimates was tested and calibrated on standardized image data sets generated with the TeiGen software (Jiřík et al., 2018). The area fraction of elastin, collagen, and actin was then calculated for each staining method by dividing the number of points hitting the tissue component of interest by the number of points hitting the reference space. The reference space was the profile area of the tunica intima and media within the image field. The values from the four micrographs per staining method and vascular segment were averaged. The quantification was performed blindly by two operators (P.T. and Z.T.) who had no knowledge on the biological status of the specimens that were labelled by laboratory codes only. Each of the two observers was trained to achieve low intraobserver variability with a mean intraclass correlation coefficient for repeated estimations above 0.92 according to Shrout and Fleiss (1979). The interobserver variability had a mean intraclass correlation coefficient 0.90.

The combined thickness of the intima and media was measured. Using the linear probes of the Fiji software (Schindelin et al., 2012),

the distance between the intimal surface profile and the media-adventitia border profile was measured four times in each sample and then averaged (Fig. 2E). Similarly, the wall thickness was measured as the distance between the intimal surface profile and the outermost layer of the compact connective tissue of the vascular tunica externa. To avoid bias, the outer layer of adjacent loose connective tissue was not considered, as this is known to be greatly affected by anatomical dissection (Kim et al., 2015; Witter et al., 2017).

Additionally, a pilot study of the distribution of collagen within the adventitia was done. It was based on three randomly selected porcine CCAs (n = 30 segments) that were compared to three pairs of randomly selected human coronary arteries (n = 21 segments) and three human ITAs (n = 9 segments).

The complete overview of all the quantitative parameters used in this study for morphometry of the arterial segments is provided in Table 2.

2.7. Assessing the atherosclerotic changes in human coronary arteries

To provide a better characterization of the human coronary arteries and ITAs, any findings of atherosclerotic lesions were classified according to Stary et al. (1994) and Stary (2000). Briefly, this protocol included the following stages: 0 — no atherosclerosis or only adaptive thickening of the intima present; I — initial lesions with isolated macrophage foam cells; II — multiple foam cell layers formed; III — isolated extracellular lipid pools; IV — confluent extracellular lipid core formed; V — fibromuscular tissue layers produced; VI — surface defects, thrombosis; VII — predominant calcification; VIII — predominant fibrous tissue changes. The data will be discussed in the context or regarding more realistic expectations when testing vascular grafts with prospective application to coronary arteries.

2.8. Statistics

In total, 404 segments of porcine CCAs, 147 segments of human coronary arteries, and 63 segments of human ITAs were analyzed. For each vascular segment, the values from each set of micrographs (Table 2) were averaged. As Shapiro–Wilk's test showed aberrations from the normal distribution in some of the variables, nonparametric statistics were applied. The Wilcoxon matched pairs test was used to compare the data on the left vs. right CCA of the same porcine individuals. No comparison was possible between male vs. female pigs, as the female individuals were older and had a higher body weight than the male ones. Kruskal–Wallis ANOVA was used to assess the differences between the porcine CCAs, human coronary arterial segments, and human ITA segments. Correlations among the quantitative variables were evaluated using the Spear- man correlation coefficient. These tests were used as available in the Statistica Base 11 package (StatSoft, Inc., Tulsa, OK, USA). A power analysis according to Chow et al. (2008) was performed to

Table 2

Quantitative parameters used in this study for morphometry of the arterial segments. The magnification of the microscope objective that was used for quantification of each parameter is provided. The number of micrographs that were sampled is shown as well. See also the Section 2. The A_A (collagen, adventitia) was quantified in 30 segments of CCAs and 30 segments of human arteries as a pilot study only.

Quantitative parameter abbreviation and units	Definition, reference area, interpretation and units	Objective used	Micrographs taken
A_A (elastin, int + med) (−)	The area fraction of elastin stained with orcein within the tunica intima and media reference area.	40×	4
A_A (collagen, int + med) (−)	The area fraction of collagen stained with picrosirius red and observed under polarized light within the tunica intima and media reference area.	40×	4
A_A (collagen, adventitia) (−)	The area fraction of collagen stained with picrosirius red and observed under polarized light within the tunica adventitia reference area.	20×	4
A_A (actin, int + med) (−)	The area fraction of a-smooth muscle actin stained immunohistochemically within the tunica intima and media reference area.	40×	4
Int + media thickness (IMT) (μm)	The combined thickness of the intima and media, measured as the mean distance between the intimal surface profile and the media-adventitia border profile.	4×	2
Wall thickness (WT) (μm)	The wall thickness, measured as the mean distance between the intimal surface profile and the outermost layer of the compact connective tissue of the vascular tunica externa.	4×	2

calculate the sample size needed to detect the expected increase or decrease in the fractions of the tunica intima and media in porcine CCAs.

3. Results

3.1. Gross anatomical findings and variations of porcine carotid and adjacent arteries in the present study

The most common branching pattern is shown in Fig. 3A–C. Three out of 21 cases exhibited anatomical asymmetry between the right and left sides. The findings included an aberrant artery branching from the right subclavian artery (Fig. 3D), an aberrant branch (supplying the thyroid gland) originating from the right CCA (Fig. 3E), and doubled right external carotid arteries (Fig. 3F).

3.2. Right side vs. left side and segmental differences in the microscopic structure of porcine CCAs

The complete morphometric data for all the vascular segments under study are provided in Supplement 1. Comparison of paired right vs. left porcine carotids (Supplement 2) revealed no differences in the area fractions of collagen and actin. No differences were found in the intima media thickness, wall thickness, and IMT/WT ratio. The right porcine CCA showed a greater fraction of elastin than the left CCA (Wilcoxon matched pairs p = 0.043). After excluding three animals with gross anatomical variations on the right side from the statistical analysis, there was no difference between the right vs. left side at all.

Comparison along the proximodistal direction revealed considerable differences in the composition of the tunica intima and media among the porcine carotid arterial segments (Fig. 4A). The area fraction of elastin within the media decreased in the proximodistal direction (Kruskal–Wallis ANOVA p < 0.001). At the same time, the area fraction of actin increased in the proxi- modistal direction (p < 0.001). The fraction of collagen remained approximately the same along the whole length. The intima-media thickness (Fig. 4B) showed a decrease in the proximodistal direc- tion (p < 0.001), but the total wall thickness varied and tended to increase in the distal segments (p < 0.001). Thus, the proportion of the intima-media thickness to the total wall thickness decreased in the proximodistal direction (p <0.001).

Table 3 presents descriptive statistics for calculating the min- imum number of samples needed to compare two means when performing a power analysis as part of designing future exper- iments involving porcine carotid arteries. For this purpose, data from the left and right four proximal segments (1-4 cm from the bifurcation), four middle segments (5–8 cm), and four distal seg- ments (9–12 cm) were pooled.

3.3. Differences between porcine CCAs, human coronary arteries and ITAs

An overall comparison shown in Fig. 5 revealed that neither the mean fractions of actin, elastin, and collagen (Fig. 5A) nor the thicknesses of intima + media and the whole wall (Fig. 5B) can be generally considered equivalent between porcine carotids and human coronary or ITAs.

The morphometric findings are also illustrated histologically in Figs. 6–8. While proximal segments of porcine CCAs (Fig. 6A) con- tained repeating elastic lamellae as the prevailing component of the tunica media, its middle segments showed approximately balanced proportions of elastin and smooth muscle (Fig. 6B). Distal segments consisted mostly of vascular smooth muscle cells (Fig. 6C). Elastin decreased in the proximodistal direction, while actin increased (Fig. 8A–C). The fraction of collagen oscillated around approxi- mately the same values (Fig. 8A–C) along the whole CCA. The human coronary arteries (Fig. 7A–B) very often lacked rotational symme- try; they contained very often eccentric atherosclerotic lesions (see Supplement 2 for detailed scoring of atherosclerosis). The amounts of elastin and actin were lower than those in porcine CCAs, often reduced only to fragments of the inner and outer elastic laminae (Fig. 8D–E). Either the positivity for actin was diffusely lost, or there were larger actin-negative foci. The ITA (Fig. 7C) was mostly free of atherosclerosis or showed not only adaptive thickening of the intima but also retained a regular pattern of elastic lamellae and actin positivity (Fig. 8F). The elastin was well preserved, occurring in the form of repeating concentric lamellae that alternated with smooth muscle cells.

A detailed visualization of the morphometric results in all the vascular segments under study is shown in Fig. 9. Porcine CCAs had a tendency towards containing more elastin (Fig. 9A) and actin (Fig. 9C) than the other vascular segments under study. Unlike the case in human arteries, actin and elastin were the dominant con- stituents of the intima and media in porcine CCAs (Fig. 9C–E). The thickness of the intima-media, the wall thickness, and the IMT/WT ratio partially overlapped between porcine CCAs and the human LCA, RCA, and ITA arterial segments under study (Fig. 9F–H). The complete data set with all the morphometric results for all of the samples of all arterial segments is provided in Supplement 3.

3.4. Fraction of collagen within Tunica adventitia

The outcome of the pilot study is shown in Fig. 10 (see Supple- ment 4 for complete primary data) and Supplement 5. The fraction
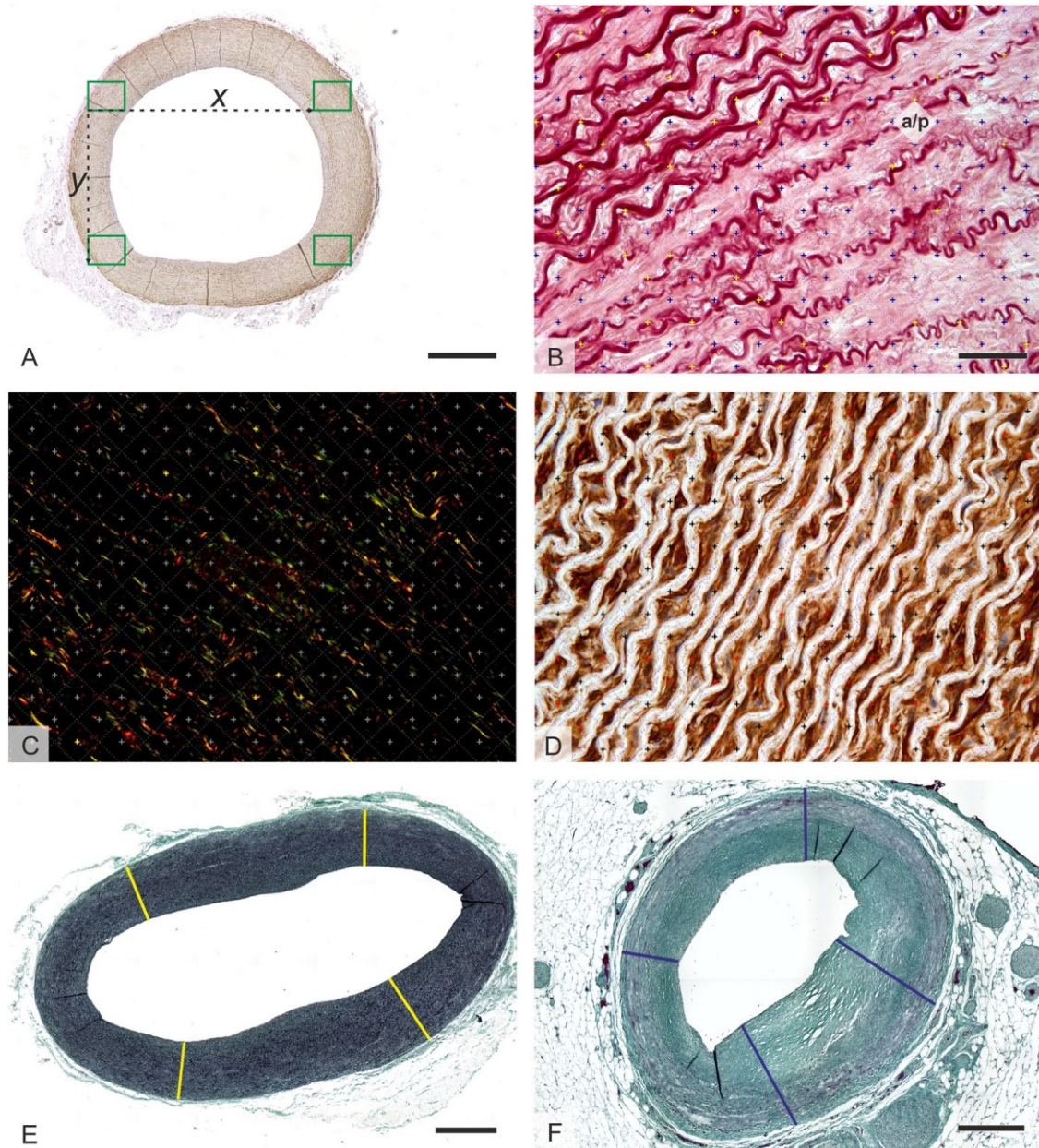
Fig. 2. Histological sampling and quantification of the components and thickness of the arterial segments. (A) Rectangles demonstrate the four micrographs sampled from the reference space of the tunica intima and media for each tissue sample and staining method. The *(x,y)* distances between the micrographs were uniform in a particular section to cover the entire cross-sectional area of the tunica intima and media, including the image fields bordering either the adventitia or the lumen. The size of the uniform sampling step *(x,y)* was modified proportionally to the size of any particular vascular segment. (B) A stereological point grid was projected on the micrographs, and the number of points hitting the elastin (highlighted in yellow) was counted. The area associated statistically with each point is labeled as (a/p). The reference area of the tunica intima and media was quantified using the same point grid. (C) The number of points hitting the collagen (highlighted in yellow) was counted as well. (D) The number of points hitting the elastin (highlighted in red) was counted accordingly. (E) The intima-media thickness was measured as the mean distance between the intimal surface profile and the media-adventitia border profile (four equidistant measurements per image, line probes highlighted in yellow). An example is given in the proximal porcine carotid segment. (F) The wall thickness was measured as the mean distance between the intimal surface profile and the outermost layer of the compact connective tissue of the tunica externa. An example is given in the circumflex branch of the human left coronary artery. Immunohistochemical detection of alpha-smooth muscle actin, visualization horseradish peroxidase/diaminobenzidine, and counterstaining with hematoxylin (A, D) orcein stain (B), picrosirius red stain observed under circularly polarized light (C), Verhoeff's hematoxylin and green trichrome (E, F). Scale bar: 1000 μm (A, E), 50 μm (B–D), and 500 μm (F).

of collagen varied within the range of 0.4–0.7 along the whole length of CCA (mean SD 0.57±0.08). Human coronary arteries (collagen fraction 0.32 0.12) as well as human ITAs (0.33 0.13) had a tendency towards lower fractions and a greater variability of collagen within adventitia than porcine CCA. The areas occupied by larger vasa vasorum were mostly negative in collagen (Supplement 5).

3.5. Correlation between the quantitative histological parameters

In porcine carotids, the amounts of elastin correlated negatively with collagen (Spearman R = 0.156; p < 0.05), actin (R = 0.760), and positively with the intima-media thickness (R = 0.302). In human coronary arteries, elastin correlated positively with actin (R = 0.230), but it was statistically independent of actin or intima-
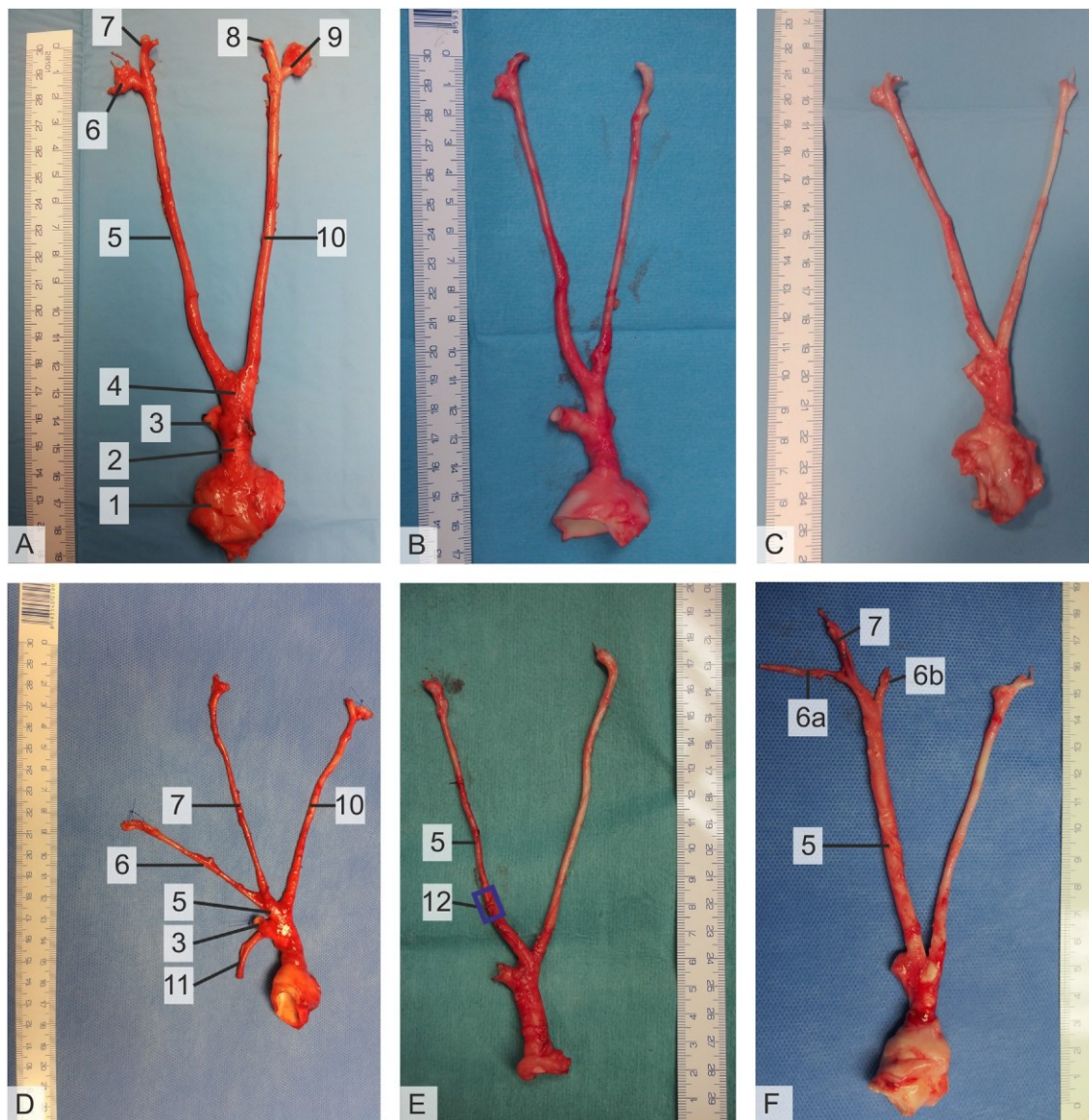
Fig. 3. Gross anatomical findings and variations of porcine common carotid arteries (CCA) and adjacent arteries in the present study. (A) The most common branching pattern, clockwise: aortic arch (1), brachiocephalic trunk (2), right subclavian artery (3), bicarotid trunk (4), right CCA (5), right external carotid artery (6), right internal carotid artery (7), left internal carotid artery (8), left external carotid artery (9), left CCA (10). (B) The same regular branching pattern. (C) The same branching pattern with shorter carotid arteries in a younger individual. (D) Branching pattern with a very short right CCA (5) and a very long right external carotid (6) and right internal carotid (7). Additionally, there was an aberrant artery (11), most likely the residual right aortic arch branching from the right subclavian artery (3). On the left side, the CCA (10) had a regular proportion. (E) An aberrant branch (12, branching site within the blue rectangle) for the thyroid gland originated from the right CCA (5). (F) There were two right external carotid arteries (6a, 6b) branching from the right common carotid (5). One of the right external carotid arteries (6b) originated proximally to the branching of the right internal carotid artery (7).

media thickness. The complete list of correlations for each type of arterial segment is shown in Table 4.

## 4. Discussion

### 4.1. Variations in gross anatomy have to be anticipated and considered during experiments

All gross anatomical variations of the regular branching patterns were found on the right side (three animals out of 21, Fig. 3D–F). In particular, the short right common carotid (Fig. 3D) might bias any evaluation of surgical experiments. When testing vascular grafts, a complete anatomical preparation comparable to our study would probably not be performed. Thus, either the external or the internal carotid arteries might be mistaken for the right common carotid, but there would be significant asymmetry when compared to a

thicker common carotid on the left side. Another variation that might have an implication for using the common carotid as a model organ would be aberrant branches of the common carotid, such as additional branches supplying the thyroid gland (Fig. 3E). The presence of unexpected extra branching sites might bias any consequent histological morphometric analyses.

The sum of the area fractions of elastin, collagen, and actin was considerably greater in the porcine CCAs than in the human coronary arteries and ITAs. This finding was primarily due to the additional tissue components present in arterial segments of human individuals aged 55–80 years, such as lipid-laden foam cells, extracellular lipids, and cholesterol crystals. Another possible explanation that needs to be confirmed in the future is the potentially larger fraction of glycosaminoglycans in human arteries than in CCAs of relatively young pigs.
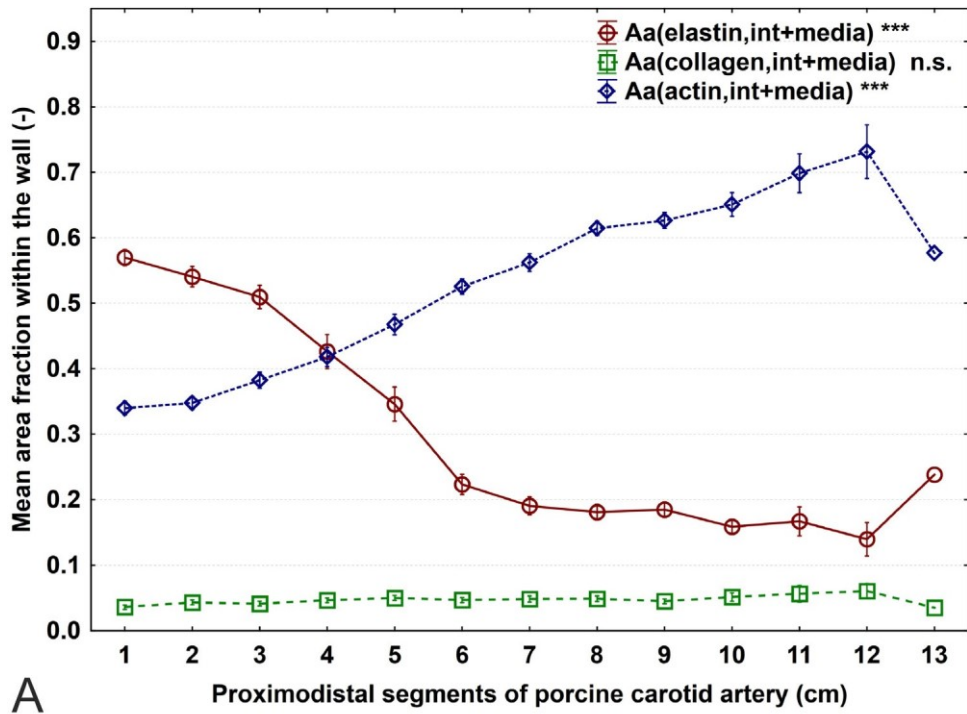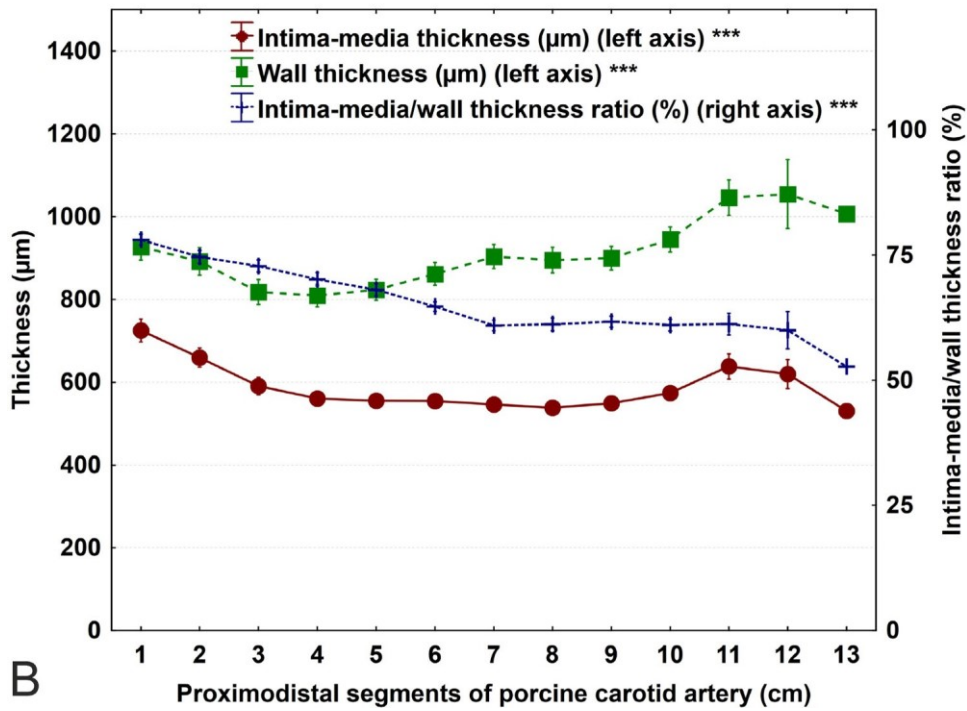
Fig. 4. Comparison among the proximal, middle, and distal segments of the porcine common carotid arteries (CCAs). The *x*-axis shows the proximodistal position of each segment in centimeters. Samples (n = 404) from right and left CCAs (n = 41) from all the animals (n = 21) were pooled in this graph. (A) The area fraction of elastin within the media decreased in the proximodistal direction (Kruskal–Wallis ANOVA p < 0.001). The area fraction of actin increased in the proximodistal direction (p < 0.001). The fraction of collagen remained approximately the same along the whole length. (B) The intima-media thickness, the wall thickness (left *y*-axis), and their mutual ratio (right *y*-axis) changed considerably along the CCAs (p < 0.001 in all three parameters). Data are displayed as the means ± standard error of the means. See Supplement 1 for complete primary data.

4.2. Segmental differences in the porcine CCAs — from elastic to muscular type

Within a range of 2–3 cm, porcine CCAs dramatically changed their phenotype from mostly elastic to mostly muscular (Fig. 4A).

Interestingly, some long blood vessels show a considerable uniformity of their microscopic structure along macroscopically long segments, such as vasa vasorum density (Tonar et al., 2012) or smooth muscle distribution (Kochová et al., 2014) along human saphenous veins. Some blood vessels, such as the aorta, show con-

Table 3

Descriptive statistics for calculating the minimum number of samples needed to compare two means when performing a power analysis as part of designing future experiments involving porcine common carotid arteries (CCAs). For this purpose, data from the left and right four proximal segments (1–4 cm from the bifurcation), four middle segments (5–8 cm), and four distal segments (9–12 cm) were pooled. The means and standard deviations are rounded. The number of arterial segments (n) used for calculation of each part is shown in the first column. AA (component) represents the area fraction of the respective component within the tunica intima and media reference spaces; IMT, the intima-media thickness; and WT, the wall thickness. See Supplement 3 for the complete set of primary data.

Segments of porcine CCAs	Quantitative parameter	Mean	Standard deviation
Proximal segments (1–4 cm) (n = 164 segments)	A_A (elastin) (−)	0.512	0.130
	A_A (collagen) (−)	0.042	0.023
	A_A (actin) (−)	0.372	0.082
	IMT (μm)	634	157
	WT (μm)	862	201
Middle segments (5–8 cm) (n = 164 segments)	A_A (elastin) (−)	0.235	0.131
	A_A (collagen) (−)	0.049	0.027
	A_A (actin) (−)	0.543	0.099
	IMT (μm)	549	104
	WT (μm)	871	182
Distal segments (9–12 cm) (n = 76 segments)	A_A (elastin) (−)	0.172	0.066
	A_A (collagen) (−)	0.049	0.027
	A_A (actin) (−)	0.650	0.086
	IMT (μm)	572	92
	WT (μm)	944	169

Table 4

Spearman rank order correlations between the quantitative parameters.

		A_A (collagen)	A_A (actin)	IMT	WT	IMT/WT ratio
Porcine CCA segments (n = 404)	A_A (elastin)	**−0.156***	**−0.760***	**0.302***	−0.083	**0.623***
	A_A (collagen)	–	0.095	**0.191***	**0.253***	**−0.105***
	A_A (actin)	–	–	**−0.218***	**0.139***	**−0.564***
	IMT	–	–	–	**0.772***	**0.252***
	WT	–	–	–	–	**−0.363***
Human coronary artery segments (n=147)	A_A (elastin)	**0.230***	0.058	−0.029	−0.038	0.080
	A_A (collagen)	–	0.053	**0.322***	**0.318***	**0.232***
	A_A (actin)	–	–	**−0.321***	**−0.331***	−0.063
	IMT	–	–	–	**0.963***	**0.529***
	WT	–	–	–	–	**0.302***
Human ITA segments (n=63)	A_A (elastin)	−0.059	−0.145	**0.300***	**0.255***	0.083
	A_A (collagen)	–	0.162	−0.159	**−0.276***	0.182
	A_A (actin)	–	–	0.114	0.028	0.145
	IMT	–	–	–	**0.912***	0.200
	WT	–	–	–	–	−0.171

The data are shown for each type of arterial segment. A_A(component) represents the area fraction of the respective component within the tunica intima and media reference spaces; IMT, the intima-media thickness; and WT, the wall thickness. All correlations significant at p < 0.05 are marked (*) and typed in **bold** face. The remaining correlations were not statistically significant (p > 0.05). Autocorrelations and repeating values are replaced by the (–) sign. CCA — common carotid artery. ITA — internal thoracic artery.

siderable changes in their histological and mechanical properties (Sokolis, 2007; Sokolis et al., 2008; Tonar et al., 2016). A regional difference in the composition of blood vessels has consequences on their mechanical properties (Avril et al., 2015). García et al. (2011) suggested that this shift from the elastic to muscular phenotype in a short course determines the biomechanical properties of individual arterial segments in the proximodistal direction, which can significantly affect the results of experiments targeting the biomechanics of these arteries. We believe that the data on the segmental variability of elastin, collagen, and actin content provided in the present study might also partially explain the mechanical properties of various segments of porcine CCAs. The contribution of the three components quantified in the present study to the passive mechanics of porcine CCAs has been experimentally estimated by Kochová et al. (2012). Selective destruction of elastin, collagen, and smooth muscle while measuring the deformation of the outer diameter of pressurized porcine CCAs revealed the range of stresses in which these constituents are responsible for maintaining the pressure/diameter ratio. Destruction of elastin resulted in enlargement of the carotid diameter but not stiffening or softening of the wall as elastic fiber integrity is known for maintaining CCA integrity (Ferruzzi et al., 2016). Destruction of collagen led to loss of stiffness of the carotid wall. Eliminating smooth muscle cells led to enlarge-

ment of the diameter at pressures up to 120 mm Hg and mechanical stiffening at higher pressures.

Most of the numerical results in the present study are in good agreement with other publications that applied similar methods and well-documented anatomical sampling of proximodistal position of the CCA samples. Wyatt et al. (2016) reported the CCA wall thickness of 0.86 0.17 mm which matches the 0.87 0.18 mm found in the middle segment in our study (Table 3). The fraction of elastin in the middle segment 26.3 11.5% found by Wyatt et al. (2016) and the values 22 9% published by Kochová et al. (2012) are also very close to our findings (23.5 13.1%). Similarly, the differences in the elastin fraction found in our study between the proximal (51.2 13%) and distal (17.2 7%) CCA segments are in agreement with the values published by García et al. (2011), namely 52.6 6.7% for the proximal segments and 19.6 4.1 for the distal segments. Our results on smooth muscle fraction in proximal CCA (37.2 8.2%) are very close to those found by García et al. (2011) (31.0 3.3%); however, the fraction of smooth muscle in distal CCA was greater in our study (65.0 8.6%) than in the paper by García et al. (2011) (44.3 4.2%). The fraction of elastin within human coronary arteries in our study (Fig. 9A) overlaps with the range reported by Ozolanta et al. (1998) (7.5–10.02%).
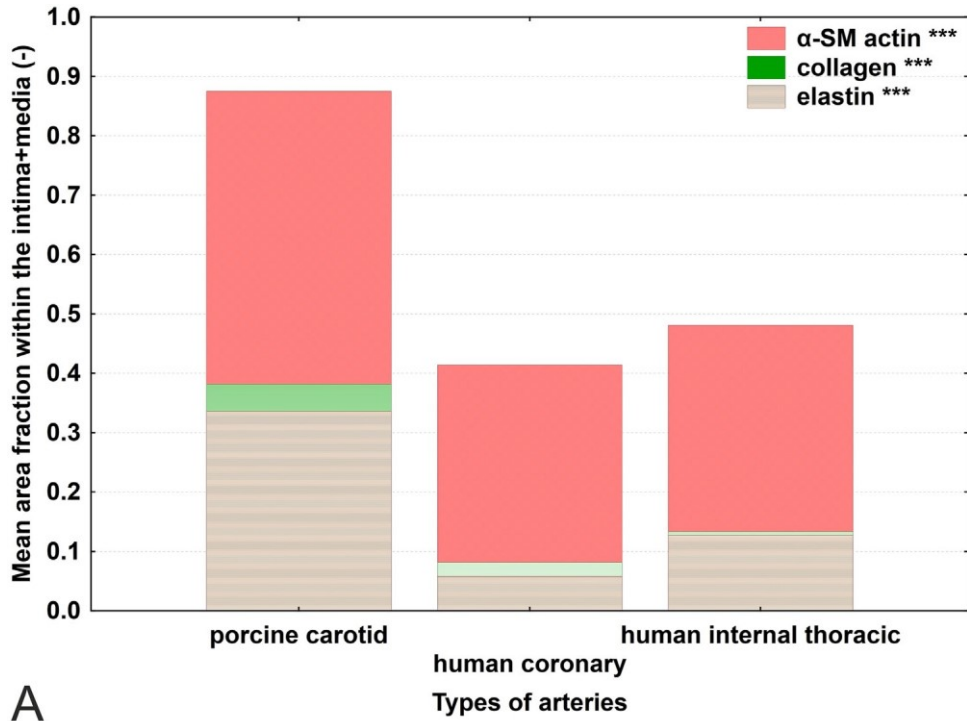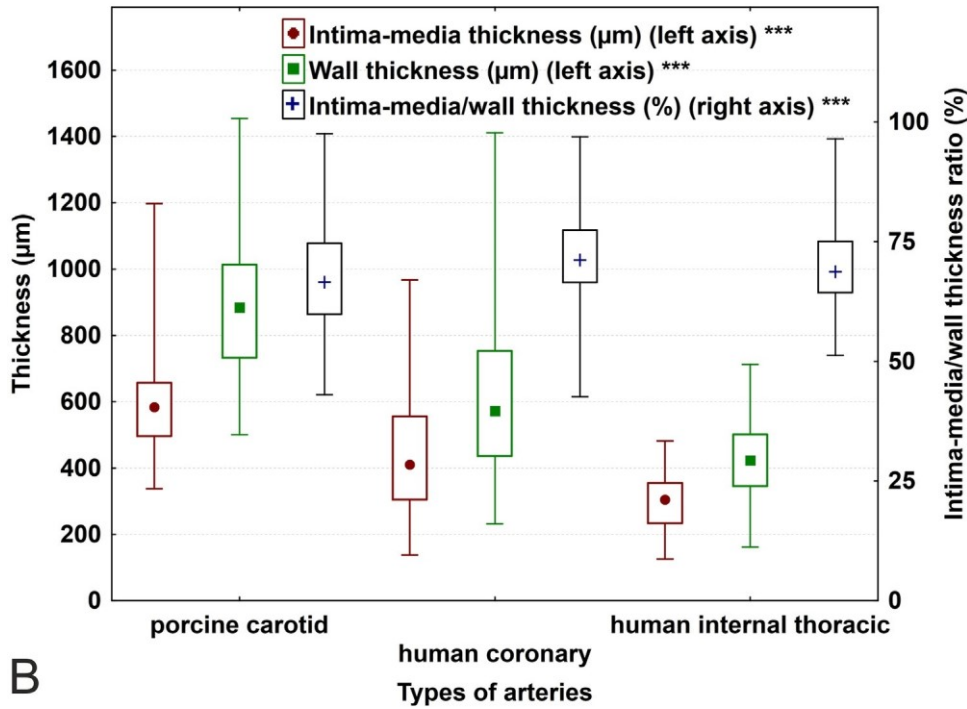
Fig. 5. Overall visualization of fractions of actin, collagen, and elastin within the tunica intima and media of porcine carotid arteries (left), human coronary arteries (middle), and human internal thoracic arteries (right). The segments from all the individuals were pooled for the purpose of this comparison. (A) The mean fractions of neither actin, elastin, nor collagen can be considered equivalent among the three groups of arterial segments (Kruskal–Wallis ANOVA p < 0.001 in all three variables). Data are displayed as cumulations of mean fractions. (B) There were considerable differences in the intima-media thickness, wall thickness, and their ratio when comparing the three groups of arterial segments (p < 0.001). Data are displayed as median values with boxes spanning the upper limits of the first and third quartiles and with whiskers spanning the minimum and maximum values. See Supplement 1 for complete primary data.

4.3. Challenges for manufacturing artificial CABG grafts when proceeding from animal models to human patients

Young porcine animal models are typically used for testing of novel vascular prosthesis as stated in Zilla et al. (2007). In most of studies, 3–6 months old pigs are used (Teebken et al., 2001;

Rotmans et al., 2005; Ueberrueck et al., 2005; Quint et al., 2011; Mrowczynski et al., 2014; Koens et al., 2015; Rothuizen et al., 2016; Dahan et al., 2017). Rather than age, their weight is commonly recorded. Implantation period also varies. The majority of studies are short term with final prosthesis assessment after about one month (Rotmans et al., 2005; Quint et al., 2011; Mrowczynski et al.,
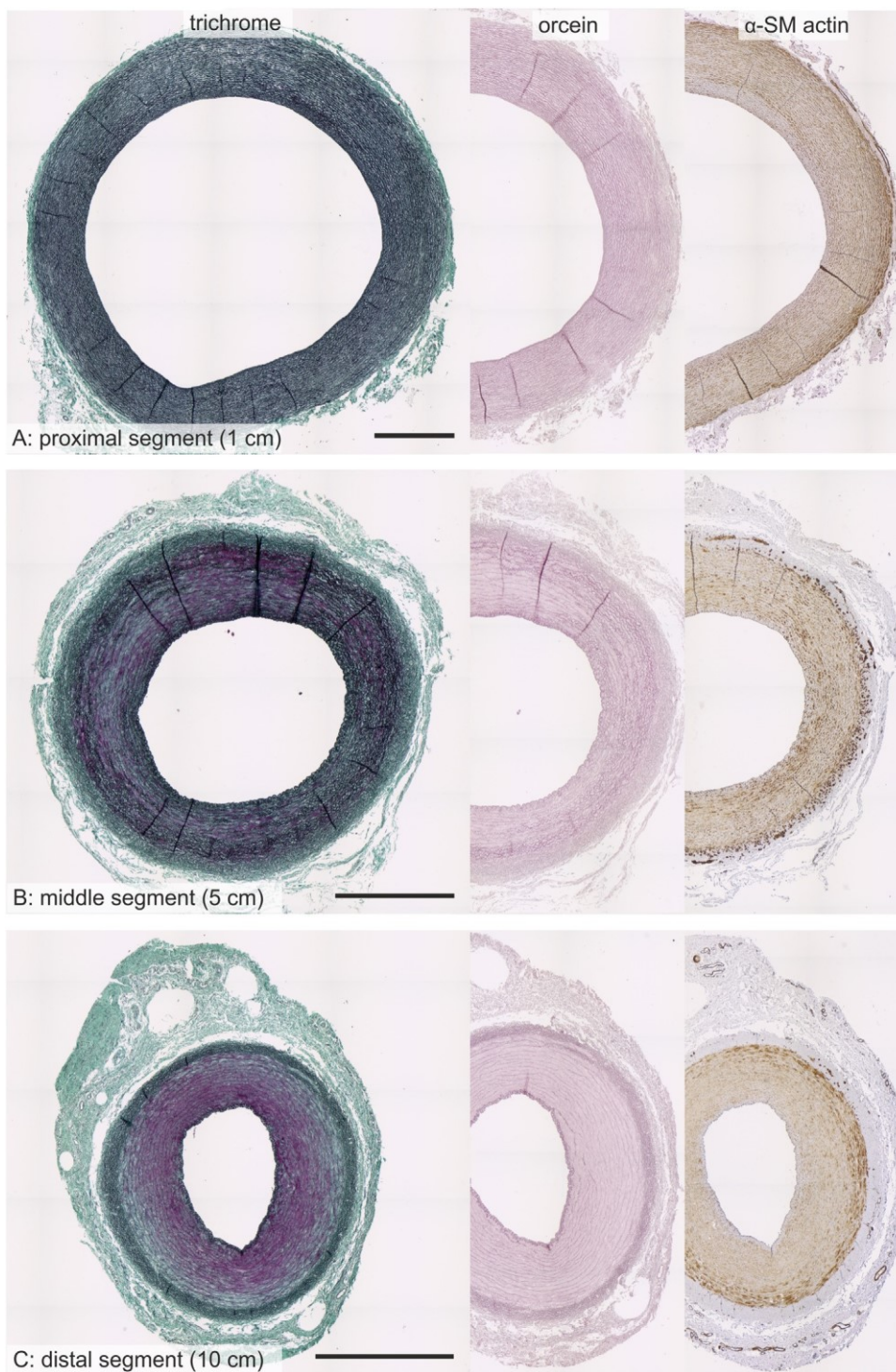
Fig. 6. Comparison of the overall morphology of the proximal, middle, and distal segments of porcine carotid arteries. (A) In proximal segments (1 cm from the bicarotid trunk), repeating elastic lamellae prevailed in the tunica media. (B) In the middle segments (5 cm from the bicarotid trunk), the proportion of elastin and smooth muscle was approximately balanced. (C) In the distal segments (10 cm from the bicarotid trunk), vascular smooth muscle was the prevailing component of the media. Verhoeff's green trichrome (left), orcein stain for elastin (middle), immunohistochemical detection of alpha-smooth muscle actin (right). Scale bar: 1 mm.

2014; Koens et al., 2015; Rothuizen et al., 2016). Long term evaluation was assessed for example for four months (Teebken et al., 2001), or three and six months (Ueberrueck et al., 2005). Interestingly, sex is specified only in some of the cited papers, namely Mrowczynski et al. (2014) used male pigs, whereas Rotmans et al. (2005); Ueberrueck et al. (2005); Koens et al. (2015), and Rothuizen et al. (2016) used female pigs.

Even before the present study, it was obvious that one of the limitations of using porcine CCAs as models for testing vascular grafts intended for human coronary arteries was the discrepancy in age of human patients undergoing CABG vs. relatively low age of animals used as experimental models. The porcine CCAs lacked the histopathological alterations and degenerative changes typical for atherosclerosis common in human patients. The most important challenges to which the bioengineered grafts have to be adapted
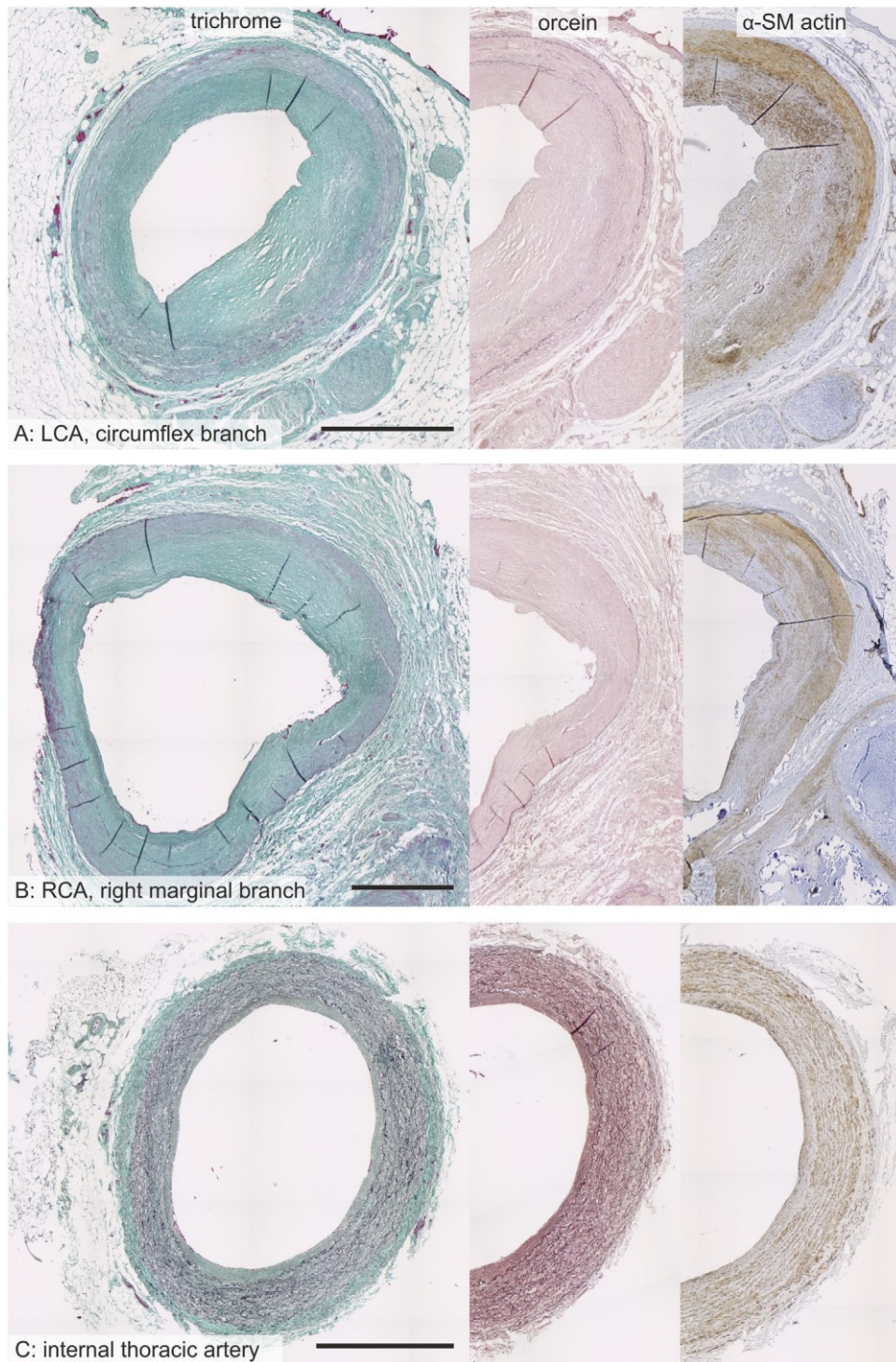
Fig. 7. Examples of the overall morphology of human arteries: arterial segments representing the left coronary artery (LCA), right human coronary artery (RCA), and internal thoracic artery. (A and B**)** The human coronary arteries often lacked rotational symmetry and often contained eccentric atherosclerotic lesions (see Supplement 2 for detailed scoring of atherosclerosis). The amounts of elastin and actin were lower than those in porcine carotid arteries. Either the positivity for actin was diffusely lost, or there were larger actin-negative foci. (C) The internal thoracic artery was mostly free of atherosclerosis or showed only adaptive thickening of intima. The elastin was well preserved, occurring in the form of repeating concentric lamellae that alternated with smooth muscle cells. Verhoeff's green trichrome (left), orcein stain for elastin (middle), immunohistochemical detection of alpha-smooth muscle actin (right). Scale bar: 1 mm.

even after being successfully tested in porcine carotids are the following: (i) lack of rotational symmetry, which cannot be assumed in human coronary arteries; (ii) focal or diffuse loss of elastin and smooth muscle actin; (iii) the presence of atherosclerotic plaques; (iv) additional presence of other substances that do not occur in model animals, such as deposits of lipids or accumulation of

glycosaminoglycans. Additionally, the correlations between the composition and thickness of the arterial wall, which are usually found in healthy arteries (Table 4), are not to be expected in human coronary arteries. However, with the present data mapping the segmental variability, we demonstrated that at least some of the segments of porcine carotids partially overlap with the natural vari-
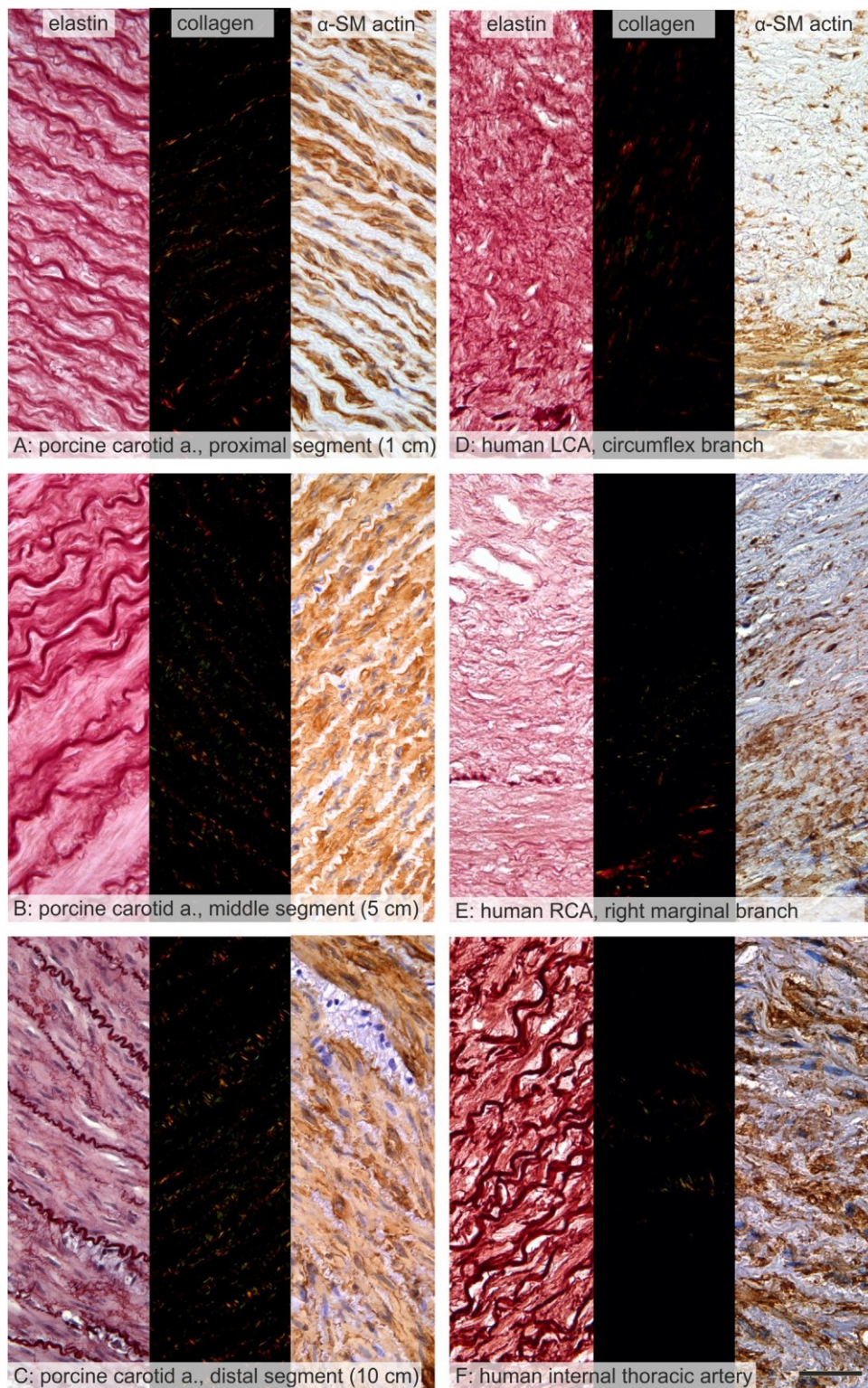
Fig. 8. Elastin, collagen, and actin content in examples of the tunica media of the proximal, middle, and distal segments of porcine carotid arteries (A–C) and in samples of the left human coronary arterial segments (D), right human coronary arterial segments (E), and human internal thoracic arterial segments (F). See Fig. 6 for a detailed quantitative comparison. In carotid arteries (A–C), the arrangement of the tunica media was regular. Elastin (left) decreased in the proximodistal direction, while actin (right) increased. The fraction of collagen (middle) oscillated around approximately the same values. In human coronary arteries (D, E), only fragments of the inner and the outer elastic laminae were found (left), while the internal thoracic arteries showed regular patterns of elastic lamellae (F). Variable areas of the media of the coronary arteries (D, E) contained no smooth muscle (right) but atherosclerotic plaques of various stages (see Supplement 2 for detailed scoring). The internal thoracic artery (F) had a regular pattern of actin positivity. Although the immunohistochemistry provided reliable and unambiguous identification of all the positive areas, it can be noted that porcine CCAs (A–C) that were fixed immediately after harvesting had no background staining at all, while samples of human arteries showed weakly positive counterstaining also in the cytoplasm and extracellular matrix (E–F). Elastin stained with orcein (left); collagen stained with picrosirius red and observed under circularly polarized light (middle); immunohistochemical detection of alpha-smooth muscle actin (right). Scale bar: 30 μm.
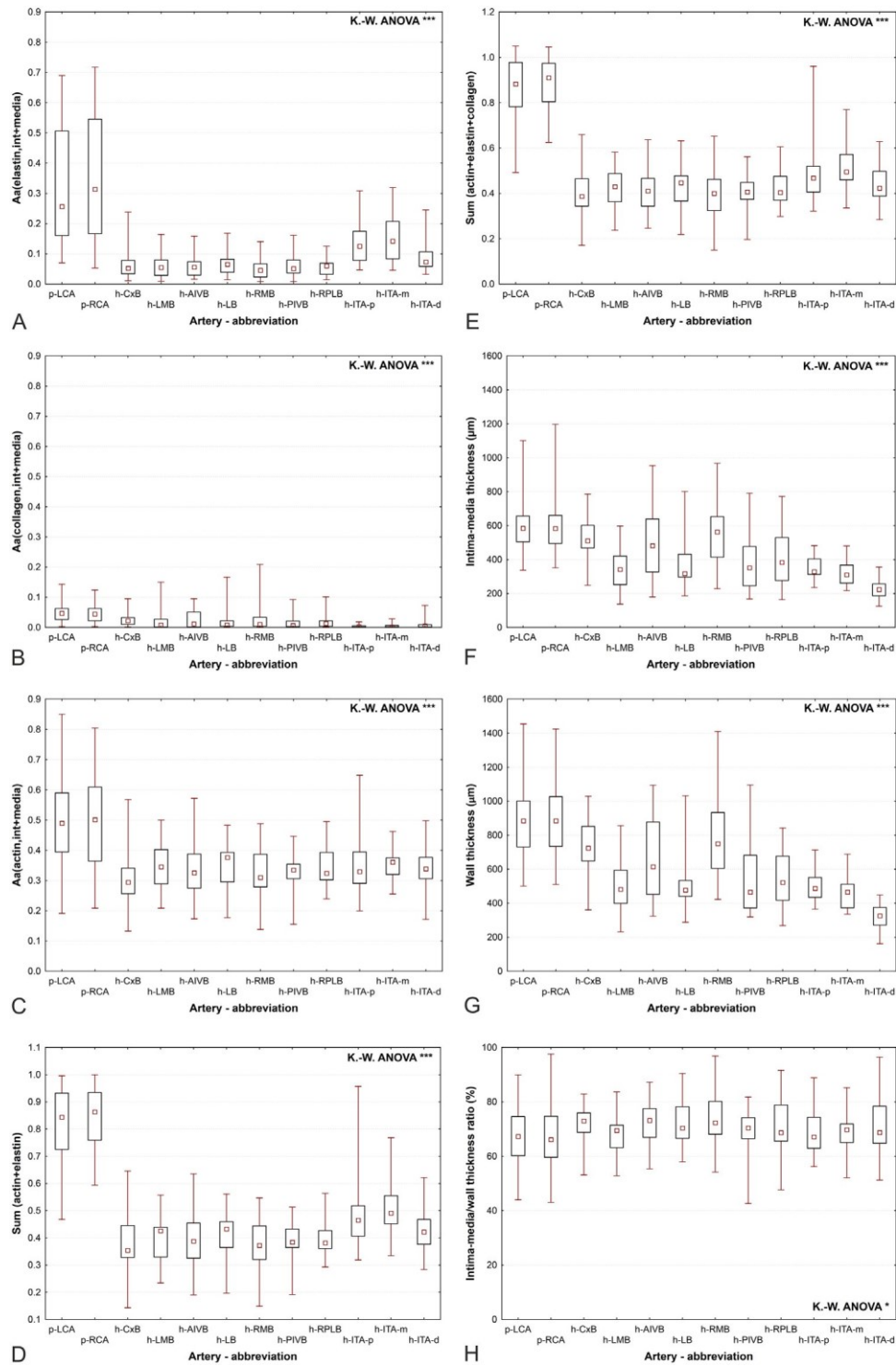
Fig. 9. Detailed visualization of the morphometric results in all the vascular segments under study: Fractions of actin, collagen, and elastin and their sums within the tunica intima and media (A–E); Intima-media thickness (F), wall thickness (G), and their ratio (H). The arterial segments are presented under the following abbreviations: p-LCA — porcine left coronary artery; p-RCA — porcine right carotid artery; h-CxB — (human) circumflex branch; h-LMB – (human) left marginal branch; h-AIVB — (human) anterior interventricular branch; h-LB — (human) lateral branch; h-RCA — (human) right coronary artery; h-RMB — (human) right marginal branch; h-PIVB — (human) posterior interventricular branch; h-RPLB — (human) right posterolateral branch; ITA — (human) internal thoracic artery. Porcine carotid arteries had a tendency towards containing more elastin (A) and actin (C) than the other vascular segments under study. Actin and elastin were the dominant constituents of the intima and media in porcine carotid arteries (C–D), unlike the case in human arteries. The thickness of the intima-media, the wall thickness, and the IMT/WT ratio overlapped between porcine carotid arteries and the remaining arterial segments under study (F–H). Data are displayed as median values with boxes spanning the upper limits of the first and third quartiles and with whiskers spanning the minimum and maximum values. See Supplement 1 for complete primary data. The p-values of the Kruskal–Wallis ANOVA are shown.

ability of human coronary arteries and with the ITA in the fraction of collagen (Fig. 9B), in the intima-media thickness (Fig. 9F), in the wall thickness (Fig. 9H), and in the IMT/WT ratio (Fig. 9H). Despite these limitations, porcine CCAs remain the most widely used and best characterized realistic animal model in studies testing new generations of CABG conduits.
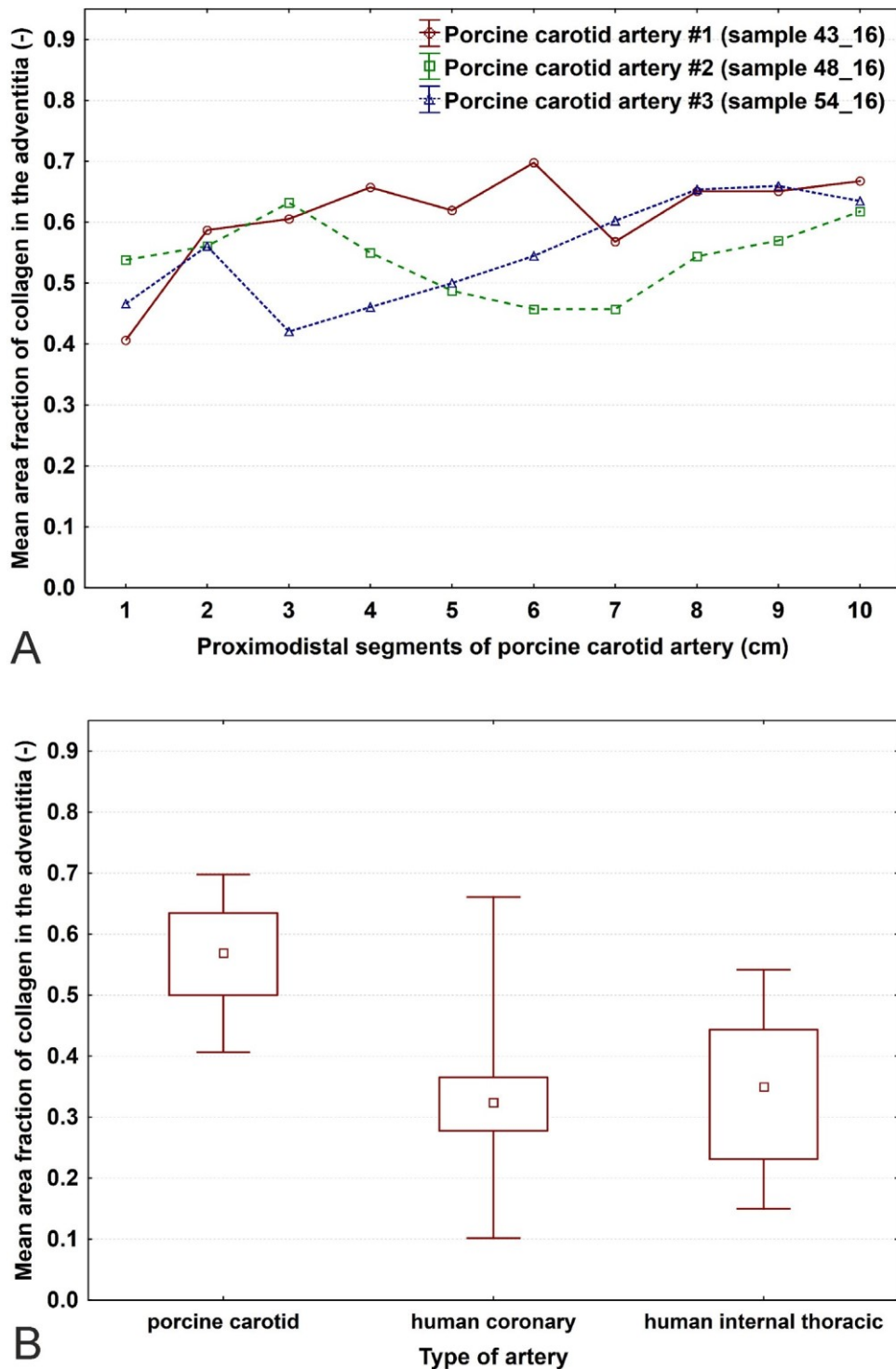
Fig. 10. Visualization of the pilot study on the fraction of collagen within the adventitia based on three randomly selected porcine common carotid arteries (CCAs) (A) and compared to three pairs of randomly selected human coronary arteries and three human internal thoracic arteries (ITAs) (B). (A) Samples (n = 30 segments) from porcine CCAs (n = 3 animals) are displayed. The *x*-axis shows the proximodistal position of each segment in centimeters. The fraction of collagen varied between the range of 0.4–0.7 along the whole length, the mean values $\pm$ SD were 0.61 ± 0.08 (mean $\pm$ SD; artery #1), 0.54 ± 0.06 (artery #2), and 0.55 ± 0.09 (artery #3). (B) Comparison between pooled segments of porcine CCAs (left, n = 30 segments), human coronary arteries (middle, n = 21 segments of LCA, CxB, LMB, AIVB, LB, RCA, RMB, PIVB, and RPLB), and human ITAs (n = 9 segments). There was a tendency towards lower fractions and a greater variability of collagen within the adventitia in human coronary arteries (0.32 ± 0.12) and ITAs (0.33 ± 0.13) than in porcine arteries (0.57 ± 0.08). Data are displayed as median values with boxes spanning the upper limits of the first and third quartiles and with whiskers spanning the minimum and maximum values. See Supplement 4 for complete primary data and Supplement 5 for histological findings.

To reflect the requirements listed above, mimicking the natural layered architecture of blood vessels seems to be a solution for the construction of an ideal vascular graft. For example, bilayered grafts have been manufactured by electrospinning of PCL (de

Valence et al., 2012a,b). In the inner or outer side of the prosthesis, a barrier layer composed of densely packed small diameter fibers can be added. Vascular prostheses with inner barriers may lead to reduced blood leakage and allow cell invasion from the adventi-

tial side (de Valence et al., 2012a,b). Another recent study reported the fabrication of trilayered grafts (Wu et al., 2018) simulating the structure of native blood vessels. The inner layer was composed of axially aligned fibers made from poly(l-lactide-cocaprolactone) and collagen, the middle layer consisted of circumferentially oriented poly(lactide-coglycolide) and silk fibroin yarns, and the outer layer was created by random fibers made from polymers used in the luminal side. Such structures exhibited good mechanical properties and promoted endothelial and smooth muscle cell proliferation in vitro.

Designing artificial vascular grafts requires a basic knowledge of target-tissue anatomical structure. Especially in the case of a tissue engineering approach when mimicking of native morphology is the aim, we believe that even though the data provided in our study possibly do not represent the whole range of findings in patients undergoing CABG, the primary data provided in Supplement 3 might inspire the manufacturing of bioengineered grafts. For example, the data on the intima-media and the total wall thickness are ready to be used for designing multilayered grafts with the benefits described above. Unfortunately, studies mapping the natural variability of various blood vessels of human potential recipients are generally missing and so is their critical comparison with the animal models used for preliminary testing.

4.4. Practical study implications

The histological structure of the left and right porcine CCAs (Supplement 1) might be considered to be equivalent provided that gross anatomical variations of the regular branching patterns are excluded. Therefore, one of these arteries can be used as a healthy or sham-operated control in the same animal. This approach of using the contralateral CCA as a control was already applied e.g. by Kritharis et al. (2012). However, proximal, middle, and distal segments are definitely not mutually interchangeable, and data acquired from either of these segments cannot be extrapolated to the remaining segments, not even in the same animal.

For further studies that involve assessment of elastin, collagen, or smooth muscle actin content and the thickness of the carotid wall, the minimum number of samples per group compared can be calculated from Table 3. For example, when planning an experiment and expecting the mean fraction of actin to be decreased by 20% in the middle carotid segments (i.e., from 0.543 to 0.427), the minimum number of samples required per group would be nine, using the typical test power $\beta = 0.8$ (the type II error) and $\alpha = 0.05$ (type I error) (Chow et al., 2008). Similarly, detecting a 25% increase of the intima-media thickness in proximal segments (i.e., thickening from 634 μm to 792 μm) would require 13 samples. This consideration is important, especially in pigs, as in a large animal model, where experiments are usually planned with a relatively small number of animals. Calculating the expected number of samples to prove a scientific hypothesis is also an ethical issue as it is essential for justifying the sacrifice of the animals — see also the principles of the '3Rs' (replacement, reduction, and refinement; Emerson, 2010). Moreover, the data provided are available for computer modeling and biomechanical phenotyping of regional variations in the structural and mechanical properties of CCA (Bersi et al., 2016; Bellini et al., 2017).

Although the pilot study on collagen in adventitia showed a tendency towards its greater fraction in CCA than in human coronary arteries and ITA (Fig. 10, Supplement 4), it appeared that the quantification was influenced by the size and quantity of larger collagen-negative areas occupied by vasa vasorum and nervi vasorum (see Supplement 5). We suggest that a biologically meaningful assessment of adventitia should contain also quantification of the density and size of vasa vasorum (Tonar et al., 2012) and nervi vasorum (Nedorost et al., 2013). It showed that the analysis of adventitia

would deserve a more complex study that goes far beyond aims and ambitions of the present paper. Moreover, the "no-touch" harvesting technique that preserves most of the adventitia (Dreifaldt et al., 2011) is strongly recommended. This would also make possible to quantify the total content of the wall constituents, including the adventitia.

4.5. Study limitations and remarks on the methods

Although the present study presents, to our knowledge, the largest collection mapping the biological variability of porcine CCA published so far, age groups in both sexes are not represented in a way allowing for testing how these variables are affecting the structure of porcine CCA. The morphometric data come from formalin-fixed paraffin sections. While the fractions of elastin, collagen, and actin are not biased by tissue shrinkage, the data on the intima-media and wall thickness are biased by at least two factors: (i) tissue shrinkage during processing and (ii) postmortem spasm of the arteries. Theoretically, this could be partially avoided using perfusion fixation under mean arterial pressure in the future.

Another limitation appears when looking at the sums of the fractions of elastin, collagen, and actin within the tunica media of the porcine carotids (Fig. 9E) and the primary data in Supplement 3. The summed fractions of the three components exceeded the theoretical maximum value of 1.00 by 0.003–0.049 in 46 out of 614 measurements. This finding suggests that the fraction of some of the components was rather overestimated than underestimated. However, this relative error ranging between 0.3–4.9% probably did not bias the whole study, as none of the conclusions were drawn from the borderline of statistical significance.

The present literature (including our paper) mostly lacks data on glycosaminoglycans as a part of testing vascular grafts. Analyses of glycosaminoglycans seem to be underestimated despite their relevance to manufacturing of decelluarized arterial grafts (Liao et al., 2009), neointimal formation (Tang et al., 2010), promoting of hemocompatibility and endothelization (Lu et al., 2013), or intravascular metabolism of antithrombogenic molecules (Klement et al., 2010). At least the following types of glycosaminoglycans should be analyzed in the future: hyaluronic acid, heparan sulphate, dermatan sulphate, and chondroitin sulphate (Stevens et al., 1976; Malfait, 2018).

5. Conclusion

Segmental differences and the biological variability in the fractions of elastin, collagen, actin, and in the intima-media thickness and wall thickness were mapped histologically in porcine CCAs. Left and right porcine CCAs can be considered equivalent, but the proximal elastic carotid transitions in the range of 2–3 cm to more muscular middle and distal segments, which are not interchangeable. The resulting morphometric data set shows the biological variability of the artery and is made available for biomechanical modeling and for performing a power analysis and calculating the minimum number of samples per group when planning further experiments with this widely used large animal model.

Comparison of porcine carotids with human coronary arteries and one of the preferred arterial autologous conduits for CABG, namely, the ITA, revealed the limitations of using porcine CCAs as a valid model for testing bioengineered small-diameter CABG vascular conduits. Morphometry of human coronary arteries and ITA provided more realistic data for tailoring multilayered artificial vascular prostheses and the ranges of values within which the conduits should be tested in the future. Despite their limitations, porcine CCAs remain a widely used, well-characterized large animal model available for a variety of experiments in vascular surgery.

Ethical statement

The authors of the manuscript entitled "Histological mapping of porcine carotid arteries — an animal model for the assessment of artificial conduits suitable for coronary bypass grafting in humans" by Petr Tomasek, Zbynek Tonar, Tomas Kural, Martina Grajciarova, Daniel Turek, Jana Horakova, Richard Palek, Lada Eberlova, Milena Kralickova, and Vaclav Liska, would like to provide the following ethical statement:

Referring to samples of porcine common carotid arteries

Whole carotid arteries (n = 41) and adjacent arterial branches were obtained from 21 healthy male and female Prestice Black-Pied pigs aged 12–21 weeks and weighing 20–65 kg (35.8± 13.3 kg, mean SD). All the animals were part of other research projects on experimental liver surgery and projects approved for training on surgical skills. All the projects numbers (MSMT-42178/2015- 4, MSMT-29543/2015-6, MSMT-32067/2015-5) were approved by the local ethical authorities and by the Faculty Committee for the Prevention of Cruelty to Animals. All the animals received humane care in compliance with the European Convention on Animal Care at the Experimental Surgery Facility, Biomedical Center, Faculty of Medicine in Pilsen, Charles University.

Referring to samples of coronary and internal thoracic arteries obtained from human cadavers

Vascular segments representing three human coronary arteries were obtained from 21 human cadavers aged 57–78 years (n = 14 females aged 64.8±5.6 years; n = 7 males aged 71.6± 6.5 years) dissected during 2017 at the Department of Forensic Medicine, Second Faculty of Medicine, Charles University. Collection of samples of organs routinely reviewed during a forensic autopsy is permitted according to the Czech law for educational and scientific purposes. We hold the greatest respect for the individuals from whom the samples of coronary arteries and internal thoracic arteries were taken, thus furthering our knowledge of the human body.

Acknowledgments

Appendix A. Supplementary data

Supplementary material related to this article can be found, in the online version, at doi:https://doi.org/10.1016/j.aanat.2019. 151434.

References

Anderson, J.H., Taggart, N.W., Edgerton, S.L., Cantero Peral, S., Holst, K.A., Cetta, F., Wanek Program Preclinical Pipeline, 2018. Ultrasound guided percutaneous common carotid artery access in piglets for intracoronary stem cell infusion. Lab. Anim. 52, 88–92.

Arrigoni, C.h., Camozzi, D., Remuzzi, A., 2006. Vascular tissue engineering. Cell Transplant. 15, S119–S125.

Avril, S., Bersi, M.R., Bellini, C., Genovese, K., Humphrey, J.D., 2015. Regional identification of mechanical properties in arteries. Comput. Methods Biomech. Biomed. Eng. 8 (Suppl. 1), 1874–1875.

Bancroft, J.D., Stevens, A., 1996. Theory and practice of histological techniques. Churchill Livingstone, New York.

Bellini, C., Caulk, A.W., Li, G., Tellides, G., Humphrey, J.D., 2017. Biomechanical phenotyping of the murine aorta: what is the best control? J. Biomech. Eng. 139, 4.

Bersi, M.R., Bellini, C., Di Achille, P., Humphrey, J.D., Genovese, K., Avril, S., 2016. Novel methodology for characterizing regional variations in the material properties of murine aortas. J. Biomech. Eng. 138, 7.

Best, C., Fukunishi, T., Drews, J., Khosravi, R., Hor, K., Mahler, N., Yi, T., Humphrey, J.D., Johnson, J., Breuer, C.K., Hibino, N., 2018. Oversized biodegradable arterial grafts promote enhanced neointimal tissue formation. Tissue Eng. A 24, 1251–1261.

Byrom, M.J., Bannon, P.G., White, G.H., Ng, M.K., 2010. Animal models for the assessment of novel vascular conuits. J. Vasc. Surg. 52, 176–195.

Chlupac, J., Filova, E., Bacakova, L., 2009. Blood vessel replacement: 50 years of development and tissue engineering paradigms in vascular surgery. Physiol. Res. 58, 119–139.

Chow, S.C., Wang, H., Shao, J., 2008. Sample Size Calculations in Clinical Research, second edition. Chapman & Hall/CRC Biostatistics Series, Boca Raton.

Dahan, N., Sarig, U., Bronshtein, T., Baruch, L., Karram, T., Hoffman, A., Machluf, M., 2017. Dynamic autologous reendothelialization of small-caliber arterial extracellular matrix: a preclinical large animal study. Tissue Eng. A 23, 69–79.

de Valence, S., Tille, J.C., Giliberto, J.P., Mrowczynski, W., Gurny, R., Walpoth, B.H., Moller, M., 2012a. Advantages of bilayered vascular grafts for surgical applicability and tissue regeneratinon. Acta Biomater. 8, 3914–3920.

de Valence, S., Tille, J.C., Mugnai, D., Mrowczynski, W., Gurny, R., Moller, M., Walpoth, B.H., 2012b. Long term performance of polycaprolactone vascular grafts in a rat abdominal aorta replacement model. Biomaterials 33, 38–47.

Dondelinger, R.F., Ghysels, M.P., Brisbois, D., Donkers, E., Snaps, F.R., Saunders, J., Deviere, J., 1998. Relevant radiological anatomy of the pig as a training model in interventional radiology. Eur. Radiol. 8, 1254–1273.

Dreifaldt, M., Souza, D.S., Loesch, A., Muddle, J.R., Karlsson, M.G., Filbey, D., Bodin, L., Norgren, L., Dashwood, M.R., 2011. The "no-touch" harvesting technique for vein grafts in coronary artery bypass surgery preserves an intact vasa vasorum. J. Thorac. Cardiovasc. Surg. 141, 145–150.

Eberlova, L., Tonar, Z., Witter, K., Krizkova, V., Nedorost, L., Korabecna, M., Tolinger, P., Kocova, J., Boudova, L., Treska, V., Houdek, K., Molacek, J., Vrzalova, J., Pesta, M., Topolcan, O., Valenta, J., 2013. Asymptomatic abdominal aortic aneurysms show histological signs of progression: a quantitative histochemical analysis. Pathobiology 80, 11–23.

Emerson, M., 2010. Refinement, reduction and replacement approaches to in-vivo cardiovascular research. Br. J. Pharmacol. 161, 749–754.

Ferruzzi, J., Bersi, M.R., Mecham, R.P., Ramirez, F., Yanagisawa, H., Tellides, G., Humphrey, J.D., 2016. Loss of elastic Fiber integrity compromises common carotid artery function: implications for vascular aging. Artery Res. 14, 41–52.

Fong, P.-Y., Chuang, W.-Y., Huang, Y.-Z., Chang, C.-H., 2017. Safety of carotid artery stent in repetitive transcranial magnetic stimulation—the histopathological proof from swine carotid artery. Neurosci. Lett. 657, 194–198.

García, A., Martínez, M.A., Peña, E., 2013. Determination and modeling of the inelasticity over the length of the porcine carotid artery. J. Biomech. Eng. 135, 31004.

García, A., Pena, E., Laborda, A., Lostalé, F., De Gregorio, M.A., Doblaré, M., Martínez, M.A., 2011. Experimental study and constitutive modelling of the passive mechanical properties of the porcine carotid artery and its relation to histological analysis: implications in animal cardiovascular device trials. Med. Eng. Phys. 33, 665–676.

Gaudino, M., Prati, F., Caradonna, E., Trani, C., Schiavoni, G., Glieca, F., Possati, G., 2005. Implantation in the coronary circulation induces morphofunctional transformation of radial grafts from muscular to elastomuscular. Circulation 112 (Suppl. 9), I208–I211.

He, G.W., 2013. Arterial grafts: clinical classification and pharmacological management. Ann. Cardiothorac. Surg. 2, 507–518.

Howard, C.V., Reed, M.G., 1998. Unbiased Stereology. Three-dimensional Measurement in Microscopy. Springer, New York.

Jaramillo, J., Valencia-Rivero, K.T., Cedano-Serrano, F.J., López, R., Sandoval, N., Briceño, J.C., 2018. Design and evaluation of a structural reinforced small intestinal submucosa vascular graft for hemodialysis access in a porcine model. ASAIO J. 64, 270–277.

Jiang, Y., Li, Y., Xu, X., Yu, Y., Liu, W., Liu, X., 2016. An in vitro porcine model evaluating a novel stent retriever for thrombectomy of the common carotid artery. Catheter. Cardiovasc. Interv. Off. J. Soc. Card. Angiogr. Interv. 87, 457–464.

Jiřík, M., Bartoš, M., Tomášek, P., Malečková, A., Kural, T., Horáková, J., Lukáš, D., Suchý, T., Kochová, P., Hubálek Kalbáčová, M., Králíčková, M., Tonar, Z., 2018. Generating standardized image data for testing and calibrating quantification of volumes, surfaces, lengths, and object counts in fibrous and porous materials using X-ray microtomography. Microsc. Res. Tech. 81, 551–568.

Johnson, J., Ohst, D., Hettercheidt, S., Jones, M., 2015. Development of novel, bioresorbable, small-diameter electrospun vascular grafts. J. Tissue Sci. Eng. 6, 1–7.

Junatas, K.L., Tonar, Z., Kubíková, T., Liška, V., Pálek, R., Mik, P., Králíčková, M., Witter, K., 2017. Stereological analysis of size and density of hepatocytes in the porcine liver. J. Anat. 230, 575–588.

Kakisis, J.D., Liapis, C.D., Breuer, C., Sumpio, B.E., 2005. Artificial blood vessel: the Holy Grail of peripheral vascular surgery. J. Vasc. Surg. 41, 349–354.

Kim, E.K., Maldonado, A.A., Jeong, W.S., Hong, J.P., Song, D.H., 2015. Microvascular vessel preparation: what are we really removing during adventitial stripping? J. Plast. Reconstr. Aesthet. Surg. 68, 1568–1573.

Klement, P., Berry, L.R., Liao, P., Wood, H., Tressel, P., Smith, L.J., Haque, N., Weitz, J.I., Hirsh, J., Paredes, N., Chan, A.K., 2010. Antithrombin-heparin covalent complex reduces microemboli during cardiopulmonary bypass in a pig model. Blood 116, 5716–5723.

Kocova, J., 1970. Overall staining of connective tissue and the muscular layer of vessels. Fol. Morphol. 18, 293–295.

Kochová, P., Kuncová, J., Svíglerová, J., Cimrman, R., Miklíková, M., Liška, V., Tonar, Z., 2012. The contribution of vascular smooth muscle, elastin and collagen on the passive mechanics of porcine carotid arteries. Physiol. Meas. 33, 1335–1351.

Kochová, P., Witter, K., Tonar, Z., 2014. Distribution of orientation of smooth muscle bundles does not change along human great and small varicose veins, Ann. Anat. 196, 67–74.

Koens, M.J., Krasznai, A.G., Hanssen, A.E., Hendriks, T., Praster, R., Daamen, W.F., van der Vliet, J.A., van Kuppevelt, T.H., 2015. Vascular replacement using a layered elastin-collagen vascular graft in a porcine model: one week patency versus one month occlusion. Organogenesis 11, 105–121.

Koh, A., Carpenter, A.W., Slomberg, D.L., Schoenfisch, M.H., 2013. Nitric oxide-releasing silica nanoparticle-doped polyurethane electrospun fibers. ACS Appl. Mater. Interfaces 5, 7956–7964.

Kritharis, E.P., Giagini, A.T., Kakisis, J.D., Dimitriou, C.A., Stergiopulos, N., Tsangaris, S., Sokolis, D.P., 2012. Time course of flow-induced adaptation of carotid artery biomechanical properties, structure and zero-stress state in the arteriovenous shunt. Biorheology 49, 65–82.

Kubíková, T., Kochová, P., Brázdil, J., Špatenka, J., Burkert, J., Králíčková, M., Tonar, Z., 2017. The composition and biomechanical properties of human cryopreserved aortas, pulmonary trunks, and aortic and pulmonary cusps. Ann. Anat. 212, 17–26.

Lawson, J.H., Glickman, M.H., Ilzecki, M., Jakimowicz, T., Jaroszynski, A., Peden, E.K., Pilgrim, A.J., Prichard, H.L., Guziewicz, M., Przywara, S., Szmidt, J., Turek, J., Witkiewicz, W., Zapotoczny, N., Zubilewicz, T., Niklason, L.E., 2016. Bioengineered human acellular vessels for dialysis access in patients with end-stage renal disease: two phase 2 single-arm trials. Lancet 387, 2026–2034.

Liao, D., Wang, X., Lin, P.H., Yao, Q., Chen, C.J., 2009. Covalent linkage of heparin provides a stable anti-coagulation surface of decellularized porcine arteries. J. Cell. Mol. Med. 13, 2736–2743.

Lindsey, P., Echeverria, A., Cheung, M., Kfoury, E., Bechara, C.F., Lin, P.H., 2017. Lower extremity bypass using bovine carotid artery graft (artegraft): an analysis of 124 cases with long-term results. World J. Surg. 42, 295–301.

Liu, T., Liu, Y., Chen, Y., Liu, S., Maitz, M.F., Wang, X., Zhang, K., Wang, J., Wang, Y., Chen, J., Huang, N., 2014. Immobilization of heparin/poly-(L)-lysine nanoparticles on dopamine-coated surface to create a heparin density gradient for selective direction of platelet and vascular cells behavior. Acta Biomater. 10, 1940–1954.

Loop, F.D., Lytle, B.W., Cosgrove, D.M., Stewart, R.W., Goormastic, M., Williams, G.W., Golding, L.A., Gill, C.C., Taylor, P.C., Sheldon, W.C., 1986. Influence of the internal mammary-artery graft on 10-year survival and other cardiac events. N. Engl. J. Med. 314, 1–6.

Loskot, P., Tonar, Z., Baxa, J., Valenta, J., 2016. The descending branch of the lateral circumflex femoral artery as an alternative conduit for coronary artery bypass grafting: experience from an anatomical, radiological and histological study. Clin. Anat. 29, 779–788.

Lossi, L., D'Angelo, L., De Girolamo, P., Merighi, A., 2016. Anatomical features for an adequate choice of experimental animal model in biomedicine: II. Small laboratory rodents, rabbit, and pig. Ann. Anat. 204, 11–28.

Lu, S., Zhang, P., Sun, X., Gong, F., Yang, S., Shen, L., Huang, Z., Wang, C., 2013. Synthetic ePTFE grafts coated with an anti-CD133 antibody-functionalized heparin/collagen multilayer with rapid in vivo endothelialization properties. ACS Appl. Mater. Interfaces 5, 7360–7369.

Malfait, F., 2018. Vascular aspects of the ehlers-danlos syndromes. Matrix Biol. 71–72, 380–395.

Martínez-González, B., Reyes-Hernández, C.G., Quiroga-Garza, A., Rodríguez-Rodríguez, V.E., Esparza-Hernández, C.N., Elizondo-Omana, R.E., Guzmán-López, S., 2017. Conduits used in coronary artery bypass grafting: a review of morphological studies. Ann. Thorac. Cardiovasc. Surg. 23, 55–65.

McClure, M.J., Simpson, D.G., Bowlin, G.L., 2012. Tri-layered vascular grafts composed of polycaprolactone, elastin, collagen, and silk: optimization of graft properties. J. Mech. Behav. Biomed. Mater. 10, 48–61.

Menasche, P., Flaus, P., Huc, A., Piwnica, A., 1984. Collagen vascular grafts: a step towards improved compliance in small-calibre bypass surgery; preliminary report. Life Support Syst. 2, 233–237.

Mrowczynski, W., Mugnai, D., de Valence, S., Tille, J.C., Khabiri, E., Cikirikcioglu, M., Möller, M., Walpoth, B.H., 2014. Porcine carotid artery replacement with biodegradable electrospun poly-e-caprolactone vascular prosthesis. J. Vasc. Surg. 59, 210–219.

Naito, Y., Shinoka, T., Duncan, D., Hibino, N., Solomon, D., Cleary, M., Rathore, A., Fein, C., Church, S., Breuer, C., 2011. Vascular tissue engineering: towards the next generation vascular grafts. Adv. Drug Deliv. Rev. 30, 312–323.

Nedorost, L., Uemura, H., Furck, A., Saeed, I., Slavik, Z., Kobr, J., Tonar, Z., 2013. Vascular histopathologic reaction to pulmonary artery banding in an in vivo growing porcine model. Pediatr. Cardiol. 34, 1652–1660.

Negishi, J., Funamoto, S., Kimura, T., Nam, K., Higami, T., et al., 2011. Effect of treatment temperature on collagen structures of the decellularized carotid artery using high hydrostatic pressure. J. Artif. Organs 14, 223–231.

Nikoubashman, O., Heringer, S., Feher, K., Brockmann, M.-A., Sellhaus, B., Dreser, A., Kurtenbach, K., Pjontek, R., Jockenhövel, S., Weis, J., Kießling, F., Gries, T., Wiesmann, M., 2018. Development of a polymer-based biodegradable neurovascular stent prototype: a preliminary in vitro and in vivo study. Macromol. Biosci. 18, e1700292.

Ong, C.S., Zhou, X., Huang, C.Y., Fukunishi, T., Zhang, H., Hibino, N., 2017. Tissue engineered vascular grafts: current state of the field. Expert Rev. Med. Devices 14, 383–392.

Otsuka, F., Yahagi, K., Sakakura, K., Virmani, R., 2013. Why is the mammary artery so special and what protects it from atherosclerosis? Ann. Cardiothorac. Surg. 2, 519–526.

Ozolanta, I., Tetere, G., Purinya, B., Kasyanov, V., 1998. Changes in the mechanical properties, biochemical contents and wall structure of the human coronary arteries with age and sex. Med. Eng. Phys. 20, 523–533.

Pashneh-Tala, S., MacNeil, S., Claeyssens, F., 2016. The tissue-engineered vascular graft — past, present and future. Tissue Eng. B Rev. 22, 68–100.

Popesko, P., 1978. Atlas of Topographical Anatomy of the Domestic Animals, second edition. W.B. Saunders Co., Philadelphia.

Qiu, X., Lee, B.L., Ning, X., Murthy, N., Dong, N., Li, S., 2017. End-point immobilization of heparin on plasma-treated surface of electrospun polycarbonate-urethane vascular graft. Acta Biomater. 51, 138–147.

Quint, C., Kondo, Y., Manson, R.J., Lawson, J.H., Dardik, A., Niklason, L.E., 2011. Decellularized tissue-engineered blood vessel as an arterial conduit. Proc. Natl. Acad. Sci. U.S.A. 108, 9214–9219.

Rich, L., Whittaker, P., 2005. Collagen and Picrosirius Red staining: a polarized light assessment of fibrillar hue and spatial distribution. Braz. J. Morphol. Sci. 22, 97–104.

Rothuizen, T.C., Damanik, F.F.R., Lavrijsen, T., Visser, M.J.T., Hamming, J.F., Lalaj, R.A., Duijs, J.M.G.J., van Zonneveld, A.J., Hoefer, I.E., van Blitterswijk, C.A., Rabelink, T.J., Moroni, L., Rotmans, J.I., 2016. Development and evaluation of in vivo tissue engineered blood vessels in a porcine model. Biomaterials 75, 82–90.

Rotmans, J.I., Heyligers, J.M., Verhagen, H.J., Velema, E., Nagtegaal, M.M., de Kleijn, D.P., de Groot, F.G., Stroes, E.S., Pasterkamp, G., 2005. In vivo cell seeding with anti-CD34 antibodies successfully accelerates endothelialization but stimulates intimal hyperplasia in porcine arteriovenous expanded polytetrafluoroethylene grafts. Circulation 112, 12–18.

Rychter, M., Gaucher, C., Boudier, A., Leroy, P., Lulek, J., 2016. S-Nitrosothiols-NO donors regulating cardiovascular cell proliferation: insight into intracellular pathway alterations. Int. J. Biochem. Cell Biol. 78, 156–161.

Sarkar, S., Sales, K.M., Hamilton, G., Seifalian, A.M., 2007. Addressing thrombogenicity in vascular graft construction. J. Biomed. Mater. Res. B Appl. Biomater. 82, 100–108.

Schindelin, J., Arganda-Carreras, I., Frise, E., Kaynig, V., Longair, M., Pietzsch, T., Preibisch, S., Rueden, C., Saalfeld, S., Schmid, B., Tinevez, J.Y., White, D.J., Hartenstein, V., Eliceiri, K., Tomancak, P., Cardona, A., 2012. Fiji: an open-source platform for biological-image analysis. Nat. Methods 9, 676–682.

Shin, Y.M., Lee, Y.B., Kim, S.J., Kang, J.K., Park, J.C., Jang, W., Shin, H., 2012. Mussel-inspired immobilization of vascular endothelial growth factor (VEGF) for enhanced endothelialization of vascular grafts. Biomacromolecules 13, 2020–2028.

Shrout, P.E., Fleiss, J.L., 1979. Intraclass correlations: uses in assessing rater reliability. Psychol. Bull. 86, 420–428.

Sisto, T., Isola, J., 1989. Incidence of atherosclerosis in the internal mammary artery. Ann. Thorac. Surg. 47, 884–886.

Sokolis, D.P., 2007. Passive mechanical properties and structure of the aorta: segmental analysis. Acta Physiol. (Oxf.) 190, 277–289.

Sokolis, D.P., Boudoulas, H., Karayannacos, P.E., 2008. Segmental differences of aortic function and composition: clinical implications. Hellenic J. Cardiol. 49, 145–154.

Sokolis, D.P., Sassani, S., Kritharis, E.P., Tsangaris, S., 2011. Differential histomechanical response of carotid artery in relation to species and region: mathematical description accounting for elastin and collagen anisotropy. Med. Biol. Eng. Comput. 49, 867–879.

Stary, H.C., 2000. Natural history and histological classification of atherosclerotic lesions: an update. Arter. Thromb. Vasc. Biol. 20, 1177–1178.

Stary, H.C., Chandler, A.B., Glagov, S., Guyton, J.R., Insull Jr., W., Rosenfeld, M.E., Schaffer, S.A., Schwartz, C.J., Wagner, W.D., Wissler, R.W., 1994. A definition of initial, fatty streak, and intermediate lesions of atherosclerosis. A report from the Committee on Vascular Lesions of the Council on Arteriosclerosis, American Heart Association. Circulation 89, 2462–2468.

Stevens, R.L., Colombo, M., Gonzales, J.J., Hollander, W., Schmid, K., 1976. The glycosaminoglycans of the human artery and their changes in atherosclerosis. J. Clin. Invest. 58, 470–481.

Stewart, J.K., Perkins, S.S., Kim, C.Y., 2017. Creation of an extraluminal arterial bypass graft using a commercially available self-expanding stent graft: feasibility study in a porcine model. Cardiovasc. Intervent. Radiol. 40, 1447–1453.

Sun, J., Sun, K., Bai, K., Chen, S., Wang, F., Zhao, F., Hong, N., Hu, H., 2019. A novel braided biodegradable stent for use in congenital heart disease: short-term results in porcine iliac artery. J. Biomed. Mater. Res. A 107, 1667–1677.

Szafron, J.M., Ramachandra, A.B., Breuer, C.K., Marsden, A.L., Humphrey, J.D., 2019. Optimization of tissue-engineered vascular graft design using computational modeling. Tissue Eng. C Methods 25, 561–570.

Tang, X.F., Liu, J.J., Wu, Y.J., Chen, K.M., Jin, Y., Gao, P.J., Zhu, D.L., Shen, G.X., 2010. Effect of hirulog-like peptide on balloon catheter injury-induced neointimal formation in femoral arteries of minipigs and relationship with inflammatory mediators. J. Vasc. Res. 47, 262–269.

Tara, S., Kurobe, H., Rocco, K.A., Maxfield, M.W., Best, C.A., Naito, Y., Breuer, C.K., Shinoka, T., 2014. Well-organized neointima of large-pore poly(L-lactic acid) vascular graft coated with poly (L-lactic-co-c-caprolactone) prevents calcific deposition compared to small-pore electrospun poly(L-lactic acid) graft in a mouse aortic implantation model. Atherosclerosis 237, 684–691.

Teebken, O.E., Pichlmaier, A.M., Haverich, A., 2001. Cell seeded decellularised allogeneic matrix grafts and biodegradable polydioxanone-prostheses compared with arterial autografts in a porcine model. Eur. J. Vasc. Endovasc. Surg. 22, 139–145.

Tonar, Z., Kubíková, T., Prior, C., Demjén, E., Liška, V., Králíčková, M., Witter, K., 2015. Segmental and age differences in the elastin network, collagen, and smooth muscle phenotype in the tunica media of the porcine aorta. Ann. Anat. 201, 79–90.

Tonar, Z., Kural Jr., T., Kochova, P., Nedorost, L., Witter, K., 2012. Vasa vasorum quantification in human varicose great and small saphenous veins. Ann. Anat. 194, 473–481.

Tonar, Z., Tomášek, P., Loskot, P., Janáček, J., Králíčková, M., Witter, K., 2016. Vasa vasorum in the tunica media and tunica adventitia of the porcine aorta. Ann. Anat. 205, 22–36.

Tschanz, S., Schneider, J.P., Knudsen, L., 2014. Design-based stereology: planning, volumetry and sampling are crucial steps for a successful study. Ann. Anat. 196, 3–11.

Tzchori, I., Falah, M., Shteynberg, D., Levin Ashkenazi, D., Loberman, Z., Perry, L., Flugelman, M.Y., 2018. Improved patency of ePTFE grafts as a hemodialysis access site by seeding autologous endothelial cells expressing Fibulin-5 and VEGF. Mol. Ther. 26, 1660–1668.

Ueberrueck, T., Meyer, L., Zippel, R., Nestler, G., Wahlers, T., Gastinger, I., 2005. Healing characteristics of a new silver-coated, gelatine impregnated vascular prosthesis in the porcine model. Zentralbl. Chir. 130, 71–76.

Vrtkova, I., 2015. Genetic admixture analysis in Prestice Black-Pied pigs. Arch. Anim. Breed 58, 115–121.

Wang, K., Zhang, Q., Zhao, L., Pan, Y., Wang, T., Zhi, D., Ma, S., Zhang, P., Zhao, T., Zhang, S., Li, W., Zhu, Y., Zhang, J., Qiao, M., Kong, D., 2017. Functional modification of electrospun poly(c-caprolactone) vascular grafts with the fusion of protein VEGF-HGFI enhanced vascular regeneration. ACS Appl. Mater. Interfaces 9, 11415–11427.

Wang, S.D., Zhang, Y.Z., Yin, G.B., Wang, H.W., Dong, Z.H., 2010. Fabrication of a composite vascular scaffold using electrospinning technology. Mater. Sci. Eng. C Mater. Biol. Appl. 30, 670–676.

Weizsäcker, H.W., Zierler, E., Juch, H., 2014. A simple method for vital staining of elastin in arterial tissue. Biomed. Tech. (Berl.) 59, 367–373.

Wharton, S.B., Cary, N.R.B., Gresham, G.A., 1994. Observations on detailed histology of the internal thoracic artery and their relevance to its comparatively low incidence of atheroma. Clin. Anat. 7, 215–218.

Wise, S.G., Byrom, M.J., Waterhouse, A., Bannon, P.G., Weiss, A.S., 2011. A multi-layered synthetic human elastin/polycaprolactone hybrid vascular grafts with tailored mechanical properties. Acta Biomater. 7, 295–303.

Witter, K., Tonar, Z., Matejka, V.M., Martinca, T., Jonak, M., Rokosny, S., Pirk, J., 2010. Tissue reaction to three different types of tissue glues in an experimental aorta dissection model: a quantitative approach. Histochem. Cell Biol. 133, 241–259.

Witter, K., Tonar, Z., Schöpper, H., 2017. How many layers has the adventitia? Structure of the arterial Tunica externa revisited. Anat. Histol. Embryol. 46, 110–120.

Wu, T., Zhang, J., Wang, Y., Li, D., Sun, B., El-Hamshary, H., Yin, M., Mo, X., 2018. Fabrication and preliminary study of a biomimietic tri-layered graft based on fibers and fiber yarns for vascular tissue engineering. Mater. Sci. Eng. C Mater. Biol. Appl. 82, 121–129.

Wyatt, H.L., Richards, R., Pullin, R., Yang, T.J., Blain, E.J., Evans, S.L., 2016. Variation in electrosurgical vessel seal quality along the length of a porcine carotid artery. Proc. Inst. Mech. Eng. 230, 169–174.

Yazdani, K.S., Otsuka, F., Nakano, M., Ladich, E., Virmani, R., 2013. Pathology of saphenous vein grafts. Interv. Cardiol. Clin. 2, 241–249.

Zhou, Z.-H., Peng, J., Meng, Z.-Y., Chen, L., Huang, J.-L., Huang, H.-Q., Li, L., Zeng, W., Wei, Y., Zhu, C.-H., Chen, K.-N., 2016. Novel A20-gene-eluting stent inhibits carotid artery restenosis in a porcine model. Drug Des. Dev. Ther. 10, 2341–2351.

Zilla, P., Bezuidenhout, D., Human, P., 2007. Prosthetic vascular grafts: wrong models, wrong questions and no healing. Biomaterials 28, 5009–5027.

Seznam příloh

11.3 Příloha III

Grajciarová, M., Turek, D., Malečková, A., Pálek, R., Liška, V., Tomášek, P., Králíčková, M., Tonar, Z. Are ovine and porcine carotid arteries equivalent animal models for experimental cardiac surgery: A quantitative histological comparison. Ann. Anat. 2022 Jun;242:151910. DOI: 10.1016/j.aanat.2022.151910 **IF(JCR2021)=2.698. Q1(Anatomy&Morphology)** https://pubmed.ncbi.nlm.nih.gov/35189268/
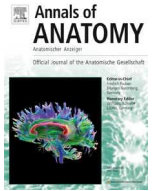
Research Article

Are ovine and porcine carotid arteries equivalent animal models for experimental cardiac surgery: A quantitative histological comparison

Martina Grajciarová [a], Daniel Turek [b,c], Anna Malečková [a], Richard Pálek [d], Václav Liška [d], Petr Tomášek [a,e], Milena Králíčková [a], Zbyněk Tonar [a,*]

[a] Department of Histology and Embryology and Biomedical Center, Faculty of Medicine in Pilsen, Charles University, Karlovarska 48, 301 00 Pilsen, Czech Republic
[b] First Faculty of Medicine, Charles University, Katerinska 32, 121 08 Prague 2, Czech Republic
[c] Department of Cardiac Surgery, Institute for Clinical and Experimental Medicine, Videnska 1958/9, 140 21 Prague, Czech Republic
[d] Department of Surgery and Biomedical Center, Faculty of Medicine in Pilsen, Charles University, Husova 3, 301 00 Pilsen, Czech Republic
[e] Department of Forensic Medicine, Second Faculty of Medicine, Charles University and Na Bulovce Hospital, Budinova 2, 180 81 Prague, Czech Republic

ARTICLE INFO

ABSTRACT

Background: Coronary artery bypass grafting (CABG) is a common cardiac surgery. Manufacturing small-diameter (2–5 mm) vascular grafts for CABG is important for patients who lack first-choice autologous arterial, or venous conduits. Ovine and porcine common carotid arteries (CCAs) are used as large animal models for in vivo testing of newly developed tissue-engineered arterial grafts. It is unknown to what extent these models are interchangeable and whether the left and right arteries of the same subjects can be used as experimental controls. Therefore, we compared the microscopic structure of paired left and right ovine and porcine CCAs in the proximodistal direction and compared these animal model samples to samples of human coronary arteries (CAs) and human internal thoracic arteries (ITAs).

Methods: We compared the histological composition of whole CCAs of sheep (n = 22 animals) with whole porcine CCAs (n = 21), segments of human CAs (n = 21), and human ITAs (n = 21). Using unbiased sampling and stereological methods, we quantified the fractions of elastin, total collagen, type I collagen, type III collagen, smooth muscle actin (SMA) and chondroitin sulfate (CS) A, B, and C. We also quantified the densities and distributions of nuclear profiles, nervi vasorum and vasa vasorum as well as the thickness of the intima-media and total wall thickness.

Results: The differences between the paired samples of left and right CCAs in sheep were substantially greater than the differences in laterality in porcine CCAs. The right ovine CCAs had a smaller fraction of elastin (p < 0.001), greater fraction of SMA (p < 0.01), and greater intima-media thickness (p < 0.001) than the paired left side CCAs. In pigs, the right CCAs had a greater fraction of elastin (p < 0.05) and a greater density of vasa vasorum in the media (p < 0.001) than the left-side CCAs. The fractions of elastin and CS decreased and the fraction of SMA increased in the proximodistal direction in both the ovine (p < 0.001) and porcine (p < 0.001) CCAs. Ovine CCAs had a muscular phenotype along their entire length, but porcine CCAs were elastic-type arteries in the proximal segments but muscular type arteries in middle and distal segments. The CCAs of both animals differed from the human CAs and ITAs in most parameters, but the ovine CCAs had a comparable fraction of elastin and CS to human ITAs.

Conclusions: From a histological point of view, ovine and porcine CCAs were not equivalent in most quantitative parameters to human CAs and ITAs. Left and right ovine CCAs did not have the same histological composition, which is limiting for their mutual equivalence as sham-operated controls in experiments. These differences should be taken into account when designing and interpreting experiments using these models in cardiac surgery. The complete morphometric data obtained by quantitative evaluation of arterial segments were provided to facilitate the power analysis necessary for justification of the minimum number of samples when planning further experiments. The middle or distal segments of ovine and porcine CCAs remain the most realistic and the best characterized large animal models for testing artificial arterial CABG conduits.

© 2022 Elsevier GmbH. All rights reserved.

* Corresponding author.
 *E-mail address:* tonar@lfp.cuni.cz (Z. Tonar).

1. Introduction

1.1. Coronary artery bypass grafting

Coronary artery bypass grafting (CABG) is a common cardiac surgery method used worldwide. Despite the frequent use of this surgical technique, the CABG procedure continues to evolve. One of the first operations of the coronary circulation was the surgery of cardiac anastomoses in a dog in 1910 (Carrel, 1910). In 1951, the left internal thoracic artery (ITA) was successfully implanted in the wall of the left ventricle of the myocardium (Vineberg and Miller, 1951). The first CABG in humans was performed using the tantalum ring method, in which the right ITA was used as an anastomosis (Goetz et al., 1961). The gold standard of CABG is the method that was first used by Green et al. (Green et al., 1968).

Among the most commonly used autologous blood vessel conduits for CAGB are arteries (the left and right ITA, the radial artery, and the less common right gastroepiploic artery) and veins (namely, the great saphenous veins) (Bawany et al., 2014; Desai and Fremes, 2007; Ji et al., 2018; Nicolini et al., 2017; Taggart, 2013). ITAs have better long-term patency and greater resistance to atherosclerosis than saphenous veins (Goldman et al., 2004; Otsuka et al., 2013). Arteries are more resistant to vasoactive substances and contain a higher pressure than veins (He et al., 1988; He, 2013). He et al. divided arterial grafts into three types: type I - somatic arteries (ITA, subscapular artery), type II - splanchnic arteries (gastroepiploic artery, splenic artery), and type III - limb arteries (radial artery, ulnar artery) (He, 2013).

1.2. Sheep and pigs as large animal models

Commonly used large animal models in vascular surgery are sheep and pigs because of their comparable size to humans and similarity of the cardiovascular system (García et al., 2011; Schleimer et al., 2018), reflecting the principles of translational research (Lossi et al., 2016). Ovine and porcine CCAs are paired arteries with relatively easy accessibility for both surgery and sonography. However, their length is a source of considerable variability in their microscopic structure along the proximodistal gradient, as they quickly change from an elastic phenotype in proximal segments to a more distally positioned muscular arterial phenotype (García et al., 2011; Sokolis et al., 2011; Weizsäcker et al., 2014). Ovine and porcine common carotid arteries (CCAs) stem from the bicarotid trunk, which originates in the common brachiocephalic trunk (Popesko, 1978; Rao et al., 2016). The ovine CCA has 7 branches, and the porcine CCA has 5 branches. The CCA consists of the following branches: caudal thyroid artery (pig only on left side, sheep on both sides), nonconstant muscle branches (sternocleidomastoid branches (only in sheep, absent in pigs), pharyngeal branches, laryngeal branches), cranial thyroid artery, cranial laryngeal artery, pharyngeal ascending artery (only in sheep), palatine ascending artery (only in sheep), and internal carotid artery (König and Liebich, 2009; Popesko, 1978). CCAs continue directly as external carotid arteries in both species (Popesko, 1978).
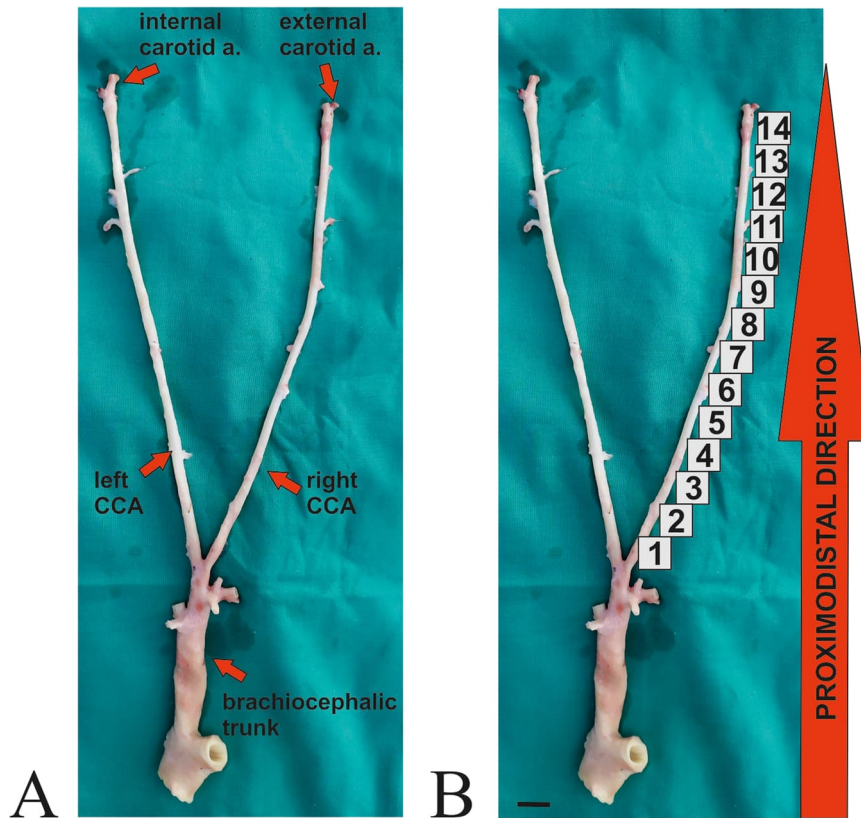
Fig. 1. Sampling of the ovine arterial segments. A – The left and right ovine common carotid arteries (CCAs) were surgically removed from the brachiocephalic trunk to the branching site of the internal and external carotid arteries. B – The CCAs were cut into 1 cm long segments in the proximodistal direction. Scale bar 1 cm (A, B).

Table 1

Histological staining methods. The sections were stained using a combination of six histological staining methods and four immunohistochemical reactions to visualize microscopic structures of the artery wall.

Staining	Purpose
Hematoxylin-eosin (Bancroft, 2008)	Overall morphology
Verhoeff´s hematoxylin and green trichrome (Kocová, 1970)	Overall morphology, connective tissue and smooth muscle
Gill´s hematoxylin	The nuclei of cells
Orcein (Tanzer´s orcein, Bowley Biochemical Inc., Danvers, MA, USA)	Elastin fibers and membranes
Picrosirius red (Rich and Whittaker, 2005; Calderón et al., 2019)	Type I (yellow-red color) and type III collagen (green color) in polarized light
Alcian blue (Mulisch and Welsch, 2015)	Chondroitin sulfate A, B, C
Immunohistochemistry with antibody anti-alpha smooth actin (Clone 1A4, 1:500 dilution, DakoCytomation, Glostrup, Denmark)	Contractile phenotype of vascular smooth muscle
Immunohistochemistry with antibody anti-neurofilament protein (Clone 2F11, 1:500 dilution, DakoCytomation, Glostrup, Denmark)	Nervi vasorum
Immunohistochemistry with antibody anti-CD31 (Clone JC70A, 1:100 dilution, DakoCytomation, Glostrup, Denmark)	Endothelium of the vasa vasorum in human arteries
Immunohistochemistry with antibody anti-von Willebrand factor (1:1000 dilution, DakoCytomation, Glostrup, Denmark)	Endothelium of the vasa vasorum in ovine and porcine arteries

1.3. Testing of small-diameter vascular grafts on ovine and porcine CCAs

The production and testing of bioengineered small-diameter (2–5 mm) vascular grafts is one of the main tasks in experimental vascular surgery that would be beneficial to patients who lack first-choice autologous vascular conduits (Cai et al., 2019). Unfortunately, small-diameter vascular grafts usually lose their function due to intimal hyperplasia and the formation of thrombi (Walpoth et al., 2007), therefore requiring more optimization (Szafron et al., 2019). Newly manufactured bioartificial vascular grafts are often tested on the CCAs of sheep and pigs because of the similar diameter to that of human CAs (Bastijanic et al., 2016; Stewart et al., 2017). Porcine and ovine CCAs were used as animal models for designing various types of intravascular grafts, such as electrospun poly-ε-caprolactone nanofibers (PCL), polytetrafluoroethylene (ePTEE), and CorMartrix (CMX) (Kritharis et al., 2012; Eghbalzadeh et al., 2019; Fallon et al.,
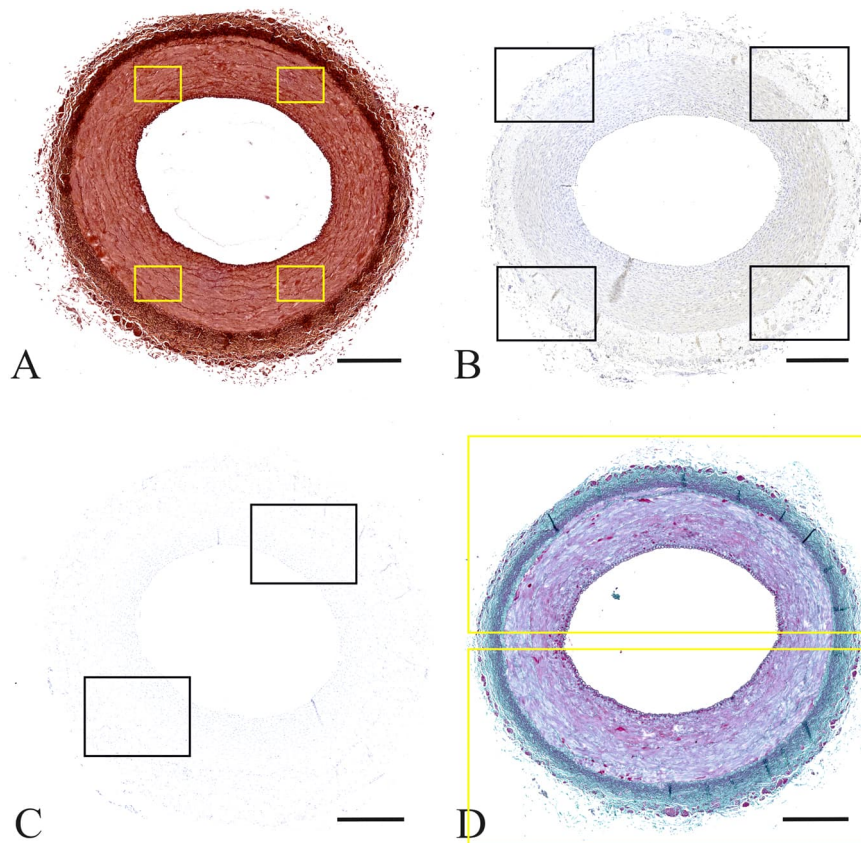
Fig. 2. Uniform sampling of microphotographs, which is demonstrated by rectangles. A – Four microphotographs were used to evaluate the fractions of elastin, type I and type III collagen, smooth muscle actin, chondroitin sulfate and vasa vasorum in the tunica media and tunica adventitia using a 40x objective. **B** – Four microphotographs were used to quantify the density of the nervi vasorum in tunica adventitia using a 20x objective. **C** – Two microphotographs were taken to evaluate the density of nuclear profiles in the tunica media using a 20x objective. **D** – Two microphotographs were taken to evaluate the intima-media thickness and wall thickness using a 4x objective. Scale bars 500 μm (A-D).

Table 2
Quantitative histological parameters. Microphotographs were taken in a systematic, uniform and random manner.

Quantitative parameter (unit)	Biological significance	Objective used	Micrographs taken
A_A (elastin, int+media) (-)	The area fraction of elastin fibers and membranes within the tunica intima and media.	40x	4
A_A (type I collagen, int+media) (-)	The area fraction of type I collagen (yellow-red color) within the tunica intima and media	40x	4
A_A (type III collagen, int+media) (-)	The area fraction of type III collagen (green color) within the tunica intima and media	40x	4
A_A (actin, int+media) (-)	The area fraction of actin within the tunica intima and media	40x	4
A_A (chondroitin sulfate, int+media) (-)	The area fraction of chondroitin sulfate A, B, C within the tunica intima and media	40x	4
Q_A (nuclear profiles, int+media) (mm^{-2})	The quantity of nuclear profiles within the tunica intima and media	20x	2
Q_A (nervi vasorum, int+media) (mm^{-2})	The quantity of nervi profiles within the tunica intima and media	20x	4
Q_A (vasa vasorum, int+media) (mm^{-2})	The quantity of vascular profiles within the tunica intima and media	40x	4
Q_A (vasa vasorum, adventitia) (mm^{-2})	The quantity of vascular profiles within the tunica adventitia	40x	4
Intima-media thickness (IMT) (µm)	The thickness of tunica intima and media	4x	2
Wall thickness (WT) (µm)	The thickness of tunica intima, media and adventitia	4x	2

2012; Fukunishi et al., 2016; Li et al., 2014; Mrówczyński et al., 2014; Stowell et al., 2020; Tzchori et al., 2018; Verbrugghe et al., 2013; Wulff et al., 2017). Synthetic grafts such as ePTEE had good results after implantation to arteries with diameters larger than 6 mm, while usage of smaller diameters always failed, and thrombosis and intimal hyperplasia resulted in occlusion (Walpoth et al., 1998; Zhao and Zhu, 2013). This requires more data for making the size of the grafts more proportional to the native vessels (Best et al., 2018).

1.4. Aims of the study

Recently, we performed extensive mapping of the histological structure of all segments of porcine CCAs (Tomášek et al., 2020) and discussed the benefits and limitations of their use as artificial conduits suitable for coronary bypass grafting in humans. However, we found neither such critical morphological analysis of the ovine CCAs nor their comparison to porcine CCAs or human CAs and the most common type of arterial conduits, such as the ITA. This knowledge gap prevents us from comparing and interpreting results obtained in these two large animal models, as well as from a reasonable planning of further studies on both models that would reflect the biological variability of the vascular segments to navigate the experimental surgical procedures. As recent work on porcine CCAs revealed (Tomášek et al., 2020), respecting the variability of the histological phenotype of proximodistal CCA segments can substantially help researchers obtain more consistent results. The data on interindividual and intraindividual histological variability of animal CCAs can be used to justify the minimum number of samples per group when planning further experiments from both ethical and scientific viewpoints. Obtaining these descriptive data, namely, the means and standard deviations, could eliminate the present methodological gaps and facilitate the design of experiments based on power sample analysis. Another practical output of mapping the interindividual and regional anatomical differences among CCA vascular segments is to provide realistic data for tailoring multilayered artificial vascular prostheses. To bridge this gap in the case of ovine CCAs, the aims of the present study were to test the following null hypotheses:

H_0(A): There are no differences between the paired left and right ovine CCAs, such that these can be used interchangeably as controls during the experiment.

H_0(B): There are no proximodistal segmental differences of ovine CCAs, such that the variable position of the surgical anastomoses during the experiments is not a possible source of bias.

H_0(C): There are no differences among ovine CCAs, porcine CCAs, human CAs, and human ITAs, such that sheep and pigs can be regarded as equivalent large animal models with a good fit to the modeled problem (i.e., CABG in humans).

H_0(D): The histological parameters under study do not correlate with each other.

Additionally, our next aim was to provide descriptive statistics suitable for a power sample analysis for estimating the minimum number of samples necessary for detecting a presumed difference in all the parameters under study.

2. Material and methods

2.1. Collecting ovine carotid arteries

Left and right paired ovine CCAs (n = 44) were collected from Suffolk sheep (n = 22) aged 24–144 weeks and weighing 48.9 ± 11.1 kg (mean ± SD). The female sheep (n = 11) were aged 57.1 ± 51.1 weeks and weighed 45.8 ± 11.7 kg; the male sheep (n = 11) were aged 36.9 ± 18.7 weeks and weighed 52 ± 10 kg. The samples were obtained from animals involved in research projects on testing bioengineered artificial tubular grafts in the arterial system of sheep, and all the relevant projects funded by the Ministry of Health of the Czech Republic (Projects No. MZDR-52084/2018-4/OVZ, and MZDR 40987/2019-4/OVZ) were approved by the local ethical authorities and the Faculty Committee for the Prevention of Cruelty to Animals. All animals received humane care in compliance with the European Convention on Animal Care at the Experimental Medicine Centre of the Institute for Clinical and Experimental Medicine in Prague, Czech Republic. The animals were premedicated (with ketamine and domitor), anesthetized intravenously (with propofol, and midazolam), and intubated. Following myorelaxation with rocuronium, the animals were intubated, mechanically ventilated and anesthetized using inhalation agent (isoflurane). Analgesia was achieved with opioids (Sufentanyl). The animals were euthanized with anesthetics overdose. In all animals, the left and right CCAs were surgically removed from the brachiocephalic trunk to the branching site of the internal and external carotid arteries (Fig. 1A). Immediately after removal, the CCAs were stored in 10% neutral buffered formalin solution. The CCAs were cut into 1-cm long segments in the proximodistal direction (Fig. 1B), which resulted in 11–17 segments with a median value of 14 ± 1.5 segments per artery (see Supplement 1 for the numbering of samples and further details).

2.2. Porcine CCAs

All archived paraffin tissue blocks of porcine CCAs were obtained from a previous study (Tomášek et al., 2020). Briefly, 41 CCAs were
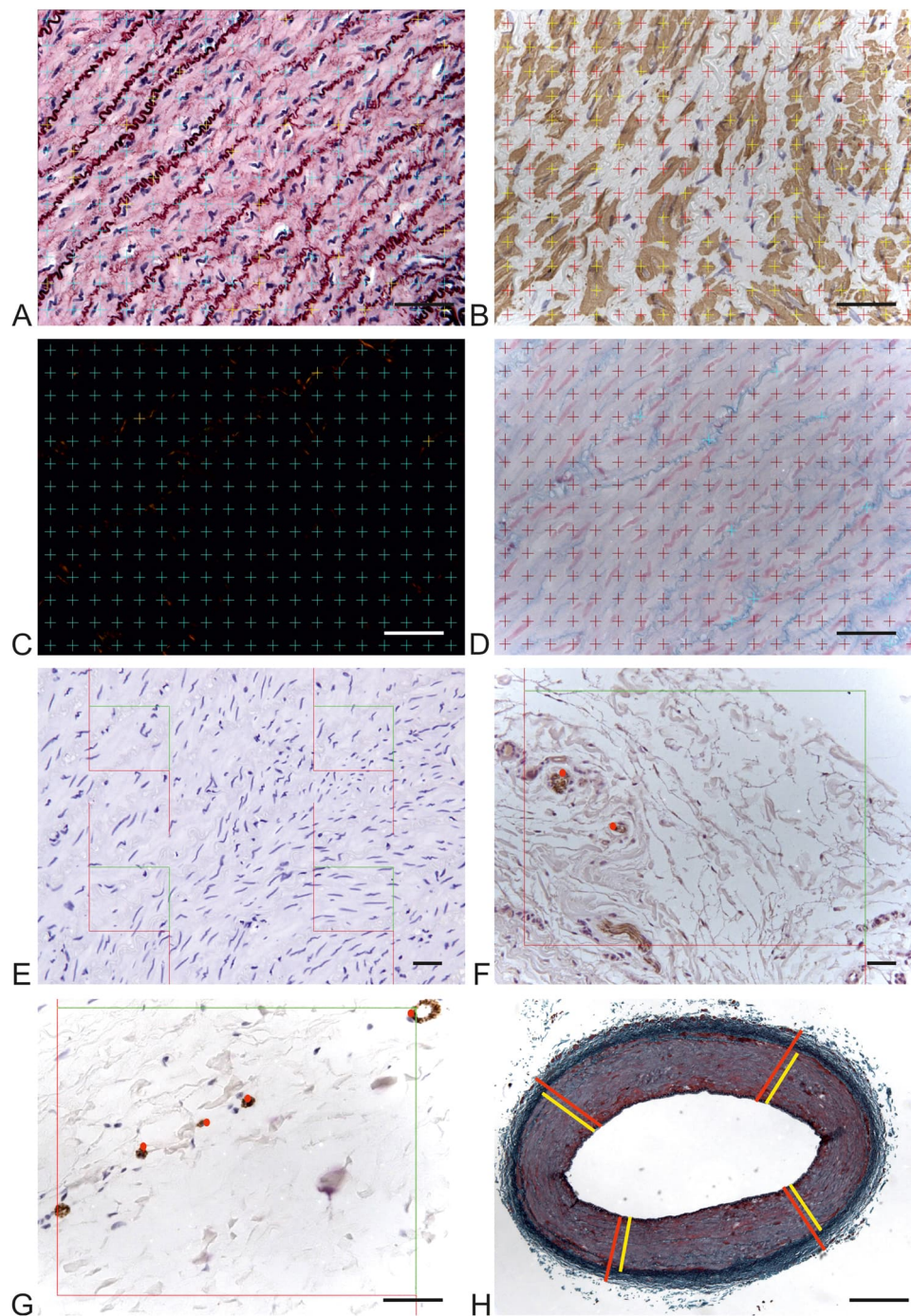
Fig. 3. Quantification of the microscopic structures and thickness of arterial segments. A stereological point grid and the Cavalieri principle were used to evaluate the fractions of elastin (**A**), smooth muscle actin (**B**), collagen (**C**) and chondroitin sulfate (**D**). The unbiased counting frames were used to quantify the density of nuclear profiles (**E**), nervi vasorum (**F**) and vasa vasorum (**F**). Intima-media thickness and wall thickness were quantified as a value of measurements by linear probes (yellow- intima-media thickness; red- wall thickness) (**H**). Scale bars 50 μm (A-G) and 500 μm (H).

collected from 12 female (aged 17.3 ± 3 weeks and weighed 40.7 ± 14.5 kg) and 9 male (aged 14.6 ± 2.7 weeks and weighed 39.2 ± 7.2 kg) Prestice Black-Pied pigs. The animals participated in projects on experimental surgery and training projects for surgical skills (MSMT-42178/2015–4, MSMT-29543/2015–6, MSMT-32067/2015–5). The total number of 1-cm long segments from one CCA ranged between 8 and 13, with a median value of 10 ± 1.2 per artery (Supplement 1).

Table 3
Left vs. right differences in common carotid arteries (CCAs). The left ovine CCAs had a greater fraction of elastin than the right CCAs (Wilcoxon matched pairs test p < 0.001). In contrast, the right ovine CCAs had a greater fraction of smooth muscle actin (p < 0.01) and greater intima-media thickness (p < 0.001). The right porcine CCAs had a higher fraction of elastin (p < 0.05) and density of the vasa vasorum in the media (p < 0.001) than the left CCAs. Data are displayed as the means and standard deviations (SD). The p values of the Wilcoxon matched pairs tests are shown * for p < 0.05, ** for p < 0.01, *** for p < 0.001, not statistically significant (n.s.) for p > 0.05.

Quantitative parameter (unit)	Ovine CCAs		Porcine CCAs	
	Left (mean ± SD)	Right (mean ± SD)	Left (mean ± SD)	Right (mean ± SD)
A_A (elastin, int+media) (-)	greater (***) 0.15 ± 0.11	smaller (***) 0.13 ± 0.11	smaller (*) 0.30 ± 0.16	greater (*) 0.33 ± 0.17
A_A (type I collagen, int+media) (-)	n.s. 0.01 ± 0.01	n.s. 0.01 ± 0.01	n.s. 0.05 ± 0.03	n.s. 0.05 ± 0.03
A_A (type III collagen, int+media) (-)	n.s. 0.0002 ± 0.0006	n.s. 0.0002 ± 0.0004	n.s. 0.003 ± 0.004	n.s. 0.003 ± 0.004
A_A (actin, int+media) (-)	smaller (**) 0.575 ± 0.11	greater (**) 0.583 ± 0.11	n.s. 0.40 ± 0.11	n.s. 0.39 ± 0.12
A_A (chondroitin sulfate, int+media) (-)	n.s. 0.10 ± 0.03	n.s. 0.10 ± 0.03	n.s. 0.09 ± 0.04	n.s. 0.09 ± 0.04
Q_A (nuclear profiles, int+media) (mm²)	n.s. 1448 ± 253	n.s. 1473 ± 256	n.s. 2448 ± 369	n.s. 2403 ± 366
Q_A (nervi vasorum, int+media) (mm²)	n.s. 8.09 ± 5.02	n.s. 8.08 ± 5.07	n.s. 3.96 ± 3.71	n.s. 3.78 ± 3.45
Q_A (vasa vasorum, int+media) (mm²)	n.s. 0.52 ± 2.36	n.s. 0.49 ± 1.74	smaller (***) 0.99 ± 3.09	greater (***) 2.61 ± 7.13
Q_A (vasa vasorum, adventitia) (mm²)	n.s. 45.76 ± 21.40	n.s. 45.05 ± 20.76	n.s. 64.73 ± 29.60	n.s. 66.56 ± 26.49
Intima-media thickness (IMT) (μm)	thinner (***) 604 ± 154	thicker (***) 623 ± 167	n.s. 607 ± 116	n.s. 618 ± 136
Wall thickness (WT) (μm)	n.s. 875 ± 180	n.s. 890 ± 196	n.s. 907 ± 172	n.s. 926 ± 184

2.3. Segments of human CAs and ITAs

Human CAs and ITAs were obtained in the form of paraffin-embedded archive tissue blocks from a previous study (Tomášek et al., 2020). Briefly, 7 female cadavers (aged 64.8 ± 5.6 years) and 14 male cadavers (aged 71.6 ± 6.5 years) were dissected at the Department of Forensic Medicine, Second Faculty of Medicine, Charles University. Coronary arteries were dissected, specifically the left coronary artery (samples were taken from the circumflex branch (A1), left marginal branch (A2), anterior interventricular branch (B1) and diagonal branch (B2)) and the right coronary artery (samples were taken from the right border of the heart (C1), the posterior interventricular branch (C2) and the right posterolateral branch (C3)). Three segments were obtained from the left ITAs (the proximal third (D1), the middle third (D2) and the distal third (D3) of the ITA).

2.4. Histological processing and microphotographs

All ovine, porcine, and human arterial samples were processed in a uniform way as follows: Samples were fixed in 10% formalin solution, dehydrated in ethanol, embedded in paraffin blocks and cut into 5 μm-thick sections (Leica RM2255 microtome). The sections were deparaffinized, dehydrated and stained using a combination of six histological staining methods and four immunohistochemical reactions to visualize microscopic structures of the artery wall. The methods and their purpose in the present study are listed in Table 1. Microphotographs were taken based on systematic uniform sampling of the arterial wall (Fig. 2), as summarized in Table 2, and more deeply explained previously by Kolinko et al. (2022). Sampling was used for each of the 1235 vascular segments under study, and the total number of microphotographs was 30,924.

2.5. Stereological quantification

The fractions of elastin, type I and type III collagen, SMA and CS were evaluated using a stereological point grid and the Cavalieri principle (Fig. 3A-D) (Howard and Reed, 2004) as previously described in vascular research (Witter et al., 2010; Eberlova et al., 2013; Tonar et al., 2015). These fractions were calculated as the ratio of structures of interest and reference area. The ratio between the most common types of arterial collagen, i.e., the type III to type I ratio, was assessed. The results of fractions of elastin and SMA in porcine CCAs from the

previous study were assessed again to precisely correct their overestimation. The overestimation (approximately 3% for elastin, 10% for SMA) in the results previously published on porcine CCAs (Tomášek et al., 2020) became obvious after adding CS staining to the present study. At least 150 intersections of the point grid with the structure of interest were used, as recommended by Tschanz et al. (2014). In a preliminary study, the precision of the point grid estimates was tested and calibrated using TeiGen software (Jiřík et al., 2018). The two densities of the nuclear profiles in the media and nervi vasorum and vasa vasorum in the media and adventitia were estimated using the unbiased counting frame (Fig. 3E-G) (Gundersen, 1977). The intima-media thickness and wall thickness were quantified as a value of eight measurements from linear probes (Fig. 3H). As the outer layer of adventitial loose connective tissue is known to be affected by anatomical preparation (Witter et al., 2017), we considered only the dense connective tissue of the adventitia for the purpose of these measurements. All stereological counting and measurement procedures were performed using Ellipse software (ViDito, Košice, Slovak republic). The operator (M.G.) was blinded to the biological status of the specimens, which were labeled by numeric codes only.

2.6. Statistics

Statistical analysis was performed for ovine CCAs (621 segments), porcine CCAs (404 segments), human CAs (147 segments), and human ITAs (63 segments) using the software Statistica Base 11 package (StatSoft, Inc., Tulsa, OK, USA). Some data did not pass the Shapiro–Wilk test for normality; thus, nonparametric methods were used. The left and right CCAs were compared using the Wilcoxon matched pairs test, testing the $H_0(A)$ hypothesis. The Kruskal–Wallis ANOVA test was used to compare ovine and porcine CCAs in proximodistal segments when testing the $H_0(B)$ hypothesis and to analyze the differences among ovine CCAs, porcine CCAs, human CAs and human ITAs when testing the $H_0(C)$ hypothesis. The Mann–Whitney U test was used to compare ovine CCAs with porcine CCAs in the proximal, middle and distal segments. The Spearman correlation coefficient was used for analysis of the correlation $H_0(D)$ hypothesis. According to Chow et al. (2008), power analysis was used to calculate the sample size needed to detect the expected change in fractions and densities in the ovine and porcine CCAs.
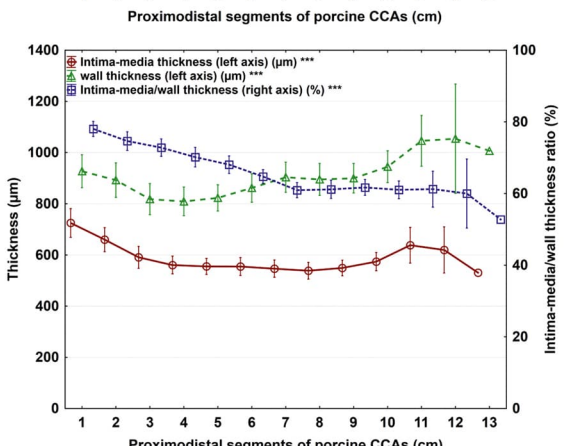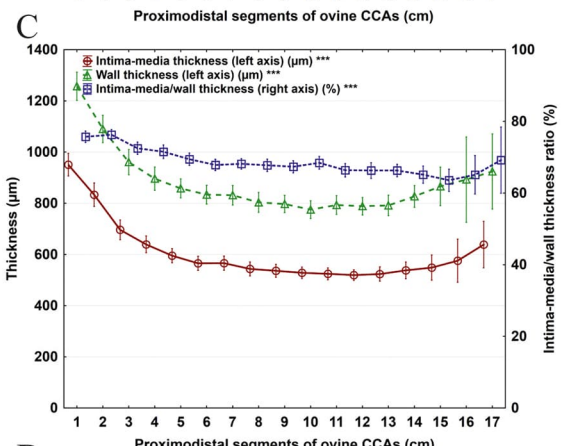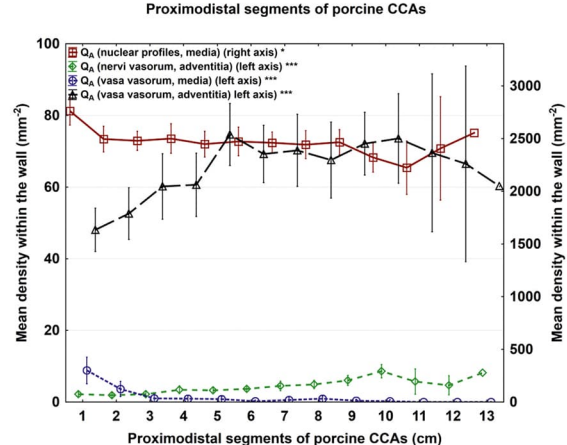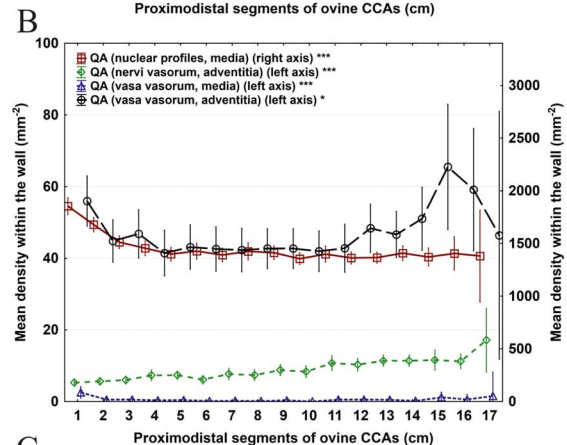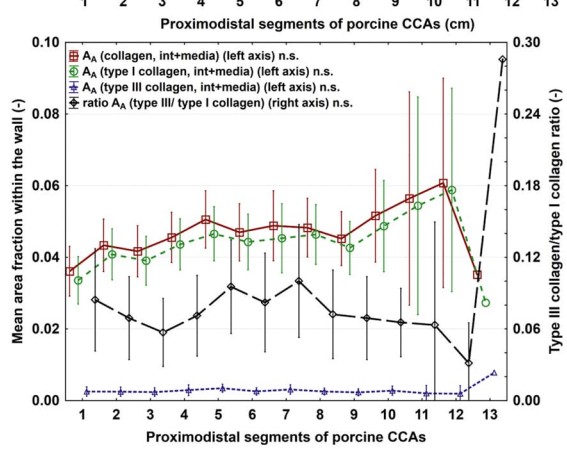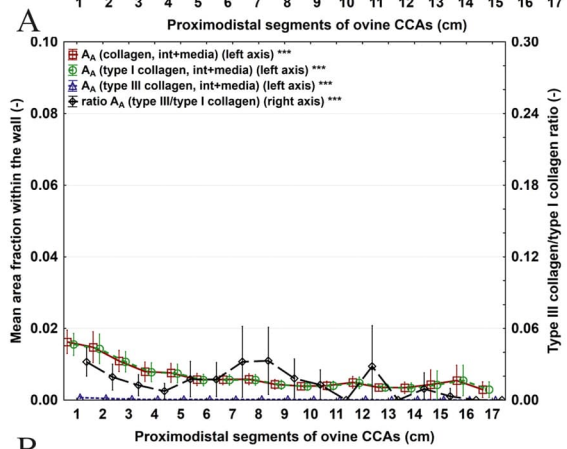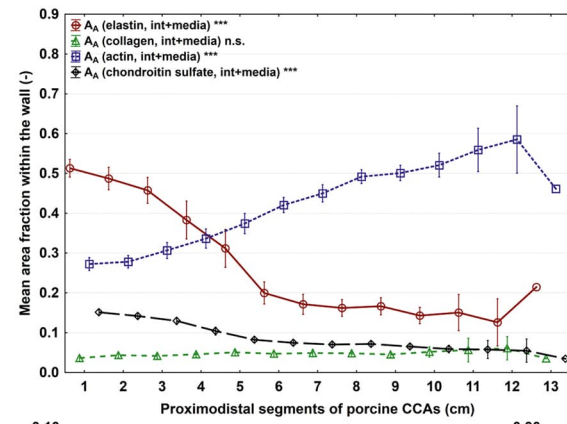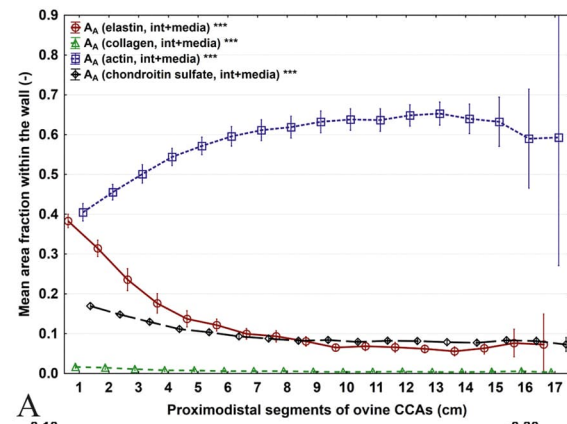
(caption on next page)

Fig. 4. Proximodistal segmental differences of ovine and porcine common carotid arteries (CCAs). **A –** In both CCAs, the fractions of elastin and chondroitin sulfate decreased in the proximodistal direction (Kruskal–Wallis ANOVA p < 0.001). The fraction of total collagen decreased in ovine CCAs (p < 0.001) in the proximodistal direction, but in the porcine CCAs, the fraction of total collagen was the same along the entire length. The fraction of actin in both CCAs increased in the proximodistal direction (p < 0.001). **B –** In ovine CCAs, the fractions of total collagen, type I collagen, and type III collagen (p < 0.001) decreased in the proximodistal direction. The fractions of total collagen, type I collagen, type III collagen and the ratio of type III to type I collagen in porcine CCAs were the same throughout the entire length. **C –** The density of nuclear profiles in ovine (p < 0.001) and porcine CCAs (p < 0.05) decreased in the proximodistal direction. In both CCAs, the density of the nervi vasorum increased in the proximodistal direction (p < 0.001). In ovine CCAs, the densities of the vasa vasorum in the media (p < 0.001) and adventitia (p < 0.05) decreased for the first three centimeters but increased in the last five centimeters. In porcine CCAs, the densities of the vasa vasorum in the media decreased but increased in the adventitia in the proximodistal direction (p < 0.001). **D –** In both CCAs, the intima-media thickness and ratio of intima-media thickness to wall thickness decreased in the proximodistal direction (p < 0.001). Data are displayed as the means ± standard error of the means. The p values of the Kruskal–Wallis ANOVA tests are shown * for p < 0.05, ** for p < 0.01, *** for p < 0.001.

3. Results

All primary morphometric data obtained from the quantitative histology of the samples are provided in Supplement 1.

3.1. Left- vs. right-side differences of CCAs

Complete data of the comparison of left and right CCAs are shown in Table 3. The right ovine CCAs had a smaller fraction of elastin (Wilcoxon matched pairs p < 0.001, Supplement 2A), a greater fraction of SMA (p < 0.01, Supplement 2), and a greater intima-media thickness (p < 0.001, Supplement 5 A) than the paired left-side ovine CCAs. In pigs, the right CCAs had a greater fraction of elastin (p < 0.05, Supplement 2A) and a greater density of the vasa vasorum in the media (p < 0.001, Supplement 4C) than the left CCAs. There were no statistically significant differences in the fractions of collagen between the paired samples of the left and right CCAs in either animal model (Supplement 3).

3.2. Proximodistal segmental differences of CCAs

All the differences among the segments along the CCAs are summarized in Fig. 4 for ovine and porcine CCAs separately. The ovine CCA was mostly a muscular type of artery along its entire length (Fig. 4A, Fig. 5). Proximal segments of porcine CCA were mostly elastic; the middle and distal segments were mostly muscular (Figs. 4A, 5). The fractions of elastin and CS decreased, and the fraction of SMA increased in the proximodistal direction in the ovine and porcine CCAs (Kruskal–Wallis ANOVA p < 0.001, Fig. 4A). In ovine CCAs, the fractions of total collagen, type I collagen and type III collagen decreased in the proximodistal direction (p < 0.001), but these fractions were similar across the entire length of porcine CCAs (Fig. 4B). Densities of nuclear profiles (ovine CCAs p < 0.001, porcine CCAs p < 0.05) and vasa vasorum in media (p < 0.001, Fig. 4C) decreased in the proximodistal direction. In contrast, the densities of the nervi vasorum (p < 0.001) and vasa vasorum in the adventitia (ovine CCAs p < 0.05, porcine CCAs p < 0.001, Fig. 4C) increased in the proximodistal direction. The intima-media thickness (p < 0.001, Fig. 4D) decreased in the proximodistal direction in both animal models.

3.3. Comparison among ovine CCAs, porcine CCAs, human CAs and human ITAs

Table 4 shows differences among CCAs, human CAs and human ITAs. Porcine CCAs had the greatest fraction of elastin compared to ovine CCAs, human CAs and ITAs (Kruskal–Wallis ANOVA p < 0.001, Fig. 6A). However, ovine CCAs had a comparable fraction of elastin (Fig. 6A) and CS (Fig. 6F) to human ITAs. The fraction of actin was greatest in ovine CCAs (p < 0.001, Fig. 6E). The fraction of CS was similar in porcine CCAs, human CAs and ITAs (Fig. 6F). Porcine CCAs

had the greatest density of nuclear profiles (Fig. 7A, p < 0.001). Ovine CCAs had the greatest density of nervi vasorum (Fig. 7B, p < 0.001). Human CAs had greater densities of vasa vasorum in the media and adventitia than CCAs (Fig. 7C,D, p < 0.001).Intima-media thickness and wall thickness were the same in both CCAs, but these thicknesses were greater than those in human CAs and ITAs (p < 0.001, Fig. 8A, B) .

3.4. Correlation between histological parameters

In ovine CCA segments, the fraction of elastin correlated positively with collagen (Spearman r = 0.576; p < 0.05), CS (r = 0.596), densities of nuclear profiles (r = 0.387), vasa vasorum density in the media (r = 0.125), intima-media thickness (r = 0.513), and wall thickness (r = 0.425). The fraction of elastin correlated negatively with the fraction of SMA (r = −0.580) and density of the nervi vasorum (r = −0.368). These correlations in ovine CCAs were the same as the correlations found previously in porcine CCAs (Tomášek et al., 2020). The complete correlation matrix is summarized in Supplement 6.

3.5. Descriptive statistics for the purpose of the power sample analysis

Table 5 shows the mean and standard deviation of four proximal, four middle and four distal segments of ovine and porcine CCAs. These data are ready to use for facilitating the calculation of the minimum number of samples when planning experiments on ovine CCAs and porcine CCAs. For example, 8 samples would be needed to detect a 20% decrease in SMA content in the middle segments of ovine CCAs with known biological variability (SD), test strength 0.8 and type I error of 5%. A similar analysis can be performed for any parameter according to Chow et al. (2008).

4. Discussion

4.1. Left and right CCAs are interchangeable in pigs but not in sheep

In some studies, cardiac surgeons tested synthetic grafts for CAGB only on the right side (Carmen Calles et al., 2002; Weber et al., 2018), the left side (Ahmed et al., 2014) or both sides of ovine or porcine CCAs (Hawthorne et al., 2002). One side of the CCAs is usually used as a sham-operated control (Carmen Calles et al., 2002). In our study, the left and right porcine CCAs were mostly interchangeable. In contrast, considerable differences were found between the left and right ovine CCAs. We found a greater fraction of elastin on the left side and SMA on the right side of the ovine carotid artery. The intima-media of the left ovine CCA was thinner, as was found in the study using human CCAs (Willekes et al., 1999). Despite a literature search, we found no straightforward anatomical explanation for the histological differences detected in left vs. right ovine CCAs. In other studies, the CCAs on the left side in humans was

Ovine common carotid arteries
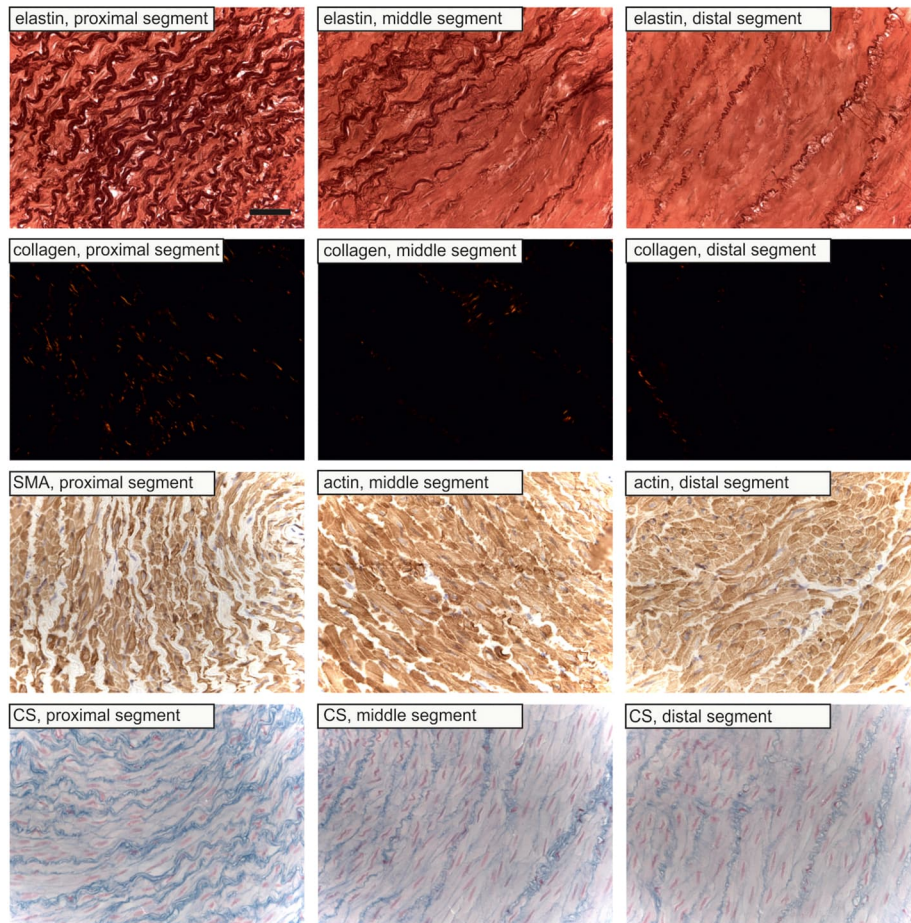
Porcine common carotid arteries
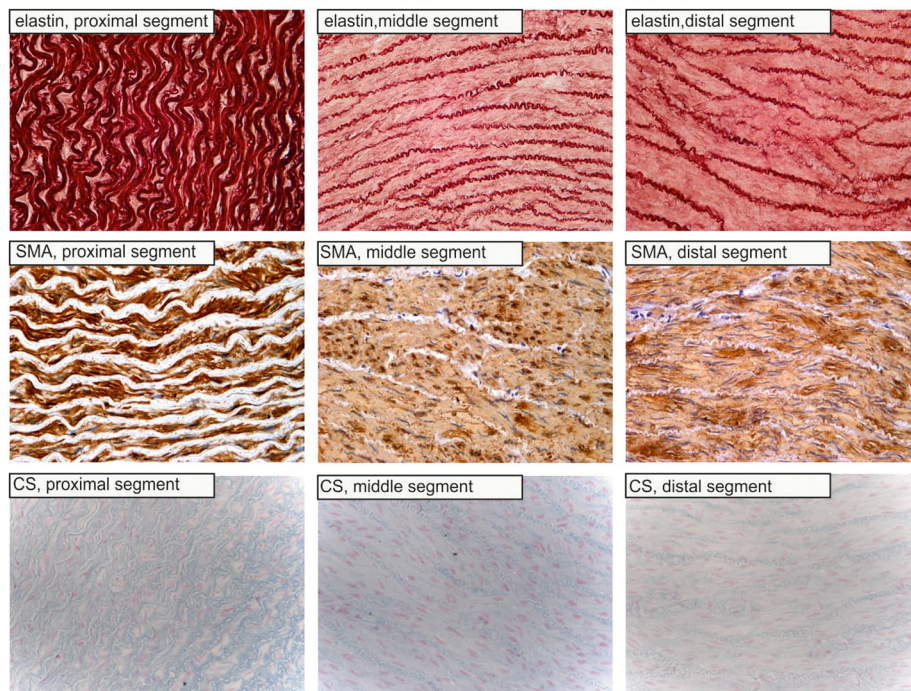
Fig. 5. Proximodistal segmental differences of ovine and porcine common carotid arteries (CCAs). In both CCAs, fractions of elastin and chondroitin sulfate (CS) decreased in the proximodistal direction (Kruskal–Wallis ANOVA p < 0.001). The fraction of total collagen decreased in ovine CCAs (p < 0.001) in the proximodistal direction. The fraction of actin increased in the proximodistal direction in both CCAs (p < 0.001). Scale bar 50 µm.

Table 4

Comparison of ovine and porcine common carotid arteries (CCAs) with human coronary arteries (CAs) and human internal thoracic arteries (ITAs). Data are displayed as the means and standard deviations (SD)The p values of the Kruskal–Wallis ANOVA tests are shown * for p < 0.05, ** for p < 0.01, *** for p < 0.001, not statistically significant (n.s.) for p > 0.05.

Quantitative parameter (unit)	Human CAs	Human ITAs	Ovine CCAs	Porcine CCAs
A_A (elastin, int+media) (-)	0.06 ± 0.04		greater (***) 0.14 ± 0.11	greater (***) 0.30 ± 0.17
		0.13 ± 0.07	n.s. 0.14 ± 0.11	greater (***) 0.30 ± 0.17
A_A (type I collagen, int+media) (-)	0.02 ± 0.03		smaller (***) 0.01 ± 0.01	greater (***) 0.04 ± 0.02
		0.005 ± 0.01	greater (***) 0.01 ± 0.01	greater (***) 0.04 ± 0.02
A_A (type III collagen, int+media) (-)	0.003 ± 0.004		smaller (***) 0.0002 ± 0.0005	n.s. 0.003 ± 0.004
		0.001 ± 0.002	smaller (***) 0.0002 ± 0.0005	greater (***) 0.003 ± 0.004
A_A (actin, int+media) (-)	0.33 ± 0.08		greater (***) 0.58 ± 0.11	greater (***) 0.40 ± 0.11
		0.35 ± 0.08	greater (***) 0.58 ± 0.11	greater (**) 0.40 ± 0.11
A_A (chondroitin sulfate, int+media) (-)	0.09 ± 0.03		greater (***) 0.10 ± 0.03	n.s. 0.10 ± 0.04
		0.10 ± 0.04	n.s. 0.10 ± 0.03	n.s. 0.10 ± 0.04
Q_A (nuclear profiles, int+media) (mm^2)	1175 ± 388		greater (***) 1460 ± 254	greater (***) 2486 ± 394
		1331 ± 508	greater (**) 1460 ± 254	greater (***) 2486 ± 394
Q_A (nervi vasorum, int+media) (mm^2)	1.94 ± 1.85		greater (***) 8.18 ± 5.04	greater (***) 3.89 ± 3.64
		1.26 ± 1.43	greater (***) 8.18 ± 5.04	greater (***) 3.89 ± 3.64
Q_A (vasa vasorum, int+media) (mm^2)	3.92 ± 5.19		smaller (**) 0.52 ± 2.09	smaller (***) 1.76 ± 5.37
		1.93 ± 3.11	smaller (*) 0.52 ± 2.09	smaller (***) 1.76 ± 5.37
Q_A (vasa vasorum, adventitia) (mm^2)	90.72 ± 32.30		smaller (***) 45.78 ± 21.34	smaller (***) 64.55 ± 28.39
		58.94 ± 26.89	smaller (***) 45.78 ± 21.34	n.s. 64.55 ± 28.39
Intima-media thickness (IMT) (μm)	442 ± 183		thicker (***) 612 ± 160	thicker (***) 588 ± 132
		297 ± 83	thicker (***) 612 ± 160	thicker (***) 588 ± 132
Wall thickness (WT) (μm)	612 ± 223		thicker (***) 881 ± 188	thicker (***) 881 ± 190
		428 ± 118	thicker (***) 881 ± 188	thicker (***) 881 ± 190

thicker than the right-side CCAs (Bots et al., 1997; Loizou et al., 2015; Luo et al., 2011; Rodríguez Hernández et al., 2003; Schmidt and Wendelhag, 1999; Sun et al., 2002). The intima-media thickness represents the endothelial response to physiological and pathological processes in the artery (Willekes et al., 1999).

4.2. Ovine CCAs were mostly muscular; porcine CCAs were elastic to muscular in nature

The microscopic composition of ovine and porcine CCAs differed along their macroscopic length. The entire length of the ovine CCAs had a mostly muscular phenotype. This was in contrast to porcine CCAs, which were elastic in the proximal segments but gradually switched to the muscle type at approx. 3–4 cm from their origin. Our results are consistent with those of other studies, which found that elastin in porcine CCAs decreased and smooth muscle cells increased in the proximodistal direction (García et al., 2011; Sokolis et al., 2011; Weizsäcker et al., 2014). The muscular phenotype of proximal ovine CCA was also reported by Bia et al. (2014). In our study, fractions of elastin and CS decreased in ovine and porcine CCAs in the proximodistal direction. This can be partially explained by the binding sites between CS and elastic fibers (Dubey and Deng, 2018; Humphrey, 2013; Reinboth et al., 2002). The density of nuclear profiles in ovine CCAs in our study decreased in proximodistal segments. However, in another study, the density was not statistically significant, and the nuclei of smooth muscle cells were distributed evenly along the length of the ovine CCA (Parchami et al., 2009). The general problem of how the microscopic composition of arteries differs along their gross anatomical structure (Sokolis, 2007; Sokolis et al., 2008; Tonar et al., 2016) and how these regional differences affect, e.g., their mechanical properties (Avril et al., 2015; Bersi et al., 2016), will surely receive further attention. We believe our comparison may at least partially explain the mechanical similarities and

differences reported among ovine and porcine CCAs by Prim et al. (2018). However, it remains unclear how the data on wall thickness and composition of these arteries based on histologically processed samples relate to their in vivo dimensions, and hemodynamic parameters such as volumetric flow rate or local changes in blood pressure.

4.3. Ovine and porcine CCAs mostly do not reflect the structure of human CAs and human ITAs

From the point of view of the surgical approach, the middle segment of animal CCAs is the most suitable for testing prostheses. The wall thickness of CCAs is also important, which was similar in sheep and pigs. The wall thickness of CAs and ITAs were thinner than those of CCAs, with the middle segment of both carotid arteries being the most suitable for prosthesis testing. The main components of the extracellular matrix of arteries are elastin fibers, collagen and glycosaminoglycans (GAGs) (Bartolini et al., 2013; Mattson et al., 2017). Both CCAs had greater fractions of elastin and SMA than human CAs and ITAs but were closest in value to the middle segment of ovine CCAs and distal segment of porcine CCAs.

4.4. Practical recommendations

Based on the extensive morphometric data analyzed in the present study, the following recommendations can be formulated: (i) Although we are currently lacking an explanation for the observed left-to right differences in ovine CCAs, these differences should be considered when selecting sham-operated controls, e.g., by alternating the side of the surgery; (ii) The different proximodistal phenotypes of ovine and porcine CCAs should be considered, as these phenotypes prevent both animal models from being used
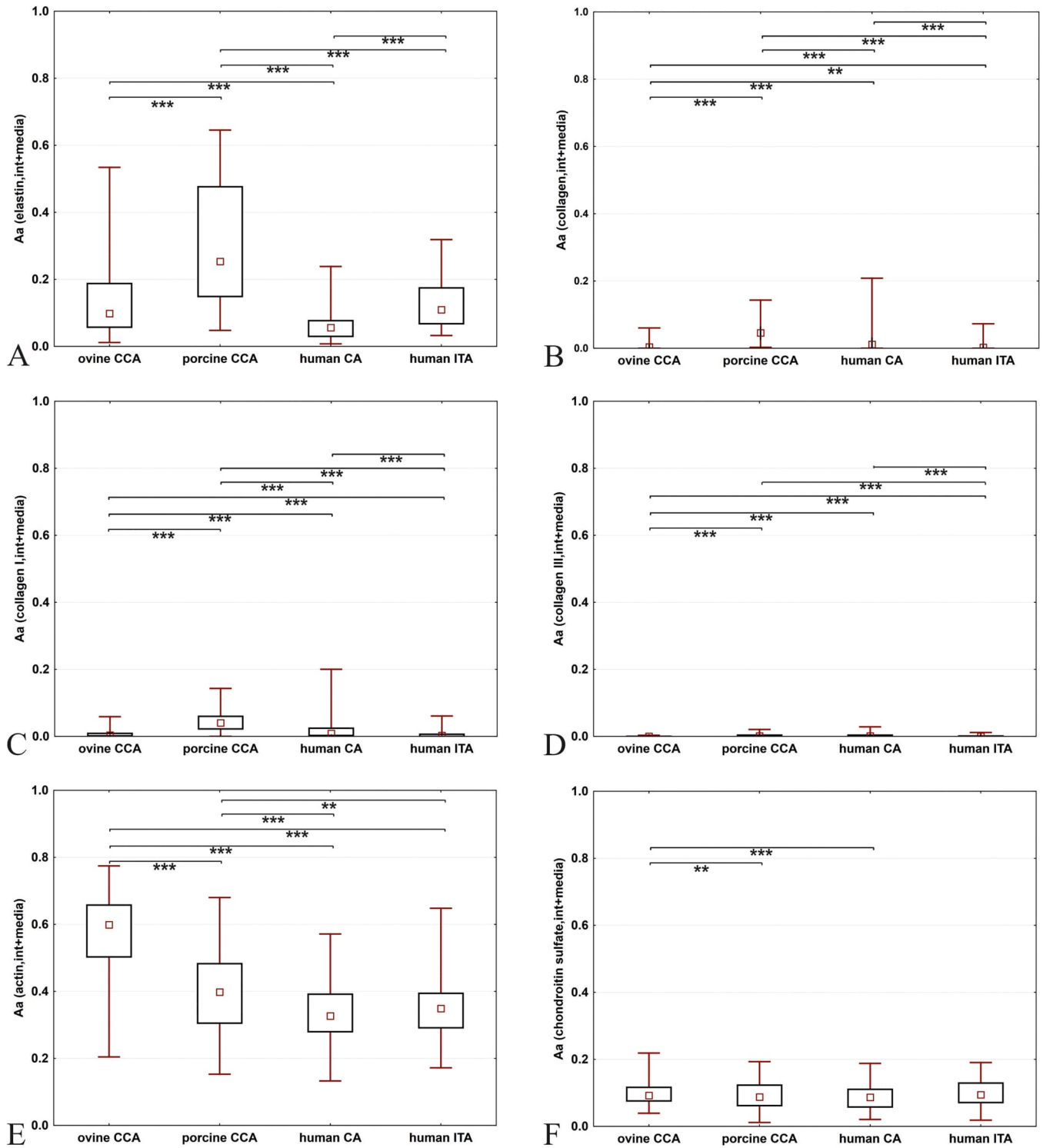
Fig. 6. Comparison of the fractions of elastin, total collagen, type I collagen, type III collagen, smooth muscle actin (SMA), and chondroitin sulfate (CS) between common carotid arteries (CCAs), human coronary arteries (CAs) and internal thoracic arteries (ITAs). A – Porcine CCAs had the greatest fraction of elastin (Kruskal–Wallis ANOVA p < 0.001). Ovine CCAs had the same fraction of elastin as ITAs. B, C - Porcine CCAs had the greatest fractions of collagen and type I collagen (p < 0.001). D – Porcine CCAs and human CAs had the same fraction of type III collagen. E – Ovine CCAs had the greatest fraction of SMA (p < 0.001). E – Neither CCA showed statistically significant differences in the fraction of CS. Data are displayed as median values with boxes that span the limits of the first and third quartiles and whiskers that span the minimum and maximum values for each group. The p values of the Kruskal–Wallis ANOVA tests are shown * for p < 0.05, ** for p < 0.01, *** for p < 0.001.
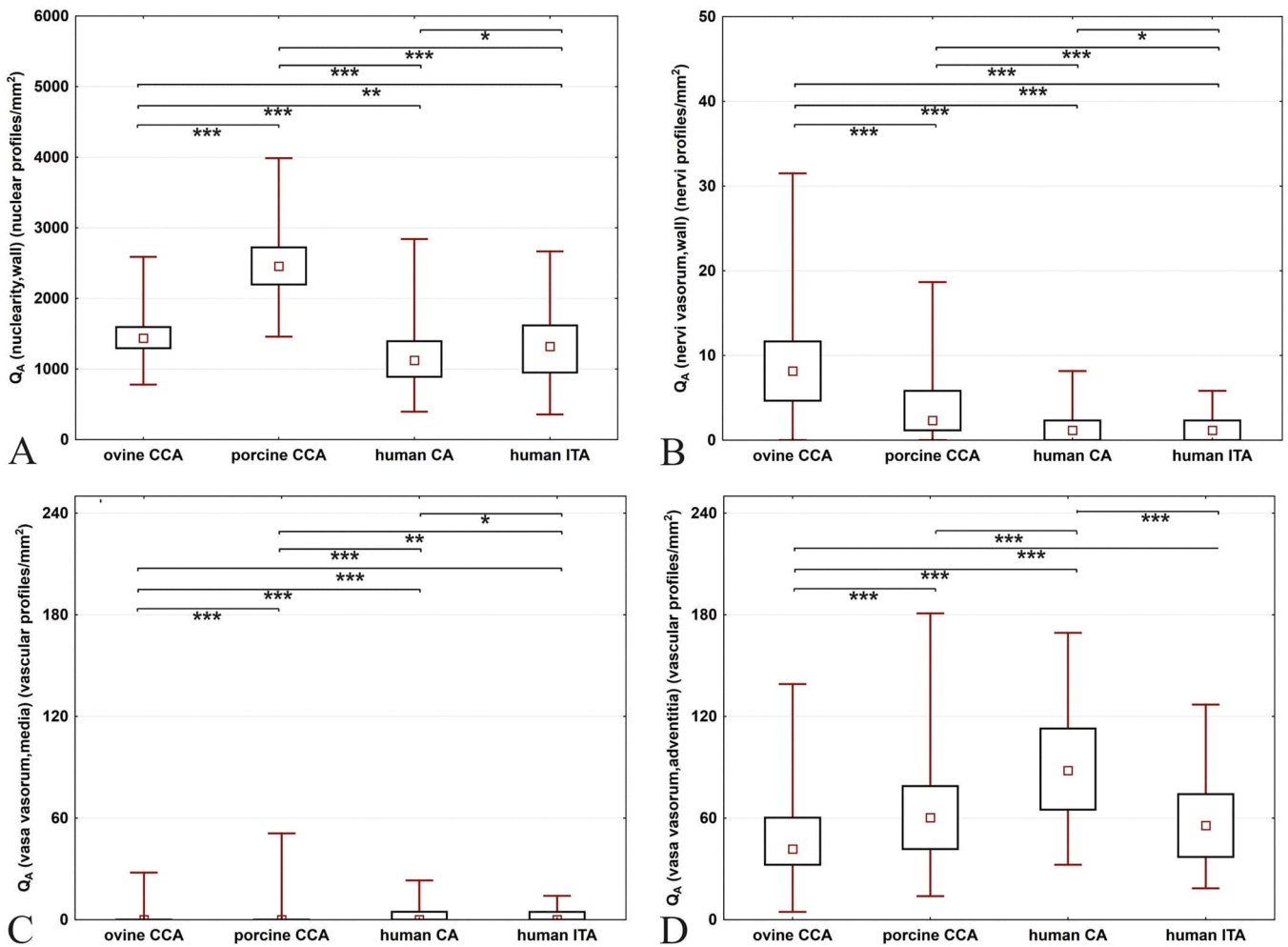
Fig. 7. Comparison of densities of nuclear profiles, nervi vasorum, vasa vasorum between common carotid arteries (CCAs), human coronary arteries (CAs) and internal thoracic arteries (ITAs). A – Porcine CCAs had the greatest density of nuclear profiles (Kruskal–Wallis ANOVA $p < 0.001$). **B** – Ovine CCAs had the greatest density of nervi vasorum ($p < 0.001$). **C, D** – Human CAs had greater densities of vasa vasorum in the media and adventitia than CCAs ($p < 0.001$). Data are displayed as median values with boxes that span the limits of the first and third quartiles and whiskers that span the minimum and maximum values for each group. The p values of the Kruskal–Wallis ANOVA tests are shown * for $p < 0.05$, ** for $p < 0.01$, *** for $p < 0.001$.

interchangeably. Additionally, the histological evaluation of experiments performed in both species is comparable only to a limited extent, as their natural differences might be a source of comparative bias; (iii) The histological differences between the CCAs of healthy and relatively young animals and the CAs and the most commonly used ITA conduits of human patients at the age of typical CABG surgery are understandable and should be considered to avoid any overinterpretation of data gathered in these models; and (iv) Both ethical and scientific viewpoints require performing a power sample analysis of ovine and porcine CCAs when designing experiments involving these models, which is now feasible. The present data facilitate such a power analysis. However, the minimum number of samples per study group should be evaluated also with respect to the biological hypotheses and variables used in any future studies testing the efficacy of potential graft tissues in these animals.

4.5. Limitations of the type III collagen quantification

The fractions of type III collagen found in our study were almost neglectable and no major conclusions were drawn from these data in healthy arterial walls of the animals under study. However, quantification of type III collagen may become more important in future studies that would include processes such as arterial healing or fibrosis. Quantification of the type III collagen combining the picrosirius red (PSR) and circularly polarized light used in our study seems to be controversial. On the one hand, Rich and Whittaker (2005) discouraged from using collagen fiber hue for discriminating the type I and type III collagen even under the circularly polarized light. The main objection was that green, thin fibers, may represent not only type III collagen fibrils, but also some of the immature thin type I fibers (especially in healing tissues), or incomplete sectional
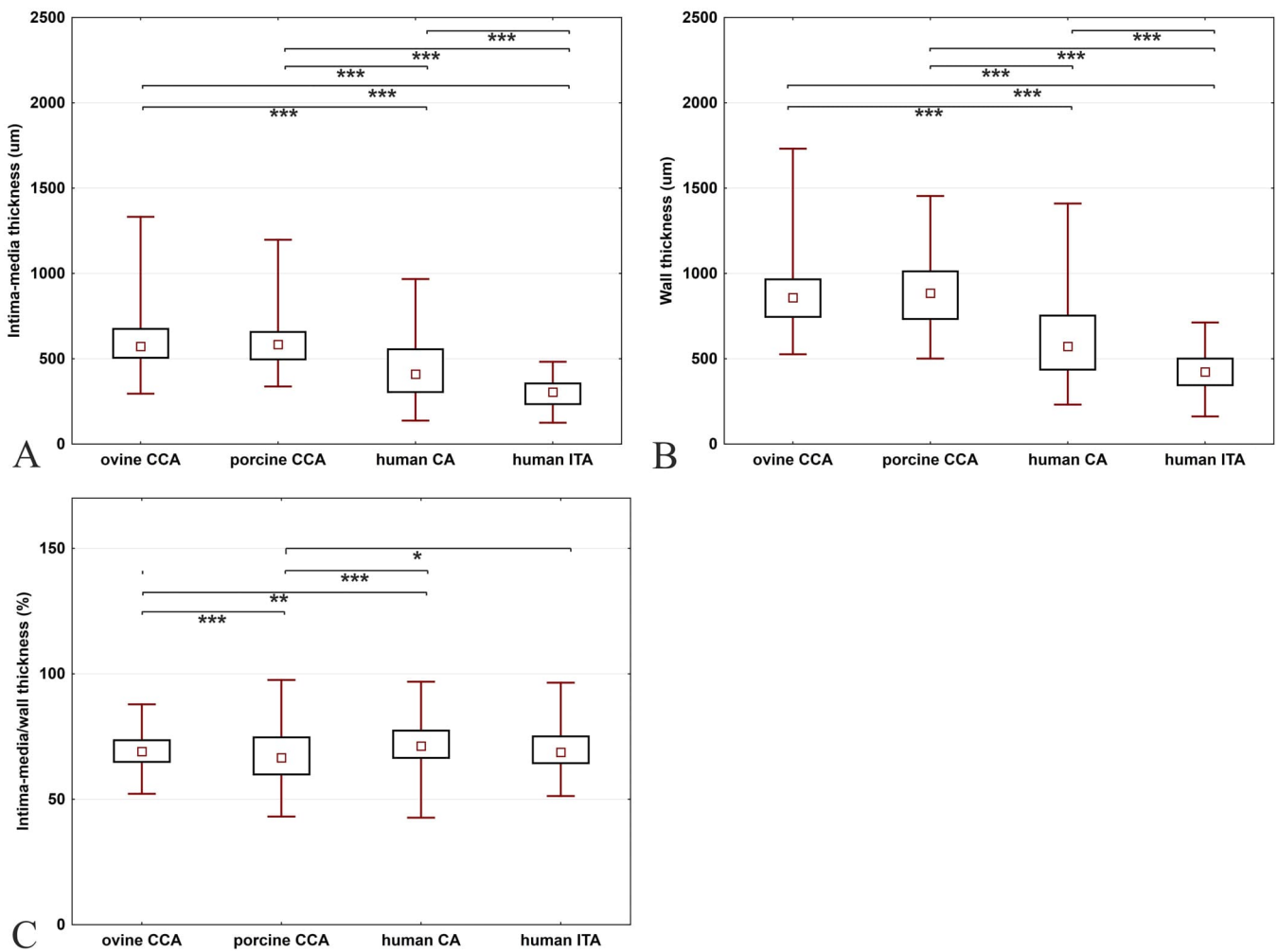
Fig. 8. Comparison of the intima-media thickness, wall thickness, and intima media and wall thickness ratio among carotid arteries (CCAs), human coronary arteries (CAs) and internal thoracic arteries (ITAs). A – The intima-media thickness was the same for ovine and porcine CCAs. Both CCAs had thicker intima-media than CAs and ITAs (Kruskal–Wallis ANOVA p < 0.001). B - The wall thickness is the same for ovine and porcine CCAs. Both CCAs had thicker walls than the CAs and ITAs (p < 0.001). C – CAs and ITAs had the same intima-media to wall thickness ratio. Data are displayed as median values with boxes that span the limits of the first and third quartiles and whiskers that span the minimum and maximum values for each group. The p values of the Kruskal–Wallis ANOVA tests are shown * for p < 0.05, ** for p < 0.01, *** for p < 0.001.

profiles belonging originally to type I fibers. On the other hand, this method is still in use (e.g., Richards et al., 2021; Zeng et al., 2019). Calderón et al. (2019) combined the PSR/polarized light approach with immunohistochemical detection of the amounts of type I and III collagen and reported on a positive correlation between PSR and type immunohistochemically detected type I collagen (R=0.82; p = 0.05) as well as between PSR and immunohistochemically detected type III collagen (R=0.78; p = 0.05). Calderón et al. (2019) consider the PSR as a less sensitive, but cheaper method that can be a good choice in some laboratories. Unlike immunohistochemistry, the PRS/polarized light technique has no issues with different antibodies and immunohistochemical protocols and visualization systems used in different species, and the staining procedure seems to have an excellent repeatability (Calderón et al., 2019; Coleman, 2011). Similarly, Lattouf et al. (2014) compared both PRS/polarized light with immunohistochemical detection of type III collagen, concluding with a positive recommendation on using the PSR/polarized light for measuring the collagen content in normal or pathological tissues qualitatively. However, the most convincing and critical comparison we found in the literature was the study by Farris et al. (2011), concluding that PSR stain was more robust and less dependent on fixation than immunohistochemistry, however, quantification of type III collagen in PSR did not provide satisfactory efficiency, and reproducibility.

Table 5

Descriptive statistics suitable for calculating the minimum number of samples for planning experiments on ovine and porcine common carotid arteries (CCAs). The means and standard deviations of four proximal, four middle and four distal segments of ovine and porcine CCAs are shown. The p values of the Mann–Whitney U tests comparing the values of ovine vs. porcine CCAs are shown: * for $p < 0.05$, ** for $p < 0.01$, *** for $p < 0.001$, not statistically significant (n.s.) for $p > 0.05$.

Segments of porcine and ovine CCAs	Quantitative parameter	Ovine CCAs		Porcine CCAs		p value
		Mean	Standard deviation	Mean	Standard deviation	
proximal	A_A (elastin) (-)	0.249	0.116	0.460	0.117	***
	A_A (collagen) (-)	0.011	0.011	0.042	0.023	***
	A_A (type I collagen) (-)	0.011	0.011	0.039	0.022	***
	A_A (type III collagen) (-)	0.000	0.001	0.003	0.004	***
	A_A (actin) (-)	0.495	0.093	0.298	0.066	***
	A_A (chondroitin sulfate) (-)	0.132	0.033	0.132	0.032	n.s.
	Q_A (nuclear profiles) (mm^{-2})	1580	280	2560	405	***
	Q_A (nervi vasorum) (mm^{-2})	6.317	3.761	2.426	2.585	***
	Q_A (vasa vasorum within media) (mm^{-2})	0.864	2.996	3.592	7.798	***
	Q_A (vasa vasorum within adventitia) (mm^{-2})	46.426	21.629	55.378	25.419	***
	IMT (μm)	743	182	634	157	***
	WT (μm)	1013	215	862	201	***
middle	A_A (elastin) (-)	0.092	0.047	0.211	0.117	***
	A_A (collagen) (-)	0.005	0.005	0.049	0.027	***
	A_A (type I collagen) (-)	0.005	0.005	0.046	0.026	***
	A_A (type III collagen) (-)	0.000	0.000	0.003	0.004	***
	A_A (actin) (-)	0.619	0.088	0.434	0.079	***
	A_A (chondroitin sulfate) (-)	0.085	0.017	0.075	0.022	***
	Q_A (nuclear profiles) (mm^{-2})	1403	225	2456	389	***
	Q_A (nervi vasorum) (mm^{-2})	7.649	4.816	4.084	3.446	***
	Q_A (vasa vasorum within media) (mm^{-2})	0.148	0.816	0.622	2.089	**
	Q_A (vasa vasorum within adventitia) (mm^{-2})	42.441	18.921	70.424	29.597	***
	IMT (μm)	548	87	549	104	n.s.
	WT (μm)	808	121	871	182	***
distal	A_A (elastin) (-)	0.064	0.034	0.154	0.059	***
	A_A (collagen) (-)	0.004	0.005	0.050	0.027	***
	A_A (type I collagen) (-)	0.004	0.005	0.047	0.027	***
	A_A (type III collagen) (-)	0.000	0.000	0.002	0.003	***
	A_A (actin) (-)	0.643	0.093	0.521	0.069	***
	A_A (chondroitin sulfate) (-)	0.080	0.015	0.062	0.023	***
	Q_A (nuclear profiles) (mm^{-2})	1382	195	2389	359.009	***
	Q_A (nervi vasorum) (mm^{-2})	10.969	5.447	6.628	4.320	***
	Q_A (vasa vasorum within media) (mm^{-2})	0.518	1.707	0.247	1.049	n.s.
	Q_A (vasa vasorum within adventitia) (mm^{-2})	48.621	23.436	71.802	26.823	***
	IMT (μm)	528	80	573	92	***
	WT (μm)	804	120	943	170	***

5. Conclusion

A detailed comparison of 11 morphometric parameters in the samples of ovine and porcine CCAs and human CAs and ITAs revealed the following: (i) From a histological point of view, the left and right CCAs were interchangeable in pigs but not in sheep; (ii) Ovine CCAs were mostly of a muscular phenotype, but porcine CCAs changed their phenotype in the proximodistal direction; (iii) Similar to porcine CCAs, ovine CCAs had a thickness comparable to that of human CAs and human ITAs, but the histological composition of both porcine and ovine CCAS was different from that of human CAs and ITAs; and (iv) The correlation patterns among the histological constituents within ovine CCAs were identical to the pattern found in porcine CCAs.

The differences between the histological composition of ovine and porcine CCAs detected in our study set some limitations to be used as completely equivalent to that of large animal models in cardiac surgery. These differences shall be considered when designing and interpreting such experiments. The complete morphometric data obtained by quantitative evaluation of arterial segments were provided to facilitate the power analysis necessary for justification of the minimum number of samples when planning further experiments. The middle or distal segments of ovine and porcine CCAs remain the most realistic and probably the best characterized large animal models for testing artificial arterial CABG conduits. We formulated practical recommendations on how to design experiments on ovine CCAs and how to use these large animal models in a way that maximizes the validity of their histological evaluation.

Declaration of Competing Interest

The authors declare that they have no known competing financial interests or personal relationships that could have appeared to influence the work reported in this paper.

Acknowledgments

Appendix A. Supporting information

Supplementary data associated with this article can be found in the online version at doi:10.1016/j.aanat.2022.151910.

References

Ahmed, M., Hamilton, G., Seifalian, A.M., 2014. The performance of a small-calibre graft for vascular reconstructions in a senescent sheep model. Biomaterials 35, 9033–9040.

Avril, S., Bersi, M.R., Bellini, C., Genovese, K., Humphrey, J.D., 2015. Regional identification of mechanical properties in arteries. Comput. Methods Biomech. Biomed. Eng. 8 (Suppl 1), 1874–1875.

Bancroft, J.D., 2008. Theory and Practice of Histological Techniques. Elsevier Health Sciences.

Bartolini, B., Thelin, M.A., Svensson, L., Ghiselli, G., van Kuppevelt, T.H., Malmström, A., Maccarana, M., 2013. Iduronic acid in chondroitin/dermatan sulfate affects directional migration of aortic smooth muscle cells. PLoS One 8, e66704.

Bastijanic, J.M., Marchant, R.E., Kligman, F., Allemang, M.T., Lakin, R.O., Kendrick, D., Kashyap, V.S., Kottke-Marchant, K., 2016. In vivo evaluation of biomimetic fluorosurfactant polymer-coated expanded polytetrafluoroethylene vascular grafts in a porcine carotid artery bypass model. J. Vasc. Surg. 63, 1620–1630.

Bawany, F.I., Khan, M.S., Khan, A., Kazi, A.N., Naeem, M., 2014. Using skeletonised grafts for coronary artery bypass grafting. J. Pak. Med. Assoc. 64, 606–610.

Bersi, M.R., Bellini, C., Di Achille, P., Humphrey, J.D., Genovese, K., Avril, S., 2016. Novel methodology for characterizing regional variations in the material properties of murine aortas. J. Biomech. Eng. 138, 7.

Best, C., Fukunishi, T., Drews, J., Khosravi, R., Hor, K., Mahler, N., Yi, T., Humphrey, J.D., Johnson, J., Breuer, C.K., Hibino, N., 2018. Oversized biodegradable arterial grafts promote enhanced neointimal tissue formation. Tissue Eng. Part A 24, 1251–1261.

Bia, D., Zócalo, Y., Cabrera-Fischer, E., Wray, S., Armentano, R., 2014. Quantitative analysis of the relationship between blood vessel wall constituents and viscoelastic properties: dynamic biomechanical and structural in vitro studies in aorta and carotid arteries. Physiol. J. 2014, 1–9.

Bots, M.L., de Jong, P.T., Hofman, A., Grobbee, D.E., 1997. Left, right, near or far wall common carotid intima-media thickness measurements: associations with cardiovascular disease and lower extremity arterial atherosclerosis. J. Clin. Epidemiol. 50, 801–807.

Cai, C., Gu, Y., Cheng, J., Li, J., Xu, Z., Xing, Y., Wang, C., Wang, Z., 2019. Decellularization, cross-linking and heparin immobilization of porcine carotid arteries for tissue engineering vascular grafts. Cell. Tissue Bank. 20, 569–578.

Calderón, L.G.R., Kobayashi, P.E., Vasconcelos, R.O., Fonseca-Alves, C.E., Laufer-Amorim, R., 2019. Characterization of collagen fibers (I, III, IV) and elastin of normal and neoplastic canine prostatic tissues. Vet. Sci. 6, E22.

Carmen Calles, M., Lima, M.A., Crisóstomo, V., Usón, J.M., Usón, J., 2002. End-to-end anastomosis in growing vessels using a novel suturing technique: VCS metallic staples. Ann. Vasc. Surg. 16, 345–352.

Carrel, A., 1910. VIII. On the experimental surgery of the thoracic aorta and heart. Ann. Surg. 52, 83–95.

Chow, S.C., Wang, H., Shao, J., 2008. Sample Size Calculations in Clinical Research, Second ed. Chapman & Hall/CRC Biostatistics Series, Boca Raton.

Coleman, R., 2011. Picrosirius red staining revisited. Acta Histochem. 113, 231–233.

Desai, N.D., Fremes, S.E., 2007. Radial artery conduit for coronary revascularization: as good as an internal thoracic artery? Curr. Opin. Cardiol. 22, 534–540.

Dubey, N.K., Deng, W.-P., 2018. 20 - Polymeric gels for cartilage tissue engineering. In: Pal, K., Banerjee, I. (Eds.), Polymeric Gels. Woodhead Publishing Series in Biomaterials. Woodhead Publishing, pp. 505–525.

Eberlova, L., Tonar, Z., Witter, K., Krizkova, V., Nedorost, L., Korabecna, M., Tolinger, P., Kocova, J., Boudova, L., Treska, V., Houdek, K., Molacek, J., Vrzalova, J., Pesta, M., Topolcan, O., Valenta, J., 2013. Asymptomatic abdominal aortic aneurysms show histological signs of progression: a quantitative histochemical analysis. Pathobiology 80, 11–23.

Eghbalzadeh, K., Guschlbauer, M., Weber, C., Wacker, M.T., Reinhardt, S., Djordjevic, I., Sabashnikov, A., Maul, A., Sterner-Kock, A., Wahlers, T.C.W., Scherner, M., Wippermann, J., 2019. Experimental studies for small diameter grafts in an in vivo sheep model-techniques and pitfalls. Thorac. Cardiovasc. Surg. 69, 649–659.

Fallon, A., Goodchild, T., Wang, R., Matheny, R.G., 2012. Remodeling of extracellular matrix patch used for carotid artery repair. J. Surg. Res. 175, 25–34.

Farris, A.B., Adams, C.D., Brousaides, N., Della Pelle, P.A., Collins, A.B., Moradi, E., Smith, R.N., Grimm, P.C., Colvin, R.B., 2011. Morphometric and visual evaluation of fibrosis in renal biopsies. J. Am. Soc. Nephrol. 22, 176–186.

Fukunishi, T., Best, C.A., Sugiura, T., Shoji, T., Yi, T., Udelsman, B., Ohst, D., Ong, C.S., Zhang, H., Shinoka, T., Breuer, C.K., Johnson, J., Hibino, N., 2016. Tissue-engineered small diameter arterial vascular grafts from cell-free nanofiber PCL/Chitosan Scaffolds in a sheep model. PLoS One 11, e0158555.

García, A., Peña, E., Laborda, A., Lostalé, F., De Gregorio, M.A., Doblaré, M., Martínez, M.A., 2011. Experimental study and constitutive modelling of the passive mechanical properties of the porcine carotid artery and its relation to histological analysis: implications in animal cardiovascular device trials. Med. Eng. Phys. 33, 665–676.

Goetz, R.H., Rohman, M., Haller, J.D., Dee, R., Rosenak, S.S., 1961. Internal mammary-coronary artery anastomosis. A nonsuture method employing tantalum rings. J. Thorac. Cardiovasc. Surg. 41, 378–386.

Goldman, S., Zadina, K., Moritz, T., Ovitt, T., Sethi, G., Copeland, J.G., Thottapurathu, L., Krasnicka, B., Ellis, N., Anderson, R.J., Henderson, W., VA Cooperative Study Group #207/297/364, 2004. Long-term patency of saphenous vein and left internal mammary artery grafts after coronary artery bypass surgery: results from a Department of Veterans Affairs Cooperative Study. J. Am. Coll. Cardiol. 44, 2149–2156.

Green, G.E., Stertzer, S.H., Reppert, E.H., 1968. Coronary arterial bypass grafts. Ann. Thorac. Surg. 5, 443–450.

Gundersen, H.J.G., 1977. Notes on the estimation of the numerical density of arbitrary profiles: the edge effect. J. Microsc. 111, 219–223.

Hawthorne, W.J., Ao, P.Y., Fletcher, J.P., 2002. Vascular closure staples reduce intimal hyperplasia in prosthesis implantation. ANZ J. Surg. 72, 862–866.

He, G.W., 2013. Arterial grafts: clinical classification and pharmacological management. Ann. Cardiothorac. Surg. 2, 507–518.

He, G.W., Angus, J.A., Rosenfeldt, F.L., 1988. Reactivity of the canine isolated internal mammary artery, saphenous vein, and coronary artery to constrictor and dilator substances: relevance to coronary bypass graft surgery. J. Cardiovasc. Pharmacol. 12, 12–22.

Howard, V., Reed, M., 2004. Unbiased Stereology: Three-Dimensional Measurement in Microscopy. Garland Science.

Humphrey, J.D., 2013. Possible mechanical roles of glycosaminoglycans in thoracic aortic dissection and associations with dysregulated TGF-β. J. Vasc. Res. 50, 1–10.

Ji, Q., Song, K., Xia, L., Shi, Y., Ma, R., Shen, J., Ding, W., Wang, C., 2018. Sequential saphenous vein coronary bypass grafting. Int. Heart J. 59, 1211–1218.

Jiřík, M., Bartoš, M., Tomášek, P., Malečková, A., Kural, T., Horáková, J., Lukáš, D., Suchý, T., Kochová, P., Hubálek Kalbáčová, M., Králíčková, M., Tonar, Z., 2018. Generating standardized image data for testing and calibrating quantification of volumes, surfaces, lengths, and object counts in fibrous and porous materials using X-ray microtomography. Microsc. Res. Tech. 81, 551–568.

Kocová, J., 1970. Overall staining of connective tissue and the muscular layer of vessels. Folia Morphol. 18, 293–295.

Kolinko, Y., Malečková, A., Kochová, P., Grajciarová, M., Blassová, T., Kural, T., Trailin, A., Červenková, L., Havránková, J., Vištejnová, L., Tonarová, P., Moulisová, V., Jiřík, M., Zavaďáková, A., Tichánek, F., Liška, V., Králíčková, M., Witter, K., Tonar, Z., 2022. Using virtual microscopy for the development of sampling strategies in quantitative histology and design-based stereology. Anat. Histol. Embryol. 51, 3–22.

König, H.E., Liebich, H.G., 2009. Veterinary anatomy of domestic mammal, fourth edition.

Kritharis, E.P., Giagini, A.T., Kakisis, J.D., Dimitriou, C.A., Stergiopulos, N., Tsangaris, S., Sokolis, D.P., 2012. Time course of flow-induced adaptation of carotid artery biomechanical properties, structure and zero-stress state in the arteriovenous shunt. Biorheology 49, 65–82.

Lattouf, R., Younes, R., Lutomski, D., Naaman, N., Godeau, G., Senni, K., Changotade, S., 2014. Picrosirius red staining: a useful tool to appraise collagen networks in normal and pathological tissues. J. Histochem. Cytochem. 62, 751–758.

Li, Y., Wu, Z., Li, X., Guo, Z., Wu, S., Zhang, Y., Shi, L., Teoh, S., Liu, Y., Zhang, Z., 2014. A polycaprolactone-tricalcium phosphate composite scaffold as an autograft-free spinal fusion cage in a sheep model. Biomaterials 35, 5647–5659.

Loizou, C.P., Nicolaides, A., Kyriacou, E., Georghiou, N., Griffin, M., Pattichis, C.S., 2015. A comparison of ultrasound intima-media thickness measurements of the left and right common carotid artery. IEEE J. Transl. Eng. Health Med. 3, 1–10.

Lossi, L., D'Angelo, L., De Girolamo, P., Merighi, A., 2016. Anatomical features for an adequate choice of experimental animal model in biomedicine: II. Small laboratory rodents, rabbit, and pig. Ann. Anat. 204, 11–28.

Luo, X., Yang, Y., Cao, T., Li, Z., 2011. Differences in left and right carotid intima-media thickness and the associated risk factors. Clin. Radiol. 66, 393–398.

Mattson, J.M., Turcotte, R., Zhang, Y., 2017. Glycosaminoglycans contribute to extracellular matrix fiber recruitment and arterial wall mechanics. Biomech. Model Mechanobiol. 16, 213–225.

Mrówczyński, W., Mugnai, D., de Valence, S., Tille, J.-C., Khabiri, E., Cikirikcioglu, M., Möller, M., Walpoth, B.H., 2014. Porcine carotid artery replacement with biodegradable electrospun poly-e-caprolactone vascular prosthesis. J. Vasc. Surg. 59, 210–219.

Mulisch, M., Welsch, U., 2015. Romeis - Mikroskopische Technik, 19th ed. SpringerSpektrum.

Nicolini, F., Vezzani, A., Romano, G., Carino, D., Ricci, M., Chicco, M.V.D., Gherli, T., 2017. Coronary artery bypass grafting with arterial conduits in the elderly. Int. Heart J. 58, 647–653.

Otsuka, F., Yahagi, K., Sakakura, K., Virmani, R., 2013. Why is the mammary artery so special and what protects it from atherosclerosis? Ann. Cardiothorac. Surg. 2, 519–526.

Parchami, A., Dehkordi, R.F., Derakhshan, A., 2009. Comparative histomorphometric study of the common carotid artery and its terminal branches in sheep and goats. Bulg. J. Vet. Med. 3, 165–170.

Popesko, P., 1978. Atlas of Topographical Anatomy of the Domestic Animals, Second ed. W.B. Saunders Co., Philadelphia.

Prim, D.A., Mohamed, M.A., Lane, B.A., Poblete, K., Wierzbicki, M.A., Lessner, S.M., Shazly, T., Eberth, J.F., 2018. Comparative mechanics of diverse mammalian carotid arteries. PLoS One 13, e0202123.

Rao, N., Kishore, K., Sujatha, K., Rao, H.R., 2016. Aortic arch arteries in man and domestic animals: a comparative study. Int. J. Anat. Res. 4, 3087–3091.

Reinboth, B., Hanssen, E., Cleary, E.G., Gibson, M.A., 2002. Molecular interactions of biglycan and decorin with elastic fiber components: biglycan forms a ternary complex with tropoelastin and microfibril-associated glycoprotein 1. J. Biol. Chem. 277, 3950–3957.

Rich, L., Whittaker, P., 2005. Collagen and Picrosirius Red Staining: a polarized light assessment of fibrillar hue and spatial distribution. J. Morphol. Sci. 22, 97–104.

Richards, C., Sesperez, K., Chhor, M., Ghorbanpour, S., Rennie, C., Ming, C.L.C., Evenhuis, C., Nikolic, V., Orlic, N.K., Mikovic, Z., Stefanovic, M., Cakic, Z., McGrath, K., Gentile, C., Bubb, K., McClements, L., 2021. Characterisation of cardiac health in the reduced uterine perfusion pressure model and a 3D cardiac spheroid model, of preeclampsia. Biol. Sex. Differ. 12, 31.

Rodríguez Hernández, S.A., Kroon, A.A., van Boxtel, M.P.J., Mess, W.H., Lodder, J., Jolles, J., de Leeuw, P.W., 2003. Is there a side predilection for cerebrovascular disease? Hypertension 42, 56–60.

Schleimer, K., Jalaie, H., Afify, M., Woitok, A., Barbati, M.E., Hoeft, K., Jacobs, M., Tolba, R.H., Steitz, J., 2018. Sheep models for evaluation of novel patch and prosthesis material in vascular surgery: tips and tricks to avoid possible pitfalls. Acta Vet. Scand. 60, 42.

Schmidt, C., Wendelhag, I., 1999. How can the variability in ultrasound measurement of intima-media thickness be reduced? Studies of interobserver variability in carotid and femoral arteries. Clin. Physiol. 19, 45–55.

Sokolis, D.P., 2007. Passive mechanical properties and structure of the aorta: segmental analysis. Acta Physiol. 190, 277–289.

Sokolis, D.P., Boudoulas, H., Karayannacos, P.E., 2008. Segmental differences of aortic function and composition: clinical implications. Hell. J. Cardiol. 49, 145–154.

Sokolis, D.P., Sassani, S., Kritharis, E.P., Tsangaris, S., 2011. Differential histomechanical response of carotid artery in relation to species and region: mathematical description accounting for elastin and collagen anisotropy. Med. Biol. Eng. Comput. 49, 867–879.

Stewart, J.K., Perkins, S.S., Kim, C.Y., 2017. Creation of an extraluminal arterial bypass graft using a commercially available self-expanding stent graft: feasibility study in a porcine model. Cardiovasc. Interv. Radiol. 40, 1447–1453.

Stowell, C.E.T., Li, X., Matsunaga, M.H., Cockreham, C.B., Kelly, K.M., Cheetham, J., Tzeng, E., Wang, Y., 2020. Resorbable vascular grafts show rapid cellularization and degradation in the ovine carotid. J. Tissue Eng. Regen. Med. 14, 1673–1684.

Sun, Y., Lin, C.-H., Lu, C.-J., Yip, P.-K., Chen, R.-C., 2002. Carotid atherosclerosis, intima media thickness and risk factors-an analysis of 1781 asymptomatic subjects in Taiwan. Atherosclerosis 164, 89–94.

Szafron, J.M., Ramachandra, A., Breuer, C.K., Marsden, A.L., Humphrey, J.D., 2019. Optimization of tissue engineered vascular graft design using computational modeling. Tissue Eng. Part C Methods 25, 561–570.

Taggart, D.P., 2013. Current status of arterial grafts for coronary artery bypass grafting. Ann. Cardiothorac. Surg. 2, 427–430.

Tomášek, P., Tonar, Z., Grajciarová, M., Kural, T., Turek, D., Horáková, J., Pálek, R., Eberlová, L., Králíčková, M., Liška, V., 2020. Histological mapping of porcine carotid arteries - an animal model for the assessment of artificial conduits suitable for coronary bypass grafting in humans. Ann. Anat. 228, 151434.

Tonar, Z., Kubíková, T., Prior, C., Demjén, E., Liška, V., Králíčková, M., Witter, K., 2015. Segmental and age differences in the elastin network, collagen, and smooth muscle phenotype in the tunica media of the porcine aorta. Ann. Anat. 201, 79–90.

Tonar, Z., Tomášek, P., Loskot, P., Janáček, J., Králíčková, M., Witter, K., 2016. Vasa vasorum in the tunica media and tunica adventitia of the porcine aorta. Ann. Anat. 205, 22–36.

Tschanz, S., Schneider, J.P., Knudsen, L., 2014. Design-based stereology: planning, volumetry and sampling are crucial steps for a successful study. Ann. Anat. 196, 3–11.

Tzchori, I., Falah, M., Shteynberg, D., Levin Ashkenazi, D., Loberman, Z., Perry, L., Flugelman, M.Y., 2018. Improved patency of ePTFE grafts as a hemodialysis access site by seeding autologous endothelial cells expressing Fibulin-5 and VEGF. Mol. Ther. 26, 1660–1668.

Verbrugghe, P., Verbeken, E., Pepper, J., Treasure, T., Meyns, B., Meuris, B., Herijgers, P., Rega, F., 2013. External aortic root support: a histological and mechanical study in sheep. Interact. Cardiovasc. Thorac. Surg. 17, 334–339.

Vineberg, A., Miller, G., 1951. Internal mammary coronary anastomosis in the surgical treatment of coronary artery insufficiency. Can. Med. Assoc. J. 64, 204–210.

Walpoth, B.H., Rogulenko, R., Tikhvinskaia, E., Gogolewski, S., Schaffner, T., Hess, O.M., Althaus, U., 1998. Improvement of patency rate in heparin-coated small synthetic vascular grafts. Circulation 98, II319–323; discussion II324.

Walpoth, B.H., Zammaretti, P., Cikirikcioglu, M., Khabiri, E., Djebaili, M.K., Pache, J.-C., Tille, J.-C., Aggoun, Y., Morel, D., Kalangos, A., Hubbell, J.A., Zisch, A.H., 2007. Enhanced intimal thickening of expanded polytetrafluoroethylene grafts coated with fibrin or fibrin-releasing vascular endothelial growth factor in the pig carotid artery interposition model. J. Thorac. Cardiovasc. Surg. 133, 1163–1170.

Weber, C., Reinhardt, S., Eghbalzadeh, K., Wacker, M., Guschlbauer, M., Maul, A., Sterner-Kock, A., Wahlers, T., Wippermann, J., Scherner, M., 2018. Patency and in vivo compatibility of bacterial nanocellulose grafts as small-diameter vascular substitute. J. Vasc. Surg. 68, 177S–187S.

Weizsäcker, H.W., Zierler, E., Juch, H., 2014. A simple method for vital staining of elastin in arterial tissue. Biomed. Tech. 59, 367–373.

Willekes, C., Hoeks, A.P., Bots, M.L., Brands, P.J., Willigers, J.M., Reneman, R.S., 1999. Evaluation of off-line automated intima-media thickness detection of the common carotid artery based on M-line signal processing. Ultrasound Med. Biol. 25, 57–64.

Witter, K., Tonar, Z., Matejka, V.M., Martinca, T., Jonak, M., Rokosny, S., Pirk, J., 2010. Tissue reaction to three different types of tissue glues in an experimental aorta dissection model: a quantitative approach. Histochem. Cell Biol. 133, 241–259.

Witter, K., Tonar, Z., Schöpper, H., 2017. How many layers has the adventitia? Structure of the arterial tunica externa revisited. Anat. Histol. Embryol. 46, 110–120.

Wulff, B., Stahlhoff, S., Vonthein, R., Schmidt, A., Sigler, M., Torsello, G.B., Herten, M., 2017. Biomimetic heparan sulfate-like coated ePTFE grafts reduce in-graft neointimal hyperplasia in ovine carotids. Ann. Vasc. Surg. 40, 274–284.

Zeng, Z., Wang, Q., Yang, X., Ren, Y., Jiao, S., Zhu, Q., Guo, D., Xia, K., Wang, Y., Li, C., Wang, W., 2019. Qishen granule attenuates cardiac fibrosis by regulating TGF-β /Smad3 and GSK-3β pathway. Phytomedicine 62, 152949.

Zhao, N., Zhu, D., 2013. Bioscaffolds development for small-diameter vascular grafts. Int. J. Biomed. Eng. Technol. 12, 113–129.

Seznam příloh

11.4 Příloha IV

Keša, P., Pokorná, E., **Grajciarová, M.**, Tonar, Z., Vočková, P., Trochet, P., Kopeček, M., Jakša, R., Šefc, L., Klener, P. Quantitative In Vivo Monitoring of Hypoxia and Vascularization of Patient-Derived Murine Xenografts of Mantle Cell Lymphoma Using Photoacoustic and Ultrasound Imaging. Ultrasound. Med. Biol. 2021 Apr;47(4):1099-1107. DOI: 10.1016/j.ultrasmedbio.2020.12.010. **IF(JCR2021)=2.998. Q1(Acoustics and Ultrasonics)** https://pubmed.ncbi.nlm.nih.gov/33455807/

• Original Contribution

QUANTITATIVE *IN VIVO* MONITORING OF HYPOXIA AND VASCULARIZATION OF PATIENT-DERIVED MURINE XENOGRAFTS OF MANTLE CELL LYMPHOMA USING PHOTOACOUSTIC AND ULTRASOUND IMAGING

Peter Kesa,* Eva Pokorna,[y] Martina Grajciarova,[z] Zbynek Tonar,[z] Petra Vockova,[y,x]
Philippe Trochet,[{] Milan Kopecek,[{] Radek Jaksa,[‖] Ludek Sefc,* and Pavel Klener[y,x]

* Center for Advanced Preclinical Imaging (CAPI), First Faculty of Medicine, Charles University, Prague, Czech Republic; [y] Institute of Pathological Physiology, First Faculty of Medicine, Charles University, Prague, Czech Republic; [z] Department of Histology and Embryology, Biomedical Center, Faculty of Medicine in Pilsen, Charles University, Pilsen, Czech Republic; [x] First Department of Medicine-Hematology, University General Hospital, First Faculty of Medicine, Charles University, Prague, Czech Republic; [{] FUJIFILM VisualSonics, Amsterdam, The Netherlands; and [‖] Institute of Pathology, University General Hospital, First Faculty of Medicine, Charles University, Prague, Czech Republic

Abstract—Tumor oxygenation and vascularization are important parameters that determine the aggressiveness of the tumor and its resistance to cancer therapies. We introduce dual-modality ultrasound and photoacoustic imaging (US-PAI) for the direct, non-invasive real-time *in vivo* evaluation of oxygenation and vascularization of patient-derived xenografts (PDXs) of B-cell mantle cell lymphomas. The different optical properties of oxyhemoglobin and deoxyhemoglobin make it possible to determine oxygen saturation (sO_2) in tissues using PAI. High-frequency color Doppler imaging enables the visualization of blood flow with high resolution. Tumor oxygenation and vascularization were studied *in vivo* during the growth of three different subcutaneously implanted patient-derived xenograft (PDX) lymphomas (VFN-M1, VFN-M2 and VFN-M5 R1). Similar values of sO_2 (sO_2 Vital), determined from US-PAI volumetric analysis, were obtained in small and large VFN-M1 tumors ranging from 37.9 ± 3.2 to 40.5 ± 5.0 sO_2 Vital (%) and 37.5 ± 4.0 to 35.7 ± 4.6 sO_2 Vital (%) for small and large VFN-M2 PDXs. In contrast, the higher sO_2 Vital values ranging from 57.1 ± 4.8 to 40.8 ± 5.7 sO_2 Vital (%) (small to large) of VFN-M5 R1 tumors corresponds with the higher aggressiveness of that PDX model. The different tumor percentage vascularization (assessed as micro-vessel areas) of VFN-M1, VFN-M2 and VFN-M5 R1 obtained by color Doppler (2.8 ± 0.1%, 3.8 ± 0.8% and 10.3 ± 3.7%) in large-stage tumors clearly corresponds with their diverse growth and aggressiveness. The data obtained by color Doppler were validated by histology. In conclusion, US-PAI rapidly and accurately provided relevant and reproducible information on tissue oxygenation in PDX tumors in real time without the need for a contrast agent. (E-mail: peter.kesa@lf1.cuni.cz) © 2020 The Author(s). Published by Elsevier Inc. on behalf of World Federation for Ultrasound in Medicine & Biology. This is an open access article under the CC BY-NC-ND license (http://creativecommons.org/licenses/by-nc-nd/4.0/).

Key Words: Photoacoustic imaging, Tumor hypoxia, Tumor vascularization, Patient-derived xenograft, Mantle cell lymphoma.

INTRODUCTION

Tumor oxygenation and vascularization are important parameters for monitoring tumor growth and can be used to detect changes within the tumor micro-environment in pre-clinical research (Fukumura and Jain 2007; Jing et al. 2019). The density and functionality of tumor vascularization are associated with the local distribution of metabolites and oxygen saturation (sO_2) in cancer tissues (Liao and Johnson 2007). Cellular hypoxia is characterized by an insufficient supply of oxygen and can be detected by means of fluorescent probes (Kiyose et al. 2010; Takahashi et al. 2012), matrix assisted laser desorption/ionization - mass spectrometry imaging (MALDI-MSI)/immunohistology staining (Jiang et al. 2015) or computed tomography/positron emission tomography (Sun et al. 2011; Fleming et al. 2015; Peeters et al. 2015). While these techniques are effective

Address correspondence to: Peter Kesa, Center for Advanced Preclinical Imaging (CAPI), First Faculty of Medicine, Charles University, Salmovska 3, 120 00 Prague 2, Czech Republic. E-mail: peter.kesa@lf1.cuni.cz

tools, they are unable to provide anatomic and molecular insight into the tumor core without the use of exogenous contrast agents in real time, which causes limitations (e. g., side effects of ionizing radiation and interactions between fluorophores and potential cancer therapies) for their routine use for the dynamic *in vivo* monitoring of lymphoma-bearing mice.

Photoacoustic imaging (PAI) is a biomedical non-invasive, non-ionizing, low-cost and real-time imaging modality that allows *in vivo* diagnostics. A photoacoustic signal is generated by a light beam from a nanosecond-pulsed laser of appropriate wavelength, which is absorbed by endogenous or exogenous agents, thereby producing localized heating. Because the optical absorption of the photoacoustic agent is followed by localized thermal expansion, the electromagnetic radiation is transformed into pressure waves that can be detected using an ultrasound (US) transducer. The signals originating from tissues are spatially localized and can be interpreted as a photoacoustic response (Xu and Wang 2006; Emelianov et al. 2009).

The use of PAI has been increased for pre-clinical imaging of small animals because of the sufficient penetration depth and excellent spatial resolution down to several tens of micrometers (Zhang et al. 2019). PAI also offers monitoring and subsequent quantification of multiple metabolites simultaneously by scanning two or more wavelengths for each tissue slice (Xia et al. 2014; Lavaud et al. 2017). The acquired data can be used to generate a final 3-D volume with a spatial localization of chromophores, thereby providing anatomic, molecular and functional imaging in real time (Toumia et al. 2018; Lavaud et al. 2020). In addition, US imaging can also detect tumor vascularization using color Doppler or power Doppler modes, which are widely used in pre-clinical and clinical diagnostics (Chen et al. 2013). Compared with optical fluorescence imaging, *in vivo* ultrasound and photoacoustic imaging (US-PAI) allows the detection of fine inner organ structure and endogenous metabolites such as deoxyhemoglobin and oxyhemoglobin using dual-wavelength (750/850 nm) scanning (Xia et al. 2014). The combined use of US-PAI is therefore a unique tool for monitoring tissue oxygenation and vascularization in subcutaneous tumors.

Mantle cell lymphoma (MCL) is a rare, usually aggressive type of B-cell non-Hodgkin lymphoma (Klener 2019). Micro-vessel density (MVD) in pre-therapeutic extra-medullary MCL samples of 177 patients negatively correlated with their survival (Vesel a et al. 2014). Several of the anti-lymphoma agents approved for the therapy of relapsed/refractory (R/R) MCL (*e.g.,* temsirolimus, lenalidomide or bortezomib) have at least partial anti-angiogenic activity (Oikawa et al. 1998; Dredge et al. 2005; Bufalo et al. 2006; Lane et al. 2009; Lu et al. 2009; Guo et al. 2018; Zarfati et al. 2019).

Patient-derived lymphoma xenografts (PDXs) are derived by the xenotransplantation of primary lymphoma cells into immunodeficient mice. It was repeatedly demonstrated that PDXs are relevant pre-clinical models for the study of the biology and pre-clinical evaluation of experimental treatment approaches (Ghapuy et al. 2016; Towsend et al. 2016; Prukova et al. 2019). The extent of vascularization (MVD and micro-vessel area [MVA]) and level of patient-derived xenograft (PDX) oxygenation during lymphoma PDX growth has not been systemically studied.

In this study, we analyzed the levels of oxygenation and vascularization percentage (as an MVA) of three different PDX models derived from patients with relapsed/refractory MCL during their growth in immunodeficient mice. The goal of this study was to examine the use of US-PAI for the anatomical and molecular imaging of tumors in the murine body, which is beyond the reach of the commonly used fluorescence-based imaging modalities. In addition, this work is the first study of PDXs of MCL using multi-modal US-PAI.

MATERIAL AND METHODS

PDX and immunodeficient mice

The PDX models used in this study (VFN-M1, VFN-M2 and VFN-M5 R1) were established at the Institute of Pathological Physiology, First Faculty of Medicine, Charles University (Prague, Czech Republic) as previously described (Klanova et al. 2014). We repeatedly demonstrated that PDX cells kept the majority of the somatic mutations found in the primary lymphoma cells from which they were derived (Prukova et al. 2019; Lemm et al. 2020).

Adult female NOD.Cg-Prkdc^{scid} Il2 rg$^{tm1 \ Wjl}$/SzJ mice (referred to as NSG mice) were purchased from The Jackson Laboratory (Bar Harbor, Maine, USA). The mice were maintained in individually ventilated cages (Tecniplast S.p. A., Buguggiate Italy) (12/12 h light/dark cycle, 22°§ 1°C, 60% §% humidity) and were supplied with food (standard breeding diet for mice and rats; 10 mm pellets, Altromin Spezialfutter GmbH & Co. KG, Lage, Germany) and water *ad libitum*. The experimental design was approved by the Institutional Animal Care and Use Committee (MSMT-7025/2018-2). On day 0 (D), PDX cells were subcutaneously injected into the right side of the abdomen of the NodCg mice (10 million cells per animal). A tumor growth curve was measured using a digital caliper in three perpendicular tumor dimensions for each animal.

Before imaging, the mice were anesthetized using an intraperitoneal application of ketamine/xylazine saline solution (80/10 mg/kg^{-1}; both ketamine and xylazine were purchased from Bioveta Inc., Ivanovice na Han e, Czech Republic) and were shaved using hair

remover shaving gel (Strep, Milan, Italy). The animals were placed on a heated table (FUJIFILM VisualSonics, Inc., Toronto, Ontario, Canada), maintaining a stable temperature (37.7°C), in a supine position and connected to four electrodes using highly conductive US gel.

High-frequency US-PAI and data post-processing

Anatomic and molecular imaging were carried out using Vevo 3100/LAZR-X (US/photoacoustic) imaging multi-modality (FUJIFILM VisualSonics, Inc.). A high-frequency US M$_S$400 transducer (256 elements linear array, 50 μm axial resolution) (FUJIFILM VisualSonics, Inc.) working at 30 MHz center frequency (OxyHemo mode) and 24 MHz (color mode) equipped with an original jacket for inserting the narrow optical fiber bundle (14 mm) optical cable (FUJIFILM VisualSonics, Inc.) was chosen to perform the US-PAI of tumors in B-mode, OxyHemo mode and color Doppler mode using mouse large abdominal preset. The total photoacoustic gain for all patterns was adjusted to 40 dB in all records. The time gain compensation settings have been optimized to see deep within tumor tissues by increasing the photoacoustic gain of each pattern (20-62-65-72-75 dB), beginning with the upper distance from the transducer surface (7 mm) and proceeding to the bottom tumor layer (US/photoacoustic field of view 7–18 mm for small and medium tumors and 7–20 mm for large tumors). The tumor skin line was positioned to 10 mm from the transducer surface to achieve the best light penetration. These parameters were kept constant during tumor growth. A bubble-free transparent US gel (OXD, Barcelona, Spain) was applied to facilitate US transmission in all US scans. Color Doppler images were acquired using the following settings: Pulse Repetition Frequency (PRF): 3; gate: 2 and 3; Doppler gain: 36 dB; beam angle: 0; sensitivity: 3 and 4; persistence: off; wall filter: medium; and priority: 80%. Different settings were used for small and large tumors (small tumors: sensitivity: 3, gain: 2; middle and large tumors: sensitivity: 4, gain: 3) to correlate the influence of blood flow to method sensitivity. During all acquisitions, the electrocardiogram activity of the patients was monitored, and respiratory gating was enabled to prevent artifacts from breathing. All 3-D US records were acquired using an 80 μm step size on a motorized Vevo Rail system (FUJIFILM VisualSonics, Inc.). The anaesthetized mice were heated on a plate heater with adjusted temperature (37.7°C) until they woke up.

The US-PAI data obtained during the procedures were post-processed using Vevo LAB V.3.2.5. software (FUJIFILM VisualSonics, Inc.). Values for tumor volume in mm^3 were determined by volumetric analysis in software Vevo LAB. Values for sO$_2$ in tissues (sO$_2$ Vital: average sO$_2$ of the color pixels that contain a signal within the photoacoustic region [%]) and tumor vasculature area (%) were obtained from tumor volumetric

analysis at four time points. The total value of sO$_2$ (sO$_2$ Total) in each tumor type was investigated using a different approach of the Vevo LAB V.3.2.5. software to process the results; all of the pixels in the photoacoustic region were examined, including the black pixels (black pixels have a value of 0%), and therefore the final results also include necrotic areas on the tumors (the hemoglobin threshold[HbT] was set to 20%). Thus, the areas in the tumor with oxygenation of less than 20% (black pixels) were assessed to be necrotic.

Specimens and histologic processing

Three pairs of PDX tissue blocks (obtained from lymphoma-bearing mice) were investigated by immunohistochemistry (IHC). In each pair, two of the PDX blocks were small subcutaneous tumors (approximately 1 cm in the largest diameter), while the other two represented large subcutaneous tumors (approximately 2 cm in the largest diameter). Five randomly oriented slides were processed from each PDX block. The endothelium was visualized using IHC rabbit anti-mouse CD31 monoclonal IgG, clone SP38 (Thermo Fisher Scientific, Rockford, IL, USA).

Quantification of MVD and MVA

Using a 40$\times$ microscope lens, 10 micrographs were taken from each slide (*i.e.,* 50 micrographs per tissue block) using systematic uniform random sampling (Fig. S1; for details, see Tonar et al. 2008 and Vesel a et al. 2014). Two parameters were used to quantify the intratumoral micro-vessels (Supplementary Table S1, online only). First, the MVD (Fig. S2A) was quantified as the number of CD31-positive micro-vessel profiles per area of the section. Using a method similar to those described in previous publications (Vesel a et al. 2014; Petrakis et al. 2019), a countable vessel was defined as any profile of CD31-positive endothelial cells or endothelial cell clusters that was separate from adjacent micro-vessels. Vessel profiles located fully inside the un-biased counting frame (Gundersen 1977) or those intersecting the acceptance line, but not the rejection line, was counted. Second, the MVA (Fig. S2B) was estimated as the sum of the area profiles of CD31-positive micro-vessels divided by the total area of the tissue (Petrakis et al. 2019). The histologic quantification was performed using the CountingFrame and PointGrid modules in Ellipse stereological software (ViDiTo, Ko sice, Slovak Republic).

Statistical analysis

All numerical data were analyzed using OriginPro 8 (OriginLab Corporation, Northampton, MA, USA) software and are presented as mean $\pm$ standard error of mean (mean $\pm$ SEM). One-way analysis of variance was used for comparison of the vascularization percentage

(MVA), percentage rate of sO_2 vital and sO_2 Total of the three tumors (VFN-M1, VFN-M2 and VFN-M5 R1). The tumors were compared at the same timepoint. A p -value of <0.05 was considered significant.

RESULTS

Anatomic and molecular imaging of PDXs derived from patients with MCL: from hypoxia to necrosis

The combined approach of photoacoustic monitoring of sO_2 in tissues and US Doppler imaging allows the non-invasive spatial determination of oxygenated and necrotic areas together with tumor perfusion in real time. Three different lymphoma PDXs, namely VFN-M1 (n = 3 mice), VFN-M2 (n = 3 mice) and VFN-M5 R1 (n =3 mice) were used in this study.

In all three PDX models, levels of sO_2 Total ($p = 0.04134$) and MVA (percentage of vascularization obtained from color Doppler measurements) decreased significantly with increasing tumor volumes (Fig. 1). The average sO_2 Vital ($p = 0.80459$) values (mean § SEM) (from small to large tumor size) in the VFN-M1 and VFN-M2 models were similar and ranged from 37.9 § 2.2 to 40.5 § 6.0 sO_2 Vital (%) for VFN-M1 (Fig. 1a) and from 37.5 §0 to 35.7 4.6 §O_2 Vital (%) for VFN-M2 (Fig. 1b). In contrast, the values for VFN-M5 R1 were higher and ranged from 57.1 § 4.8 to 40.8 § 5.7 sO_2 Vital (%) (Fig. 1c). VFN-M5 R1 engrafted and reached a tumor size of approximately 250 mm^3 significantly earlier (D+13) than VFN-M1 (D+21) and VFN-M2 (D+20). Compared to VFN-M5 R1 (Fig. 2), both VFN-M1 and VFN-M2 tumors were markedly less oxygenated and had several clearly discernible necrotic areas already at small tumor sizes (Fig. 3 and 4). Because of increasing necrotic areas, increasing differences between sO_2 Vital (%) and sO_2 Total (%) were observed between the small and large tumors across all three PDX models (Table 1).

The vascularization of the analyzed PDX tumors is shown as a 3-D visualization in Figure 3. A steady decrease in the extent of vascularization was observed in VFN-M1 and VFN-M2 with increasing tumor size (Fig. 1; $p = 0.00329$). In contrast, the development of vascularization in VFN-M5 R1 was more complex, with an initial decrease (at the stage of middle-sized tumors) followed by a terminal increase (at the stage of large tumors).

Comparison of vascularization between histology and US data

An external evaluation of the vascularization of the analyzed PDX tumors was performed by examining CD31-positive endothelial cells to verify the results provided by the US color Doppler mode.
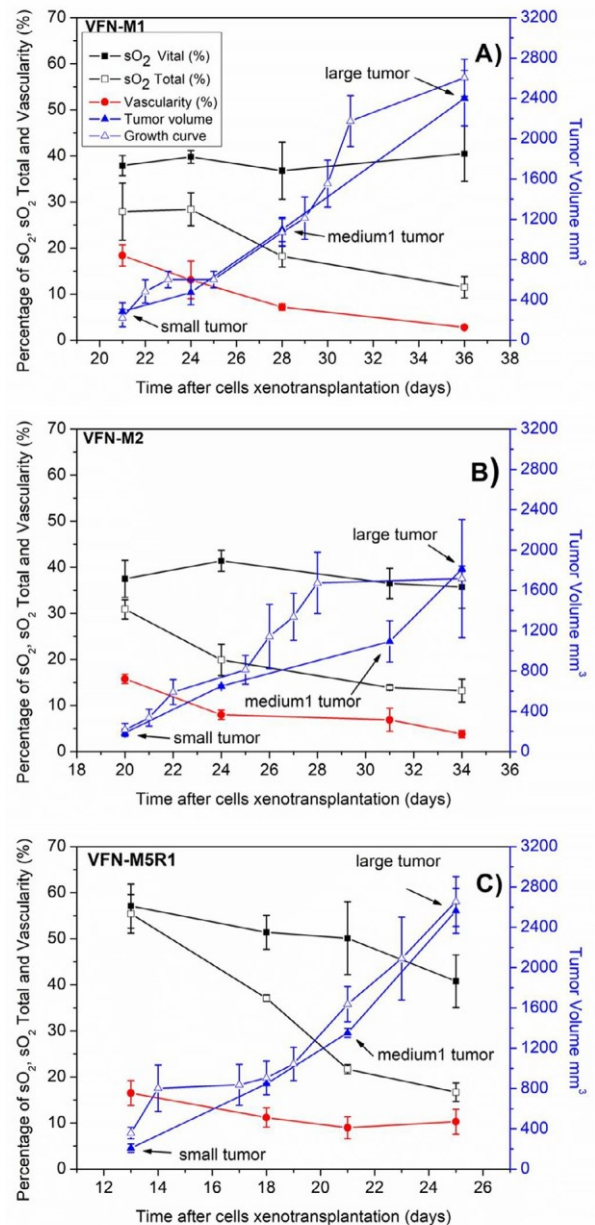

Fig. 1. Graphical representation of tumor hypoxia, vascularization and tumor volume versus time after cell xenotransplantation. Tumor hypoxia was determined by saturated oxygen (sO_2 Vital) (*full black squares*), tumor oxygenation including necrotic areas (sO_2 Total, *empty black squares*) and the percentage of tumor micro-vessel area in the tumor obtained by color Doppler (*red circles*). Tumor volume in mm^3 was determined by ultrasound (US) volumetric analysis (*blue triangles*), and tumor growth curves were calculated from three perpendicular tumor dimensions measured by digital caliper (*blue empty triangles*) plotted versus time (d) after cells xenotransplantation for VFN-M1 (a), VFN-M2 (b) and VFN-M5 R1 (c) tumors. Oxygen saturation (sO_2 Vital; $p = 0.80459$), sO_2 Total ($p = 0.04134$) and micro-vessel area (percentage of vascularization; $p = 0.00329$) were evaluated for the entire tumor volume.
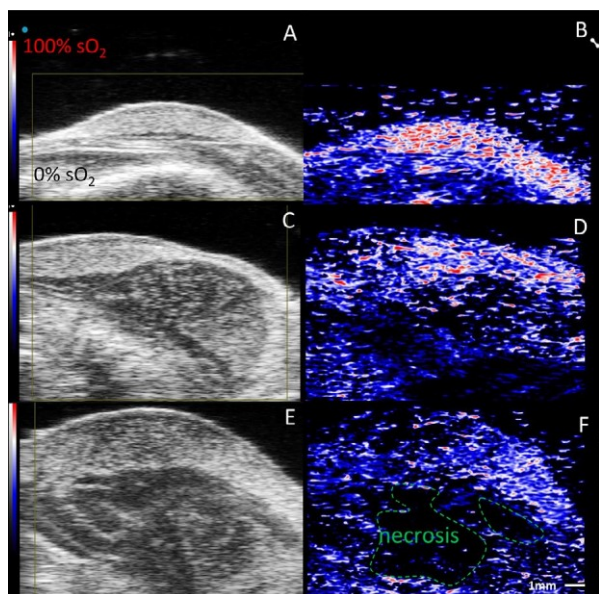
Fig. 2. Representative set of anatomic images of VFN-M5 R1 tumor recorded in B-mode and OxyHemo mode. Different tissue architecture (brighter shade vs. darker areas) clearly corresponds to photoacoustic slides (b, d, f) of small, medium and large tumors and depicts vital areas (brighter pixels in a B-mode and more oxygenated places in photoacoustic OxyHemo mode observed as blue and red pixels, respectively) and less oxygenated and thus, necrotic areas inside tumors. Because of the necrotic areas, increasing differences between sO_2 Vital and Total sO_2 (%) were obtained between the medium1 tumors (50.1 § 7.9 and 21.7 § 1.0) and large tumors (40.8 § 5.7 and 16.7 § 2.0). Scale bar 1 mm.

The values of quantified CD31 positive micro-vessel profiles (MVA) were found to be lower in all small PDX models (*i.e.,* VFN-M1, VFN-M2 and VFN-M5 R1 [6.8% § 0.2%, 8.0% § 0.7% and 6.9% § 0.5%]) compared with the data obtained by the color Doppler (18.4% § 2.3%, 15.8% § 1.0% and 16.5% § 2.7%). In contrast, at the stage of large PDX models, MVAs by IHC were significantly higher than those measured by color Doppler in VFN-M1 (4.8% 0§% and 2.8% § 0.1%) and VFN-M2 (8.6% 0§% and 3.8% 0.8% § and were comparable in VFN-M5 R1 (10.7% § 0.8% and 10.3% §.7%). The MVA sectional profiles in the VFN-M1 PDX model are shown in Figure 4. The results of the histologic analysis of the small and large tumors are shown in Table 2.

Comparison of MVD and MVA between small and large lymphomas in individual PDX models

According to the histology, there were no significant differences in either MVD or MVA between small and large VFN-M1 and VFN-M2 PDX tumors. In contrast, differences in MVD and MVA were observed between small and large VFN-M5 R1 tumors.

DISCUSSION

General findings of MCL PDX oxygenation and vascularization

PDX models enable the study of the biology of aggressive lymphomas *in vivo*, including the complex process of neo-vascularization and its impact on the engraftment, growth and spread of lymphoma cells. In this study, we described a highly relevant, non-invasive and reproducible method that provides dynamic imaging of sO_2 and MVA during lymphoma growth in immuno-deficient mice.

Our results demonstrated that sO_2 Vital levels (measured from the viable tumor areas) of VFN-M1 and VFN-M2 models remained virtually unchanged from the stage of small (approximately 250 mm^3) to large (approximately 1500 mm^3) tumors. In VFN-M5 R1 a moderate decrease in sO_2 Vital levels was observed at the stage of large tumors. In sharp contrast, sO_2 Total (which included necrotic areas) showed a significant decrease with increasing tumor size across all PDX models. The observed difference between sO_2 Vital and sO_2 Total values clearly corresponds to the presence of vital and necrotic areas inside the tumors (Rich and Seshadri 2016). The areas inside the tumor core with a total sO_2 of less than 20% can be assessed as necrotic tissues (Gerling et al. 2014). The presence of early necrotic areas found in VFN-M1 and VFN-M2 tumors resulted in a decrease in sO_2 Total of around 10%, while VFN-M5 R1 tumors exhibited a minimal change between sO_2 Vital and sO_2 Total at small tumor sizes because of a lack of discernible necrotic areas.

Analogously, the vascularization evaluated by color Doppler from the total tumor decreased with increasing tumor size in VFN-M1 and VFN-M2 PDX models. We suggest that the decrease is caused by increasing numbers of necrotic areas. The vascularization of viable tumor areas in VFN-M1 and VFN-M2 PDX models evaluated by histology remain comparable. In contrast, VFN-M5 R1 exhibited increased vascularization at the stage of large tumors, which was confirmed by increased MVD by IHC. We can speculate that the increased MVD and MVA at the stage of large VFN-M5 R1 tumors might be at least partially caused by decreased sO_2.

Both the shortest engraftment time (13 d in VFN-M5 R1 compared with 21 and 20 d in VFN-M1 and VFN-M2, respectively), and the highest MVA and MVD, both by IHC analysis and US-PAI, suggest that VFN-M5 R1 possesses the highest biological aggressiveness, probably as a result of more effective pro-angiogenic activity. Medium VFN-M5 R1 (500–1000 mm^3) tumors were also supported by a large number of detectable narrow blood vessels, especially in the upper section of the tumor, which supplied increased levels of oxygen (Fig. 2d). We
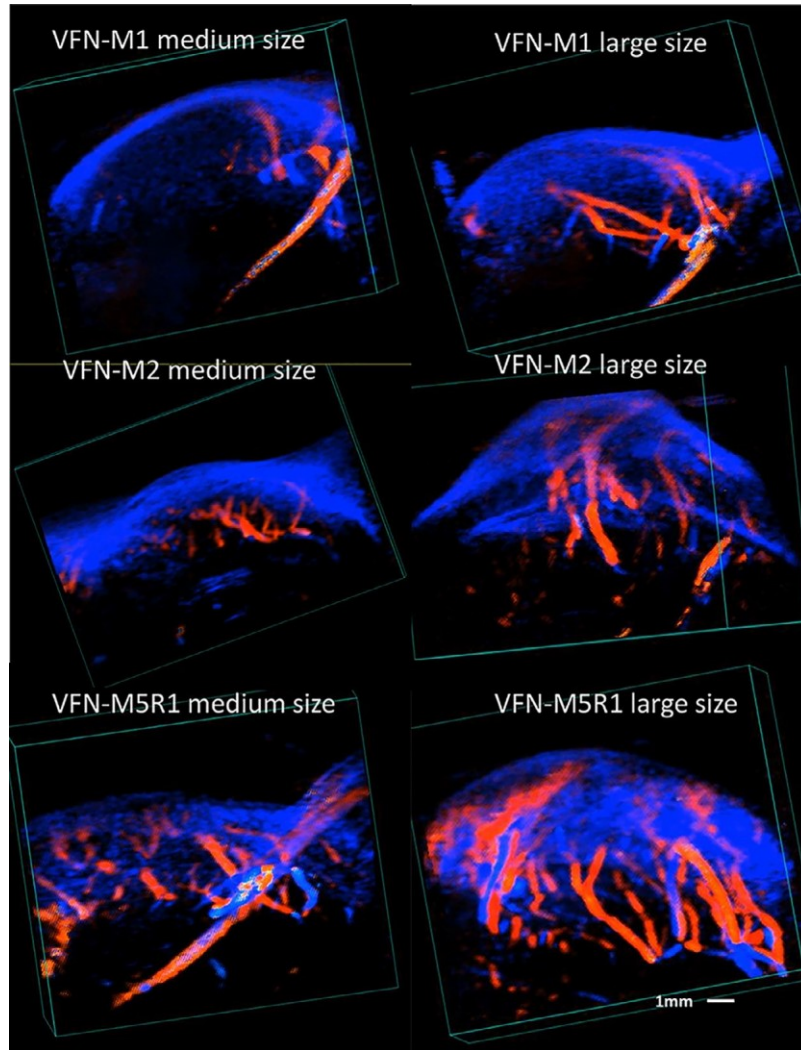
Fig. 3. Sets of 3-D color Doppler models of tumor vascularization visualized in a render mode. Different stages of patient-derived xenograft (PDX) tumors in tumor vascularization of medium1 (left column) and large (right column) tumors of VFN-M1 (top), VFN-M2 (middle) and VFN-M5 R1 (bottom). Blue color represents blood flow away from the transducer, and red depicts blood flow toward the transducer. Scale bar 1 mm.

hypothesize that the observed early tumor formation may be at least partially supported by these narrow micro-vessels. In contrast, regions in which no micro-vascularization was detected were characterized by high level of necrosis, while vital areas alone were supplied through neo-vascularization and showed measurable levels of sO_2. Compared to VFN-M1 and VFN-M2, VFN-M5 R1 xenografts maintained rich and chaotic vascularization at the stage of large tumors, a feature which facilitates survival and growth.

Comparison between US and IHC: advantages and disadvantages of both methods

The main advantages of US-PAI and color Doppler are that they eliminate the need for exogenous contrasts, thus offering the possibility of non-invasive *in vivo* monitoring,
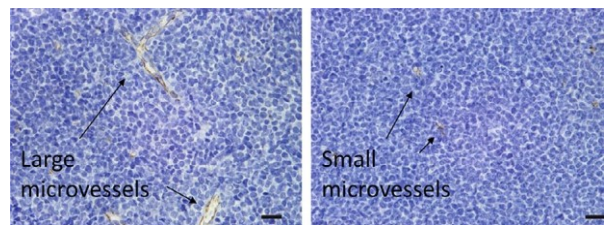

Fig. 4. Representative example of VFN-M1 xenograft CD31 immunohistochemistry. Sample of tumor larger micro-vessels (a) and smaller micro-vessels (b) found in different tissue slides of VFN-M1. These examples illustrate the presence of areas without smaller (a) and larger (b) micro-vessels in the tumor (for more details, see Fig. 1). The heterogeneity of distribution of micro-vessel densities and areas underlines the importance of extensive histologic sampling. CD31-positive endothelial cells are labelled in brown. Scale bar 20 μm.

Table 1. Mean values and standard errors of mean values (mean ± SEM) of sO₂ Vital (%), sO₂ Total (%) and MVA (%) obtained from US-PAI for VFN-M1, VFN-M2 and VFN-M5 R1 at four time points

PDX model	VFN-M1			VFN-M2			VFN-M5 R1		
Parameter/ timepoint	sO₂ Vital (%)	sO₂ Total (%)	MVA (%)	sO₂ Vital (%)	sO₂ Total (%)	MVA (%)	sO₂ Vital (%)	sO₂ Total (%)	MVA (%)
First (small)	37.9 ± 2.2	27.9 ± 6.2	18.4 ± 2.3	37.5 ± 4.0	30.9 ± 2.1	15.8 ± 1.0	57.1 ± 4.8	55.4 ± 4.2	16.5 ± 2.7
Second (medium 1)	39.8 ± 1.4	28.4 ± 3.6	13.1 ± 4.1	41.4 ± 2.3	19.9 ± 3.4	8.0 ± 1.0	51.4 ± 3.7	37.1 ± 0.7	11.2 ± 2.1
Third (medium 2)	36.8 ± 6.2	18.2 ± 2.3	7.2 ± 0.7	36.5 ± 3.3	13.9 ± 0.5	6.9 ± 2.5	50.1 ± 7.9	21.7 ± 1.0	9.0 ± 2.4
Fourth (large)	40.5 ± 6.0	11.5 ± 2.3	2.8 ± 0.1	35.7 ± 4.6	13.2 ± 2.5	3.8 ± 0.8	40.8 ± 5.7	16.7 ± 2.0	10.3 ± 2.7

Computed p values: 0.80459 (sO₂ Vital); 0.04134 (sO₂ Total); 0.00329 (MVA).
MVA, micro-vessel areas; PDX, patient-derived xenograft; US-PAI ultrasound and photoacoustic imaging.

in contrast to the usually used procedures such as IHC analysis. On the other hand, the impact of anesthesia during the *in vivo* imaging is also important. Greening et al. (2018) have reported that isoflurane concentrations greater than 2% can affect tissue hemoglobin (HbO₂) concentration, thereby requiring the use of ketamine/xylazine solutions. Another method that can be used for the measurement of sO₂ in tissue instead of PAI, diffuse reflectance spectroscopy, does not provide anatomic imaging (Awan et al. 2011; Dadgar et al. 2018). Diffuse optical tomography (DOT) can also provide oxygenation information capability concurrently with anatomic imaging using MRI or US as an anatomic co-registering imaging modality (Merritt et al. 2003; Durduran et al. 2010), but the feasibility and spatial resolution is not comparable (Bauer et al. 2011; Li et al. 2018) to low-cost US-PAI in which both anatomic and molecular information is obtainable in real-time and in one step.

The observed discrepancies between MVA obtained by IHC and color Doppler could be caused by several factors. First, formaldehyde fixation, paraffin embedding and histologic sectioning leads to tissue shrinkage. In this situation, micro-vessel profiles have a strong tendency toward post-mortem collapse, which can result in artificial diminishing of the tumor MVA on slides (West 2013). This may be the main reason for the observed lower values of MVA obtained by IHC compared with PAI with small tumors. Second, while IHC analysis was evaluated from viable tumor areas, vascularization assessed by PAI was measured from the whole tumor, including necrotic areas. As a result, vascularization by color Doppler was significantly lower than MVA obtained by IHC at the stage of large PDX tumors, which exhibited the largest areas of necrotic tissue in the VFN-M1 and VFN-M2 PDX models. In addition, higher color Doppler settings (of sensitivity and gate) were used to provide uniform conditions for small (less than 500 mm³) and medium (approximately 1000 mm³) tumors. In contrast, large VFN-M1 and VFN-M2 xenografts were defined by a vascular profile formed by a wider individual venous system without any significant presence of small vessels, and this can explain why the

Table 2. Histologic analysis of small and large PDX tumors by immunohistochemistry analysis of murine CD31.

PDX model	Tumor size	Micro-vessel density (MVD) (vascular profiles/mm²)	Micro-vessel area (MVA) (%)
VFN-M1	Small	88 ± 3.3	6.8 ± 0.2
VFN-M1	Large	87 ± 6.5	4.8 ± 0.3
VFN-M2	Small	101.4 ± 8.8	8.0 ± 0.7
VFN-M2	Large	98.1 ± 3.6	8.6 ± 0.6
VFN-M5 R1	Small	66.3 ± 3.6	6.9 ± 0.5
VFN-M5 R1	Large	110.2 ± 7.7	10.7 ± 0.8

Mean values and standard error of mean (mean ± SEM) for each individual tumor were calculated from ten samples.
PDX, patient-derived xenograft.

values obtained for VFN-M1 and VFN-M2 from the *in vivo* color Doppler measurements are lower than those of the histologic analysis. Using these settings, color Doppler was not sensitive enough to detect lower levels of blood flow in capillaries with a diameter measured in several tens of microns. The similar MVA obtained from IHC analysis and color Doppler measurement for the VFN-M5 R1 xenograft is related to the rich and chaotically organized vascularization of these tumors and suggests that the VFN-M5 R1 tumors lack a significant network of narrow vessels. We speculate that the observed higher aggressivity and faster growth of VFN-M5 R1 are results of the high extent of tumor perfusion together with the increased levels of sO₂ in the vital sections of the tumor.

Insufficient sensitivity of color Doppler in detection of tiny capillaries: current and future situation

The results of this study show that the color Doppler method is unable to detect capillaries with a diameter of less than approximately 50 μm because of the low level of blood flow in tiny vessels. The Doppler effect is used to measure differences in movement. The color Doppler mode is not sensitive enough to detect blood motion in tiny capillaries and, of course, the color Doppler sensitivity depends on the transducer frequency. It must be

emphasized that this method does not require any exogenous contrast agents. Although exogenous contrast agents are not the topic of our study, a dynamic contrast-enhanced ultrasound imaging technique does exist, which uses micrometer-sized micro-bubbles based on a gas core and lipid shell for the dynamic detection of fine blood flow in capillaries with a diameter down to 10 μm. (Pysz et al. 2011; Bar-Zion et al. 2016; Toumia et al. 2018).

Potential future refinements of US-PAI as a tool for the direct assessment of tumor oxygenation and micro-vascularization include the possibility of developing nanoplatforms for the oxygen-enhanced diagnosis of hypoxia, vascularization and necrosis (Tomaszewski et al. 2018). Trimodal US-PAI/MRI oxygenated theragnostic nanoplatforms alleviating tumor hypoxia in combination with oxygen-enhanced chemotherapy may also have a positive effect on tumor growth (Zhou et al. 2019). The early detection of tumor aggressiveness by US-PAI measurements of tumor oxygenation and vascularization and subsequent oxygen-enhanced treatment of PDX MCL tumors, together with appropriately adjusted conventional therapy, could be the next step in PDX treatment.

CONCLUSIONS

The level of sO$_2$ and extent of neo-vascularization are critical factors that impact tumor aggressivity. Multimodal US-PAI offer a new approach for rapid, reliable and direct assessment of sO$_2$ in PDX tumors of various origins with no need for an exogenous contrast agent. This high-resolution anatomic imaging method, with detail as fine as 50 μm, supported by the detection of blood flow, can be used for the dynamic *in vivo* assessment of tumor vascularization and oxygenation or for evaluating the impact of anti-angiogenic, or nano-scale treatment approaches that rely on the enhanced permeability and retention effect on tumor vascularization and oxygenation.

SUPPLEMENTARY MATERIALS

Supplementary material associated with this article can be found in the online version at doi:10.1016/j.ultrasmedbio.2020.12.010.

REFERENCES

Awan ZA, Häggblad E, Wester T, Kvernebo MS, Halvorsen PS, Kvernebo K. Diffuse reflectance spectroscopy: Systemic and microvascular oxygen saturation is linearly correlated and hypoxia leads to increased spatial heterogeneity of microvascular saturation. Microvasc Res 2011;81:245–251.

Bar-Zion A, Yin M, Adam D, Foster FS. Functional flow patterns and static blood pooling in tumors revealed by combined contrast-enhanced ultrasound and photoacoustic imaging. Cancer Res 2016;76:4320–4331.

Bauer AQ, Nothdurft RE, Erpelding TN, Wang LV, Culver JP. Quantitative photoacoustic imaging: Correcting for heterogenous light fluence distributions using diffuse optical tomography. J Biomed Opt 2011;16 096016.

Bufalo DD, Ciuffreda L, Trisciuoglio D, Desideri M, Cognetti F, Zupi G, Milella M. Antiangiogenic potential of the mammalian target of rapamycin inhibitor temsirolimus. Cancer Res 2006;66:5549–5554.

Chapuy B, Cheng H, Watahiki A, Ducar MD, Tan Y, Chen L, Roemer MGM, Ouyang J, Christie AL, Zhang L, Gusenleitner D, Abo RP, Farinha P, von Bonin F, Thorner AR, Sun HH, Gascoyne RD, Pinkus GS, van Hummelen P, Wulf GG, Aster JC, Weinstock DM, Monti S, Rodig SJ, Wang Y, Shipp MA. Diffuse large B-cell lymphoma patient-derived xenograft models capture the molecular and biological heterogeneity of the disease. Blood 2016;127:2203–2213.

Chen JJ, Fu SY, Chiang CS, Hong JH, Yeh CK. A preclinical study to explore vasculature differences between primary and recurrent tumors using ultrasound doppler imaging. Ultrasound Med Biol 2013;39:860–869.

Dadgar S, Troncoso JR, Rajaram N. Optical spectroscopic sensing of tumor hypoxia. J Biomed Opt 2018;23 067001.

Dredge K, Horsfall R, Robinson SP, Zhang LH, Lu L, Tang Y, Shirley MA, Muller G, Schafer P, Stirling D, Dalgleish AG, Bartlett JB. Orally administered lenalidomide (CC-5013) is anti-angiogenic in vivo and inhibits endothelial cell migration and Akt phosphorylation in vitro. Microvasc Res 2005;69:56–63.

Durduran T, Choe R, Baker WB, Yodh AG. Diffuse optics for tissue monitoring and tomography. Rep Prog Phys 2010;73 076701.

Emelianov SY, Li PC, O'Donnell M. Photoacoustics for molecular imaging and therapy. Phys Today 2009;62:34–39.

Fleming IN, Manavaki R, Blower PJ, West C, Williams KJ, Harris AL, Domarkas J, Lord S, Baldry C, Gilbert FJ. Imaging tumour hypoxia with positron emission tomography. Br J Cancer 2015;112:238–250.

Fukumura D, Jain RK. Tumour microvasculature and microenvironment: Targets for anti-angiogenesis and normalization. Ultrasound Med Biol 2007;74:72–84.

Gerling M, Zhao Y, Nania S, Norberg KJ, Verbeke CS, Englert B, Kuiper RV, Bergström Å, Hassan M, Neesse A, Löhr JM, Heuchel RL. Theranostics 2014;4:604–613.

Greening GG, Miller KP, Spainhour CR, Cato MD, Muldoon TJ. Effects of isoflurane anesthesia on physiological parameters in murine subcutaneous tumor allografts measured via diffuse reflectance spectroscopy. Biomed Opt Express 2018;9:2871–2886.

Gundersen HJ. Notes on the estimation of the numerical density of arbitrary profiles: The edge effect. J Microsc 1977;111:219–223.

Guo H, Sun L, Yang L, Liu X, Nie Z, Luo J. Microvesicles shed from bortezomib-treated or lenalidomide-treated human myeloma cells inhibit angiogenesis in vitro. Oncol Rep 2018;39:2873–2880.

Jiang L, Chughtai K, Purvine SO, Bhujwalla ZM, Raman V, Tolic P, Heeren RMA, Glunde K. MALDI-MASS spectrometric imaging revealing hypoxia-driven lipids and proteins in a breast tumor model. Anal Chem 2015;87:5947–5956.

Jing X, Yang F, Shao C, Wei K, Xie M, Shen H, Shu Y. Role of hypoxia in cancer therapy by regulating the tumor microenvironment. Mol Cancer 2019;18:157.

Kiyose K, Hanaoka K, Oushiki D, Nakamura T, Kajimura M, Suematsu M, Nishimatsu H, Yamane T, Terai T, Hirata Y, Nagano T. Hypoxia-sensitive fluorescent probes for in vivo real-time fluorescence imaging of acute ischemia. J Am Chem Soc 2010;132:15846–15848.

Klanova M, Soukup T, Jaksa R, Molinsky J, Lateckova L, Maswabi BCL, Prukova D, Brezinova J, Michalova K, Vockova P, Hernandez Ilizalituri F, Kulvait V, Zivny J, Vokurka M, Necas E, Trneny M, Klener P. Mouse models of mantle cell lymphoma, complex changes in gene expression and phenotype of engrafted MCL cells: Implications for preclinical research. Lab Invest 2014;94:806–817.

Klener P. Advances in molecular biology and targeted therapy of mantle cell lymphoma. Int J Mol Sci 2019;20:4417.

Lane HA, Wood JM, McSheehy PMJ, Allegrini PR, Boulay A, Brueggen J, Littlewood-Evans A, Maira SM, Martiny-Baron G, Schnell CR, Sini P, O'Reilly T. mTOR inhibitor RAD001 (everolimus) has antiangiogenic/vascular properties distinct from a VEGFR tyrosine kinase inhibitor. Clin Cancer Res 2009;15:1612–1622.

Lavaud J, Henry M, Coll JL, Josserand V. Exploration of melanoma metastasis in mice brains using endogenous contrast photoacoustic imaging. Int J Pharm 2017;532:704–709.

Lavaud J, Henry M, Gayet P, Fertin A, Vollaire J, Usson Y, Coll JL, Josserand V. Noninvasive monitoring of liver metastasis development via combined multispectral photoacoustic imaging and fluorescence diffuse optical tomography. Int J Biol Sci 2020;16:1616–1628.

Lemm EA, Valle-Argos B, Smith LD, Richter J, Gebreselassie Y, Carter MJ, Karolova J, Svaton M, Helman K, Weston-Bell NJ, Karydis L, ChT Williamson, Lenz G, Pettigrew J, Harwig C, Stevenson FK, Cragg M, Forconi F, Steele AJ, Cross J, Mackenzie L, Klener P, Packham G. Preclinical evaluation of a novel SHIP1 phosphatase activator for inhibition of PI3 K signaling in malignant B cells. Clin Cancer Res 2020;26:1700–1711.

Li M, Tang Y, Yao J. Photoacoustic tomography of blood oxygenation: A mini review. Photoacoustics 2018;10:65–73.

Liao D, Johnson RS. Hypoxia: A key regulator of angiogenesis in cancer. Cancer Metastasis Rev 2007;26:281–290.

Lu L, Payvandi F, Wu L, Zhang LH, Hariri RJ, Man HW, Chen RS, Muller GW, Hughes CCW, Stirling DI, Schafer PH, Bartlett JB. The anti-cancer drug lenalidomide inhibits angiogenesis and metastasis via multiple inhibitory effects on endothelial cell function in normoxic and hypoxic conditions. Microvasc Res 2009;77:78–86.

Merritt S, Bevilacqua F, Durkin AJ, Cuccia DJ, Lanning R, Tromberg BJ, Gulsen G, Yu H, Wang J, Nalcioglu O. Coregistration of diffuse optical spectroscopy and magnetic resonance imaging in a rat tumor model. Appl Opt 2003;42:2951–2959.

Oikawa T, Sasaki T, Nakamura M, Shimamura M, Tanahashi N, Omura S, Tanaka K. The proteasome is involved in angiogenesis. Biochem Biophys Res Commun 1998;246:243–248.

Peeters SGJA, Zegers CML, Lieuwes NG, van Elmpt W, Eriksson J, van Dongen GAMS, Dubois L. Lambin PA Comparative study of the hypoxia PET tracers (18 F)HX4, (18 F)FAZA, and (18 F) FMISO in a preclinical tumor model. Int J Radiat Oncol Biol Phys 2015;91:351–359.

Petrakis G, Veloza L, Clot G, Gine E, Gonzalez-Farre B, Navarro A, Bea S, Mart ınez A, Lopez-Guillermo A, Amador V, Ribera-Cortada I, Campo E. Increased tumour angiogenesis in SOX11-positive mantle cell lymphoma. Histopathology 2019;75:704–714.

Prukova D, Andera L, Nahacka Z, Karolova J, Svaton M, Klanova M, Havranek O, Soukup J, Svobodova K, Zemanova Z, Tuskova D, Pokorna E, Helman K, Forsterova K, Pacheco-Blanco M, Vockova P, Berkova A, Fronkova E, Trneny M, Klener P. Cotargeting of BCL2 with venetoclax and MCL1 with S63845 is synthetically lethal in vivo in relapsed mantle cell lymphoma. Clin Cancer Res 2019;25:4455–4465.

Pysz MA, Foygel K, Panje CM, Needles A, Tian L, Willmann JK. Assessment and monitoring tumor vascularity with contrast-enhanced ultrasound maximum intensity persistence imaging. Invest Radiol 2011;46:187–195.

Rich L, Seshadri M. Photoacoustic monitoring of tumor and normal tissue response to radiation. Sci Rep 2016;6:21237.

Sun X, Niu G, Chan N, Shen B, Chen X. Tumor hypoxia imaging. Mol Imaging Biol 2011;13:399–410.

Takahashi S, Piao W, Matsumura Y, Komatsu T, Ueno T, Terai T, Kamachi T, Kohno M, Nagano T, Hanaoka K. Reversible off–on fluorescence probe for hypoxia and imaging of hypoxia–normoxia cycles in live cells. J Am Chem Soc 2012;134:19588–19591.

Tomaszewski MR, Gehrung M, Joseph J, Gonzalez I Q, Disselhorst JA, Bohndiek SE. Oxygen-enhanced and dynamic contrast-enhanced optoacoustic tomography provide surrogate biomarkers of tumour vascular function, hypoxia and necrosis. Cancer Res 2018;78:1033.

Tonar Z, Egger GF, Witter K, Wolfesberger B. Quantification of microvessels in canine lymph nodes. Microsc Res Tech 2008;71:760–772.

Toumia Y, Cerroni B, Trochet P, Lacerenza S, Oddo L, Domenici F, Paradossi G. Performances of a pristine graphene-microbubble hybrid construct as a dual imaging contrast agent and assessment of its biodistribution by photoacoustic imaging. Part Syst Charact 2018;35 1800066.

Townsend EC, Murakami MA, Christodoulou A, Christie AL, Köster J, DeSouza TA, Morgan EA, Kallgren SP, Liu H, Wu SC, Plana O, Montero J, Stevenson KE, Rao P, Vadhi R, Andreeff M, Armand P, Ballen KK, Barzaghi-Rinaudo P, Cahill S, Clark AR, Cooke VG, Davids MS, DeAngelo DJ, Dorfman DM, Eaton H, Ebert BL, Etchin J, Firestone B, Fisher DC, Freedman AS, Galinsky IA, Gao H, Garcia JS, Garnache-Ottou F, Graubert TA, Gutierrez A, Halilovic E, Harris MH, Herbert ZT, Horwitz SM, Inghirami G, Intlekofer AM, Ito M, Izraeli S, Jacobsen D, Jacobson CA, Jeay S, Jeremias I, Kelliher MA, Koch R, Konopleva M, Kopp N, Kornblau SM, Kung AM, Kupper TA, LeBoeuf NR, Lees E, Li LS, Look AT, Murakami M, Muschen M, Neuberg D, Ng SY, Odejide OO, Orkin SH, Paquette RR, Place AE, Roderick JE, Ryan JA, Sallan SE, Shoji B, Silverman LB, Soiffer RJ, Steensma DP, Stegmaier K, Stone RM, Tamburini J, Thorner AR, van Hummelen P, Wadleigh M, Wiesmann M, Weng AP, Wuerthner JU, Williams DA, Wollison BM, Lane AA, Letai A, Bertagnolli MM, Ritz J, Brown M, Long H, Aster JC, Shipp MA, Griffin JD, Weinstock DM. The public repository of xenografts enables discovery and randomized phase II-like trials in mice. Cancer Cell 2016;29:574–586.

Vesel a P, Tonar Z, Salek D, Vokurka S, Trn en y M, Kodet R, Moulis M, Ka sparov a P, Vernerov a Z, Velensk a Z, Str ıtesky J, Michal M, Boudov a L. Microvessel density of mantle cell lymphoma. A retrospective study of its prognostic role and the correlation with the Ki-67 and the mantle cell lymphoma international prognostic index in 177 cases. Virchows Arch 2014;465:587–597.

West MJ. Tissue shrinkage and stereological studies. Cold Spring Harb Protoc 2013;2013 pdb.top071860.

Xia J, Yao J, Wang LHV. Photoacoustic tomography: Principles and advances. Prog Elecromagn Res 2014;147:1–22.

Xu M, Wang LV. Photoacoustic imaging in biomedicine. Rev Sci Instrum 2006;77 041101.

Zarfati M, Avivi I, Brenner B, Katz T, Aharon A. Extracellular vesicles of multiple myeloma cells utilize the proteasome inhibitor mechanism to moderate endothelial angiogenesis. Angiogenesis 2019;22:185–196.

Zhang P, Li L, Lin L, Shi J, Wang LV. In vivo super resolution photoacoustic computed tomography by localization of single dyed droplets. Light Sci Appl 2019;8:36.

Zhou Y, Xue Ch, Hou Y, Li M, Ju Y, Chen Q, Li Y, Li K, Song G, Cai K, Luo Z. Oxygenated theranostic nanoplatforms with intracellular agglomeration behaviour for improving the treatment efficacy of hypoxic tumors. Biomaterials 2019;197:129–145.

Seznam příloh

11.5 Příloha V

Jakša, R., Karolová, J., Svatoň, M., Kazantsev, D., **<u>Grajciarová, M.</u>**, Pokorná, E., Tonar, Z., Klánová, M., Winkowská, L., Maláriková, D., Vočková, P., Forsterová, K., Renešová, N., Dolníková, A., Nožičková, K., Dundr, P., Froňková, E., Trněný, M., Klener, P. Complex genetic and histopathological study of 15 patient-derived xenografts of aggressive lymphomas. Lab. Invest. 2022 Apr 29. DOI: 10.1038/s41374-022-00784-w. **IF(JCR2021)=5,662 Q1(Physiology)** https://pubmed.ncbi.nlm.nih.gov/35488033/

ARTICLE   OPEN

Check for updates

Complex genetic and histopathological study of 15 patient-derived xenografts of aggressive lymphomas

Radek Jakša[1], Jana Karolová[2,3], Michael Svatoň [4], Dmitry Kazantsev[2], Martina Grajciarová[5], Eva Pokorná[2], Zbyněk Tonar [5], Magdalena Klánová[2,3], Lucie Winkowska[4], Diana Máliková[2,3], Petra Vočková[2,3], Kristina Forsterová[3], Nicol Renešová[2], Alexandra Dolníková[2], Kristýna Nožičková[2], Pavel Dundr[1], Eva Froňková[4], Marek Trněný [3] and Pavel Klener [2,3 ✉]

Non-Hodgkin lymphomas (NHL) represent the most common hematologic malignancies. Patient-derived xenografts (PDXs) are used for various aspects of translational research including preclinical in vivo validation of experimental treatment approaches. While it was repeatedly demonstrated that PDXs keep majority of somatic mutations with the primary lymphoma samples, from which they were derived, the composition of PDX tumor microenvironment (TME) has not been extensively studied. We carried out a comparative genetic and histopathological study of 15 PDX models derived from patients with various types of NHL including diffuse large B-cell lymphoma (DLBCL; $n = 7$), Burkitt lymphoma (BL; $n = 1$), mantle cell lymphoma (MCL; $n = 2$), and peripheral T-cell lymphomas (PTCL; $n = 5$). Whole exome sequencing (WES) of the PDXs and primary lymphoma cells was implemented in 13 out of 15 cases with available DNA samples. Standard immunohistochemistry (IHC) was used to analyze the composition of PDX TME. WES data confirmed that PDXs maintained the genetic heterogeneity with the original primary lymphoma cells. In contrast, IHC analysis revealed the following recurrently observed alterations in the composition of PDX tumors: more blastoid lymphoma cell morphology, increased proliferation rate, lack of non-malignant cellular components including T cells and (human or murine) macrophages, and significantly lower intratumoral microvessel density and microvessel area composed of murine vessels. In addition, PDX tumors derived from T-NHL displayed additional differences compared to the primary lymphoma samples including markedly lower desmoplasia (i.e., the extent of both reticular and collagen fibrosis), loss of expression of cytotoxic granules (i.e., perforin, TIA, granzyme B), or loss of expression of T-cell specific antigens (i.e., CD3, CD4, CD8). Our data suggest that despite keeping the same genetic profiles, PDX models of aggressive NHL do not recapitulate the microenvironmental heterogeneity of the original lymphomas. These findings have implications on the relevance of PDX models in the context of preclinical research.

Laboratory Investigation; https://doi.org/10.1038/s41374-022-00784-w

INTRODUCTION

Non-Hodgkin lymphomas (NHL) represent the most common hematologic malignancies[1,2]. Murine patient-derived xenograft (PDX) models of human malignancies represent relevant tools for various aspects of preclinical and translational research in (hemato)oncology including the study of lymphoma biology, prediction of personalized treatment, or exploration of mechanisms of drug resistance[3,4]. It has been repeatedly demonstrated that PDXs share genetic mutational landscapes with the primary lymphoma cells, from which they were derived[5,6]. In contrast, the composition of the PDX TME and its relevance compared to the original primary TME has been less extensively investigated[7]. Several studies have reported that PDXs maintain the same histopathologic and immunophenotypic features compared to the original lymphoma cells. However, they have largely focused on the expression of lymphoma surface antigens (CD20), disease markers (PAX5, cyclin D1) and proliferation rate by Ki-67[8].

Pathogenesis of cancer, survival of malignant cells, as well as mode-of-activity (MoA) of many types of anti-cancer therapies, however, can be both directly and indirectly impacted by non-malignant cells of the TME (e.g., T-lymphocytes, macrophages, natural killer (NK) cells), or the extent of neovascularization and desmoplasia[9,10]. MoA of T-cell engaging therapies, immunomodulatory agents, therapeutic monoclonal antibodies, antiangiogenic drugs, or liposome-encapsulated cytostatics all depend not only on the biology of the lymphoma cells, but also on the TME factors[11].

In this study we analyzed 15 newly derived PDX models of NHL and provide their complex genetic and histopathological analysis compared to their respective primary lymphoma tumors (i.e., infiltrated lymph nodes, or extranodal lymphoma masses). Besides whole exome sequencing (WES)-based analysis of landscapes of somatic mutations and predicted copy number variants (CNVs), we provide a comprehensive IHC-based study of the composition

[1]Institute of Pathology, University General Hospital Prague and First Faculty of Medicine, Charles University, Prague, Czech Republic. [2]Institute of Pathological Physiology, First Faculty of Medicine, Charles University, Prague, Czech Republic. [3]First Department of Medicine- Hematology, University General Hospital Prague and First Faculty of Medicine, Charles University, Prague, Czech Republic. [4]CLIP- Childhood Leukaemia Investigation Prague, Department of Pediatric Haematology and Oncology, Second Faculty of Medicine, Charles University and University Hospital Motol, Prague, Czech Republic. [5]Department of Histology and Embryology and Biomedical Center, Faculty of Medicine in Pilsen, Charles University, Pilsen, Czech Republic. ✉email: pavel.klener2@lf1.cuni.cz

of the PDX TME that address not only the PDX lymphoma cells, but also the non-malignant TME components.

MATERIALS AND METHODS
Patients and samples
Informed consent to donation of lymphoma samples for the derivation of murine PDXs was obtained from all patients according to the Declaration of Helsinki. The study was approved by the institutional Ethics Committee (48/18). For the purpose of whole exome sequencing, B-NHL and T-NHL samples were sorted for CD19-positive B-cells using CD19 microBeads (Miltenyi Biotec), and CD45-positive cells using CD45 microBeads (Miltenyi Biotec), respectively. Lymphoma cell infiltration of each sample was verified by flow cytometry.

Establishment of PDXs
The study was approved by the Animal Care and Use Committee (MSMT-21527/2017-8). Female immunodeficient NOD.Cg-$Prkdc^{scid}$ $Il2rg^{tm1Wjl}$/SzJ mice (purchased from the Jackson Laboratory, Bar Harbor, Maine, USA, commonly referred to as NSG mice) were maintained in individually ventilated cages at the Center of Experimental Biomodels of the First Faculty of Medicine, Charles University, Prague, Czech Republic. The donated primary lymphoma specimens were cut into small pieces and homogenized through 45-microM nylon mesh, suspended in phosphate buffered saline (PBS), and subcutaneously injected ($10–30 \times 10^6$ cells/mouse) into the left abdominal flank of adult female NSG mice. Alternatively, small pieces of lymphoma (approx. $2 \times 2 \times 2$ mm) and/or homogenized lymphoma cells suspended in BD Matrigel Matrix (BD Biosciences) were surgically inserted into sub-renal capsules of mice under anesthesia. When tumors of the SC-injected mice reached 2 cm in the largest dimension or when engraftment of tumors in the sub-renal region became discernible by ultrasound examination (Vevo 3100/LAZR-X), the animals were euthanized, and tumors excised and used for subsequent analyses.

Next generation exome sequencing and copy number variant analyses
Genomic DNA was extracted using DNeasy Blood & Tissue Kit (QIAGEN, Germany) according to the manufacturer's protocol. Samples were sequenced by our facility (CLIP, Prague, Czech Republic) on the NextSeq 500 instrument (Illumina, San Diego, CA) according to manufacturer's protocols with sequencing libraries prepared using the SureSelectXT Human All Exon V6 + UTR kit (Agilent Technologies, Santa Clara, CA). Primary lymphoma samples and PDX samples were analyzed as described previously[12]. Only nonsynonymous variants in the gene coding regions with coverage of at least 10 reads with mapping quality and base quality higher than 20 in all related samples were compared together based on their frequency. Variants present in patient's germline DNA at frequency higher than 0.05 were excluded from analysis in all cases. We compared variants with an allele fraction ≥0.1 in at least one of the compared samples that were present in at least 3 reads in both the primary sample and the corresponding PDX sample. All variant filtering was done in RStudio and frequencies and counts of variants were plotted using the ggplot2 library. These variants were then manually reviewed in Integrative Genomics Viewer (http://www.broadinstitute.org/igv) to clear sequencing artefacts or variants present but not called in the germline sample. Curated gene lists for each lymphoma subtype among our PDX models (diffuse large B-cell lymphoma, DLBCL, mantle cell lymphoma, MCL, peripheral T-cell lymphomas, PTCL, Burkitt lymphoma, BL) were created based on recent publications of frequently and recurrently mutated genes in the respective diseases and variants present in these genes were selected and marked in resulting diagrams and tables[13–42]. These lists are provided in the Supplementary Table 4 (sheet S1D).

Copy number variants (CNVs) were predicted using CNVkit and a pooled reference from normal control samples[43,44]. Variants with copy numbers higher or lower than 2 were plotted for each patient and PDX sample using the circlize package for R[45]. To generate color-coded tables, CNVs were filtered by a list of genes of interest for CNV (Supplementary Table 4, sheet S1E) and the most prominent changes were plotted.

Immunohistochemical analysis of patient lymphoma biopsies and their respective PDX models. The immunohistochemical (IHC) analysis was performed using 4 µm thick sections of formalin-fixed and paraffine-embedded (FFPE) tissue blocks (involved lymph nodes or infiltrated extranodal tissue) obtained from patients with newly diagnosed or treatment-refractory lymphomas, as well as from PDX tissue blocks obtained from lymphoma-bearing mice. The expression of the following antigens was examined: CD45, Ki-67, MYC, human CD31, mouse CD31, human CD68, mouse CD68, CD3, CD4, CD8, CD56, CD20, bcl2, bcl6, CD10, IRF4/MUM1, cyclin D1, SOX11, CD5, ALK, CD23, PD-1, CD7, granzyme B, perforin, TIA-1. The clones, manufacturers, dilution, and staining instruments for all antibodies are summarized in Supplementary Table 1. The immunohistochemical results were assessed semi-quantitatively according to the overall percentage of positive cells (0–100%). For Ki67 scoring, any brown staining of the nucleus above the background was regarded as positive. Global assessment of the whole tumor tissue area was performed. The scoring was based on estimation of areas with high, medium and low Ki-67 index. From each area, at least 100 nuclei were counted. The global score was then calculated for each sample and the results were reported in 10% cut-offs. The presence of Epstein-Barr virus (EBV) infected cells was detected by INFORM EBER (Epstein-Barr virus early RNA) probe on a BenchMark ULTRA automated platform followed manufacturer´s protocol (Ventana Benchmark, Roche, Basel, Switzerland). Reticular and collagen fibers on the tumor background were visualized by Gordon-Sweet and van Gieson staining. Grading of fibrosis was assessed semi-quantitatively as G0 (no fibrosis – scattered fine reticular fibers), G1 (mild fibrosis – loose network of intersecting reticular fibers), G2 (severe fibrosis – dense network of intersecting thick reticular and collagen fibers), or G3 (sclerosis – compact areas of hyalinized collagen).

Quantification of microvessel density (MVD) and microvessel area (MVA)
Four pairs of tissue blocks were evaluated. In each pair, one tissue block represented a patient's bioptic sample, the other one represented the corresponding PDX tumor. Five randomly oriented sections from each tissue block were stained immunohistochemically using human and murine CD31 antibodies binding to endothelium of the microvessels (Supplementary Table 1). The histological quantification of microvessels was done as described previously and with sampling optimized according to Kolinko et al.[46,47]. Briefly, 10 fields of view were captured in a systematic uniform way from each section using a 40× objective (Olympus Optical Co., Ltd., Tokyo, Japan) (Supplementary Fig. 1)[48,49]. The intratumoral microvessels were evaluated using MVD and MVA (Supplementary Table 2). MVD of CD31-positive microvessel profiles was estimated using the unbiased CountingFrame[49,50]. MVA was evaluated using a stereological PointGrid and the Cavalieri principle (Supplementary Fig. 2)[50,51].

These two quantitative parameters are considered as complementary: MVD gives the 2-D density of microvessel profiles per sectional area of the tumor, while the MVA provides information on the fraction occupied by microvessel profiles within the tumor. The histological quantification was done on 4 randomly selected PDX models (VFN-D1, VFN-D5, VFN-M5R1, VFN-R4) and the respective primary lymphoma samples (P3, P5, P9 and P15) using the Ellipse software (ViDiTo, Košice, the Slovak Republic) (Supplementary Table 3).

RESULTS
Establishment of PDX tumors
In total, 15 PDXs were derived from 15 patients (9 males, 6 females) with diverse types of NHL at diagnosis ($n = 5$) or at disease relapse ($n = 10$). The PDXs included DLBCL ($n = 7$) including one transformed DLBCL (tDLBCL) from marginal zone lymphoma, and one double-hit lymphoma (with *MYC* and *BCL2* gene rearrangements), BL ($n = 1$), MCL ($n = 2$), angioimmunoblastic T-cell lymphoma (AITL, $n = 2$), peripheral T-cell lymphoma, not otherwise specified (PTCL, NOS, $n = 1$), anaplastic large cell lymphoma (ALCL, anaplastic lymphoma kinase (ALK)-positive ($n = 1$), and ALCL, ALK-negative ($n = 1$). Baseline characteristics of the lymphoma subtypes, disease stage and previous therapies (where applicable) are summarized in Table 1.

PDXs retained most somatic mutations and copy number variants found in the respective primary lymphoma biopsies
WES was implemented in 13 out of 15 cases with available DNA. Non-malignant patients´ DNA was used to filter out gene

Table 1. Baseline characteristics of the analyzed samples.

Pt	Gender	Dg	Subtype	Disease status	Sample origin	WES	Therapy	PDX
1	F	DLBCL	non-GC	Dg	LN	Yes	Untreated	VFN-D3
2	M	DLBCL	non-GC	Dg	LN	Yes	Untreated	VFN-D6
3	M	DLBCL	non-GC	R/R	LN	Yes	G-CHOP	VFN-D1
4	M	DLBCL	GC	R/R	EN (soft tissues)	Yes	R-CHOP + venetoclax; R-ESHAP; R-GIFOX; RT	VFN-D4
5	F	DLBCL	non-GC	R/R	LN	Yes	R-CHOP; R-ESHAP; R-GIFOX; RT	VFN-D5
6	M	tDLBCL	GC, transformed from MZL	Dg	LN	No	R-COP	VFN-D12
7	F	DLBCL	double-hit	R/R	LN	Yes	R-CHOP / R-ESHAP	VFN-D20
8	M	Burkitt		R/R	EN (stomach)	Yes	R-Hyper-CVAD, R-MTX-HD-araC	VFN-B3
9	M	MCL		R/R	LN	Yes	Nordic protocol	VFN-M5R1
10	F	MCL		R/R	LN	Yes	Nordic protocol	VFN-M1
11	M	AITL		R/R	LN	Yes	CHOEP	VFN-T3
12	F	AITL		R/R	LN	No	Untreated	VFN-T7
13	F	PTCL, NOS		R/R	LN	Yes	CHOEP	VFN-T6
14	M	ALCL	ALK-negative	Dg	LN	Yes	Untreated	VFN-T5
15	M	ALCL	ALK-positive	Dg	LN	Yes	Untreated	VFN-T4

AITL angioimmunoblastic T-cell lymphoma, *ALCL* anaplastic large cell lymphoma, *ALK* anaplastic lymphoma kinase, *araC* cytarabine, *COP* cyclophosphamide; vincristine; prednisone, *CHOP* COP + doxorubicin, *CHOEP* CHOP + etoposide, *Dg* diagnosis, *DLBCL* diffuse large B-cell lymphoma, *EN* extra-nodal, *ESHAP* etoposide; solumedrole; high-dose araC; cisplatin, *FL* follicular lymphoma, *G-CHOP* obinutuzumab plus CHOP, *GC* germinal center, *GIFOX* gemcitabine; ifosfamide; oxaliplatin, *HD-araC* high dose araC, *hyperCVAD* hyperfractionated cyclophosphamide; doxorubicin, vincristine; dexamethasone, *LN* lymph node, *MCL* mantle cell lymphoma, *MZL* marginal zone lymphoma, *MTX* methotrexate, *Pt* patient, *PTCL* peripheral T-cell lymphoma, *R* rituximab, *RM* rituximab maintenance, *R/R* relapsed, *RT* radiotherapy, *tDLBCL* transformed DLBCL.

polymorphisms. WES data confirmed that the established PDX models kept majority of somatic mutations of the original lymphoma cells, from which they were derived ("shared" mutations, Figs. 1, 2, Supplementary Figs. 4–17). A list of all relevant variants detected by WES is shown in Supplementary Table 4 (https://doi.org/10.5281/zenodo.6035345). Median allele frequencies of the shared mutations were comparable between the PDXs and the respective primary lymphoma samples (Supplementary Table 5).

Somatic mutations that were not detected in the PDX cells but that were present in the primary lymphoma samples (labeled as "newly undetected" [N/U] in PDX, Fig. 2) comprised predominantly low-frequency mutations (median allele frequency 0.15 in primary lymphoma samples, Table 2). These N/U mutations rarely comprised genes from the positive gene list (Supplementary Table 2C).

Somatic mutations that were detected in the PDX cells but not in the primary lymphoma samples (labeled as "newly detected" [N/D] in PDX, Fig. 2) were observed more frequently than the N/U mutations, but also comprised predominantly low-frequency mutations (median allele frequency 0.18 in the PDXs, Table 2). The N/D mutations often included genes from the positive gene lists (Supplementary Table 2C). The majority of N/D mutations were not detectable in the corresponding primary lymphoma samples (i.e., their allele frequency in the primary lymphoma samples were 0), and mostly consisted of nucleotide transitions (Supplementary Figs. 18 and 19). Some N/D mutations were detected in the primary lymphoma samples, but their allele frequency was below the pre-defined detection threshold (i.e., >0, but <10%).

Consistently observed phenotypic differences between the primary lymphoma biopsies and the respective PDXs

To investigate the composition of the TME, all PDX tumors were analyzed by standard IHC methods and compared to their respective primary samples (Supplementary Table 1, Supplementary Figs. 4–17). Several PDXs were characterized by more aggressive (blastoid) morphology and accelerated proliferation

rate measured via Ki-67 expression (Fig. 3A, B). Absence of T-lymphocytes and macrophages was observed in all analyzed PDX tumors (Fig. 3C, D). Moreover, no murine macrophages were detected in the PDX tumors despite their presence in murine spleen, liver, and bone marrow (Fig. 3D). The vasculature of the PDX tumors was composed of vessels of murine origin, and both MVA and MVD were significantly decreased compared to the primary lymph node biopsies (Fig. 3E, F).

Phenotypic differences between PDX tumors of T-NHL and the primary lymphoma biopsies

Significantly lower extent of desmoplasia (reticular and collagen fibrosis) was found in the majority of T-NHL and several B-NHL models (Fig. 4A, Supplementary Figs. 3–17). Additionally, loss of expression of CD3 and other T-cell-specific markers (CD4, CD8), as well as loss of expression of cytotoxic granules (perforin, T-cell-restricted intracellular antigen [TIA], granzyme B) was observed in PDX cells derived from T-NHL (Fig. 4B, C, Supplementary Figs. 15–17). The PDX tumors derived from the two patients with AITL had discrepant expression of CD20 (Fig. 4D). While VFN-T7 had no detectable CD20-positive cells compared to the significant proportion of CD20 positive cells in the parental P12 biopsy, virtually all PDX cells of VFN-T3 (derived from P11) stained CD20-positive. Despite expressing CD20, the genetic profile of VFN-T3 cells was similar to that of primary lymphoma cells (Fig. 2, Supplementary Fig. 13).

DISCUSSION

We implemented a complex genetic and histopathological screening approach to compare 15 newly derived PDX models of aggressive lymphomas with their respective primary lymphoma biopsies. The established PDX models comprised all major aggressive NHL subtypes, including DLBCL of the germinal center (GC) and non-GC immunophenotypes, double-hit DLBCL, transformed DLBCL, MCL, Burkitt lymphoma, PTCL, AITL, ALCL, ALK-positive, and ALCL, ALK-negative. The genetic comparison by WES
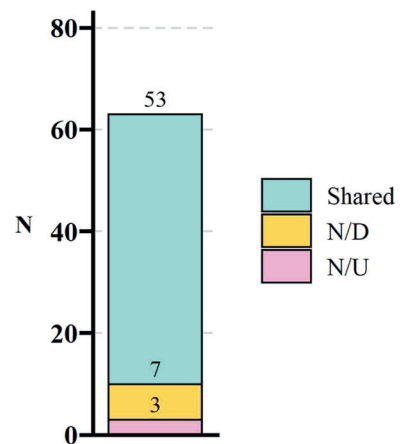
R. Jakša et al.

VFN-D1 vs P3
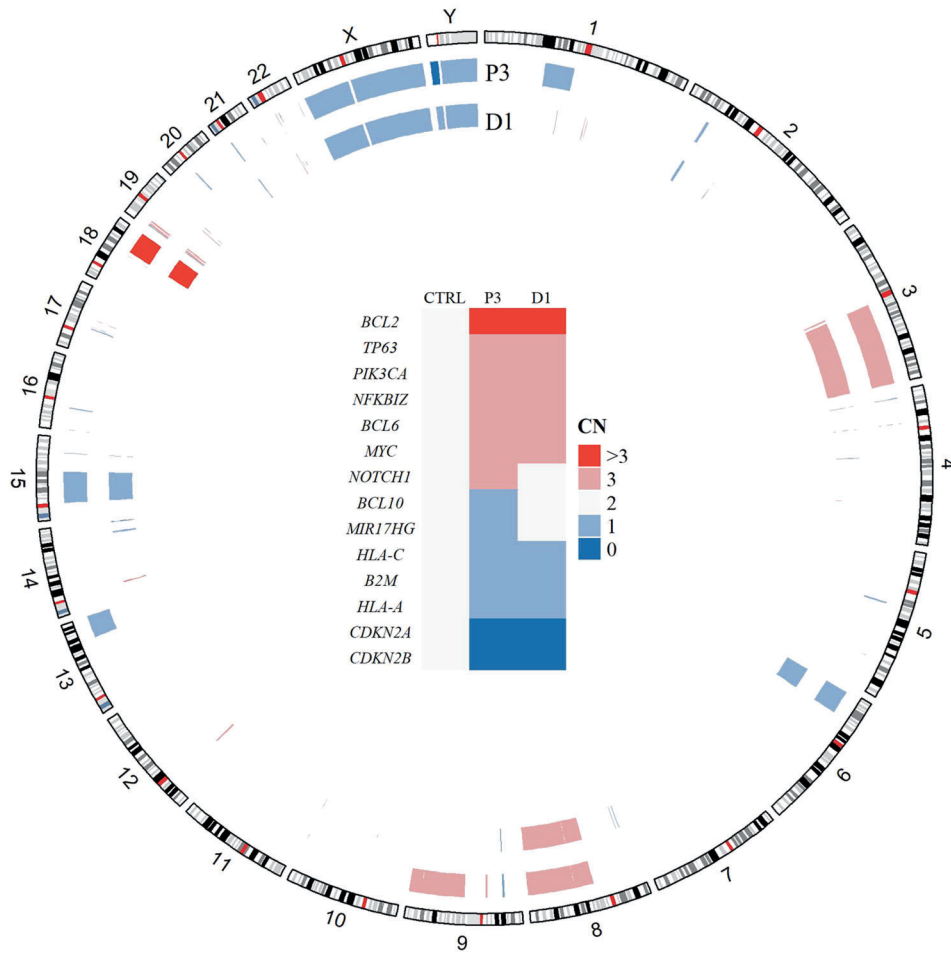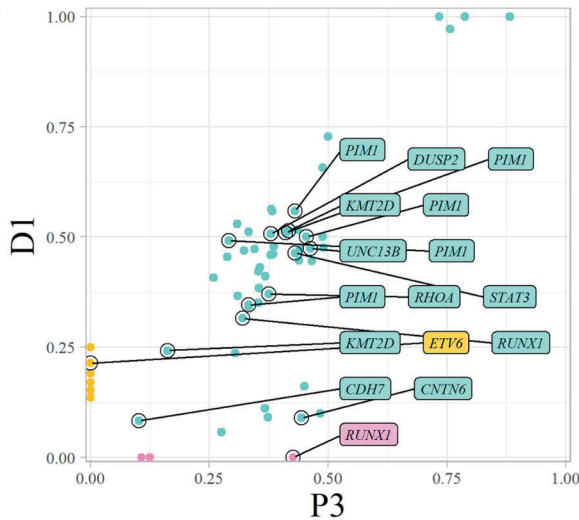
confirmed that the PDXs retained most somatic mutations and copy number variants present in the primary lymphoma cells. This finding is in agreement with previously published data[6,8,52,53]. Moreover, the PDXs shared not only similar numbers of somatic mutations, but also similar allele frequencies of these mutations.

Besides comparable mutational landscapes, similar profiles of predicted CNVs were found in PDXs compared to the respective primary lymphoma samples. The WES data thus confirmed that, from the genetic perspective, the majority of the established PDXs did not represent mere subclones of the original, more

Fig. 1 Whole exome sequencing of the original lymphoma cells obtained from patient P1 and the derived PDX model VFN-D3. A A circular ideogram showing the predicted copy number variants (CNVs) for the patient's sample (P1) and the corresponding PDX model (D3). Outer track represents chromosomal positions of the predicted CNVs. Gene deletions are marked in shades of blue ("1": predicted monoallelic deletion, "0": predicted biallelic deletion). Gene amplifications are marked in shades of red ("3": gain of 1 allele, ">3": gain of more than 1 allele). Graphical table at the center is showing CNV of genes of special interest. **B** Scatter plot showing the allele frequency of shared, newly-detected (N/D), and newly-undetected (N/U) variants in the PDX model sample compared to the sample from which it was derived. Labels show variants found in genes of special interest for the analyzed lymphoma subtype, described in the methods. **C** Stacked bar plot showing numbers of shared, N/D and N/U variants in the patient and the PDX sample. P patient sample, CN copy number, CTRL germline control DNA from patient, N number.
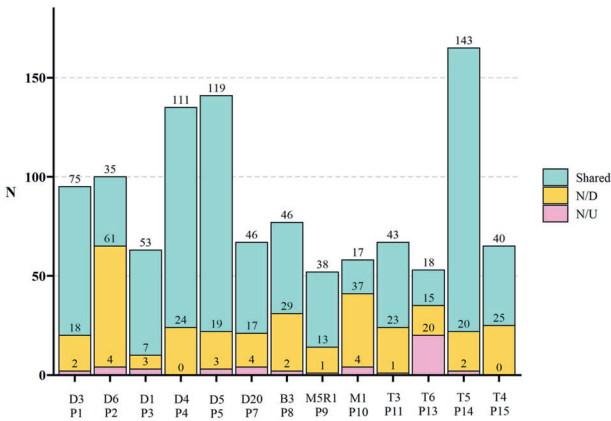
Fig. 2 Number of somatic mutations shared, newly detected (N/D), and newly undetected (N/U) in the PDXs compared to the primary lymphoma samples according to WES analysis. A stacked bar plot showing numbers of shared, N/D and N/U variants in all analyzed PDX models (VFN-D3, D6, D1, D4, D5, B3, M5R1, M1, T3, T6, T5, and T4) compared to the primary patient (P) samples.

Table 2. Median allele frequencies and types of somatic mutations newly detected or undetected in PDX models.

A.	Median AF of N/D mutations in PDXs	Median AF of N/U mutations in patient samples
All PDX models	0.18	0.15
DLBCL	0.27	0.14
MCL	0.18	0.36
T-NHL	0.15	0.14
BL[a]	0.17	0.11
B.	**N/D from the Gene-list**	**N/U from the Gene-list**
VFN-D1 vs P3	ETV6	RUNX1
VFN-D3 vs P1	PDGFRA	0
VFN-D4 vs P4	NF1, HIPK3	0
VFN-D5 vs P5	ITPKB, ENAM	0
VFN-D6 vs P2	IRF4, RNF213, MYC, FOXO1, KLHL14, KLHL14, OSBPL10	0
VFN-D20 vs P7	0	0
VFN-M1 vs P10	0	0
VFN-M5R1 vs P9	0	0
VFN-T3 vs P11	STAT1, ZNF708, RHOA	0
VFN-T4 vs P15	SPEN, FSIP2, DCC, ZNF532	0
VFN-T5 vs P14	AIRD1B, VPS13A, MYD88	0
VFN-T6 vs P13	IRF2BP2, VAV1, TCF20	BIRC6
VFN-B3 vs P8	0	0

A Median allele frequencies (AF) of newly detected (N/D) mutations in PDX models and newly undetected (N/U) mutations in primary lymphoma samples, *B* N/D and N/U variants from the list of genes of special interest (Gene-list), *0* no gene list variant, *BL* Burkitt lymphoma, *DLBCL* diffuse large B-cell lymphoma, *MCL* mantle cell lymphoma, *P1-P15* patient primary lymphoma samples, *T-NHL* T-cell non-Hodgkin lymphomas, *VFN* PDX models derived from primary lymphoma samples P1-P15.
[a]Only 1 PDX model.

heterogeneous tumors, but maintained their genetic diversity. In most of the analyzed PDXs, the numbers of shared mutations were higher than the sums of N/D and N/U mutations. Higher proportions of N/D and N/U mutations were observed only in 3 (out of 13) analyzed PDXs, namely in the PDX tumors VFN-D6 (P2), VFN-M1 (P10), and VFN-T6 (P13). Across all analyzed PDX models (except for VFN-T6), the numbers of N/D mutations were markedly higher than the numbers of N/U mutations. Notably, most N/D mutations were not found in the primary lymphoma samples (i.e., allele frequency 0) and comprised nucleotide transitions. These observations suggest that the vast majority of N/D mutations were de novo acquired during sustained cell divisions of PDX cells in the murine organism, e.g., by the operating somatic hypermutation process, which is also consistent with previously published data[54,55]. On the other hand, most N/U mutations were plausibly "lost" because of relative underrepresentation of disease sub-clones with low-frequency bystander mutations during the propagation of the PDX tumors in murine organism[56].

In contrast to the generally shared genetic profiles, the histopathologic analysis revealed several consistently observed phenotypic alterations of the PDX cells and PDX TME compared to the original lymphoma cells and original lymphoma TME, respectively. The morphology of most PDX models displayed more aggressive features than the original lymphoma cells. Higher proliferation rates by Ki-67 were observed in several PDX models compared to the corresponding primary lymphoma biopsies. These observations suggest more aggressive phenotypes of the engrafted PDX tumors compared to the respective primary lymphoma samples. Considering the overall genetic similarity between the PDXs and the original lymphoma cells, these differences might be explained by differences in the composition of the PDX TME.

Indeed, we confirmed absence of any human non-malignant cells (lymphocytes, macrophages) within the PDX tumors, even though unsorted primary samples (containing both lymphoma cells and non-malignant cells of the TME) were injected into NSG mice. Curiously, murine macrophages were not detected in the PDX TME either, even though they could be found in the murine spleen, liver, and bone marrow. Moreover, the PDX tumors had significantly lower MVD and MVA compared to the original lymph node biopsies. Importantly, only murine, not human vessels were detected in the PDX tumors. The lower MVD/MVA profiles might be a consequence of suboptimal stimulation of the murine sprouting angiogenesis with human vascular endothelial growth factor (VEGF) produced by lymphoma cells under hypoxia. The significantly lower MVD/MVA of murine origin may have large-scale implications for the results of preclinical studies with anti-angiogenic agents, or drugs based on passive accumulation in the tumor tissue, e.g., liposome-encapsulated formulations of cytostatics.

In addition to changes in the composition of the TME, immunophenotypic alterations of PDX cells were observed as well, including low expression of SOX11 (and to a lesser extent of cyclin D1) in both PDX models of MCL; a lack of expression of cytotoxic granules and changed expression of lymphoma-associated markers (CD20, CD3) in several T-NHL PDX models. Curiously, the expression of cyclin D1 appeared weaker (compared
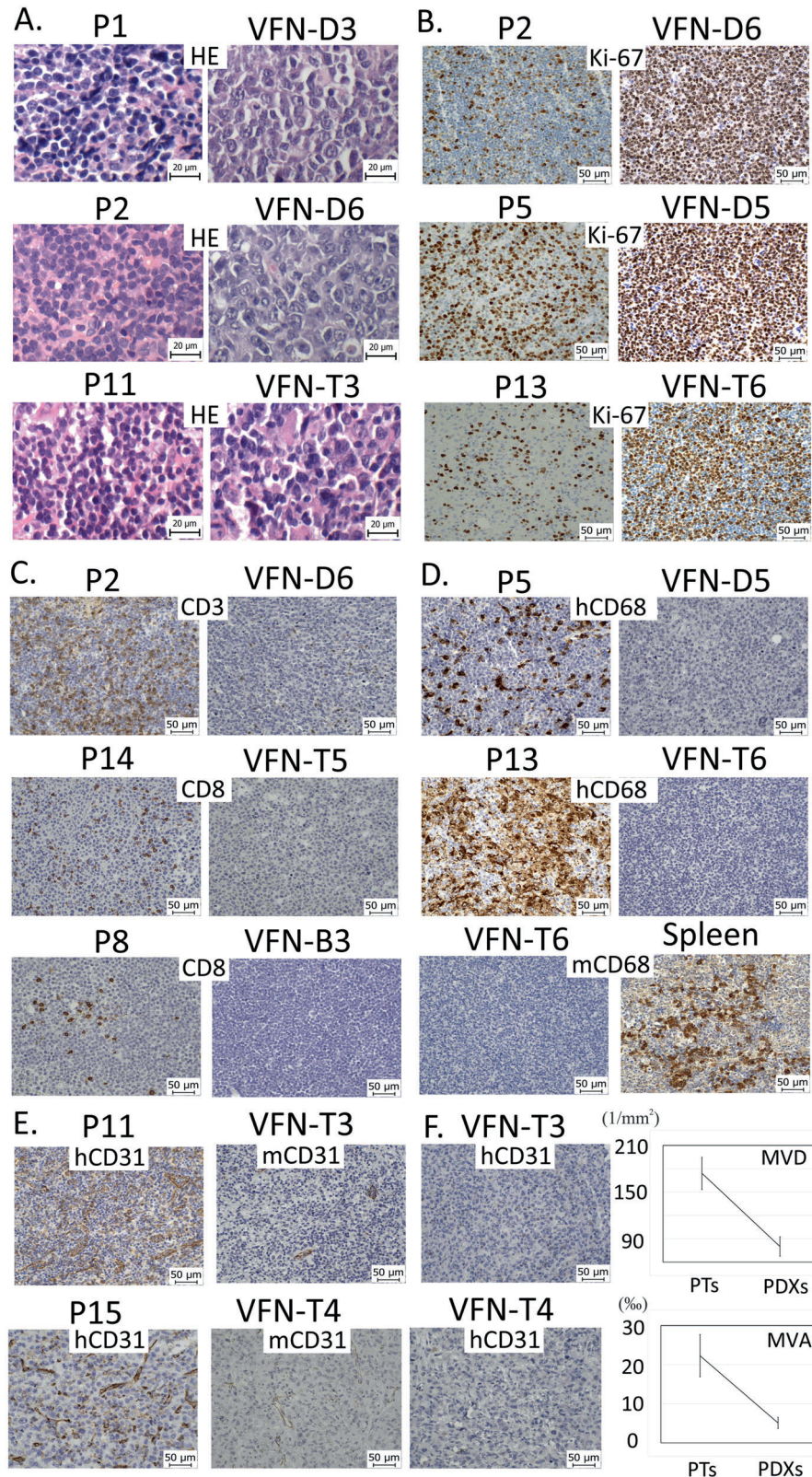
Fig. 3 **Consistently observed phenotypic alterations between primary lymphoma biopsies and the derived PDX tumors. A** More blastoid morphology of PDX cells compared to patients' primary lymphoma cells; **B** Increased proliferation rate by Ki-67 in PDX cells compared to patients' original lymphoma cells; **C** Lack of T-lymphocytes in the PDX TME; **D** Lack of both human and murine macrophages in PDX TME; presence of murine macrophages in murine spleen; **E** Lack of vessels of human origin; presence of vessels of murine origin in the PDX TME; **F** Significantly lower microvessel density (MVD) and microvessel area (MVA) in PDX tumors compared to original patients' lymph node biopsies; *Y* axis in MVD displays number of vascular profiles per 1 mm² of the tumor; *Y* axis in MVA displays microvessel area as area fraction (per mill, ‰) of the total area of CD31-positive microvessel profiles within the tumor; the data are displayed as means, bars show the standard deviations.". For more detailed information, see also Supplementary Tables 2 and 3.
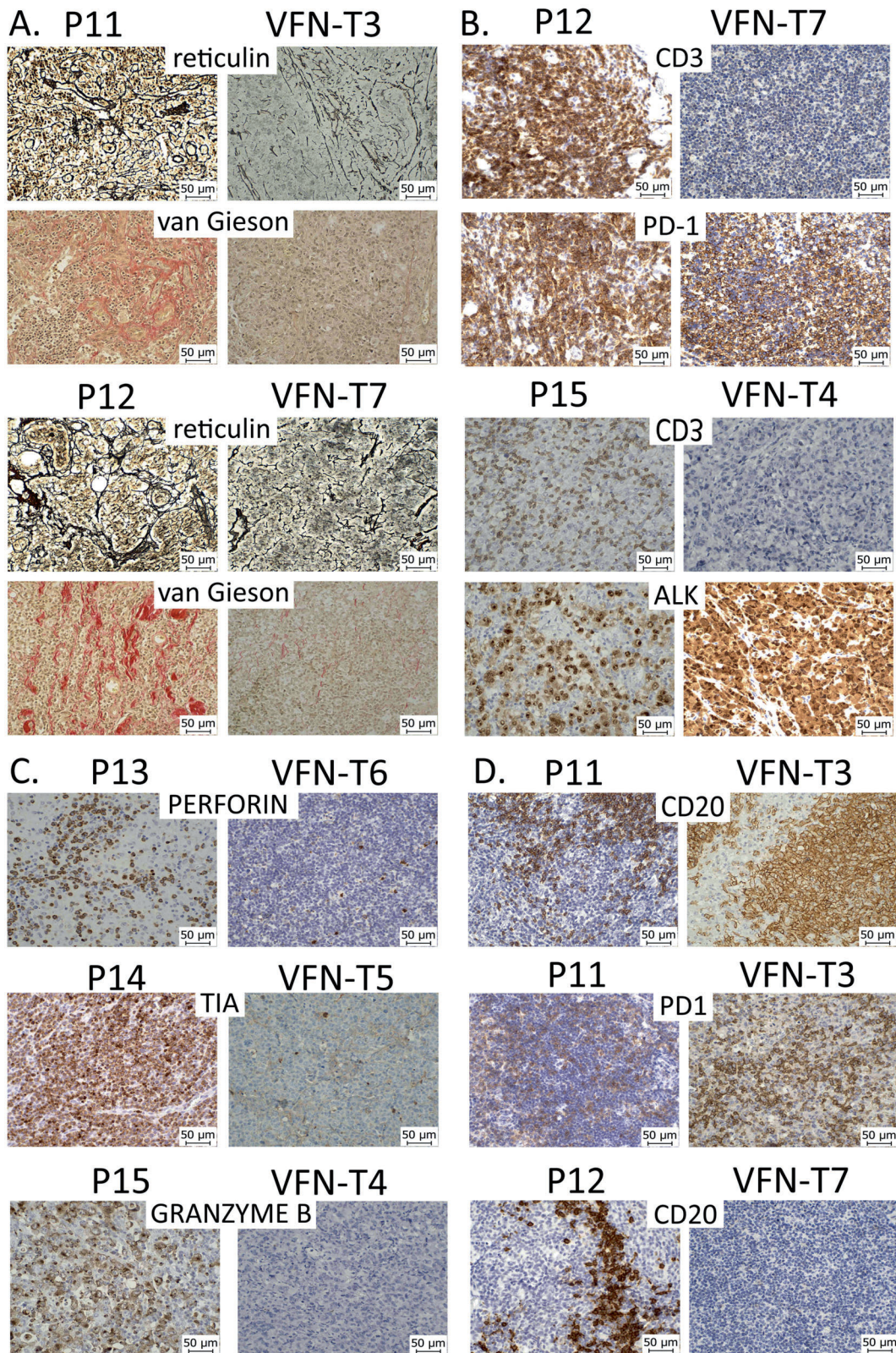
Fig. 4 **Phenotypic differences between PDX tumors of T-NHL and original lymphoma biopsies. A** Lower extent of desmoplasia in PDX tumors VFN-T3 and VFN-T7 compared to their respective lymphoma samples, P11 and P12; **B** Loss of expression of the CD3 T-cell marker, but maintained expression of PD-1 and ALK in PDX cells VFN-T7 and VFN-T4 compared to primary T-NHL cells P12 and P15 respectively; **C** Loss of expression of cytotoxic granules (perforin, T-cell intracytoplasmic antigen [TIA], granzyme B) in PDX cells VFN-T6, VFN-T5, and VFN-T4 compared to primary T-NHL cells P13, P14, and P15 respectively; **D** Aberrant expression of CD20 in VFN-T3 PDX cells; absence of CD20-positive B-cells in VFN-T7 PDX tumor compared to the primary lymphoma sample P12.

R. Jakša et al.

to the original lymphoma samples) in both PDX tumors of MCL in the manuscript by Zhang et al.[8].

In general, PDX models are established upon engraftment of primary lymphoma samples in immunodeficient mice. Several techniques have been developed, including subrenal capsule implantation and intravenous, subcutaneous or intraperitoneal injections[5,6,8,57]. The omental tumor xenograft (OTM) model, developed by Burack et al., enabled xenotransplantation and study of some non-malignant cell populations including CD4 + T-cells[7]. It is, however, not clear, whether the OTM model enables effective serial retransplantations of the engrafted PDX cells.

The PDX models described in this study maintained the genetic profiles, but clearly lost the TME heterogeneity observed in the primary lymphoma samples from which they had been derived. It might be speculated that PDX models described in this study represent a selection of PDX models with the lowest dependence on human TME. Indeed, during the 10 years of our sustained effort to develop PDX models of various NHLs, the engraftment rates of primary lymphoma samples into NSG mice were ~25–30% (data not shown). It might be hypothesized that the primary lymphoma samples that depended on the non-malignant lymphoma TME components for their survival and proliferation did not engraft. On the other hand, even the established PDX cells could not be expanded ex vivo/in vitro (data not shown) thereby indirectly confirming their dependence on the in vivo type of growth. It can only be speculated, which of the in vivo factors contributed to the survival, engraftment, and growth of the successfully established PDX tumors. These might include cell-to-cell contact, hypoxia, metabolic requirements, or other factors.

In conclusion, PDX models do represent the most relevant tools currently available for various aspects of translational research including preclinical assessment of experimental treatment approaches. However, to avoid unwanted biases, the experiments conducted on murine PDX models of aggressive lymphomas should always take into consideration potential histopathological discrepancies between PDX models and primary lymphoma samples, as described in detail in this study.

DATA AVAILABILITY
All data generated or analyzed during this study are included in this published article [and its supplementary information files].

REFERENCES
1. Swerdlow, S. H., Campo, E., Pileri, S. A., Harris, N. L., Stein, H., Siebert, R. et al. The 2016 revision of the World Health Organization classification of lymphoid neoplasms. *Blood* **127**, 2375–2390 (2016).
2. Swerdlow, S. H. & Cook, J. R. As the world turns, evolving lymphoma classifications-past, present and future. *Hum. Pathol.* https://doi.org/10.1016/j.humpath.2019.08.019 (2019).
3. Lai, Y., Wei, X., Lin, S., Qin, L., Cheng, L. & Li, P. Current status and perspectives of patient-derived xenograft models in cancer research. *J. Hematol. Oncol.* **10**, 106 (2017).
4. Sugimoto, K., Hayakawa, F., Shimada, S., Morishita, T., Shimada, K., Katakai, T. et al. Discovery of a drug targeting microenvironmental support for lymphoma cells by screening using patient-derived xenograft cells. *Sci. Rep.* **5**, 13054 (2015).
5. Townsend, E. C., Murakami, M. A., Christodoulou, A., Christie, A. L., Köster, J., DeSouza, T. A. et al. The public repository of xenografts enables discovery and randomized phase II-like trials in mice. *Cancer Cell* **29**, 574–586 (2016).
6. Chapuy, B., Cheng, H., Watahiki, A., Ducar, M. D., Tan, Y., Chen, L. et al. Diffuse large B-cell lymphoma patient-derived xenograft models capture the molecular and biological heterogeneity of the disease. *Blood* **127**, 2203–2213 (2016).
7. Burack, W. R., Spence, J. M., Spence, J. P., Spence, S. A., Rock, P. J., Shenoy, G. N. et al. Patient-derived xenografts of low-grade B-cell lymphomas demonstrate roles of the tumor microenvironment. *Blood Adv.* **1**, 1263–1273 (2017).
8. Zhang, L., Nomie, K., Zhang, H., Bell, T., Pham, L., Kadri, S. et al. B-cell lymphoma patient-derived xenograft models enable drug discovery and are a platform for personalized therapy. *Clin. Cancer Res.* **23**, 4212–4223 (2017).
9. Hanahan, D. & Coussens, L. M. Accessories to the crime: functions of cells recruited to the tumor microenvironment. *Cancer Cell* **21**, 309–322 (2012).
10. Shain, K. H., Dalton, W. S. & Tao, J. The tumor microenvironment shapes hallmarks of mature B-cell malignancies. *Oncogene* **34**, 4673–4682 (2015).
11. McMillin, D. W., Negri, J. M. & Mitsiades, C. S. The role of tumour-stromal interactions in modifying drug response: challenges and opportunities. *Nat. Rev. Drug Discov.* **12**, 217–228 (2013).
12. Prukova, D., Andera, L., Nahacka, Z., Karolova, J., Svaton, M., Klanova, M. et al. Cotargeting of BCL2 with venetoclax and MCL1 with S63845 is synthetically lethal in vivo in relapsed mantle cell lymphoma. *Clin. Cancer Res.* 25, 4455–4465 (2019).
13. Schmitz, R., Wright, G. W., Huang, D. W., Johnson, C. A., Phelan, J. D., Wang, J. Q. et al. Genetics and pathogenesis of diffuse large B-cell lymphoma. *N. Engl. J. Med.* **378**, 1396–1407 (2018).
14. Pasqualucci, L. & Dalla-Favera, R. Genetics of diffuse large B-cell lymphoma. *Blood* **131**, 2307–2319 (2018).
15. Reddy, A., Zhang, J., Davis, N. S., Moffitt, A. B., Love, C. L., Waldrop, A. et al. Genetic and functional drivers of diffuse large B cell lymphoma. *Cell* **171**, 481–494.e415 (2017).
16. Dubois, S., Viailly, P. J., Mareschal, S., Bohers, E., Bertrand, P., Ruminy, P. et al. Next-generation sequencing in diffuse large B-cell lymphoma highlights molecular divergence and therapeutic opportunities: a LYSA study. *Clin Cancer Res.* **22**, 2919–2928 (2016).
17. Karube, K., Enjuanes, A., Dlouhy, I., Jares, P., Martin-Garcia, D., Nadeu, F. et al. Integrating genomic alterations in diffuse large B-cell lymphoma identifies new relevant pathways and potential therapeutic targets. *Leukemia* **32**, 675–684 (2018).
18. Pasqualucci, L., Trifonov, V., Fabbri, G., Ma, J., Rossi, D., Chiarenza, A. et al. Analysis of the coding genome of diffuse large B-cell lymphoma. *Nat. Genet.* **43**, 830–837 (2011).
19. Zhang, J., Grubor, V., Love, C. L., Banerjee, A., Richards, K. L., Mieczkowski, P. A. et al. Genetic heterogeneity of diffuse large B-cell lymphoma. *Proc. Natl Acad. Sci. USA.* **110**, 1398–1403 (2013).
20. Lohr, J. G., Stojanov, P., Lawrence, M. S., Auclair, D., Chapuy, B., Sougnez, C. et al. Discovery and prioritization of somatic mutations in diffuse large B-cell lymphoma (DLBCL) by whole-exome sequencing. *Proc. Natl. Acad. Sci. USA.* **109**, 3879–3884 (2012).
21. Morin, R. D., Mendez-Lago, M., Mungall, A. J., Goya, R., Mungall, K. L., Corbett, R. D. et al. Frequent mutation of histone-modifying genes in non-Hodgkin lymphoma. *Nature* **476**, 298–303 (2011).
22. Zhang, J., Jima, D., Moffitt, A. B., Liu, Q., Czader, M., Hsi, E. D. et al. The genomic landscape of mantle cell lymphoma is related to the epigenetically determined chromatin state of normal B cells. *Blood* **123**, 2988–2996 (2014).
23. Bea, S., Valdes-Mas, R., Navarro, A., Salaverria, I., Martin-Garcia, D., Jares, P. et al. Landscape of somatic mutations and clonal evolution in mantle cell lymphoma. *Proc. Natl Acad. Sci. USA.* **110**, 18250–18255 (2013).
24. Yang, P., Zhang, W., Wang, J., Liu, Y., An, R. & Jing, H. Genomic landscape and prognostic analysis of mantle cell lymphoma. *Cancer Gene Ther.* https://doi.org/10.1038/s41417-018-0022-5 (2018).
25. Royo, C., Salaverria, I., Hartmann, E. M., Rosenwald, A., Campo, E. & Beà, S. The complex landscape of genetic alterations in mantle cell lymphoma. *Semin. Cancer Biol.* **21**, 322–334 (2011).
26. Wu, C., de Miranda, N. F., Chen, L., Wasik, A. M., Mansouri, L., Jurczak, W. et al. Genetic heterogeneity in primary and relapsed mantle cell lymphomas: Impact of recurrent CARD11 mutations. *Oncotarget* **7**, 38180–38190 (2016).
27. Ahmed, M., Zhang, L., Nomie, K., Lam, L. & Wang, M. Gene mutations and actionable genetic lesions in mantle cell lymphoma. *Oncotarget* **7**, 58638–58648 (2016).
28. Crescenzo, R., Abate, F., Lasorsa, E., Tabbo, F., Gaudiano, M., Chiesa, N. et al. Convergent mutations and kinase fusions lead to oncogenic STAT3 activation in anaplastic large cell lymphoma. *Cancer Cell* **27**, 516–532 (2015).
29. Larose, H., Prokoph, N., Matthews, J. D., Schlederer, M., Högler, S., Alsulami, A. F. et al. Whole Exome Sequencing reveals NOTCH1 mutations in anaplastic large cell lymphoma and points to Notch both as a key pathway and a potential therapeutic target. *Haematologica* **106**, 1693–1704 (2021).
30. Odejide, O., Weigert, O., Lane, A. A., Toscano, D., Lunning, M. A., Kopp, N. et al. A targeted mutational landscape of angioimmunoblastic T-cell lymphoma. *Blood* **123**, 1293–1296 (2014).
31. Palomero, T., Couronné, L., Khiabanian, H., Kim, M. Y., Ambesi-Impiombato, A., Perez-Garcia, A. et al. Recurrent mutations in epigenetic regulators, RHOA and FYN kinase in peripheral T cell lymphomas. *Nat. Genet.* **46**, 166–170 (2014).
32. Sakata-Yanagimoto, M., Enami, T., Yoshida, K., Shiraishi, Y., Ishii, R., Miyake, Y. et al. Somatic RHOA mutation in angioimmunoblastic T cell lymphoma. *Nat. Genet.* **46**, 171–175 (2014).
33. Vallois, D., Dobay, M. P., Morin, R. D., Lemonnier, F., Missiaglia, E., Juilland, M. et al. Activating mutations in genes related to TCR signaling in angioimmunoblastic

and other follicular helper T-cell-derived lymphomas. *Blood* **128**, 1490–1502 (2016).

34. Watatani, Y., Sato, Y., Miyoshi, H., Sakamoto, K., Nishida, K., Gion, Y. et al. Molecular heterogeneity in peripheral T-cell lymphoma, not otherwise specified revealed by comprehensive genetic profiling. *Leukemia* **33**, 2867–2883 (2019).

35. Dave, S. S., Fu, K., Wright, G. W., Lam, L. T., Kluin, P., Boerma, E. J. et al. Molecular diagnosis of Burkitt's lymphoma. *N. Engl. J. Med.* **354**, 2431–2442 (2006).

36. Love, C., Sun, Z., Jima, D., Li, G., Zhang, J., Miles, R. et al. The genetic landscape of mutations in Burkitt lymphoma. *Nat. Genet.* **44**, 1321–1325 (2012).

37. López, C., Kleinheinz, K., Aukema, S. M., Rohde, M., Bernhart, S. H., Hübschmann, D. et al. Genomic and transcriptomic changes complement each other in the pathogenesis of sporadic Burkitt lymphoma. *Nat. Commun.* **10**, 1459 (2019).

38. Panea, R. I., Love, C. L., Shingleton, J. R., Reddy, A., Bailey, J. A., Moormann, A. M. et al. The whole-genome landscape of Burkitt lymphoma subtypes. *Blood* **134**, 1598–1607 (2019).

39. Penther, D., Viailly, P. J., Latour, S., Etancelin, P., Bohers, E., Vellemans, H. et al. A recurrent clonally distinct Burkitt lymphoma case highlights genetic key events contributing to oncogenesis. *Genes Chromosomes Cancer* **58**, 595–601 (2019).

40. Richter, J., Schlesner, M., Hoffmann, S., Kreuz, M., Leich, E., Burkhardt, B. et al. Recurrent mutation of the ID3 gene in Burkitt lymphoma identified by integrated genome, exome and transcriptome sequencing. *Nat. Genet.* **44**, 1316–1320 (2012).

41. Schmitz, R., Young, R. M., Ceribelli, M., Jhavar, S., Xiao, W., Zhang, M. et al. Burkitt lymphoma pathogenesis and therapeutic targets from structural and functional genomics. *Nature* **490**, 116–120 (2012).

42. Wagener, R., Seufert, J., Raimondi, F., Bens, S., Kleinheinz, K., Nagel, I. et al. The mutational landscape of Burkitt-like lymphoma with 11q aberration is distinct from that of Burkitt lymphoma. *Blood* **133**, 962–966 (2019).

43. Talevich, E., Shain, A. H., Botton, T. & Bastian, B. C. CNVkit: Genome-wide copy number detection and visualization from targeted DNA sequencing. *PLoS Comput. Biol.* **12**, e1004873 (2016).

44. Tibshirani, R. & Wang, P. Spatial smoothing and hot spot detection for CGH data using the fused lasso. *Biostatistics* **9**, 18–29 (2008).

45. Gu, Z., Gu, L., Eils, R., Schlesner, M. & Brors, B. circlize Implements and enhances circular visualization in R. *Bioinformatics* **30**, 2811–2812 (2014).

46. Keša, P., Pokorná, E., Grajciarová, M., Tonar, Z., Vočková, P., Trochet, P. et al. Quantitative in vivo monitoring of hypoxia and vascularization of patient-derived murine xenografts of mantle cell lymphoma using photoacoustic and ultrasound imaging. *Ultrasound Med. Biol.* **47**, 1099–1107 (2021).

47. Kolinko, Y., Malečková, A., Kochová, P., Grajciarová, M., Blassová, T., Kural, T. et al. Using virtual microscopy for the development of sampling strategies in quantitative histology and design-based stereology. *Anat. Histol. Embryol.* https://doi.org/10.1111/ahe.12765 (2021).

48. Tonar, Z., Egger, G. F., Witter, K. & Wolfesberger, B. Quantification of microvessels in canine lymph nodes. *Microsc. Res. Tech.* **71**, 760–772 (2008).

49. Veselá, P., Tonar, Z., Sálek, D., Vokurka, S., Trněný, M., Kodet, R. *et al*. Microvessel density of mantle cell lymphoma. A retrospective study of its prognostic role and the correlation with the Ki-67 and the mantle cell lymphoma international prognostic index in 177 cases. *Virchows Arch.* **465**, 587–597 (2014).

50. Petrakis, G., Veloza, L., Clot, G., Gine, E., Gonzalez-Farre, B., Navarro, A. et al. Increased tumour angiogenesis in SOX11-positive mantle cell lymphoma. *Histopathology* **75**, 704–714 (2019).

51. Gundersen, H. J. Estimators of the number of objects per area unbiased by edge effects. *Microsc Acta* **81**, 107–117 (1978).

52. Forde, S., Matthews, J. D., Jahangiri, L., Lee, L. C., Prokoph, N., Malcolm, T. I. M. et al. Paediatric Burkitt lymphoma patient-derived xenografts capture disease characteristics over time and are a model for therapy. *Br. J. Haematol.* **192**, 354–365 (2021).

53. Woo, X. Y., Giordano, J., Srivastava, A., Zhao, Z. M., Lloyd, M. W., de Bruijn, R. et al. Conservation of copy number profiles during engraftment and passaging of patient-derived cancer xenografts. *Nat. Genet.* **53**, 86–99 (2021).

54. Choi, Y. Y., Lee, J. E., Kim, H., Sim, M. H., Kim, K. K., Lee, G. et al. Establishment and characterisation of patient-derived xenografts as paraclinical models for gastric cancer. *Sci. Rep.* **6**, 22172 (2016).

55. Di Noia, J. M. & Neuberger, M. S. Molecular mechanisms of antibody somatic hypermutation. *Annu. Rev. Biochem.* **76**, 1–22 (2007).

56. Ben-David, U., Ha, G., Tseng, Y. Y., Greenwald, N. F., Oh, C., Shih, J. et al. Patient-derived xenografts undergo mouse-specific tumor evolution. *Nat. Genet.* **49**, 1567–1575 (2017).

57. Klanova, M., Soukup, T., Jaksa, R., Molinsky, J., Lateckova, L., Maswabi, B. C. et al. Mouse models of mantle cell lymphoma, complex changes in gene expression and phenotype of engrafted MCL cells: implications for preclinical research. *Lab. Invest.* **94**, 806–817 (2014).

ACKNOWLEDGEMENTS

AUTHOR CONTRIBUTIONS

R.J. was responsible for investigation, methodology, visualization and draft preparation; J.K., M.S., and D.K. were responsible for formal analysis, methodology, and validation; M.G., E.P., and Z.T. were responsible for investigation, methodology, and funding acquisition; M.K. was responsible for investigation, and draft review and editing; L.W., D.M., P.V., K.F., N.R., A.D., and K.N. were responsible for investigation, and draft preparation; P.D., E.F., and M.T. were responsible for investigation, methodology, validation, and draft review and editing; P.K. was responsible for conceptualization, funding acquisition, project administration, formal analysis, supervision, and draft review and editing.

COMPETING INTERESTS

The authors declare no competing interests.

ETHICS APPROVAL AND CONSENT TO PARTICIPATE

Informed consent to donation of lymphoma samples for the derivation of murine PDXs was obtained from all patients according to the Declaration of Helsinki. The study was approved by the institutional Ethics Committee (48/18).

ADDITIONAL INFORMATION

Supplementary information The online version contains supplementary material available at https://doi.org/10.1038/s41374-022-00784-w.

Correspondence and requests for materials should be addressed to Pavel Klener.

Reprints and permission information is available at http://www.nature.com/reprints

Publisher's note Springer Nature remains neutral with regard to jurisdictional claims in published maps and institutional affiliations.

11.6 Příloha VI

Růžička, J., **<u>Grajciarová, M.</u>**, Vištejnová, L., Klein, P., Tichánek, F., Tonar, Z., Dejmek, J., Beneš, J., Bolek, L., Bajgar, R., Kuncová, J. Hyperbaric oxygen enhances collagen III formation in wound of ZDF rat. Physiol. Res. 2021 Nov29;70(5):787-798. DOI: 10.33549/physiolres.934684.   **IF(JCR2020)=1.881.**   **Q4(Physiology)** https://pubmed.ncbi.nlm.nih.gov/34505531/

Hyperbaric Oxygen Enhances Collagen III Formation in Wound of ZDF Rat

Jiří RŮŽIČKA[1,2], Martina GRAJCIAROVÁ[2,4], Lucie VIŠTEJNOVÁ[2], Pavel KLEIN[2], Filip TICHÁNEK[2,3], Zbyněk TONAR[2,4], Jiří DEJMEK[1,2], Jiří BENEŠ[1,2], Lukáš BOLEK[1,2], Robert BAJGAR[1], Jitka KUNCOVÁ[1,2]

[1]Department of Biophysics, Faculty of Medicine in Pilsen, Charles University, Pilsen, Czech Republic, [2]Biomedical Centre, Faculty of Medicine in Pilsen, Charles University, Pilsen, Czech Republic, [3]Department of Pathological Physiology, Faculty of Medicine in Pilsen, Charles University, Pilsen, Czech Republic, [4]Department of Histology and Embryology, Faculty of Medicine in Pilsen, Charles University, Pilsen, Czech Republic

Summary

Diabetic foot ulcer (DFU) is a serious complication of diabetes and hyperbaric oxygen therapy (HBOT) is also considered in comprehensive treatment. The evidence supporting the use of HBOT in DFU treatment is controversial. The aim of this work was to introduce a DFU model in ZDF rat by creating a wound on the back of an animal and to investigate the effect of HBOT on the defect by macroscopic evaluation, quantitative histological evaluation of collagen (types I and III), evaluation of angiogenesis and determination of interleukin 6 (IL6) levels in the plasma. The study included 10 rats in the control group (CONT) and 10 in the HBOT group, who underwent HBOT in standard clinical regimen. Histological evaluation was performed on the 18th day after induction of defect. The results show that HBOT did not affect the macroscopic size of the defect nor IL6 plasma levels. A volume fraction of type I collagen was slightly increased by HBOT without reaching statistical significance (1.35±0.49 and 1.94±0.67 %, CONT and HBOT, respectively). In contrast, the collagen type III volume fraction was ~120 % higher in HBOT wounds (1.41±0.81 %) than in CONT ones (0.63±0.37 %; p=0.046). In addition, the ratio of the volume fraction of both collagens in the wound ($(I+III)_w$) to the volume fraction of both collagens in the adjacent healthy skin ($(I+III)_h$) was ~65 % higher in rats subjected to HBOT (8.9±3.07 vs. 5.38±1.86 %, HBOT and CONT, respectively; p=0.028). Vessels density (number per 1 mm²) was found to be higher in CONT vs. HBOT (206.5±41.8 and 124±28.2, respectively, p<0.001). Our study suggests that HBOT promotes collagen III formation and decreases the number of newly formed vessels at the early phases of healing.

Corresponding author

J. Ruzicka, Department of Biophysics, Faculty of Medicine in Pilsen, Alej Svobody 1655/76, 323 00 Pilsen, Czech Republic. E-mail: jiri.ruzicka@lfp.cuni.cz

Introduction

Diabetic foot syndrome and its clinical manifestation in chronic defect – diabetic foot ulcer (DFU) remains a serious medical issue. It affects up to 34 % of patients suffering from diabetes and it is the most common cause of non-traumatic amputation of the lower limb, where amputation is in 85 % of cases preceded by DFU. The prevalence of DFU is about 4 to 10 %. (Jirkovská 2011, Apelquist 2008).

DFU has two principal pathophysiologic mechanisms that frequently overlap and potentiate each other: vasculopathy and neuropathy. Macroangiopathy typically affects infrapopliteal vessels, which leads to

peripheral arterial disease of the lower extremities (Hobizal and Wukich 2012). Microangiopathy is associated with a loss of the elasticity of arterioles and capillaries due to lipid deposition and thickening of the basement membrane that results in altered nutrient exchange, tissue hypoxia and microcirculation ischemia. Diabetic neuropathy damages autonomic, sensory and motor nerves predisposing diabetic patients to trauma due to decreased protective sensation, impaired stability of joints due to muscle weakness and further impairment of microvascular blood flow due to direct damage to autonomic neurons caused by sorbitol accumulation, changes in the NAD:NADH ratio, and increased oxidative and nitrosative stress (Vinik *et al.* 2003, Packer *et al.* 2021).

Treatment of DFU must be complex, consisting of local and systemic approaches and adjunct methods if applicable in the given specific case (Waniczek *et al.* 2013). The basic principles of standard care are described in the International Working Group on the Diabetic Foot (IWGDF) guidelines (Lipsky *et al.* 2019). Standard treatment of the defect consists of assessment for infection, debridement, cleaning and proper dressings in addition to systemic glucose control and maintenance of adequate perfusion to the wound and lower extremities (Dreifke *et al.* 2015). In addition, 13 adjunct therapies were evaluated by IWGDF in 2019 and only 6 of them were recommended to be used in addition to the best standard of care (Rayman *et al.* 2020). Among them, the judicious use of hyperbaric oxygen therapy (HBOT) in certain non-healing ischemic ulcers was recommended (Rayman *et al.* 2020, Wu 2018).

Although the rationale for using HBOT in the treatment of DFU is well supported by the idea that overcoming wound hypoxia could expedite the healing process and promote epithelialisation (Aydin *et al.* 2013), many clinical and experimental studies on the putative beneficial effects of HBOT on wound healing brought about inconsistent results. Meta-analyses of clinical studies dealing with the impact of HBOT on the outcome of DFU concluded both beneficial and neutral effects of hyperbaric oxygen on the healing process of the defect and the risk of above-the-knee amputation (Brouwer *et al.* 2020, Kranke *et al.* 2015, Elraiyah *et al.* 2016, Margolis *et al.* 2013) pointing out the relatively high risk of bias and methodological limitations of some clinical studies taken into analyses. In addition, some recent clinical studies have suggested that HBOT may be used as a useful adjuvant to conservative standard therapy in the

healing of DFU (Kumar *et al.* 2020, Teguh *et al.* 2020).

Animal studies dealing with the analyses of the efficiency of HBOT in the treatment of DFU also brought about controversial results. In an extensive study of HBOT effect on both non-ischemic and ischemic defects induced on the dorsal aspect of the hind feet of diabetic vs. normoglycemic rats, HBOT sped up the healing of ischemic and diabetic defects, but had no effect on non-ischemic and normoglycemic defects (André-Lévigne *et al.* 2016). In a recent study performed on streptozotocin-diabetic mice, HBOT facilitated wound healing in DFU, promoted angiogenic activities of endothelial cells, activated HIF-1α (hypoxia inducible factor) signaling, and promoted the expression of VEGF/SDF-1 (vascular endothelial growth factor/stromal cell derived factor) in fibroblast and the expression of the VEGF-R/CXCR4 receptor in endothelial cells (Huang *et al.* 2020). In contrast, other studies focused on HBOT effects in diabetic rodents did not show any improvement in macroscopic nor microscopic structure of the defect, perfusion of tissue in defect, long-term capillary-venous oxygen saturation, level of hemoglobin nor flow in microcirculation or formation of granulation tissue (or neo-dermis) after HBOT (van Neck *et al.* 2017, Tuk *et al.* 2014).

It should be noted that all the above mentioned experimental studies used animal model diabetes induced by streptozotocin, which corresponds more with Type 1 diabetes. Although DFU occurs in both Type 1 and Type 2 diabetes mellitus, Type 2 diabetes accounts for 90 to 95 % of cases worldwide (Packer *et al.* 2021). As an animal model suitable for studying wound repair in Type 2 diabetes, Zucker Diabetic Fatty (ZDF) rat has been suggested (Slavkovsky *et al.* 2011). To our best knowledge, no study focusing on the effect of HBOT on DFU in ZDF rat has been performed so far.

The aim of the present study was to analyse the effect of HBOT on wound repair in ZDF rats. Standard square wounds were induced on the back of the experimental animals randomly assigned to control (ZDF rats) and experimental groups (ZDF rats subjected to HBOT in a clinically relevant protocol). The wounds were macroscopically evaluated twice per week in the course of 18 days. In addition, quantitative histological evaluation of collagens I and III was performed on day 18 of the experiment, along with microscopical evaluation of angiogenesis. The results of our study revealed a moderate beneficial effect of adjunct HBOT on the skin defect repair that should be further explored.

Methods

The model of type 2 diabetes mellitus

Zucker Diabetic Fatty rats (ZDF rats) with a congenital mutation of the leptin receptor were used to develop the DFU model. ZDF rats were obtained from the Department of Toxicology and Laboratory Animals Breeding at the Institute of Experimental Pharmacology & Toxicology of the Slovak Academy of Sciences. The experimental animals, homozygous (fa/fa) males, were subsequently obtained by reproduction and selection at the author's workplace. The rats were housed individually throughout the experiment and received standard care according to EU directive 2010/63/EU including a 12/12 light schedule and free access to food and water.

Two months after birth rats were fed with high-fat diet type 5008 (Purina 5008, Charles River, USA). After 4 months, the animals developed Type 2 diabetes mellitus with confirmed values of glycaemia higher than 15 mmol/l (glucometer MediTouch 2, Medisana, Germany) and possessed an obese phenotype. Twenty rats were randomly assigned to control (CONT; ZDF rats, n=10) and experimental groups (HBOT; ZDF rats subjected to HBOT, n=10). The study was approved by the Animal Welfare Advisory Committee at the Faculty of Medicine in Pilsen and by the Ministry of Education, Youth and Sports of the Czech Republic (approval ID: MSMT 26570/2017-3). All experiments were performed in the Central Animal Facility of the Biomedical Centre at the Faculty of Medicine in Pilsen.

Induction of wounds and evaluation of the wound size

Wounds were induced in male diabetic rats at the average age of 140±12 days and the average weight of 392±49 g. The animals were premedicated with tramadol (10 mg/kg; Tramadol, Kalcex, Latvia) administered intraperitoneally in 4 ml of tempered sterile saline and anaesthetized by inhalation of 2-3 % isoflurane (Aerrane, Baxter, Belgium) in oxygen using a face mask. Two square full-thickness 1.5×1.5 cm wounds were made in the skin of the dorsal area of the rat, with the upper edge of the first wound reaching the scapula (Fig. 1). Tramadol in drinking water (100 mg/l; Tramal, oral solution, Stada Pharma, Germany) was then administered for the following 3 days. Pictures of wounds were taken (day 0) and wounds were covered with non-adhering dressing Cosmopor® E (Hartmann, Germany) and fixed by medical adhesive tape. The fourth day after induction

of the wounds, the HBOT group began treatment in a hyperbaric chamber.

Twice per week the wounds in both CONT and HBOT groups were re-bandaged and pictures of them were taken until complete recovery or tissue sampling. Isoflurane anesthesia was used during the replacement of wound dressings and the documentation of wounds. Samples of wounds were taken at day 18 after wound induction followed by animal sacrifice and blood collection.
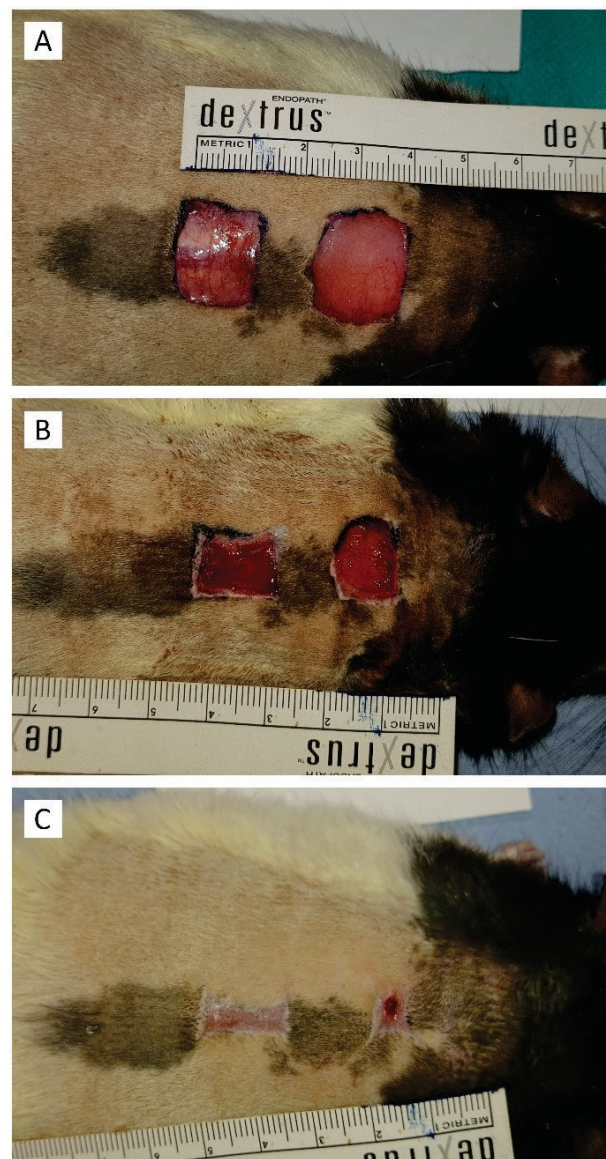
Fig. 1. Example of wounds created on the back of rat. (**A**) day 0, (**B**) day 7, (**C**) day 18 of experiment.

Hyperbaric oxygen therapy (HBOT)

Standard animal cage (3H ´800 cm³, Bioscape, Germany, EU directive 2010/63/EU) was technically

improved to administer pure oxygen and to get air samples from the inner part. Our air pressurized hyperbaric chamber (CKD Prague, Czech Republic) was adapted to house this animal cage and equipped with connectors to supply gas into the cage and to take gas samples. On the day of treatment, animals were placed into this adapted cage. The cage in the chamber was washed with pure oxygen continuously. Each isocompression phase during the HBOT session lasted for 90 min at a pressure of 0.25 MPa, 5 times per week. This protocol is similar to the one used in clinical practice (Teguh *et al.* 2020, Kumar *et al.* 2020). During the whole treatment gas samples from the cage were taken in 10 min intervals to check if more than 95 % oxygen levels were maintained.

Macroscopic evaluation of wound area

Pictures of skin defects were taken twice a week after the wound induction, i.e. on days 0, 4, 7, 11, 14, and 18. The wound area (mm^2) was measured using ImageJ software (NIH, Bethesda, USA; Schneider *et al.* 2012). Wound size at each experimental animal was expressed in %, calculated as wound area at a particular time point divided by wound area at day 4 (i.e. the day of initiation of HBOT). The exactness of measurements was raised by multiple evaluations (10 times) of one wound area.

Quantitative histological evaluation of collagen

The skin samples were fixed in 10 % formaldehyde, dehydrated in ethanol and embedded in paraffin blocks. Two 5 μm-thick sections were stained using the haematoxylin-eosin (HE) to visualize the overall morphology. Other two sections were stained using picrosirius red (PSR, Merck Millipore, Darmstadt, Germany) to visualize type I collagen (yellow-red color when observed under polarized light) and type III collagen (green color under polarized light). The advantages of this method were well described (Rich and Whittaker 2005) and recently demonstrated in tissue engineering and in detail in the healing of skin wounds (East *et al.* 2018).

Briefly, the picrosirius red enhances the birefringence of co-aligned type I collagen fibrils and fibres. This phenomenon can be used for reproducible morphological quantification of the type I collagen content with high specificity and sensitivity (Junqueira *et al.* 1979). According to the thickness, type I collagen fibres appear in yellow (thinner fibres), orange, and red color (thick bundles of fibres). The green color and

a weak birefringence represents type III collagen with loosely packed fibrils or very thin sections of the type I collaged fibres. The green color is not completely specific for the immature collagen, because the color and intensity of birefringence depends also on the section thickness (Junqueira *et al.* 1982). Linear polarization does not visualize all collagen fibres – those aligned parallel to the transmission axis remain dark, which results in underestimation of the total collagen content. To eliminate this orientation-mediated drawback, we applied circularly polarized illumination by using a circular polarizer (Hama, Monheim, Germany), while the analyser was constructed from a combination of a quarter-wave lambda plate placed below a linear polarizer (U-GAN, Olympus, Tokyo, Japan). Both filters were aligned in the crossed position using an Olympus CX41 microscope.

The samples stained with PSR were observed under circularly polarized light using the 20× objective. From each sample, two micrographs were captured representing the healthy skin adjacent to the healing lesion. Other two micrographs were sampled from the healing lesion. The amounts of the type I and the type III collagen were quantified as their volume fractions (Vv) within the two regions of interest, i.e. within the healthy skin, and within the healing lesion (Fig. 2). The volumes were quantified using the stereological grid point and the Cavalieri principle. This method of quantification of collagen has been previously established, extensively tested and proved as reliable and reroducible in several studies (Tonar *et al.* 2015, Horakova *et al.* 2018, Buzgo *et al.* 2019). The values are further presented as arithmetic mean values calculated from the micrographs per each animal and reference space. Moreover, the ratio of type III to type I collagen was calculated to investigate a possible reduction of type III collagen. This ratio is used as a measure of ongoing fibrillogenesis in early stages of wound healing (Mohammadzadeh *et al.* 2014).

Quantitative histological evaluation of angiogenesis

The skin samples were fixed in 10 % formaldehyde, dehydrated in ethanol and embedded in paraffin blocks. Two 5 μm-thick histological sections were cut from each sample. The sections were deparaffinized and rehydrated. The blood vessels in the skin were detected immunohistochemically using polyclonal rabbit anti-human von Willebrand factor antibody (dilution 1:1000; DakoCytomation, Glostrup, Denmark). The reaction was visualized using diaminobenzidine as a part of the BOND polymer refine

detection (Leica Biosystems Division of Leica Microsystems Inc., Buffalo Grove, United States).

Using 40× microscope objective, four micrographs were taken from each slide using systematic uniform random sampling (Tonar *et al.* 2008). The two-dimensional density of the microvessels profiles were quantified using the unbiased counting frame (Gundersen 1977) (Fig. 2). Stereological counting procedure was done using the Ellipse software (ViDiTo, Košice, Slovak Republic) (Witter *et al.* 2010).
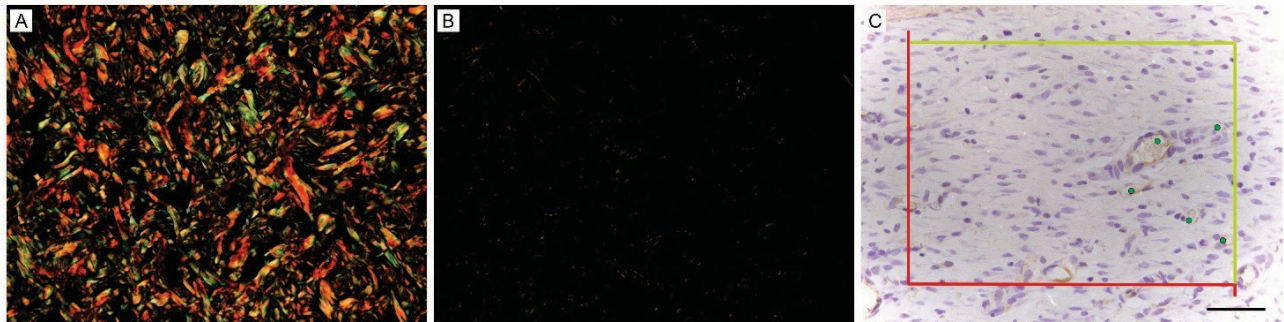
Fig. 2. Examples of histological evaluation. (**A**) skin without defect, Picrosirius red staining using polarized light to visualize type I collagen (yellow-red) and type III collagen (green), scale bar 50 µm. (**B**) healing skin defect, the same staining like A. (**C**) quantification of the microvessel density of the von Willebrand factor – positive vascular profiles (stained brown) in healing skin defect, red and green bars delimit area of interest, scale bar 50 µm.

IL6 concentrations in the plasma

Blood samples were taken from animals after their sacrifice by cardiac puncture to Li-heparin collection tubes. Samples were immediately centrifuged at 2000× g 10 min at 4 °C and plasma was collected and stored at -80 °C until analysis. IL6 concentration in plasma was determined by the Enzyme-Linked ImmunoSorbent Assay (ELISA) method using the RayBio® Rat IL6 ELISA Kit (RayBiotech, Peachtree Corners, Georgia, USA) according to the manufacturer's protocol.

Data presentation and statistics

Data are presented as means ± standard deviation. Statistical inference was performed using R statistical software (R Development Core Team 2020). Residuals of all models were visually checked to detect potential heteroscedasticity and biased predictions. All statistical models were extended by a permutational approach (5000 randomizations), which estimates statistical significances reliably even if sample sizes are small and assumptions of the fully parametric methods are not met (Good 2005).

The effect of HBOT on the volume fractions of collagen (types I and III) in the scar were modelled *via* beta regression with logit-link function using the 'mgcv' R package (Wood 2011). The ratio between collagen I and III in the scar (log2-transformed to eliminate heteroscedasticity) and the relative volume fraction of both collagens in the wound compared to the volume fraction in the adjacent healthy skin were modelled with a general linear model. As the volume fractions of collagen III and the ratio between the collagen types I and III within wound correlated with the values from the adjacent healthy skin (within-subject correlation), and inclusion of the out-of-scar measurements into models improved parsimony of the models (reflected by the decrease of 'Bayesian Information Criterion' [BIC], Burnham and Anderson 1998), the measurements from the healthy skin were included as covariates. In these cases, only the factor 'treatment' was randomized in a permutation test whereas the response variable and the covariate were unchanged.

Similarly to analysis of collagen, angiogenesis was evaluated in wounds of both groups and in adjacent healthy tissue.

To evaluate the effect of HBOT on the speed of wound area shrinking (from day 4 to day 18), we employed a linear mixed-effects model (using the 'nlme' R package; Pinheiro *et al.* 2018) with animal identity representing a random-effect factor (random intercept) and 'day', 'treatment' and 'day X treatment' interaction representing fixed-effects predictors. We used the square root transformation of the wound size to eliminate heteroscedasticity in residuals. As categorization of the 'day' led to increased BIC and the wound size decreased approximately linearly with time, the 'day' was treated as a numerical (non-categorical) variable. Only 'treatment'

was randomized (between the individuals) during the permutation test of the model.

Results

In the course of the first week after operation, 2 HBOT and 4 CONT rats died; these animals were excluded from the study that continued with 8 and 6 rats in the HBOT and CONT groups, respectively.

Macroscopic evaluation of wound area

The results of macroscopic evaluation are presented in Fig. 3 as a relative change in the defect size compared to the size on day 4, when HBOT was initiated (i.e. relative to the day 4 defect area). The data indicated that the rats subjected to the HBOT group had no tendency to heal faster than the CONT rats. The difference did not reach statistical significance at any time point evaluated.
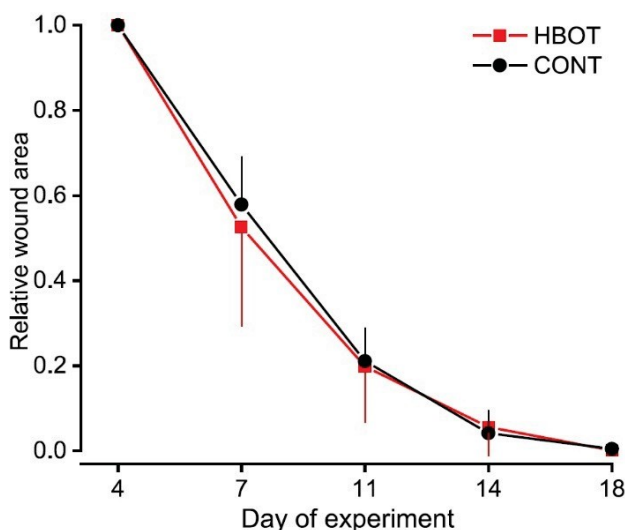

Fig. 3. Macroscopic evaluation of the wound. Wound area is relative to the area just before the first HBOT session (day 4 of the experiment). Data are means ± SD.

Quantitative histological evaluation of collagen

The results of histological analyses of the defects are shown in Fig. 4A-D. HBOT had no significant effect on the volume fraction of collagens in the skin outside the defect. As expected, the volume fractions of both collagen subtypes were substantially smaller in the defects than in the surrounding skin. The fraction of type I collagen was ~40 % higher in the HBOT wounds than in the control ones, but the values did not reach statistical significance (1.35 ± 0.49 and 1.94 ± 0.67 %, CONT and HBOT, respectively; p=0.1). In contrast,

collagen type III fraction was ~120 % higher in HBOT wounds (1.41 ± 0.81 %) than in CONT ones (0.63 ± 0.37 %; p=0.046). In addition, the ratio of the volume fraction of both collagens in the wound ($(I+III)_w$) to the volume fraction of both collagens in the adjacent healthy skin ($(I+III)_h$) was ~65 % higher in rats subjected to HBOT (8.9 ± 3.07 vs. 5.38 ± 1.86 %, HBOT and CONT, respectively; p=0.028). The collagen I/collagen III ratios did not differ significantly between the two groups (2.49 ± 0.83 and 1.63 ± 1.22 in CONT and HBOT groups, respectively; p=0.2) in the defects and reached the values 5.63 ± 4.18 and 4.52 ± 3.17 in the adjacent healthy skin of CONT and HBOT rats.
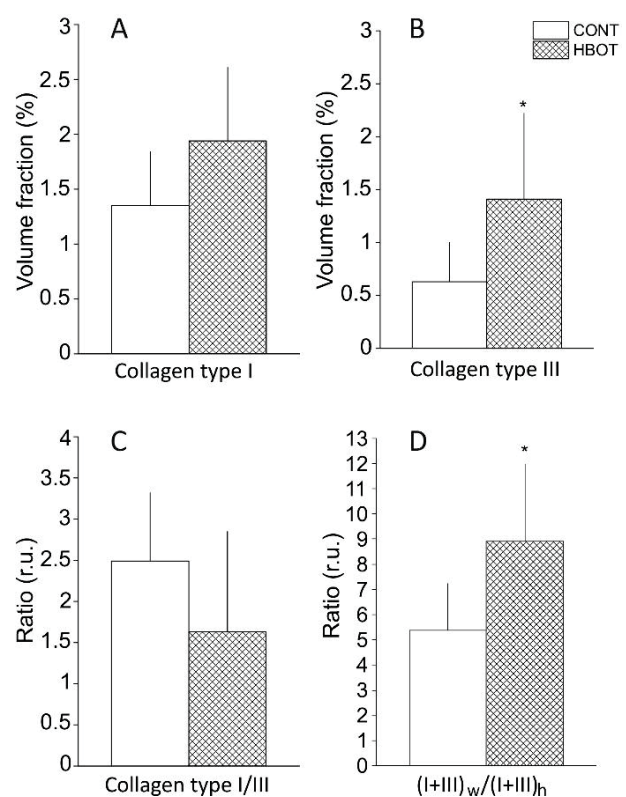
Fig. 4. Type I and type III collagen in the wound of control animals (CONT) and animals receiving hyperbaric oxygenotherapy (HBOT) after 18 days of healing. The volume fraction of type I collagen (**A**) and type III collagen (**B**) within the healing wound. The ratio between type I/type III collagens (**C**). The ratio between the volume fractions of both types of collagens within the wound to the volume fractions of both types of collagens within the adjacent healthy skin ($(I+III)_w/(I+III)_h$) (**D**). Values are means ± SD, r.u.=relative units; * p<0.05.

Quantitative histological evaluation of angiogenesis

Results are expressed as microvessel density (MVD), e.g. number of vessel profiles per 1 mm^2. As expected, MVD was much higher in the wounds compared to adjacent healthy tissue (206.5 ± 41.8 in the

wound of CONT, 78.1±20.8 in the healthy skin, p<0.001). On the contrary, HBOT did not enhance vessel generation, our results show rather opposite effect (MVD 124±28.2 in HBOT vs. 206.5±41.8 in CONT, p<0.001).

IL6 concentrations in the plasma

IL6 levels in the plasma of both CONT and HBOT rats did not exceed the detection limit of the kit, i.e. 30 pg/ml.

Discussion

The present study analyses the effects of HBOT on several parameters of wound healing in ZDF rats. The selected animal model is widely used in experimental practice to study the pathophysiology and secondary complications of Type 2 diabetes (Siwy *et al.* 2012). The ZDF model has also proven to be useful in evaluating the impact of diabetes on wound healing and neuropathy (Otto *et al.* 2011, Slavkovsky *et al.* 2011). Nevertheless, the effect of HBOT on the skin repair processes has been analyzed so far only in streptozotocin-induced diabetic rats with conflicting results (see Introduction).

Our study focused not only on the speed of reduction of the wound area, but also on the quantitative analysis of collagens I and III in the wound tissue and surrounding intact skin since the new production of collagen, its spatial distribution and metabolism play a major role in the restoration of homeostasis during the repair of skin defects (Wynn 2008). Histological evaluation of healing wounds often includes the rating of type I and type III collagens expressed as volume fractions (Clore *et al.* 1979, Dale *et al.* 1996, Wang *et al.* 2017).

Although macroscopic evaluation of the wound area did not show any trend to faster skin repair after HBOT, histological analysis brought about interesting outcomes. HBOT had a significant impact on collagen formation in the injured tissue leading to an increased volume fraction of collagen III at day 18 of the experiment, i.e. after 10 completed sessions of HBOT. In the study performed on B6.BKS(D)-Lepr db/db adult diabetic mice (spontaneous Type 2 diabetic mouse model with a low capacity to regenerate skin), the skin defect was created on the dorsal surface of the animal and a silicone O-ring was placed surrounding the wound and attached to the skin to prevent wound-healing by contraction. In this setting, the authors documented accelerated healing in animals subjected to HBOT (Pena-

Villalobos *et al.* 2018); however, no such ring was used in our study. The authors hypothesized that faster skin repair in hyperbaric oxygen conditions might improve collagen synthesis and epithelization in the wound bed. In our experiments, contraction of the wounds was not prevented, which might overlay the potential beneficial effect of HBOT on other repair processes. Nevertheless, the wound skin area of rats subjected to HBOT displayed a ~120 % higher volume fraction of collagen III and a ~65 % higher ratio of both collagens in the healing wound to intact surrounding skin, suggesting that the repair process was indeed accelerated by HBOT.

Wound healing is a complex sophisticated series of events resulting in the replacement of injured or missing tissue. The process of skin repair is usually described in three overlapping stages: inflammation, proliferation and tissue remodelling (Guo and DiPietro 2010, Velnar *et al.* 2009, Young and McNaught 2011). The inflammatory response to injury is mediated by damaged cells, resident immune cells and neutrophils and macrophages recruited in response to chemokines released from the tissue. The proliferative stage comprises angiogenesis, reepithelialisation, and fibroplasia aiming to decrease the area of lesioned tissue and create a new efficient barrier against the external environment. Fibroblasts recruited from the dermis of the adjacent skin proliferate in response to a number of cytokines, e.g. transforming growth factor-β (TGF-β) or platelet-derived growth factor (PDGF) (Guo and DiPietro 2010, Velnar *et al.* 2009, Young and McNaught 2011) and participate in collagen synthesis in the proliferative and remodeling phases of wound healing. The highest amounts of type III collagen appear five days after injury and contribute to the scar formation. During later phases of healing, i.e. remodelling, type I collagen is formed from the precursor type III collagen. The resulting new type I collagen, made of thicker and longer fibrils than the type III collagen, provides strength and mechanical stability (Campelo *et al.* 2018, Wang *et al.* 2015, Young and McNaught 2011).

We have not found any positive effect of HBOT on angiogenesis, on the contrary HBOT seemed to inhibit new vessel formation. This controversial result might be explained by complex reasons. Our evaluation (18th day after operation) was performed relatively late, when defects were almost healed. It should be noted that angiogenesis is rapid in the early phase of healing, supported by inflammation and in the later phases of healing, number of vessels decreases again (Di Pietro

2016). Other studies suggest that angiogenesis is supported by HBOT only in hypoxic tissues like in defects on leg after arterial ligation, skin grafts, contused mussels etc. (Huang *et al*. 2020, Yamamoto *et al*. 2020, Buckley and Cooper 2021, Yu *et al*. 2019). It is thus possible that in our setting, HBOT accelerated angiogenetic processes and at the time of evaluation, we did not detect the peak value of the density of newly formed vessels. In addition, our defects on rat back probably did not suffer from hypoxia.

In our study, we have not revealed any trend to general inflammation as documented by IL6 levels in the plasma that barely exceeded the detection limit of the assay with no difference between CONT and HBOT rats. Collagen I volume fraction in the healing skin of HBOT rats was ~40 % higher than in CONT animals, however this difference did not reach statistical significance (p=0.09). Taken together, our study suggests that HBOT promotes collagen III formation at least in the early phases of healing of uncomplicated skin defects in ZDF rats as documented by its increased volume fraction and elevated ratio of collagen I+III content in the wound area to intact surrounding skin.

Study limitations

Increased collagen III content in the wound area after HBOT does not necessarily mean that the healing process was really improved as this type collagen formation is typical for the initial phase of healing and final mechanical stability of the scar is mainly dependent on the conversion of type III to type I collagen. The collagen I/III ratio in healthy rat skin ranges between 4.6 and 8.5 and it is taken as an indicator of the quality of the collagen fibres network (Clore *et al*. 1979, Dale *et al*. 1996, Wang *et al*. 2017). In our analysis of the skin outside the wound this ratio reached the values 5.63±4.18 and 4.52±3.17 in CONT and HBOT rats, respectively.

The decreased collagen I/III ratio could imply lower connective tissue tensile strength (Klinge *et al*. 2000) and typically occurs in immature skin wounds before the final scar remodelling (Fleischmajer *et al*. 1990). Although no significant difference in this ratio was noticed in the wound area, HBOT tended to decrease it to 1.63±1.22 compared to CONT wounds (2.49±0.83).

It thus would be useful to extend the experiment duration to also map the later phases of healing and final collagen composition of the scarred tissue to verify the putative beneficial effect of HBOT on the final quality of the scar.

Although the original area of the skin defect was relatively large (200 to 300 mm²), the wounds nearly completely closed by day 18 of the experiment in both CONT and HBOT rats. For the following experiments focused on wound healing in ZDF rats, prevention of the defect contraction could be helpful in the detailed evaluation of individual healing stages.

Another limitation was that our study did not follow any damage to the innervation of the wound, although loss of cutaneous innervation from sensory neuropathy is included among mechanisms for impaired healing of diabetic skin wounds (Cheng *et al.* 2013). However, it was previously shown that the Type 2 diabetes in ZDF rats is accompanied with functional alteration of peripheral nerves (Katsuda *et al.* 2014).

Conflict of Interest

There is no conflict of interest.

Acknowledgements

References

ANDRÉ-LÉVIGNE D, MODARRESSI A, PIGNEL R, BOCHATON-PIALLAT ML, PITTET-CUÉNOD B: Hyperbaric oxygen therapy promotes wound repair in ischemic and hyperglycemic conditions, increasing tissue perfusion and collagen deposition. Wound Repair Regen 24: 954-965, 2016. https://doi.org/10.1111/wrr.12480

APELQVIST J: The foot in perspective. Diabetes Metab Res Rev 24 (Suppl 1): 110-115, 2008. https://doi.org/10.1002/dmrr.834

AYDIN F, KAYA A, KARAPINAR L, KUMBARACI M, IMERCI A, KARAPINAR H, KARAKUZU C, INCESU M: IGF-1 increases with hyperbaric oxygen therapy and promotes wound healing in diabetic foot ulcers. J Diabetes Res 2013: 567834, 2013. https://doi.org/10.1155/2013/567834

BROUWER RJ, LALIEU RC, HOENCAMP R, Van HULST RA, UBBINK DT: A systematic review and meta-analysis of hyperbaric oxygen therapy for diabetic foot ulcers with arterial insufficiency. J Vasc Surg 71: 682-692, 2020. https://doi.org/10.1016/j.jvs.2019.07.082

BUCKLEY CJ, COOPER JS: Hyperbaric affects on angiogenesis. StatPearls [Internet]. Treasure Island (FL): StatPearls Publishing; 2021. https://www.ncbi.nlm.nih.gov/books/NBK482485/

BURNHAM KP, ANDERSON DR: *Model Selection and Inference*. Springer, New York, 1998, 355 p. https://doi.org/10.1007/978-1-4757-2917-7

BUZGO M, PLENCNER M, RAMPICHOVA M, LITVINEC A, PROSECKA E, STAFFA A, KRALOVIC M, FILOVA E, DOUPNIK M, LUKASOVA V, VOCETKOVA K, ANDEROVA J, KUBIKOVA T, ZAJICEK R, LOPOT F, JELEN K, TONAR Z, AMLER E, DIVIN R, FIORI F: Poly-e-caprolactone and polyvinyl alcohol electrospun wound dressings: adhesion properties and wound management of skin defects in rabbits. Regen Med 14: 423-445, 2019. https://doi.org/10.2217/rme-2018-0072

CAMPELO MBD, SANTOS JAF, FILHO ALM, FERREIRA DCL, SANT'ANNA LB, OLIVEIRA RA, MAIA LF, ARISAWA EÂL: Effects of the application of the amniotic membrane in the healing process of skin wounds in rats. Acta Cir Bras 33: 144-155, 2018. https://doi.org/10.1590/s0102-865020180020000006

CHENG C, SINGH V, KRISHNAN A, KAN M, MARTINEZ JA, ZOCHODNE DW: Loss of innervation and axon plasticity accompanies impaired diabetic wound healing. PLoS One 8: e75877, 2013. https://doi.org/10.1371/journal.pone.0075877

CLORE JN, COHEN IK, DIEGELMANN RF: Quantitation of collagen types I and III during wound healing in rat skin. Proc Soc Exp Biol Med 161: 337-340, 1979. https://doi.org/10.3181/00379727-161-40548

DALE PD, SHERRATT JA, MAINI PK: A mathematical model for collagen fibre formation during foetal and adult dermal wound healing. Proc Biol Sci 263: 653-660, 1996. https://doi.org/10.1098/rspb.1996.0098

DIPIETRO LA: Angiogenesis and wound repair: when enough is enough. J Leukoc Biol 100: 979-984, 2016. https://doi.org/10.1189/jlb.4MR0316-102R

DREIFKE MB, JAYASURIYA AA, JAYASURIYA AC: Current wound healing procedures and potential care. Mater Sci Eng C Materl Biol Appl 48: 651-662, 2015. https://doi.org/10.1016/j.msec.2014.12.068

EAST B, PLENCNER M, KRALOVIC M, RAMPICHOVA M, SOVKOVA V, VOCETKOVA K, OTAHAL M, TONAR Z, KOLINKO Y, AMLER E, HOCH J: A polypropylene mesh modified with poly-ε-caprolactone nanofibers in hernia repair: large animal experiment. Int J Nanomedicine 13: 3129-3143, 2018. https://doi.org/10.2147/IJN.S159480

ELRAIYAH T, TSAPAS A, PRUTSKY G, DOMECQ JP, HASAN R, FIRWANA B, NABHAN M, PROKOP L, HINGORANI A, CLAUS PL, STEINKRAUS LW, MURAD MH: A systematic review and meta-analysis of adjunctive therapies in diabetic foot ulcers. J Vasc Surg 63: 46S-58S.e1-2, 2016. https://doi.org/10.1016/j.jvs.2015.10.007

FLEISCHMAJER R, PERLISH JS, BURGESON RE, SHAIKH-BAHAI F, TIMPL R: Type I and type III collagen interactions during fibrillogenesis. Ann N Y Acad Sci 580: 161-175, 1990. https://doi.org/10.1111/j.1749-6632.1990.tb17927.x

GOOD PI: *Permutation, Parametric and Bootstrap Tests of Hypotheses*. Springer, New York, 2005, 316 p. https://doi.org/10.1007/b138696

GUNDERSEN HJG: Notes on the estimation of the numerical density of arbitrary profiles: the edge effect. J Microsc 111: 219-223, 1977. https://doi.org/10.1111/j.1365-2818.1977.tb00062.x

GUO S, DIPIETRO LA: Factors affecting wound healing. J Dent Res 89: 219-229, 2010. https://doi.org/10.1177/0022034509359125

HOBIZAL KB, WUKICH DK: Diabetic foot infections: current concept review. Diabetic Foot Ankle 3: 18409, 2012. https://doi.org/10.3402/dfa.v3i0.18409

HORAKOVA J, MIKES P, LUKAS D, SAMAN A, JENCOVA V, KLAPSTOVA A, SVARCOVA T, ACKERMANN M, NOVOTNY V, KALAB M, LONSKY V, BARTOS M, RAMPICHOVA M, LITVINEC A, KUBIKOVA T, TOMASEK P, TONAR Z: Electrospun vascular grafts fabricated from poly(L-lactide-co-ε-caprolactone) used as a bypass for the rabbit carotid artery. Biomed Mater 13:065009, 2018. https://doi.org/10.1088/1748-605X/aade9d

HUANG X, LIANG P, JIANG B, ZHANG P, YU W, DUAN M, GUO L, CUI X, HUANG M, HUANG X: Hyperbaric oxygen potentiates diabetic wound healing by promoting fibroblast cell proliferation and endothelial cell angiogenesis. Life Sci 259: 118246, 2020. https://doi.org/10.1016/j.lfs.2020.118246

HUANG X, LIANG P, JIANG B, ZHANG P, YU W, DUAN M, GUO L, CUI X, HUANG M, HUANG X: Hyperbaric oxygen potentiates diabetic wound healing by promoting fibroblast cell proliferation and endothelial cell angiogenesis. Life Sci 259: 118246, 2020. https://doi.org/10.1016/j.lfs.2020.118246

JIRKOVSKÁ A: Adherence to the international guidelines on the treatment of diabetic leg syndrome. Vnitr Lek 57: 908-912, 2011.

JUNQUEIRA LCU, BIGNOLAS G, BRENTANI RR: Picrosirius staining plus polarization microscopy, a specific method for collagen detection in tissue sections. Histochem J 11: 447-455, 1979. https://doi.org/10.1007/BF01002772

JUNQUEIRA LCU, MONTES GS, SANCHEZ EM: The influence of tissue section thickness on the study of collagen by the Picrosirius-polarization method. Histochemistry 74: 153-156, 1982. https://doi.org/10.1007/BF00495061

KATSUDA Y, OHTA T, MIYAJIMA K, KEMMOCHI Y, SASASE T, TONG B, SHINOHARA M, YAMADA T: Diabetic complications in obese type 2 diabetic rat models. Exp Anim 63: 121-132, 2014. https://doi.org/10.1538/expanim.63.121

KLINGE U, SI Z, ZHENG H, SCHUMPELICK V, BHARDWAJ S, KLOSTERHALFEN B: Abnormal collagen I to III distribution in the skin of patients with incisional hernia. Eur Surg Res 32: 43-48, 2000. https://doi.org/10.1159/000008740

KRANKE P, BENNETT MH, MARTYN-ST JAMES M, SCHNABEL A, DEBUS SE, WEIBEL S: Hyperbaric oxygen therapy for chronic wounds. Cochrane Database Syst Rev 2015: CD004123, 2015. https://doi.org/10.1002/14651858.CD004123.pub4

KUMAR A, SHUKLA U, PRABHAKAR T, SRIVASTAVA D: Hyperbaric oxygen therapy as an adjuvant to standard therapy in the treatment of diabetic foot ulcers. J Anaesthesiol Clin Pharmacol 36: 213-218, 2020. https://doi.org/10.4103/joacp.JOACP_94_19

LIPSKY BA, SENNEVILLE É, ABBAS ZG, ARAGÓN-SÁNCHEZ J, DIGGLE M, EMBIL JM, KONO S, LAVERY LA, MALONE M, VAN ASTEN SA, URBANČIČ-ROVAN V, PETERS EJG; International Working Group on the Diabetic Foot (IWGDF): Guidelines on the diagnosis and treatment of foot infection in persons with diabetes (IWGDF 2019 update). Diabetes Metab Res Rev 36 (Suppl 1): e3280, 2020. https://doi.org/10.1002/dmrr.3280

MARGOLIS DJ, GUPTA J, HOFFSTAD O, PAPDOPOULOS M, GLICK HA, THOM SR, MITRA N: Lack of effectiveness of hyperbaric oxygen therapy for the treatment of diabetic foot ulcer and the prevention of amputation: a cohort study. Diabetes Care 36: 1961-1966, 2013. https://doi.org/10.2337/dc12-2160

MOHAMMADZADEH E, NIKRAVESH MR, JALALI M, FAZEL A, EBRAHIMI V, EBRAHIMZADEH-BIDESKAN AR: Immunohistochemical study of type III collagen expression during pre and post-natal rat skin morphogenesis. Iran J Basic Med Sci 17: 196-200, 2014.

OTTO KJ, WYSE BD, CABOT PJ, SMITH MT: Longitudinal study of painful diabetic neuropathy in the Zucker diabetic fatty rat model of type 2 diabetes: impaired basal G-protein activity appears to underpin marked morphine hyposensitivity at 6 months. Pain Med 12: 437-450, 2011. https://doi.org/10.1111/j.1526-4637.2011.01067.x

PACKER CF, ALI SA, MANNA B: Diabetic ulcer. StatPearls, Treasure Island (FL), StatPearls Publishing, PMID 29763062, 2021.

PEÑA-VILLALOBOS I, CASANOVA-MALDONADO I, LOIS P, PRIETO C, PIZARRO C, LATTUS J, OSORIO G, PALMA V: Hyperbaric oxygen increases stem cell proliferation, angiogenesis and wound-healing ability of WJ-MSCs in diabetic mice. Front Physiol 9: 995, 2018. https://doi.org/10.3389/fphys.2018.00995

PINHEIRO J, BATES D, DEBROY S, SARKAR D, R CORE TEAM: nlme: Linear and nonlinear mixed effects models. 2018. https://cran.r-project.org/web/packages/nlme/citation.html. Accessed September 24, 2018.

R Development Core Team: R: A Language and Environment for Statistical Computing. 2020. https://www.r-project.org/.

RAYMAN G, VAS P, DHATARIYA K, DRIVER V, HARTEMANN A, LONDAHL M, PIAGGESI A, APELQVIST J, ATTINGER C, GAME F; International Working Group on the Diabetic Foot (IWGDF): Guidelines on use of interventions to enhance healing of chronic foot ulcers in diabetes (IWGDF 2019 update) Diabetes Metab Res Rev 36: e3283, 2020. https://doi.org/10.1002/dmrr.3283

RICH L, WHITTAKER P: Collagen and picrosirius red staining: A polarized light assessment of fibrillar hue and spatial distribution. J Morphol Sci 22: 97-104, 2005.

SCHNEIDER CA, RASBAND WS, ELICEIRI KW: NIH Image to ImageJ: 25 years of image analysis. Nat Methods 9: 671-675, 2012. https://doi.org/10.1038/nmeth.2089

SIWY J, ZOJA C, KLEIN J, BENIGNI A, MULLEN W, MAYER B, MISCHAK H, JANKOWSKI J, STEVENS R, VLAHOU A, KOSSIDA S, PERCO P, BAHLMANN FH: Evaluation of the Zucker diabetic fatty (ZDF) rat as a model for human disease based on urinary peptidomic profiles. PLoS One 7: e51334, 2012. https://doi.org/10.1371/journal.pone.0051334

SLAVKOVSKY R, KOHLEROVA R, TKACOVA V, JIROUTOVA A, TAHMAZOGLU B, VELEBNY V, REZAČOVÁ M, SOBOTKA L, KANTA J: Zucker diabetic fatty rat: a new model of impaired cutaneous wound repair with type II diabetes mellitus and obesity. Wound Repair Regen 19: 515-525, 2011. https://doi.org/10.1111/j.1524-475X.2011.00703.x

TEGUH DN, BOL RAAP R, KOOLE A, KNIPPENBERG B, SMIT C, OOMEN J, VAN HULST RA: Hyperbaric oxygen therapy for nonhealing wounds: Treatment results of a single center. Wound Repair Regen 2020: 1-7, 2020. https://doi.org/10.1111/wrr.12884

THIRUVOTH FM, MOHAPATRA DP, KUMAR D, CHITTORIA RK, NANDHAGOPAL V: Current concepts in the physiology of adult wound healing. Plast Aesthet Res 2015: 250-256, 2015. https://doi.org/10.4103/2347-9264.158851

TONAR Z, KUBÍKOVÁ T, PRIOR C, DEMJÉN E, LIŠKA V, KRÁLÍČKOVÁ M, WITTER K: Segmental and age differences in the elastin network, collagen, and smooth muscle phenotype in the tunica media of the porcine aorta. Ann Anat 201: 79-90, 2015. https://doi.org/10.1016/j.aanat.2015.05.005

TONAR Z, EGGER GF, WITTER K, WOLFESBERGER B: Quantification of microvessels in canine lymph nodes. Microsc Res Tech 71: 760-772, 2008. https://doi.org/10.1002/jemt.20619

TUK B, TONG M, FIJNEMAN EMG, VAN NECK JW: Hyperbaric oxygen therapy to treat diabetes impaired wound healing in rats. PLoS One 9: e108533, 2014. https://doi.org/10.1371/journal.pone.0108533

VAN NECK JW, TUK B, FIJNEMAN EMG, REDEKER JJ, TALAHATU EM, TONG M: Hyperbaric oxygen therapy for wound healing in diabetic rats: Varying efficacy after a clinically-based protocol. PLoS One 12, e0177766, 2017. https://doi.org/10.1371/journal.pone.0177766

VELNAR T, BAILEY T, SMRKOLJ V: The wound healing process: an overview of the cellular and molecular mechanisms. J Int Med Res 37: 1528-1542, 2009. https://doi.org/10.1177/147323000903700531

VINIK AI, MASER RE, MITCHELL BD, FREEMAN R: Diabetic autonomic neuropathy. Diabetes Care 26: 1553-1579, 2003. https://doi.org/10.2337/diacare.26.5.1553

WANG T, GU Q, ZHAO J, MEI J, SHAO M, PAN Y, ZHANG J, WU H, ZHANG Z, LIU F: Calcium alginate enhances wound healing by up-regulating the ratio of collagen types I/III in diabetic rats. Int J Clin Exp Pathol 8: 6636-6645, 2015.

WANG Z, WANG Q, WANG L, XU W, HE Y, LI Y, HE S, MA H: Improvement of skin condition by oral administration of collagen hydrolysates in chronologically aged mice. J Sci Food Agric 97: 2721-2726, 2017. https://doi.org/10.1002/jsfa.8098

WANICZEK D, KOZOWICZ A, MUC-WIERZGOŃ M, KOKOT T, SWIĘTOCHOWSKA E, NOWAKOWSKA-ZAJDEL E: Adjunct methods of the standard diabetic foot ulceration therapy. Evid Based Complement https://doi.org/10.1155/2013/243568

WITTER K, TONAR Z, MATEJKA VM, MARTINCA T, JONÁK M, ROKOSNÝ S, PIRK J: Tissue reaction to three different types of tissue glues in an experimental aorta dissection model: a quantitative approach. Histochem Cell Biol 133: 241-259, 2010. https://doi.org/10.1007/s00418-009-0656-3

WOOD SN: Fast stable restricted maximum likelihood and marginal likelihood estimation of semiparametric generalized linear models. J Royal Stat Soc Stat Methodol 73: 3-36, 2011. https://doi.org/10.1111/j.1467-9868.2010.00749.x

WU Q: Hyperbaric oxygen for treatment of diabetic foot ulcers: love you more than I can say. Ann Transl Med 6: 228, 2018. https://doi.org/10.21037/atm.2018.04.33

WYNN TA: Cellular and molecular mechanisms of fibrosis. J Pathol 214: 199-210, 2008. https://doi.org/10.1002/path.2277

YAMAMOTO N, OYAIZU T, ENOMOTO M, HORIE M, YUASA M, OKAWA A, YAGISHITA K: VEGF and bFGF induction by nitric oxide is associated with hyperbaric oxygen-induced angiogenesis and muscle regeneration. Sci Rep 10: 2744, 2020. https://doi.org/10.1038/s41598-020-59615-x

YOUNG A, McNAUGHT CE: The physiology of wound healing. Surgery 29: 475-479, 2011. https://doi.org/10.1016/j.mpsur.2011.06.011

YU M, YUAN HS, LI Q, LI Q, TENG YF: Combination of cells-based therapy with apelin-13 and hyperbaric oxygen efficiently promote neovascularization in ischemic animal model. Eur Rev Med Pharmacol Sci 23: 2630-2639, 2019. https://doi.org/10.26355/eurrev_201903_17413